Numerical Modeling & Experimental Casting of AA6111 Aluminium Alloy and Advanced High Strength Steels (AHSS) produced through Horizontal Single Belt Casting (HSBC) Process

Usman Niaz

Department of Mining and Materials Engineering
McGill University
Montreal, Canada

July 2020

A thesis submitted to McGill University in partial fulfillment of the requirement of the degree of Doctor of Philosophy

ABSTRACT

This thesis investigates the possibility of producing high quality AA6111 aluminum alloy, and Advanced High Strength Steel, thin strips via the Horizontal Single Belt Casting (HSBC) process. For this purpose, both physical (using the HSBC simulator and HSBC pilot scale system) and numerical modeling, via Computational Fluid Dynamics (CFD) and computational thermodynamics, were conducted. Two and Three-dimensional models, incorporating the effects of turbulence, partial solidification, multiphase phase flow, and interface tracking were developed. CFD modeling was conducted using ANSYS Fluent 14.5 software, whereas FactSage software was employed to predict the composition type and relative amounts, as well as the stability of the solid phase present, depending on whether freezing occurs under equilibrium, or Scheil (rapid), cooling conditions, typical of an HSBC process.

The numerical simulations illustrated various complex phenomena, such as a) the sudden thickening (jump) of the entering molten metal on the inclined refractory plane and then onto the moving belt, b) a possible mechanism for air entrapment due to oscillating fluctuations of the molten metal/air interface near to the melt's impingement on the inclined refractory plane, c) the inward lateral flows of molten metal from its edges towards the centreline of the moving belt, and most importantly, d) the complete damping, or annihilation, of free surface waves downstream along the belt, (e) the effect of inclination angle on the stability of the falling molten metal free stream, (f) as well as, the increase in turbulent kinetic energy of molten metal at the triple point, due to an increase in the velocity of moving belt.

Similarly, Olson-Cohen modeling was carried out to determine the Stacking Fault Energy (SFE). This helped in understanding the phenomenon of Transformation Induced Plasticity (TRIP) as well as of Twinning Induced Plasticity (TWIP) in some Advanced High Strength Steels (AHSS), during their plastic deformation. Various analyses, such as microstructures, heat treatment, surface roughness, and composition, were also conducted. Results proved the wide applicability of this HSBC process to produce high-quality AA6111 and AHSS sheet material. The numerical modeling results were all found to be in close agreement with the experimental results.

RESUME

L’objectif de cette recherche est d ‘étudier la possibilité de réaliser des bandes minces de hautes qualités en alliage d’aluminum A6111 et en acier à haute propriétés mécaniques par le procédé de coulée en bandes. A cet effet, la modélisation numérique du procédé a été réalisée en utilisant le logiciel Ansys Fluent. Un model 2D et 3D incorporant les effets de turbulences, de la solidification partiel, de l’écoulement multiphasique, et la suivie de l’interface a été développé. Le logiciel FactSage a été utilisé pour prédire le type de composition et les quantités relatives, ainsi que la stabilité des phases solides présentes, selon que la solidification se produit à l'équilibre ou dans des conditions de refroidissement de Scheil (rapides) typiques d'un processus HSBC.

La simulation numérique a mis en relief des phénomènes complexes à savoir : le saut abrupte du métal liquide entrant sur plan de réfractaire incliné et puis sur la ceinture en mouvement, la possibilité de piéger de l’air à cause des oscillations du métal liquide a l’interface du plan incliné au niveau du point de contact avec le métal en fusion, les écoulement et les flux latéraux intérieurs de métal en fusion, de ses bords vers l'axe du tapis en mouvement, et surtout, l'amortissement complet ou l'annihilation des ondes de surface libres en aval le long de la ceinture. Ces ondes ont été générées à la suite de sauts abruptes à la surface du métal en fusion dans le plan réfractaire incliné et sur la ceinture en mouvement.

Par ailleurs, une modélisation Olson-Cohen a été réalisée pour déterminer l’énergie de défaut d’empilement (SFE). Cela a permis de mieux comprendre le phénomène de la plasticité induite par la transformation (TRIP), et aussi du maclage induit par la plasticité (TWIP) au cours de la déformation plastique de l’acier. Diverses analyses, telles que les microstructures, le traitement thermique, la rugosité et la composition, ont également été effectuées. Les résultats ont montré que le procédé de coulée en bande (HSBC) était largement applicable à la production de matériaux en feuille en AA6111 et en acier de haute propiétés AHSS. Les résultats de la modélisation numérique se sont tous avérés être en parfait accord avec les résultats expérimentaux.

Acknowledgments

This thesis has been the outcome of many years of learning, experimentation, critical analysis at every phase of its development, and sheer hard work. This would not have been possible without the able guidance and continued support in my research, received from my supervisors. I am indeed indebted to, Professor Roderick I.L Guthrie and Dr. Mihaiela Minea Isac for sharing with me their experience and vast knowledge. I shall not be honest if I do not acknowledge the useful contribution of Dr. Luis Calzado for his time to time advice and useful comments. Also, I would like to express my gratitude and thanks to Mr. Justin Lee and Mr Jason Hsin for their support throughout this study.

Last, but not least, I am grateful to my whole family, particularly my parents, for their continued moral support, encouragement, and patience for all these years. I dedicate this work to my living parents.

Contribution of Authors

This Ph.D. study is a collection of paper manuscripts, drafted by the candidate. I developed the theory, performed the numerical computations, designed and executed the experimental work associated with these publications. Professor Roderick. I. L. Guthrie and Dr. Mihaiela Isac, provided conceptual and technical guidance for all aspects of this research, and supervised the findings of this work. All authors discussed and contributed towards the final manuscripts.

The published manuscripts, or under publication review that are included in this thesis, are as follows:

Chapter 5 - Usman Niaz, Mihaiela M. Isac & Roderick I. L. Guthrie, "Numerical Modeling of Transport Phenomena in the Horizontal Single Belt Casting (HSBC) Process for the Production of AA6111 Aluminum Alloy Strip", publisher MPDI, in the Journal "Processes", 2020, Volume 8, pp: 529 - 538.

Chapter 6 - Usman Niaz, Mihaiela M. Isac & Roderick I.L. Guthrie "Horizontal Single Belt Casting (HSBC) of Thin Strips of an Advanced High Strength Steel (Fe-21%Mn-2.5%Al-2.8%Si-0.08 %C wt. %)", submitted to the Journal of "Steel Research International", presently under peer review.

Chapter 7 - Usman Niaz, Mihaiela M. Isac & Roderick I. L. Guthrie, "Numerical Modeling and Experimental Casting of 17%Mn–4%Al–3%Si–0.45%C wt. % TWIP Steel via the Horizontal Single Belt Casting (HSBC) Process", publisher Taylor & Francis, in the Journal of "Ironmaking & Steelmaking", 13 March 2020, pp: 1-14.

Table of Contents

Chapter 1

1.0. Introduction

The automotive industry is continuing improving their vehicles, in terms of classical performance, while maintaining tough engineering standards; the vehicles developed must adequately satisfy safety constraints, rigorous emission tests, and fuel efficiency standards. These performance metrics are heavily dependent on the use of a suitable material. These include the use of various metallic and non-metallic materials such as aluminum alloys, Advanced High Strength Steels (AHSS's), and Fiber Reinforced Polymer Composites (FRPC) [1, 2]. The main challenge is to reduce the weight of the vehicle's Body-In-White (BIW), while maintaining its passenger capacity and structural integrity [3]. (BIW means the weight of the automotive structure and exterior panels) [4].

The two most common engineering materials, replacing plain carbon steels are aluminum alloys (e.g. AA6111), and Light Weight Advanced High Strength Steels (TWIP/TRIP) [1, 2]. AA6111 alloy (density ≈ 2.69g/cm^3) possesses high tensile strength and can be readily molded into complex shapes [5]. The incorporation of A6111 alloy could easily decrease the weight of the Body-In-White (BIW) by up to 47 %, approximately [1]. However, the increased cost associated with aluminum production and its low ductility and modulus (1/3 that of steel) at room temperatures, remain significant obstacles for it to contend with steel, i.e., the draw-ability of the aluminum is not as high as its steel counterpart [5].

On the other hand, Advanced High Strength Steel (AHSS) are lighter than regular plain carbon steels because they contain lightweight elements, such as aluminum and silicon, and have unique combinations of mechanical strength and formability characteristics, making them candidate materials for automotive applications [2]. Additionally, the higher tensile strength (> 1000 MPa) of AHSS offsets its density (≈ 6-6.5 g/cm^3); making AHSS a better choice than AA6111 alloy when considering the aspect of relative safety [5].

1.1. Objectives of the Research Study

On the basis of the above discussion, it can be said that both aluminum alloys and AHSS have associated advantages and disadvantages. However, both materials have gained considerable importance in the design of automotive structures. The present Ph.D. work, therefore, focuses on the development of AA6111 alloy and AHSS strip using the Horizontal Single Belt Casting (HSBC) process. The HSBC process can bring a number of economic advantages, versus the conventional Continuous Casting (CC)/Direct Chill (DC) casting methods for steel/aluminum strip production [6]. The Continuous Casting process requires many processing steps, such as slab casting followed by multiple hot deformation steps (roughing and finishing), before it can be subsequently cold rolled to finished gauges [7]. By contrast, the HSBC method involves the feeding of molten metal at a preselected flow rate onto a chilled, moving belt, on which it solidifies to form 3mm - 15mm thick strip [8]. After casting, the strip is guided through a pinch roll, and one, or two hot rolling stands, where its thickness is reduced to the desired dimension [8]. By a simple comparison, the HSBC processing routes are much shorter than CC/DC, since the thickness of HSBC cast product is 7– 10 times less than CC/DC cast products i.e. 70 mm. It therefore requires less reduction passes to produce the desired final thickness of sheet material, with a much more versatile, and relatively inexpensive machine [8]. A brief overview of the strip casting processes is presented as follows

1.2. An Overview of Strip Casting

Ferrous and non-ferrous sheets are required to produce automotive Body-In-white (BIW). These sheets are typically of the order of 1-2 millimeters and are produced through a series of hot/cold deformations processes. The process, through which automotive sheets are produced, has evolved over time. Chiefly, after the advent of continuous casting/direct casting processes, ingot casting was classified as an obsolete and outdated process [9]. In the ingot casting process, the liquid metal is first poured into metallic molds. After the solidification is completed, the ingots are taken out of the molds and introduced into a soaking pit or furnace. After they have reached the appropriate working temperature, a series of hot/cold deformations are applied, until desired thickness sheet material is obtained [9].

Unlike ingot casting, continuous casting is a process whereby molten metal is solidified into a semi-finished product such as a billet, bloom, or slab [10]. The semi-finished products are further rolled in the finishing mills which are integrated with the CC machine. This improves the overall efficiency/yield of the process, as compared to the ingot casting process [7, 10].

In 1989, the Thin Slab Casting (TSC) process was introduced, having the capability to produce 50-60 mm thick slabs, directly from the hot metal. Subsequent casting and rolling setups are integrated into a continuous process. Since fewer hot deformation steps are required to produce desired thickness sheet material, the overall efficiency and cost-effectiveness of TSC is considerably higher, as compared to the CC process [7].

Based on the concept presented above, the strip casting processes can bring down the overall cost associated with hot rolling operations, since the as-cast thickness is only 10-20 mm and fewer hot deformation steps are required to produce desired thickness of sheet material. Two most common types of strip casting processes are the Horizontal Single Belt Casting (HSBC) and Twin Roll Casting processes. HSBC and TRC processes are also known as Near Net Shape Casting (NNSC) processes since the cast thickness nearly approaches the final product thickness [8]. Since cast thickness is of the order of few millimeters for HSBC, higher heat extraction rates can be achieved. Due to high cooling rates, the resulting cast structure is fine, with negligible macro-segregation [11].

The distinctive feature of the Strip Casting Processes is the ‘moving mold’ design, unlike CC process in which the mold oscillates at a predefined frequency. As the name suggests, TRC utilizes a revolving water-cooled mold as opposed to the HSBC process which consists of a mold moving in a horizontal direction. They can be further classified as Single- and Twin-Rolled Casting (SRC and TRC) and Single- and Twin Belt Casting (SBC and TBC) [11, 12].

The growth of strip production technologies is summarized in Figure 1, There it shows how these technologies evolved with the passage of time. Starting from the continuous casting process leading to the production of the strip using the Horizontal Single Belt Casting (HSBC) and the Twin Roll Casting (TRC) processes, the decrease in equipment size and processing stages can be clearly observed [11.12].

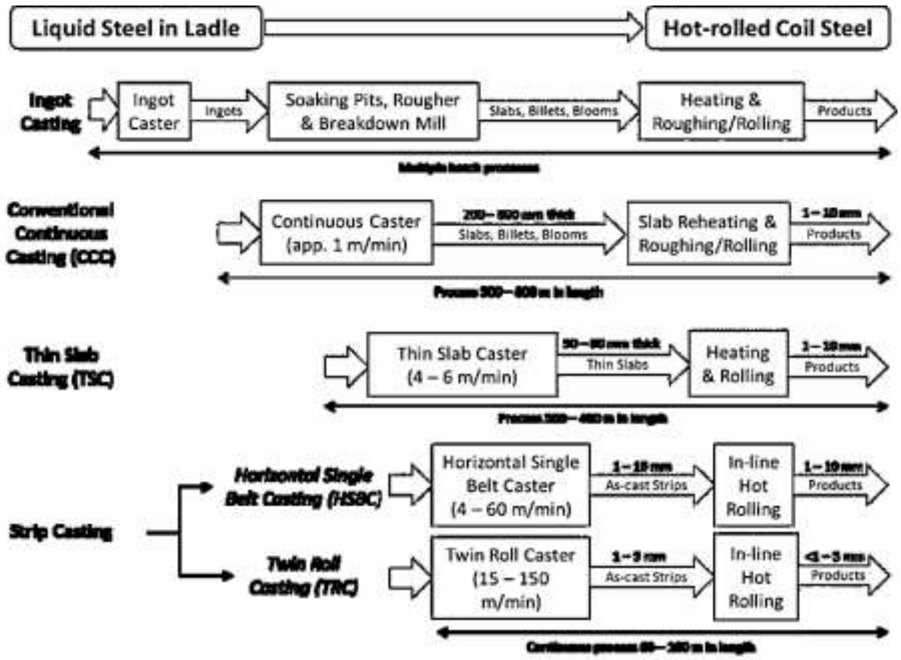

Figure 1: Evolution of hot strip production [12].

1.3. Structure of the Current Thesis

This thesis consists of eight chapters, wherein **Chapter 2** gives a brief history of the development of AA6111 alloy for the automotive industry. Described afterward are the effects of the alloying elements on the mechanical properties of AA6111 alloy and heat treatment that can be applied to automotive-grade sheet material production. Presented later are the various categories of Advance High Strength Steels with a focus on the TRIP/TWIP steels in which both TRIP/TWIP mechanisms coexist during plastic deformation. The latter part of this chapter discusses the Horizontal Single Belt Casting (HSBC) process in detail.

Chapter 3 describes the experimental procedure involved in the production of AA6111alloy and AHSS strips via HSBC process. In this chapter, the general operation of the HSBC pilot and HSBC simulator systems, along with heat treatment procedures employed to develop fully austenitic high manganese steels are presented. Additionally, details related to shear punch testing, as well as to surface roughness evaluation using a 3D profilometer, are also provided.

Chapter 4 provides the details, related to the use of the numerical models and methods. Furthermore, the procedures to solve the governing equations are explained. Finally, the specific method to calculate the Stacking Fault Energy (SFE) with a special focus on measuring a Gibbs free energy of transformation via Regular Solution Modeling approach is also illustrated.

Chapter 5 presents the paper entitled "Numerical Modeling of Transport Phenomena in the Horizontal Single Belt Casting (HSBC) Process, for AA6111 Alloy Strip" published in "Processes" Journal**.** This chapter discusses the casting of AA6111 aluminum alloy strip, 250 mm wide and 6mm thick via the Horizontal Single Belt Pilot Caster. In this research study, a three-dimensional CFD model was developed, to examine the flow of the molten AA6111 alloy in HSBC process. The phenomenon behind the formation of center shrinkage defect is explained and remedial measures to prevent its occurrence are proposed. The experimental findings are in accord with the model predictions. The microstructures of the strip produced, were evaluated using optical and scanning electron microscopes. Surface roughness was measured using the Nanovea 3D optical profilometer.

Chapter 6 presents the paper entitled "Horizontal Single Belt Casting (HSBC) of Thin Strips of a TRIP/TWIP Steel (Fe-21%Mn-2.5%Al-2.8%Si-0.08 %C wt.%)" submitted to "Steel Research International" Journal, currently under review.

Chapter 7 presents the paper "Numerical Modeling and Experimental Casting of 17%Mn-4%Al-3%Si-0.45%C wt.%) TWIP Steel via Horizontal Single Belt Casting (HSBC) Process", published in the "Iron Making & Steel Making" Journal. These two chapters, Chapter 6 & 7 discuss the numerical modeling and experimental casting of Advanced High Strength Steel (AHSS) via the HSBC process. The significance of iso-kinetic feeding of molten metal over the moving belt in the HSBC process, as well as the phenomenon of air entrainment caused by the oscillatory flow of molten metal over the inclined refractory plane and the moving belt, is explained in the light of the CFD numerical modeling results. The phenomenon of the molten metal/air interface fluctuations over an inclined refractory plane is also illustrated. The Stacking Fault Energy (SFE) of the alloy is determined using the Olson-Cohen modeling approach, whereas FactSage software was used to predict the liquidus and solidus temperatures, as well as the types and amounts of the solid phases present, under the relevant, rapid (Scheil)-cooling conditions. Mechanical properties of the hot deformed and heat-treated strip were evaluated via the Shear Punch Test (SPT) technique, whereas surface roughness was measured using the Nanovea 3D optical profilometer.

Chapter 8 presents a summary and conclusions of the work described in this thesis, and present my original contributions to knowledge in this field of engineering.

Chapter 2

2.0. Literature Review

2.1. Aluminum Alloys & Advanced High Strength Steels (AHSS) used in the Automotive Industry

The development and use of aluminum alloys in the automotive industry dates back to 1982, when the Energy Conservative Vehicle (ECV) programs were launched. ECV brought new ideas to automotive manufacturers and was a significant development program, to explore the feasibility of ultra-fuel-efficient vehicles. The bodyweight of the ECV 3 was 138 kg, against 247 kg for the equivalent steel structure [13]. The internal space was the same as the average mid-range car. The ECV program inspired many companies, such as the Rover company, Bertone, Pontiac, MG, Jaguar, and Ferrari., in the mid-and late-1900's, to use aluminum alloys (5xxx and 6xxx), in the manufacture of their vehicles [13].

The unprecedented use of aluminum alloys in the automotive industry continued thereafter with 5xxx and 6xxx series aluminum alloys remaining at the forefront, in the production of automotive components. In fact, almost all present-day automotive companies such as Audi, Volkswagen, Toyota, Daihatsu, Honda, Subaru, Mazda, Mitsubishi, Ford, and BMW, are now utilizing aluminum alloys in automobile manufacturing [3, 13].

After witnessing the immensely successful use of aluminum in BIW, steel manufacturers sought to realize even more robust vehicles through the incorporation of AHSS. Their objective was to fulfill the industry's requirements of better fuel economy (decreasing the weight) and safety (increasing the dent-resistant) of the vehicle [14]. Several projects were initiated, in which the Ultra-Light Steel Auto Body (ULSAB) program, was the first. Started later, was the Ultra-Light Steel Auto Closures (ULSAC) program, in which different automotive components such as hoods, doors, and deck lids, were successfully manufactured using Advanced High Strength Steels (AHSS). The ULSAC program was followed by the Ultra-Light Steel Auto Body-Advance Vehicle Concept (ULSAB-AVC), and the Future Steel Vehicle (FSV) program, which introduces Giga Pascal steels, and further refines the fabrication methods associated with AHSS [3, 4].

Both 6xxx aluminum alloys and AHSS's are very successfully fulfilling the US government safety regulations, such as those for impact resistance and tensile strength, therefore, providing both economic and environmental incentives during the use of the vehicles. Several Life Cycle Assessment (LCA) studies have shown that aluminum alloys and AHSS's, when used in the automotive industry, can result in a reduced carbon footprint, in comparison with other engineering materials. As a result, aluminum alloys and AHSS have been developed, so as to remain fully competitive, by providing the correct balance between strength for performance and good ductility for ease of production, as compared to other materials, such as plastics and composites [3].

2.2. Aluminum Alloys used in Automobiles

For automobile applications, 2xxx, 6xxx and 7xxx aluminum alloys are commonly used. However, 6xxx are mostly preferred by automotive manufacturers owing to their high strength to weight ratio, good formability, ease of joining and corrosion resistance as compared to 2xxx and 7xxx aluminum alloy series [1, 5]. The designation of wrought aluminum and its alloys are presented in Table 1.

6xxx aluminum alloys are strengthened through grain boundary, solid solution, work and precipitation/age hardening mechanisms. The principle alloying elements present in this system are aluminum, magnesium, silicon, and copper [5]. Details will be presented in later paragraphs.

Table 1: Designation of wrought aluminum and its alloys [5].

Alloying elements	Series designation
Pure aluminum	AA1XXX
Copper	AA2XXX
Manganese	AA3XXX
Silicon	AA4XXX
Magnesium	AA5XXX
Magnesium and Silicon	AA6XXX
Zinc	AA7XXX
Lithium	AA8XXX

2.3. Processing of 6XXX Aluminum Alloys

Mechanical properties of 6xxx aluminum alloys, depend on several factors, such as concentration of alloying elements in the alloy i.e. the composition should be such that it renders a superior microstructure with an optimum quantity of precipitates dispersed throughout the matrix, an appropriate forming method that ensures the production of a high-quality product, and finally, the selection of an appropriate heat treatment procedure [15-20].

This is true for aluminum alloys where temper designation describes the sequence of processing methods that can be applied to cast products, for example, a temper designation H describes a work hardening process plus two other elevated temperature treatments such as partial recrystallization annealing and stabilization heat treatment [20, 21]. The subdivisions of work hardening (H) are mentioned in Table 3. Table 2 show various other temper designations [20, 21].

Table 2: Basic temper designations of aluminum alloys [20, 21].

Temper	Treatment	Description
F	Fabricated	For cast and hot/cold worked products.
O	Annealed	Annealing heat treatment applied to restore ductility and to obtain lowest strength temper.
H	Strain Hardened	Work hardening applied to wrought products with or without supplementary high-temperature treatment. H is always followed by two or more digits to specify processing conditions.
W	Solution Treated	Room temperature aging after solution heat treatment, the number follows to indicate the time of the aging.
T	Stable Tempers	Stable temper after heat treatment with or without supplementary work hardening.

Table 3: Subdivision of H temper [20, 21].

Subdivision	Treatment	Description
H1	Work Hardened	Work hardened products without elevated temperature heat treatment. H1 is followed by digits to specify the amount of work hardening.
H2	Work hardened and partially annealed	Work hardened products which are annealed to reduce the strength. The H2 is followed by digits showing the extent of work hardening after annealing.
H3	Work hardened and stabilized	Work hardened products are stabilized for the following two reasons: (a) Low-temperature treatment or (b) Heat introduce during the deformation process. H3 is followed by digits, showing remaining work hardening after stabilization.

Table 4: Designation of elevated temperature treatments [20, 21].

Temper	Treatment	Description
T1	Stable temper applied after elevated temperature processing of products.	Only elevated temperature processing is applied to a product followed by natural aging at room temperature. The final product's properties are not representative of room temperature processing.
T2	Elevated temperature processing followed by room temperature working and temper aging to a stable condition.	The product properties are enhanced by cold working and natural aging treatment after cooled from some high-temperature processing such as rolling or extrusion
T3	The solution heat treatment is followed by cold working and temper aging to a stable condition.	The product properties are enhanced by cold working and natural aging treatment, after solution heat treatment.
T4	The solution heat treatment followed by temper aging to a stable condition.	The product properties are enhanced by natural aging treatment, after solution heat treatment. Room temperature working is not performed.
T5	The material is artificially aged after elevated temperature working.	The product properties are enhanced by artificial aging without undergoing any room temperature processing.
T6	Solution heat-treated and then artificially aged.	The product is artificially aged after solution heat treatment without undergoing any room temperature working. The final product's properties are not representative of room temperature processing such as straightening or flattening.
T7	Solution heat treated and overaged/stabilized.	Material's strength decreases after artificial aging process due to the formation of over-aged precipitates. However, the resistance to stress

		corrosion cracking, or exfoliation corrosion is considerably improved.
T8	Solution heated, ambient temperature worked, and then artificially aged.	The product properties are enhanced by ambient temperature working followed by artificial aging treatment.
T9	Solution heat treated, artificially aged, and then work hardened.	The work hardening is performed after the artificial aging process. This treatment greatly improves the mechanical strength of the alloy.
T10	Cooled from elevated temperature processing, cold worked and artificially aged.	The material is worked at room temperature and artificially aged after elevated temperature processing. This treatment greatly improves the mechanical strength of the alloy.

2.3.1 Homogenization Process

In the homogenization process, the 6xxx aluminum alloy is exposed to a high temperature (460°C-550°C). The general purpose of homogenization is not only to reduce the micro segregation present in cast structure but also to smoothly execute the downstream processing such as hot deformation, etc. Furthermore, uniformity in chemical composition can be readily achieved via a homogenization process [22-25]. It is important to mention that the homogenization process is effectively fast when diffusion distances are small. As such, the HSBC cast product with narrow range of SDAS values across the thickness should homogenize much faster than a thicker DC cast product [22-25].

The homogenization time depends on the type and quantity of the alloying elements present in aluminum alloys. Cr, Mn, V, and Zr have a relatively low diffusion rate through the aluminum matrix and aluminum alloys containing these alloying elements normally require longer homogenization times. On the other hand, aluminum alloys, containing copper, magnesium, and silicon, which are known to diffuse faster, tends to homogenize in comparatively less time [26-28]. Lastly, homogenization time also depends on sample dimensions, and the characteristics of the cast structure, i.e., if the distance between the primary and secondary dendrite arm spacing is small, the diffusion distances will be shorter which in turn accelerates the homogenization process as described above [26-28].

2.3.2 Plastic Deformation

Rolling, forging and extrusion are the most common types of hot working processes used to transform cast aluminum alloy structures into useful products [15]. Rolling and forging are regarded as direct compression type deformation processes, whereas the extrusion process comes under the category of indirect compression. Stretch forming is another kind of deformation process in which the material is deformed under tension. Generally, the metalworking process is broadly classified into two type's namely hot working and cold working. Hot-working of 6xxx aluminum alloys is done at an elevated temperature (>0.5T_O), where T_O is the melting temperature of 6xxx alloy in Kelvin units [24, 29-31]. Continuous recrystallization during hot deformation allows for a large deformation in one pass, as opposed to cold working processes. The conventional hot rolling of 6xxx aluminum alloys is done in two stages. In the first stage, the cast product is hot deformed in a break down mill, which produces a transfer slab of 30-50 mm thickness [24]. In the second stage the final reduction is carried out in a tandem mill. This produces 6mm thick plate of 6xxx aluminum alloys [15, 24].

Some of the advantages of hot deformation process are:

(a) Break down of cast dendritic structure.
(b) During hot reduction, the aluminum alloys are continuously recrystallized, and form strain-free equiaxed grains.
(c) There is no strain hardening of material during hot plastic deformation manifested by constant flow stress throughout the deformation process.
(d) The dynamic recrystallization of metal depends on the amount of strain or critical strain rate applied during hot rolling. This leads to the nucleation of strain-free grains which further grows to replace the deformed ones [19, 24].

One of the disadvantages of hot working is the formation of the oxide layer. The higher the temperature of the material at which hot reduction is performed, the larger will be the chances of surface oxidation. Furthermore, the recrystallization temperature also depends on the degree of deformation. Also, if the material is heavily deformed, the recrystallization temperature is further decreased. The upper limit for the deformation temperature is determined by heavy surface oxidation, or localized melting of segregated alloying elements, at grain boundaries.

The hot rolling of 6xxx is generally carried out in multiple passes. The temperature of the metal in every pass is kept above the temperature of recrystallization, except for the last pass, in which the temperature is considerably lower, to enhance the formation of fine grains [15]. The salient features of the hot working of 6xxx aluminum alloy are discussed below [27]:

(a) Formability of 6xxx aluminum alloys increases with an increase in the deformation temperature.
(b) Chemical inhomogeneities present in a cast material are appreciably reduced, after plastic deformation.
(c) Blowholes/pinholes present in the cast product get welded after plastic deformation.
(d) The dendritic structure of the cast product is replaced by strain-free equiaxed grain after plastic deformation.

2.3.3. Cold Working

Cold working is generally carried out, so as to improve the surface finish of a hot-rolled product. This is required since after hot reduction, the surface is rough due to oxidation and contraction/expansion of metal at high temperature. Another purpose of cold deformation is to improve the strength of the alloy via work hardening phenomena [15]. This topic is briefly explained in the following paragraphs.

The cold deformation of 6xxx aluminum alloys is generally carried out in multiple passes i.e. in small increments, since these alloys demonstrate low plasticity at room temperature, and this restricts a large reduction in one pass.

Additionally, the strength and hardness of cold-rolled plates gradually increase with cold deformation. Optical microscopy reveals that with each deformation pass, the aspect ratio of the grains increases until they appear to look like a band, parallel to the working direction [32].

2.3.4. Annealing Treatment

6xxx aluminum alloys are annealed prior to cold working or in between cold working (intermediate, or process annealing). The batch annealing process for 6xxx aluminum alloys consists of raising the temperature of hot-rolled sheets in between 380°C-460°C, followed by cold deformation. In continuous annealing, a slightly higher temperature is used i.e. 510°C [33]. For 6xxx aluminum alloys, the annealing process is generally carried out to soften the sheet material for increasing its deformation capabilities during the cold deformation process [15].

The formation of strain-free grains after the annealing process induces softness into the sheet material. As a result, the sheet material can be further cold roll until the desired thickness is achieved. However, in the last deformation step, the annealing process can simply be omitted in order to produce high strength sheet material. Additionally, the strength and hardness of the final gauge can be varied by modifying the cold rolling and the intermediate annealing process [15].

2.3.5 Aging Process

Aging treatment is generally carried out to increase the properties of 6xxx aluminum alloy. This treatment consists in raising the temperature of the material to an elevated temperature i.e. in between 520°C - 550°C, holding it there for an appropriate time (solutionizing), followed by quenching to room temperature, in order to obtain a supersaturated solid solution (SSS). Slow cooling is avoided, so as to prevent the precipitation of equilibrium phases [34-37].

After quenching, the material is either naturally aged (at room temperature) or artificially aged (at an elevated temperature) in the range 160°C-180°C [34-37]. The aging process increases the mechanical strength of the alloy via the precipitation of non-equilibrium metastable, or transition phases such as Guinier-Preston (GP) zones, and hexagonal $\beta^{//}$ and $\beta^{/}$(Mg2Si) regions. These secondary particles are coherent with the matrix which strengthens the alloy against plastic deformation [34-37].

Additionally, other precipitates can also exist in 6xxx aluminum alloys, such as hexagonal $Q^{/}$

and Q phases which are responsible for increasing the strength of the alloy. Unlike $\beta^{/}$ that has needle shape, $Q^{/}$ and Q phases have “lath” features [36].

Precipitation hardening is remarkably effective if the metastable/transition phases are coherent with the aluminum matrix, i.e., the dislocation motion will be impeded by the precipitates, making the plastic deformation difficult. However, often the phases grow to the extent where they become incoherent with the matrix, thereby resulting in reducing the strength of the 6xxx aluminum alloys. This topic has been explained in the following sections [35, 36].

The strength of the 6xxx aluminum alloys can also be increased via reversion and re-aging (RRA) heat treatment. The RRA technique is generally adopted by the automotive industry to improve the surface properties of the sheet material i.e. to refine the grain structure near the surface. In RRA, artificially aged 6xxx aluminum alloys are heated to above the GP solvus, and then quickly aged to a temperature below GP solvus [38].

2.4. Strengthening Methods for 6xxx Aluminum Alloys

The mechanical properties of 6xxx aluminum alloys can be improved through the following strengthening mechanisms.

(1) Grain-Boundary Strengthening.
(2) Precipitation Strengthening
(3) Work Hardening

2.4.1. Grain Boundary Strengthening

At the microscopic scale, plastic deformation is due to motion of dislocation within the material. The general purpose of grain boundary strengthening is to increase the resistance to the motion of dislocation. This could be readily achieved via increasing the number of grain boundaries within a material. After continuous deformation, the dislocations started to pile up at grain boundaries making it hard for dislocations to move. As a result, the strength of the material increases. The Hall-Petch equation can also be used to evaluate the dependence of yield strength of grain size for 6xxx aluminum alloys [15].

By properly setting up the solidification and plastic deformation processes (hot rolling and cold rolling sequences) followed by heat treatment procedures, the grain structure/mechanical properties of the final product can be tailored as per the specifications. For example, a higher solidification rate of the 6xxx aluminum alloys during the casting process can reduce the dendritic cell size or more appropriately dendritic arm spacing length. Furthermore, addition of minimal amount of master alloy (Al-5%Ti-1%B) before the casting can significantly refine the microstructure of the cast product. The following mechanisms are involved with the addition of Al-5% Ti-1%B master alloy [39-42].

(a) Heterogeneous nucleation of TiB_2, $(TiAl)B_2$, and TiC particles, which thereby provides nucleation sites for new grains to grow.

(b) In polycrystalline 6xxx aluminum alloy, the work hardening rate of the individual grains depends on the texture, which means that each grain has different deformation capabilities. This is reflected by the Taylor Factor (M_σ), used to relate the yield strength, Y, of polycrystals of cubic metals to the critical resolved shear stress (CRSS), of a reference single crystal, such that: $M_\sigma = \frac{Y}{\tau_O}$. In 6xxx aluminum alloys, the average value of this factor is approximately equal to 3.10, this texture hardening can be 10 times higher than for a single crystal of 6xxx material.

2.4.2. Precipitation Strengthening

6xxx aluminum alloys can be strengthened via the precipitation hardening phenomenon. The precipitates are coherent with the matrix and impede with the motion of the dislocations, thereby increasing the strength of the alloy [36]. $\beta^{/}$ and $\beta^{//}$ are needle-shaped, unlike $Q^{/}$ precipitates that have a lath structure. $Q^{/}$ precipitates form when copper is added into the aluminum, magnesium and silicon system, whereas $\beta^{/}$ and $\beta^{//}$ form without the addition of copper. Both, $\beta^{/}$, $\beta^{//}$ and $Q^{/}$ precipitates are coherent with the matrix [36].

In 6xxx aluminum alloy, the tensile strength and hardness decrease with over-aging. Over aging is a condition in which a precipitate loses its coherency within the matrix (lattice mismatch). Coherency strain field does not exist around incoherent precipitates. As a result, a dislocation can easily by-pass hard, incoherent precipitates, instead of interacting with them. This interaction is important, as it hinders the motion of the dislocation and strengthens the material. The higher the volume fraction of these precipitates, the larger will be the strengthening effect [43-49].

Furthermore, the yield strength of the precipitates is higher than the yield strength of the matrix, this increases the overall lattice friction stress i.e. Peierl’s stress, for the movement of dislocations. This strengthening effect increases with volume fraction and size of the precipitates. For incoherent precipitates, the strengthening comes from dislocation bowing around the precipitates with certain interparticle distance [25].

2.4.3. Work Hardening

Work hardening is a phenomenon in which the strength of the 6xxx can be increased via plastic deformation mechanism. With continuous deformation, the density of the dislocations within the material increases, due to dislocation emission from the step and ledges of grain boundaries. This is the so-called Frank-Read mechanism of dislocation regeneration, when a moving dislocation is pinned between precipitates, solutes, etc., and by multiple cross-slip mechanisms [50-53].

The restriction in the movement of a dislocation, caused by its interactions with jogs, kinks, grain boundaries, precipitates, etc., results in a dislocation pile-up on a slip plane, which thereby generates a high back stress against an applied stress [50-53].

Furthermore, in 6xxx aluminum alloys, Frank-Read partial dislocations form. These are a sessile type of barrier. In addition to Frank-Read partial dislocations, another dislocation reaction, which gives rise to the generation of sessile barrier is Lomer-Cottrel effect. Further details can be read from the references provided. These two different kinds of sessile barriers make the plastic deformation of 6xxx aluminum alloy much more difficult [50-53].

2.5. Characteristics of AA6111 aluminum alloy

AA6111, an alloy of aluminum, magnesium, silicon and copper, is considered the most promising candidate for the manufacturing of automotive body panels. AA6111aluminum alloys possess higher mechanical strength (i.e., 400 MPa), good formability, and good corrosion resistance. However, AA6111 has poor weldability and is prone to weld cracking, due to grain boundary liquation, that can occur in AA6111-T4 welds. However certain welding conditions can help in reducing the hot cracking. These measures include reducing joint restraint by proper preheating of the workpiece, improving weld geometry, or controlling the weld metal composition/solidification structure. The main mechanism behind AA6111's increased strength, is precipitation hardening, along with solid solution and work strengthening. The alloying elements present in AA6111 are briefly discussed as follows [5].

AA6111 are strengthened via a combination of processing conditions such as solution annealing, quenching, natural and artificial aging [54]. For AA6111, T4 and T6 temper heat treatment are commonly applied [54, 55]. Details related to T4 and T6 tempers have been described before and are therefore not repeated here.

2.5.1. Alloying Elements Present in AA6111 Aluminum Alloy, and their Effects on Properties

Alloying elements are generally added to improve the mechanical and physical properties along with formability, and corrosion resistance of the material. Alloying elements decrease the mobility of dislocations by solid-solution and precipitation hardening mechanisms and their influence on grain sizes, precipitation kinetics and recrystallization behavior of the alloy. AA6111 contains magnesium, and silicon, as the principal alloying elements, along with many other trace elements, such as iron, chromium, and titanium [9, 54].

2.5.1.1. Effects of Silicon and Magnesium Content

Magnesium and silicon are the main solutes in AA6111 and are typically introduced in the ratio of 1.73, in order to facilitate the precipitation of Mg_2Si compounds. These precipitates restrict grain growth, and result in fine-grained microstructures [56].

Apart from the combined effect of magnesium and silicon resulting in improved mechanical strength of the AA6111 (due to the precipitation of Mg_2Si compounds) as explained above, the excess silicon ($Mg/Si<1.73$), decreases the ductility of AA6111 without the presence of additional alloying elements. This is due to segregation of free silicon at grain boundaries which later transforms into Mg_2Si particles during heat treatment [57]. Additionally, corrosion resistance increases with raising the Mg/Si ratio [56]. Silicon tends to increase the strength of the alloy by precipitation strengthening as discussed above. However, if added in excessive amounts, it increases the risk of intergranular fracture [56].

2.5.1.2. Effects of Copper

In AA6111, the addition of copper results in a significant increase in the mechanical properties by refining the microstructure and changing the precipitation sequence [58, 59]. The addition of copper also results in solid-solution and precipitation strengthening, in the presence of magnesium and silicon, but decreases the corrosion resistance and weldability [60].

2.5.1.3. Effects of Iron

Iron reacts with silicon to form intermetallic compounds of the following stoichiometry: $FeAl_3$, Fe_2SiAl_8, $FeMg_3Si_6Al_8$, and $FeAl_6$, all of which can be harmful to the properties of AA6111 [56]. Iron reduces the strength and decreases the corrosion and fatigue resistance of the alloy. Iron also hampers ductility and toughness through the formation of coarse constituents with aluminum. Chromium and Manganese are added as an "iron corrector" in AA6111 aluminum alloy, in ord
er to alter the shape and size of iron-bearing precipitates [27, 56, 61].

2.5.1.4. Effects of Manganese

The addition of manganese inhibits the precipitation of Mg_2Si at grain boundaries hindering their grain refining effect. The presence of manganese not only raises the recrystallization temperature, but also provides additional strengthening via the dispersion hardening mechanism. Mn also significantly increases the degree of work hardening [56].

2.5.1.5. Effects of Ti and B

In AA6111, the addition of Ti and B elements result in grain refinement, which is in direct relation to the increase in strength due to the Hall-Petch effect [62].

2.5.1.6. Trace Elements [56]

Trace elements such as iron, sodium, lithium, calcium, titanium, vanadium, chromium, together with their compounds such as oxides, nitrides, borides, carbides, etc., are generally within the melt from the Hall-Herault Process, whereby aluminum is extracted from alumina. Not all trace elements are harmful. For example, chromium, titanium, and lithium, increase the strength of the alloy. Therefore, they are sometimes intentionally introduced into the metal alloys. However, some trace elements are harmful to the properties of 6xxx aluminum alloys. For example, the absorption of hydrogen results in the formation of gas porosity. The presence of sulphur, magnesium and lithium, increases the absorption of hydrogen, whereas silicon, scandium, copper, and beryllium reduce it. Iron and silicon, if present in between 0.1-1.0 (wt. %), form Al_3Fe and AlFeSi compounds. These compounds reduce the fatigue and fracture properties of aluminum alloys. Furthermore, the presence of sodium, lithium and calcium in aluminum alloys promote the formation of the aluminum-silicon eutectic structure, which results in high strength properties.

However, this might make rolling difficult, because of edge-cracking effects. Additionally, titanium, vanadium, chromium, and manganese, all retard recrystallization during deformation, and refine the grain structure during solidification. The addition of bismuth and lead increases the machinability of the alloy.

2.6. Precipitation Kinetics [63]

The natural aging kinetics can be described by the following equation:

$$\sigma_{NA} = \sigma_1 + k_{NA} \log t$$

Here σ_{NA} is the yield stress after aging the alloy some time t at room temperature, σ_1 and k_{NA} are constants. For understanding the artificial aging kinetics of T4 and pre-aged condition, the following equation is used

$$Y = 1 - \exp((kt)^n)$$

where Y is defined as:

$$Y = \frac{(\sigma_t - \sigma_i)}{(\sigma_p - \sigma_i)}$$

σ_t, σ_i, and σ_p are the yield stress at time t during artificial aging, initial yield stress, and the peak strength, respectively.

Studies show that the artificial aging response of AA6111 is affected by the cluster/GP zone, which forms during natural aging. It has been determined that dissolution of these clusters/zones could be the responsible for the slow age hardening and/or paint baking response of the naturally aged AA6111 alloy. On the other hand, artificial aging response of pre-aged material (the solution heat-treated at ~560°C, followed by aging in the temperature range of 60°C-120°C is much better as compared to naturally aged material. This occurs due to the formation of fully developed/large size precipitates, acting as nuclei for further precipitation during artificial aging. The Johnson-Mehl, Avrami, Kolmogorov (JMAK) model depicts a simple picture of the kinetics of the overall transformation process. However, this is not considered very useful in terms of providing a complete picture of the kinetics of the overall transformation process. For more information, please refer to the work of Kearns & Cooper (1997) [63].

2.7. Kinetics of Isothermal Precipitation [63]

The precipitation kinetics for isothermal transformation may be expressed by JMAK model, which can be represented by the following equation

$$f_r = 1 - \exp(-kt^n)$$

where f_r is the fraction transformed i.e. the relative volume fraction of precipitates, during aging time, t. "n" is a numerical exponent, independent of temperature, provided there is no change in the nucleation mechanism, n is equal to 0.5-2.5 for diffusional controlled growth, whereas n=1 for the growth of needles and plates of finite long dimensions, with comparatively small distance in between. A plot of ln $\left(\frac{1}{1-f_r}\right)$ vs ln t is a straight line which is used to determined n and k. The value of n is not constant but changes continuously with time as the precipitation reactions proceed. Details are not provided here. However, they can be read from the references provided [63].

2.8. Advanced High Strength Steels used in Automobiles

The microstructure, which determines the strength, ductility and toughness properties of AHSS, is highly dependent on the chemical composition, the rate of plastic deformation, and the specifics of the heat treatment cycle [64, 65, and 66]. Presented below is a set of brief discussions related to the diverse types of microstructures found in AHSS. They can be broadly classified into the first, second, and third-generation AHSS, as shown in Figures 2 and 3. Figure 2 & 3 plot the total elongation versus tensile strength, for the first two generations of AHSS (1st and 2nd) [64 - 66].

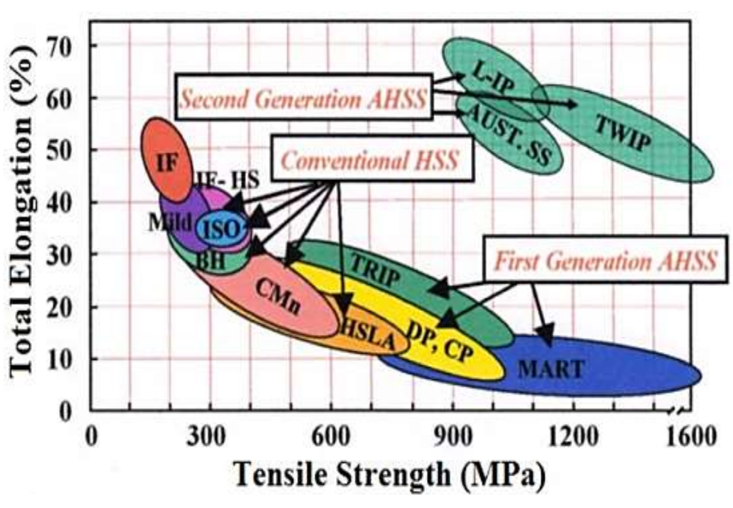

Figure 2: The representation of 1st and 2nd generation steels in total elongation versus total strength plot [64 - 66].

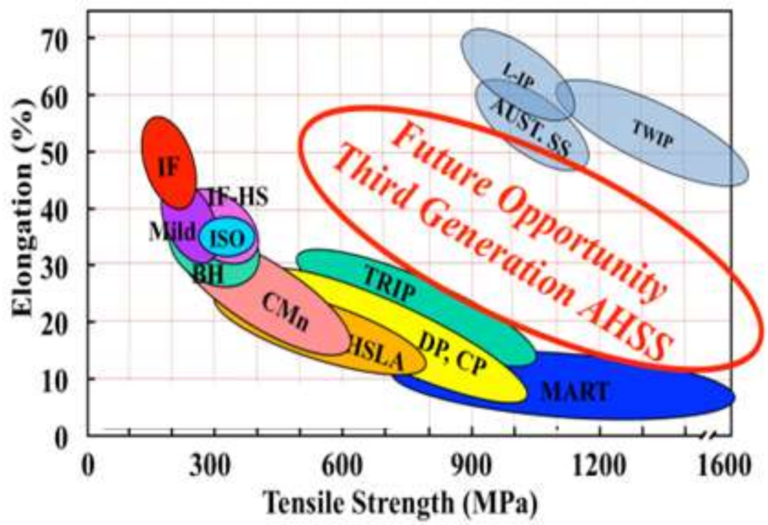

Figure 3: The representation of 3rd generation steels in total elongation versus total strength plot [64 - 66].

2.8.1. First Generation AHSS

The first generation AHSS covers ferrite-based steels, including 1) Dual-Phase (DP) Steels, 2) Martensitic Steels (MS or MART), 3) Complex-Phase (CP) steels, and 4) Transformation-Induced Plasticity (TRIP) steels [67]. However, the inverse relationship between strength and ductility observed in the 1st generation AHSS, limits their applicability, especially in applications where a deep-drawing ability is required, as in automotive applications [68].

2.8.2. Dual-Phase (DP) Steels

Dual-Phase (DP) Steels consist of discrete islands of martensite dispersed in a soft ferrite matrix, as shown in Figure 4. They have excellent strength-ductility ratios, as a result of the combination of hard and soft phases. DP steels typically contain carbon, silicon, phosphorus, manganese, chromium, molybdenum, vanadium and nickel [14, 66]. Presented below are the details related to DP steels [64, 68].

2.8.2.1 Properties

DP steels have: 1) High strength 2) Excellent elongation, 3) High work hardening rates, 4) High bake hardening, and 5) Good fatigue strength [64].

2.8.2.2 Applications

The applications of DP Steels include the following: 1) Automotive body parts such as door and outer hood, 2) Front and rear rails beam, 3) Floor panels and, 4) Various safety cage components, such as B-pillars. [64].

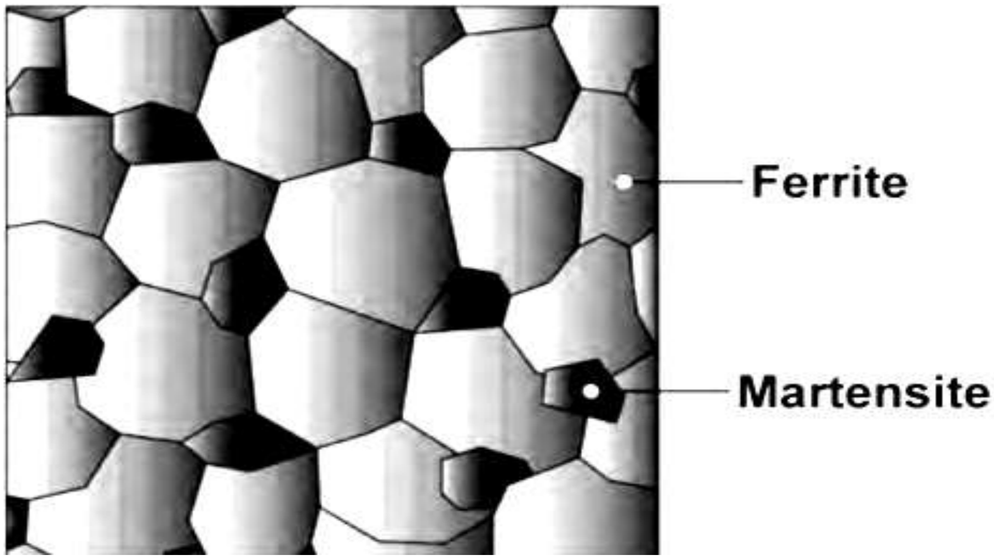

Figure 4: Micrograph of DP steel [64].

2.8.3. Ferritic/Bainitic (FB) Steels

FB steels contain the hard bainite phase dispersed in a soft ferrite matrix. The microstructure is shown in Figure 5. FB steels can easily be stretched, particularly at shear edges, thereby making them a suitable material for tailored blank applications. The alloying elements present in FB steels are aluminum, boron, niobium, and titanium [64]. Some of the properties along with applications are presented below.

2.8.3.1. Properties

FB steels have: 1) High formability and stretch-ability, 2) Good in dynamic loading conditions and, 3) Can easily be welded, but have longer spot-welding times [64].

2.8.3.2. Applications

FB steels are used in the manufacture of: 1) Automotive suspensions, 2) Chassis parts, due to their excellent fatigue properties, and 3) Rim pedal arm, etc. [64].

Figure 5: Microstructure of FB steel [64].

2.8.4. Complex Phase (CP) Steels

CP steels have complex multi-phases, containing a ferrite/bainite matrix with bits of martensite, retained austenite, and pearlite, as shown in Figure 6. These steels can achieve the desired mechanical properties by applying different grain refinement procedures. Additionally, microalloying elements such as titanium and niobium can also be used to achieve precipitation strengthening. CP steels contain carbon, silicon, phosphorus, manganese, chromium, molybdenum, nickel, titanium, niobium and vanadium [64].

2.8.4.1. Properties

CP steels have: 1) High yield strength and elongation, 2) Good stretch-ability and formability, 3) High wear resistance, 4) Good fatigue properties and, 5) are easily bake hardened [64].

2.8.4.2. Applications

CP steel applications include: 1) Fender beams, 2) Door impact beams, 3) Rear suspension brackets, etc. [64].

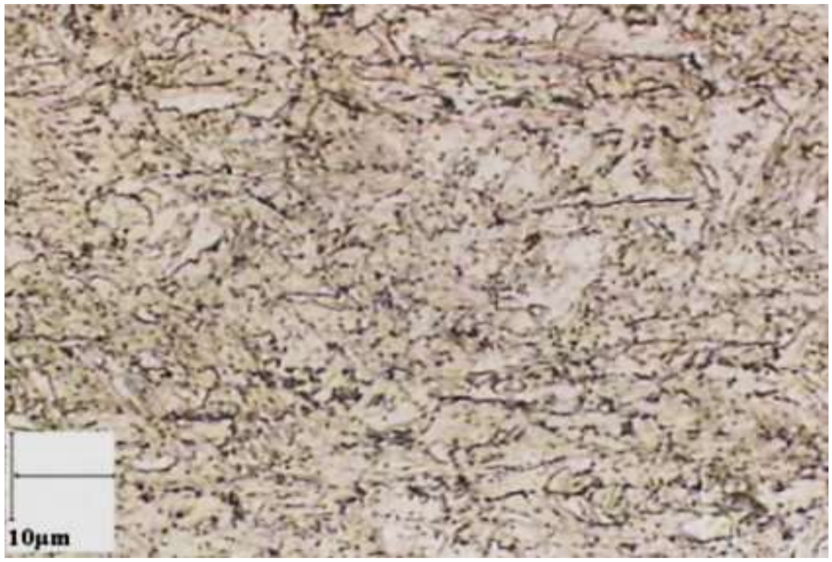

Figure 6: Microstructure of CP steels [64].

2.8.5. Martensitic Steels (MS)

MS steels contain martensite, along with a small quantity of very fine ferrite and bainite phases. This structure typically results due to the phase transformation of austenite (γ) to martensite (α), during quenching heat treatment, followed by post-tempering. The resulting microstructure is lath martensitic, as shown in Figure 7. These steels contain the following alloying elements, silicon, chromium, manganese, boron, nickel, molybdenum and vanadium [64].

Figure 7: Microstructure of MS Steels, showing a lath martensite structure [64].

2.8.6. TRansformation Induced Plasticity (TRIP) Steels/Modern TRIP Assisted Steels

The TRIP effect was demonstrated in low-alloy steels comprising 0.2 % carbon, 1-2 % manganese and 1-2 % silicon (all weight %). A TRIP steel consists of residual austenite (10-30 vol %), carbide-free bainite (20-30 vol %), and allotrio-morphic ferrite (50-60 vol %). TRIP steels have exceptional mechanical properties i.e. (1000 to 1500 MPa), and elongations of 20-30 %, at failure. The carbon-free bainite transformation results in a very stable, carbon-enriched, austenite at room temperature. Silicon and aluminum accelerate the ferrite/bainite formation [64]. These steels will be referred to as TRIP-assisted, later in this report, so as to distinguish them from the austenite-based TRIP steels. Upon plastic deformation, the retained austenite transforms to martensite. As a result, these steels exhibit high work hardenability throughout a wide range of strain levels, and thus show good stretchability. The amount of strain required to initiate the transformation of austenite to martensite can also be managed by careful selection of alloying elements, chiefly carbon. With less stability, the transformation begins as soon as the deformation starts, which is not desirable. Likewise, if the austenite is ultra-stable then the martensite transformation is delayed until an elevated level of strain is reached, typically beyond those of the forming process [64, 65, 68]. The typical compositions of TRIP-Assisted Steels are presented in Table 5. Other factors which affect the transformation are: (a) Temperature, (b) Strain rate and, (c) Mode of deformation.

Table 5: Typical chemical compositions (wt.%) of TRIP-Assisted Steels [64, 68].

Alloying Elements (Wt %)								
C	**Si**	**Mn**	**Al**	**P**	**Nb**	**Mo**	**Cu**	**Fe**
0.38	1.53	0.83	-	0.007	-	-	-	Remaining
0.18	2.0	1.5	0.037	0.015	-	-	-	Remaining
0.19	2.48	1.49	0.036	0.014	-	-	-	Remaining
0.11	0.59	1.55	1.5	0.012	-	-	-	Remaining
0.14	0.53	1.57	-	0.204	-	-	-	Remaining
0.22	1.55	1.55	0.028	-	0.035	-	-	Remaining

2.8.6.1. Heat Treatment of TRIP Assisted Steels

The microstructures of TRIP-assisted steels, as described above, can be generated by hot and cold rolling operations. The hot rolling operation is generally executed at temperatures where the steel is fully austenitic [69]. Moreover, a two-stage annealing treatment is required to produce the desired microstructure in cold rolled, TRIP Assisted steels, as shown in Figure 8 [69].

In the heat treatment, the first step is to raise the temperature of the steel to where the γ and α phases coexist, generating a mixture of ferrite and austenite. This is followed by the bainite transformation, once the steel is cooled down, afterwards. However, austenite is retained in TRIP-assisted steels due to incomplete reaction phenomenon associated with the bainitic transformation. The role of the alloying elements towards suppressing carbide precipitation during the formation of bainite, will be discussed later, but it will result in carbon-enriched residual austenite in the final microstructure. However, if this enrichment is inadequate (at too low holding times), the austenite may decompose partly into martensite during cooling [69, 70]. Furthermore, if the holding time is extended, then the amount of the untransformed austenite will decrease. Microstructural evolution during the isothermal formation of bainite is identical for both hot and cold-rolled TRIP-Assisted steels. A typical transformation map is presented in Figure 9. Additionally, in TRIP steels, bainite consists of adjacent platelets that span the whole of the austenite grain, as shown in Figure 10 [69, 70].

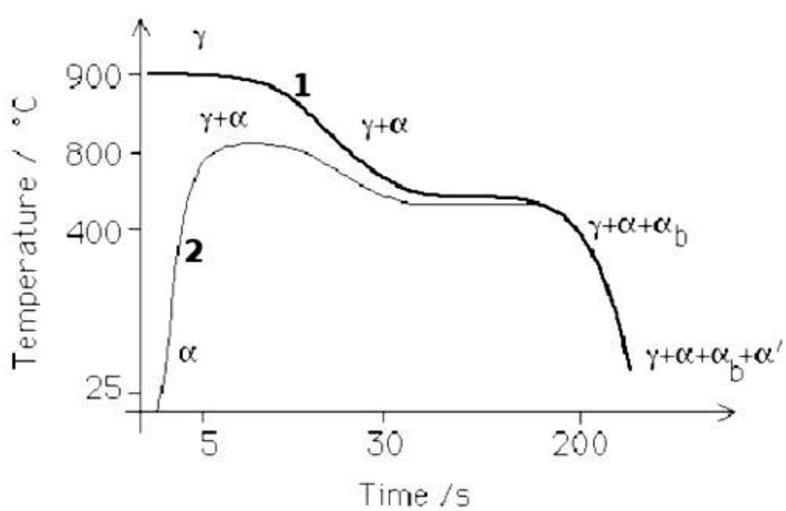

Figure 8: Schematic illustration of the two routes to generate the microstructure of TRIP-Assisted steel, with typical temperature and time data levels indicated. Curves 1 and 2 stand for the transformation from the fully austenitic state after hot rolling, and for inter critical annealing after

cold rolling, respectively. The terms $\alpha_b, \alpha', \alpha$ and γ represent bainitic ferrite, martensite, allotriomorphic ferrite, and austenite respectively [70].

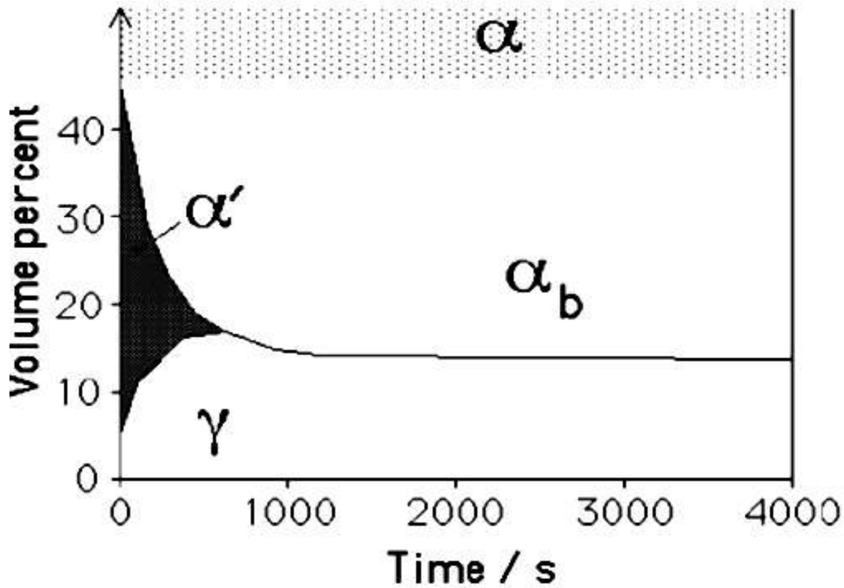

Figure 9: Typical microstructural evolution map during the bainite reaction. Retained austenite peaks at an intermediate holding time [70].

Figure 10: Bainite, consisting of adjacent ferrite platelets in TRIP-Assisted steels [70].

As discussed above, martensite is formed, at temperatures above M_S, by applying stress or strain. In this way, the shortfall in the driving force for transformation to occur above M_S will be compensated. The higher the temperature above M_S, the greater is the magnitude of the stress required to initiate the strain-induced transformation [70]. However, the proof stress of the austenite is lower at elevated temperatures. As such, once the stress required for the transformation exceeds the strength of the austenite, plastic strain precedes transformation. This lowers the overall stress requirements as shown in Figure 15. However, delaying the onset of necking is a very useful concept that explains the uniform elongation of TRIP steels, and is primarily due to the strain-induced transformation described above. This is the only reason why TRIP steels are useful [69, 70].

2.8.6.2. Properties

TRIP Steels have: 1) High work hardenings rates, and therefore have excellent formability, making them useful in applications where the deep/shallow draw-ability property of the material is required. Furthermore, 2) TRIP steels can be easily stretched and bent, thereby allowing the fabrication of complex shapes. 3) TRIP steels also have excellent bake hardening capacity [65, 71].

TRIP steels also have several disadvantages regarding: 1) Limiting local elongation, 2) Edge stretchability and, 3) Shear cracking at the interfaces between the ductile ferrite, and the hard martensite, grains or phases. However, proper design of the product, and careful control of the production process, allows one to avoid these problems. The weldability of TRIP steels is poor due to the presence of alloying elements such as carbon, manganese, etc. [70, 71].

2.8.6.3. Applications

A variety of automotive parts can be produced with TRIP steels such as: 1) Cross members, 2) Engine cradles, 3) Dash panels, 4) Bumper reinforcements, etc. [70].

2.9. Second Generation AHSS

2nd Generation AHSS are based on an austenite microstructure. A ductile austenite matrix provides for better formability as compared to the 1st generation AHSS. However, the excessive cost associated with the addition of austenite stabilizing elements, such as manganese and nickel; make them relatively expensive [72]. Second generation AHSS are classified as follows: 1) AUST

SS, 2) TWIP and, 3) Light Weight with Induced Plasticity (LIP) steels [68, 74]. (Only TWIP Steels will be further presented in the following paragraphs).

2.9.1. Twinning Induced Plasticity (TWIP) Steels

2nd Generation AHSS are based on an austenite microstructure. Therefore, it sits apart from 1st generation AHSS in total elongation versus tensile strength (Plot is shown in Figure 2). TWIP steels have received their name from their mode of deformation, i.e., deformation twinning which results in the formation of symmetric twin boundaries, which then act like obstacles to the plastic flow, thereby increasing the strength. Various alloying elements, such as manganese and carbon, are present in TWIP steels. These render them completely austenitic at room temperature. The properties along with applications are presented as follows [73, 74]. The microstructure is shown in Figure 11.

2.9.1.1. Properties of Twinning Induced Plasticity (TWIP) Steels

These steels have extremely: 1) High elongation and stretchability, 2) Good tensile strength but have, 3) Low corrosion resistance [72-73]. Furthermore, due to the presence of expensive alloying elements, they have higher cost as compared to the 1st and 3rd generation AHSS [74].

2.9.1.2. Applications of Twinning Induced Plasticity (TWIP) Steels

TWIP Steels applications include: 1) Wheel housings, 2) Front and rear bumper beams, 3) Apron reinforcement and, 4) Front rails, etc. [72].

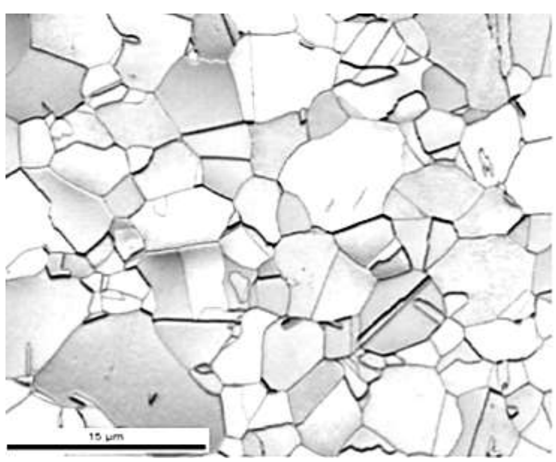

Figure 11: Microstructure of TWIP Steels [2].

2.10. Third Generation AHSS

2.10.1. Introduction

Keeping in view the limitations of 1st and 2nd generation AHSS, as described above, but to still produce a steel with better combinations of strength and ductility than a 1st generation steel, whilst at a reduced cost versus a 2nd generation AHSS, a 3rd generation steel has now evolved, as shown in Figures 2 and 3 [74, 75].

As explained earlier, 2nd generation AHSS's are sufficient in meeting all the properties required by the automotive sector, but they are often relatively expensive to produce, mainly because they contain a large quantity of expensive alloying elements [72]. The development of the third generation AHSS is therefore based on producing steels that can meet all the requirements/goals of the current automotive industries, whilst keeping costs to a minimum. Various design strategies have been proposed that can result in the 3rd generation of AHSS. They are presented below, based on the following attributes:

1. Property enhancements for DP steel through efficient processing [76].
2. Useful modifications in traditional TRIP processing [77, 78].
3. Designing/Development of high strength, ultra-fine, bainitic microstructures [79].
4. Development of Quench and Partitioned (Q & P) steels [80].
5. Development of Manganese based TRIP steels [75, 76, 81, 82].

Only Mn-based TRIP steel will be discussed briefly, later in this report, as it is the subject of my thesis. Details regarding the above-mentioned design strategies can be read from the appropriate references.

2.10.2. Development of a Manganese Based, Two-Stage TRIP Steel

2.10.2.1. Introduction of Two-Stage TRIP Steels

1st generation TRIP steels contain ferrite, martensite, and bainite, along with an appreciable quantity of metastable retained austenite [64]. These steels can resist the onset of necking when deformed plastically, by transforming FCC Austenite (γ) into a BCC Martensite (α), i.e. $\gamma \rightarrow \alpha$ [75, 76]. As such, they possess both high tensile strength and high elongation. However, with an aim to attain the tensile strength and ductility equivalent to 3rd generation AHSS, researchers have developed steels that undergo two stages of martensitic transformation: i.e., γ→ε→α. Here γ represents austenite, ε, the hexagonal close-packed (HCP) martensite, and α, the body-centered cubic (BCC) martensite [81, 82].

2.10.2.2. Explanation of Two-Stage TRIP Steels

In general, two-stage TRIP steels gain their exceptional strength by the transformation of γ into smaller segments of ε and α martensite throughout the austenite matrix [76]. These subsequently act as barriers to dislocation motion and thereby result in high UTS at their breaking points [75]. The entire transformation can be divided into two steps.

2.10.2.2.1. First Stage

In the first stage, the transformation of γ→ε occurs as the result of the destabilization of perfect a/2<110> lattice dislocation into a/6 <112> Shockley partials, which alter the stacking sequence from ABCABCAB to ABCA|CABC (|represents a stacking fault) and generates stacking fault energy (SFE), as shown in Figure 12 [83]. The first step generally occurs at an initial level of strain [83].

2.10.2.2.2. Second Stage

The second stage is associated with the transformation of ε→α, this is due to the intersection of shear bands already containing ε martensite, or the intersection of ε martensite with the deformation twins. Many researchers have shown that a stacking fault energy of less than 20 mJ/m^2, favors the (γ) to (ε) phase transformation, i.e. the TRIP phenomenon, whereas higher values of SFE, i.e. more than 20 mJ/m^2, leads to either TWIP or deformation through dislocation movements [67]. Plastic deformation through dislocation movement is normally observed at higher SFE [84-86]. Another approach proposed by Olson and Cohen, showed that two special shears are required to provide the invariant plane strain necessary for the transformation of γ→α,' i.e. to nucleate α martensite, a one third (T/3) twinning shear, which is equivalent to a/18 <112> on successive {111} γ planes in the parent austenite, is required [83]. Similarly, a one half (T/2) twinning shear, equivalent to a/12<112> on successive {111} γ planes in the parent austenite, can nucleate α martensite [83]. When T/3 and T/2 twinning shears intersect, they provide sufficient driving force to trigger the γ to α transformation [83]. The entire process is illustrated below in Figure 13.

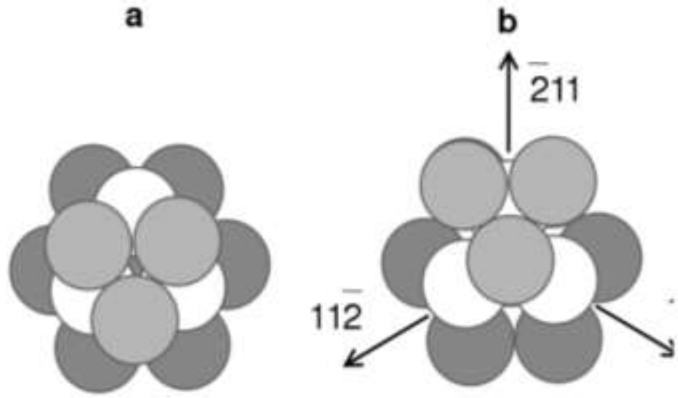

Figure 12: a) Un-faulted stacking sequence and b) stacking fault along <112> {111}, expressed in terms of the Burger Vector of the partial dislocation bp= 1/6<112>, produced during shear [83].

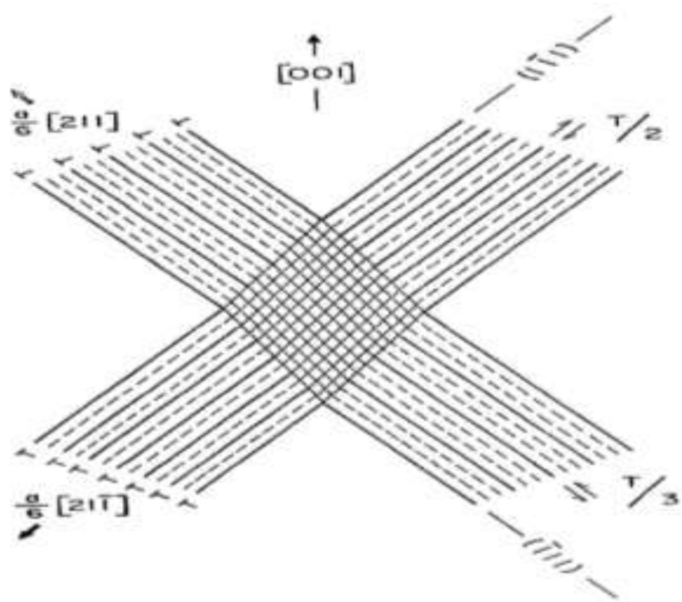

Figure 13: The nucleation of α-martensite from the intersection of a T/2 and T/3 shear packet [83].

2.10.3. Recent Studies for the Development of Mn-based TRIP Steels

One of the most recent studies in this regard has been conducted by McGrath et al. [82], in which they showed that Mn-based TRIP steels, when alloyed with aluminum and silicon, can result in exceptional increases in tensile elongation, i.e. 34.4 % elongation along with UTS of 1165 MPa. Approximately similar alloying systems have been studied by Van Aken et al. [75] and Pisarik et al. in which they showed that a dual-stage martensite transformation could lead to the development of the 3rd generation of AHSS [87]. They further demonstrated that phase transformations of $\gamma \rightarrow \alpha'$ and $\gamma \rightarrow \varepsilon$, follow the Kurdjumov-Sachs and the Shoji-Nishiyama orientation relationships, respectively [75, 87]. Both researchers have employed the Regular Solution Model to describe the thermodynamic driving forces needed to transform $\gamma \rightarrow \varepsilon$, followed by the determination of SFE using the Olson-Cohen approach, in which the critical fault thickness (n=4) has been suggested as essential to achieving the transformation of $\gamma \rightarrow \varepsilon$ [84, 86, 87]. The regular solution model will be explained in detail, in a later section of this report.

Another vital research study was conducted by Frommeyer et al., in which the microstructural properties of TRIP/TWIP steels were investigated as a function of temperature (-196 to 400°C) and strain rates ($10^{-4} \leq \epsilon \leq 10^{3}\mathrm{s}^{-1}$). This research provides the basis for understanding the strain hardening behavior (rate) of TRIP steels subjected to different values of applied strain at ambient temperatures. A critical value of SFE ($25\frac{\mathrm{mJ}}{\mathrm{mole}}$) at $G^{\gamma \rightarrow \varepsilon} > 0$ has been suggested for the twinning mechanism, whilst SFE values < $16\frac{\mathrm{mJ}}{\mathrm{mole}}$, at $G^{\gamma \rightarrow \varepsilon} < 0$ were determined for the TRIP mechanism to dominate during plastic deformation [87]. The alloying elements, along with the microstructures, are presented in Table 6.

2.10.4. Prediction of TRIP Steels Properties

In TRIP steels, the volume fraction of austenite changes with strain. As such, the approach proposed by Olson is the best suited here, as it considers stress assisted and strain-induced transformation of austenite to martensite. As we know, the 1st generation of TRIP steels are ferrite based. The only way their properties can be increased is through solid solution strengthening, grain size control, cold working, or precipitation hardening. However, there is a significant amount of literature that suggests that opportunities are limited regarding increasing strain hardening behavior of these steels at higher strains. Therefore, an appreciable quantity of austenite, if present in these steels, can increase their high strain work hardening behavior through strain-dependent control of austenite to martensite.

Another approach towards the development of AHSS with greater strength/ductility characteristics as compared to 1st generation AHSS is based on the addition of a constituent that has increased strength, i.e. martensite, and an enhanced strain hardening constituent, i.e. austenite [67]. As will be discussed below, by controlling the stability of retained austenite against deformation, one can achieve properties equivalent to 3rd generation AHSS. Steel that has over-stabilized ε-martensite structure does not undergo the ε → α' transformation. It will, therefore, tend to fracture prematurely, due to crack nucleation at the intersection of ε martensite plates, or between the intersection of ε martensite plates and twin boundaries. It is therefore essential to consider the effect of the alloying elements on the stability of ε, or α martensite [67].

Table 6: Chemical composition and microstructures for various TRIP/TWIP Steels (α' represents the summation of α-martensite and α-ferrite) [75, 82, 84, 86, 87].

Alloy		**Composition (wt %)**					**Vol % Before Tensile Test**			**Phases After Tensile Test**
		Mn	**Si**	**Al**	**C**	**N**	**Γ**	**ε**	**α'**	**α'**
McGrath et al.		15.3	2.85	2.4	0.07	0.017	27	60	13	α'
Van Aken et al.		14.2	1.85	2.38	0.06	0.019	37	29	34	α'
Pisarik et al.		15.1	1.95	1.4	0.08	0.017	14	45	41	α'
Pisarik et al.		14.3	2.97	0.89	0.16	0.022	7	75	18	α' + ε
	TRIP	15.8	3.0	2.9	0.02	< 0.003	48	16	36	α'+γ
Frommeyer et al.	TRIP/TWIP	20.1	2.8	2.9	0.04	< 0.003	78	22	0	α'+ ε +γ
	TWIP	25.6	3.0	2.8	0.03	< 0.003	100	0	0	γ
Yang et al.		21.5	0.19	--	0.24	--	93	7	0	ε + γ

2.10.5. Factors Affecting the Stability of Austenite

1. Austenite's stability against transformation, increases with a decrease in austenite grain size [88].
2. The stability of austenite increases with additions of elements such as carbon, manganese, and nickel [89].

3. The strain rate and the lattice orientation of the austenite with respect to the loading direction have an effect on its stability [85].
4. The determination of Stacking Fault Energy (SFE) is needed to predict austenite stability [90].

2.11. Alloying Elements Critical to the Properties of TWIP Steel & Stacking Fault Energy (SFE)

2.11.1. Effects of Dissolved Manganese and Carbon

Carbon promotes the stability of austenite in TWIP steels and provides additional strengthening via the precipitation of the kappa phase, $(Fe, Mn)_3AlC_x$, if added in excessive amounts i.e. > 1% carbon [91, 92]. However, the presence of the kappa phase severely reduces the impact strength of AHSS. As far as the SFE value is concerned, it generally increases with the increase in carbon content, however, the extent of increase in SFE by the addition of carbon is strongly dependent on the presence of other alloying elements such as aluminum & manganese in a steel [78, 79]. Like carbon, manganese also stabilizes the austenite phase, by decreasing the temperature at which the austenite transforms into martensite [84, 85]. Manganese also inhibits the formation of ε martensite, by increasing the stacking fault energy of the austenite. In fact, it is important to understand that the enormous increase in the SFE with the increase in manganese content of the steel, unlike aluminum and carbon, is due to an immense increase in the $\Delta G_{\mathrm{chem}}^{\gamma\rightarrow\varepsilon}$ term, present in the SFE equation [78, 79].

2.11.2. Effects of Silicon and Aluminum

Silicon increases the solid solution strengthening and stabilizes the ferrite in TWIP steels. However, silicon also reduces the galvanize-ability of the AHSS and therefore can be replaced partially, or completely, with aluminum. Additionally, the SFE decreases with an increase in the silicon content. Silicon also decreases the Neel temperature (the temperature at which the transformation of paramagnetic to antiferromagnetic occurs), thereby altering the γ/ε phase stability. On the other hand, aluminum promotes the formation of ferrite and increases solid solution strengthening. It reduces the kinetics of cementite precipitation and significantly increases the concentration of carbon in retained austenite. The addition of aluminum to TWIP steels increases the SFE, so that even the addition of 1 wt.% aluminum, inhibits the TRIP effect [78, 79].

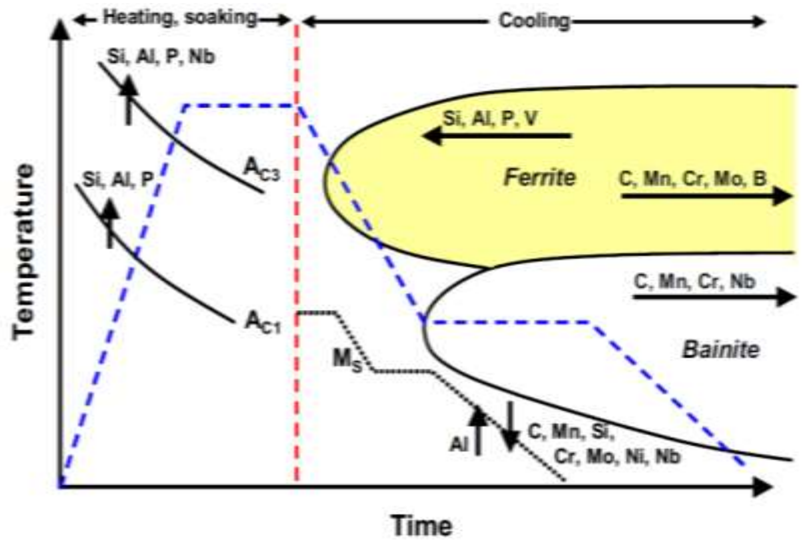

Figure 14: Effect of alloying elements on the transformation behavior during the continuous annealing of TRIP steels [93].

2.12. Austenite Stability in TRIP Steels versus Plastic Deformation and Temperature

The TRIP effect observed in AHSS involves a complex inter-relationship between the applied stress, the plastic strain, and the martensitic transformation. This interrelationship was explained by Bolling and Richman for iron-nickel-carbon and iron-nickel-carbon-chromium alloys, as shown in Figure 15, but can be applied for Mn Based TRIP steels as well [86].

In Figure 15, the M_s^{σ} temperature, which lies somewhere in between M_s and M_d, is responsible for deciding whether the formation of martensite will be stress assisted or strain-induced. M_d temperatures are the temperature at which enough activation energy is provided by the deformation, in addition to the chemical driving force, to trigger the martensitic transformation [86].

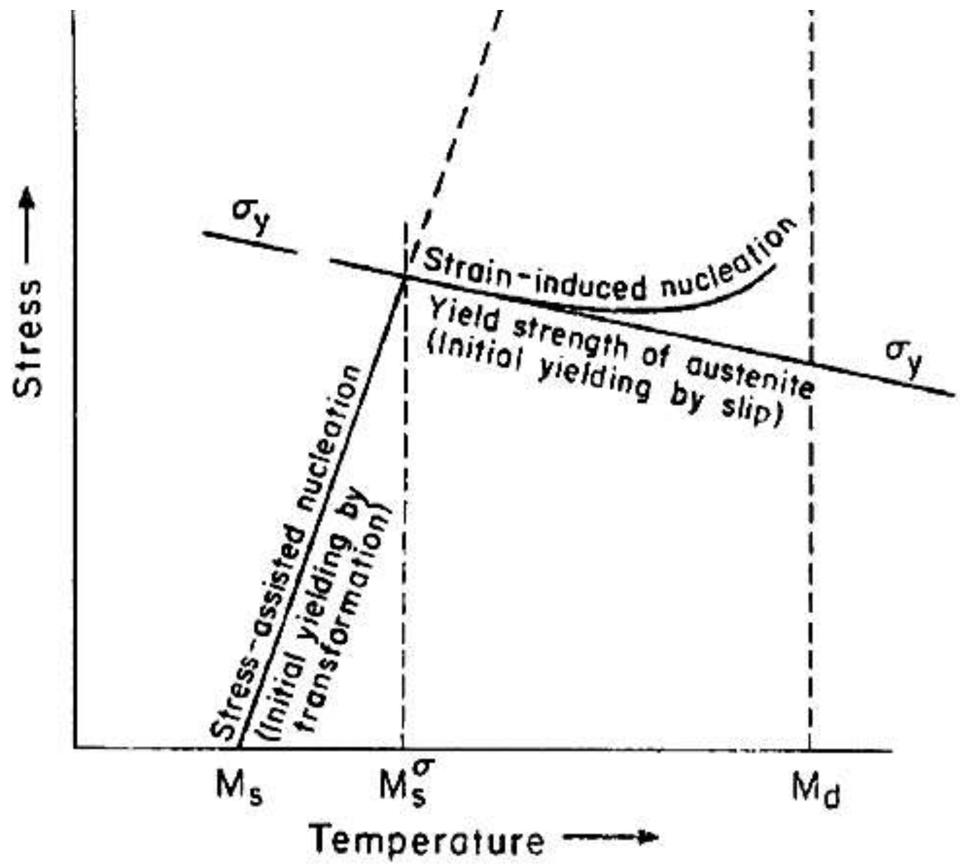

Figure 15: Increase of stress as a function of temperature [86].

The stability of the martensite transformation against plastic deformation can be directly controlled either through varying deformation stress, or temperature. It is, therefore, one of the governing factors towards optimizing and controlling the transformation rate, as shown in Figure 15. Equally important is the selection of alloying elements, because M_s, M_s^σ and M_d are highly dependent on them, as explained in reference [86], above.

The effect of the austenite stability towards tensile elongation can be explained by considering four hypothetical steels. If the transformation commences as soon as the plastic deformation begins, i.e. lower stability (condition D), then austenite does not significantly contribute to improved properties as discussed above, and therefore overlaps with the 1st generation AHSS, as shown in Figure 16 and 17 [76].

Moreover, the comparatively stable austenite not only transforms completely to martensite (condition B), as shown in Figure 16, but also provides the best combination of strength and ductility, equivalent to the property band of the 3rd generation AHSS, as shown in Figure 17 [76].

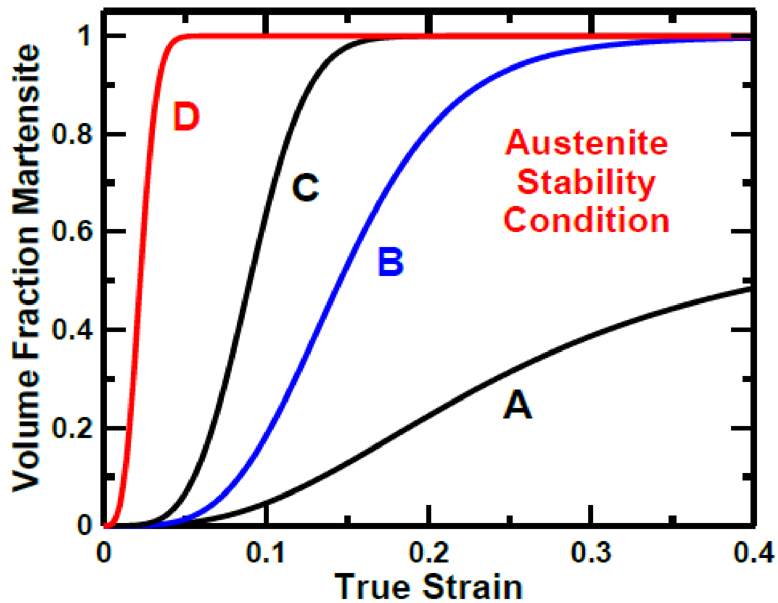

Figure 16: Effect of austenite stability on predicted mechanical property combinations for four different austenite stabilities identified as A through D [76].

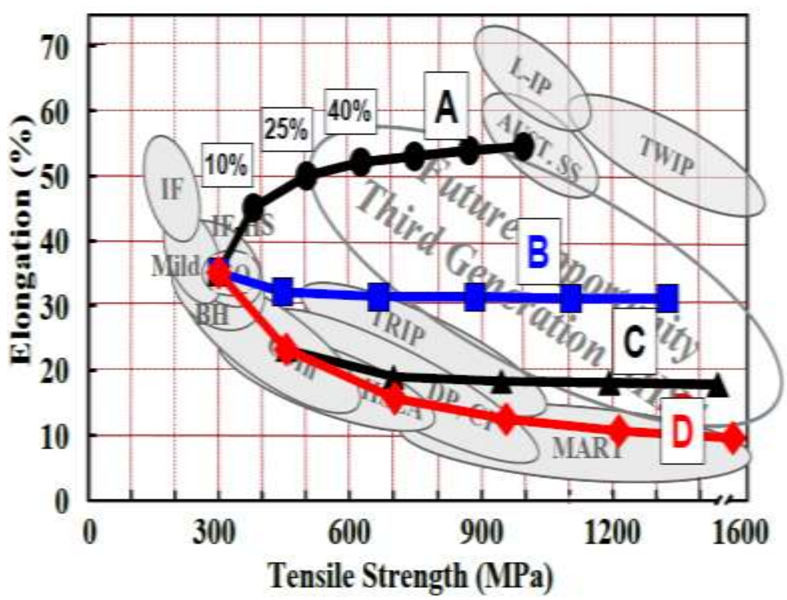

Figure 17: Predicted mechanical property combinations with the different austenite stabilities [76].

2.13. Austenite Stability in TRIP/TWIP Steels versus Plastic Deformation and Temperature (based on research conducted by Frommeyer et al.) [92]

A study on the temperature dependence of mechanical properties, such as Yield Stress [Rp (0.2)], Ultimate Tensile Stress [R (m)], Uniform Strain [ε (un)] and Ultimate Tensile Strain [ε (f)], of TRIP Steels has been conducted by Frommeyer et al. [92], as shown below in Figure 18.

The schematic mentioned below can be subdivided into three regimes. In the temperature regime between 150 °C up to 400 °C, a very slight increase in the stress with an increase in the strain was reported. This is primarily due to the strengthening caused by dislocation interactions. However, in the temperature regime between 80 °C to 150 °C, the TRIP phenomenon was observed, with a subsequent increase in stresses and strains [92].

At temperature decreases below 80° C (region 3), both εf and εun decreases, mainly because of the completion of the martensite transformation during the early stage of the deformation (driving force for γ→ε→α' transformation is high at low temperatures) whereas R (m) and R (0.2) increases up to 1250 and 400 MPa respectively at -100° C [92].

Also presented below in Figure 19 are the curves for true stress plotted against true plastic strain for TRIP, TRIP/TWIP and TWIP steels. At lower strains, i.e. less than 0.15 %, all the steel shows moderate strain hardening behavior. However, at higher strains, i.e. greater than 0.15 %, steels containing Mn content ranging between 15 to 20%, shows a sudden increase in work hardening rate, mainly due to the formation of stress-induced α martensite with a concurrent increase in elongation. This is characteristic of the TRIP behavior [92].

Comparatively less work hardening rate has been observed for TWIP steels containing 25% manganese but with enhanced plasticity due to the deformation-induced twinning behavior. Furthermore, it can be observed that steel containing 20% manganese exhibits TRIP, as well as TWIP, behavior simultaneously [92]. The alloying elements along with the microstructure observed before and after deformation are presented in Table 6.

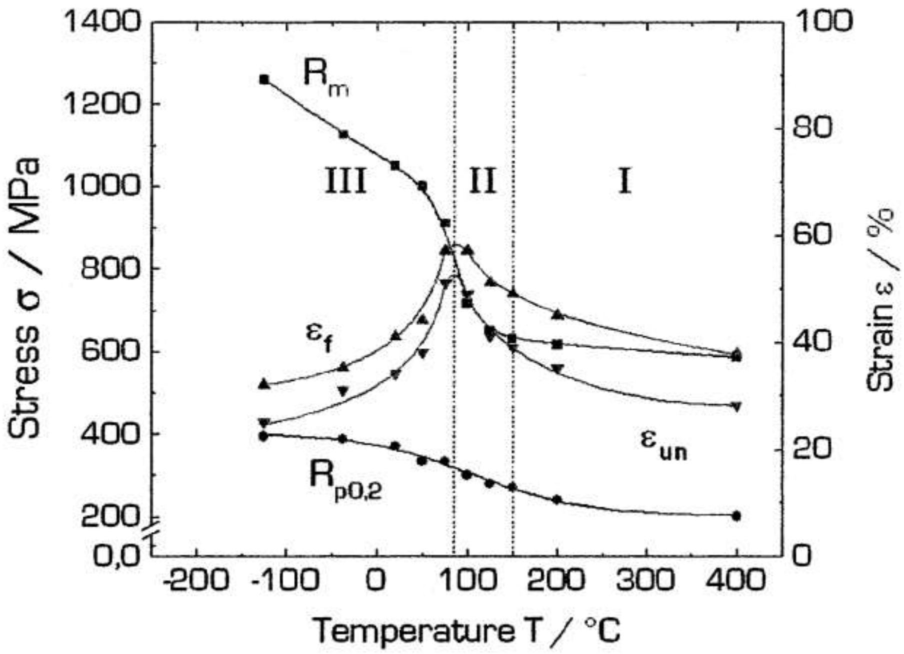

Figure 18: Stress vs. Temperature curve for TRIP, TRIP/TWIP and TWIP Steels [92].

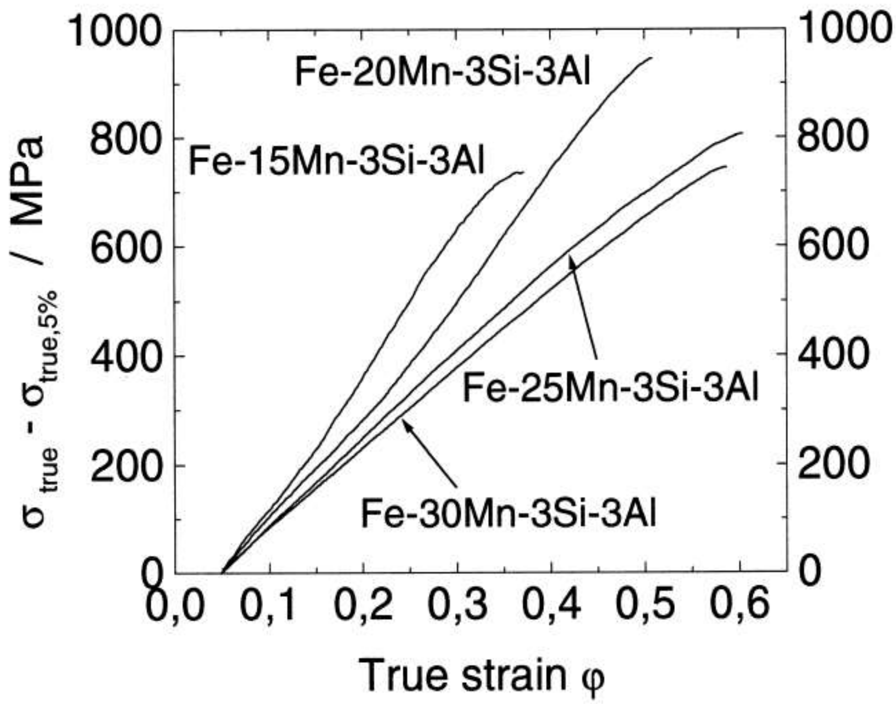

Figure 19: True Stress -True Strain curve for TRIP, TRIP/TWIP and TWIP steels [92].

2.14. Thermomechanical/Heat Treatment Processes for AHSS

"Advanced High Strength Steels", or AHSS**,** are considered as one of the kinds of "High Strength Steels" that possess superior strength and formability. On the scale of strength, steels with 210 to 550 MPa yield strength lie in the category of "High Strength", whereas anything stronger is "Advanced High Strength". Additionally, AHSS is also known as "ultra-high strength steels", since their tensile strength exceeds the 780 MPa barrier. In order to achieve these strength levels, various processing routes can be followed, all are aimed to achieve strength via TWIP, TRIP, solid solution, or precipitation hardening, apart from grain refinement, and work hardening phenomena [2]. These strengthening phenomena are described as follows:

2.14.1. Solid Solution Strengthening

In AHSS, solid solution strengthening is achieved by the addition of alloying elements such as aluminum, silicon, and carbon. These alloying elements occupy the substitutional and interstitial sites in the lattice and forms localized strain fields around them. This localized field impedes the dislocation movement, therefore increase the strength of the alloy [76].

2.14.2. Grain Refinement

The grain boundaries act as an obstacle to the motion of dislocation. As grain size decreases, the cumulative area of grain boundaries increases. As a result, the strength of the material increases. In AHSS, grain refinement can be achieved via extensive plastic deformation or manipulating the cooling rate after thermomechanical processing [94].

2.14.3. Work Hardening

As a result of cold working such as rolling, drawing, etc., the dislocation becomes entangled. This resists the motion of dislocation which means that higher stress is required to plastically deform a material. Work hardening increases the strength and hardness of the material [76].

2.14.4. Precipitation Hardening

Precipitation hardening is a phenomenon of increasing the strength of AHSS through the precipitation of secondary particles throughout the matrix. For example, the precipitation of the kappa phase [(Fe, Mn)3AlCx], or other discreet carbides or nitride in AHSS. These secondary particles impede the motion of dislocations, therefore increases the strength of the alloy [94].

2.15. Transformation Strengthening for 1st Generation of AHSS

Transformation strengthening is one of the principles strengthening mechanism used in the processing of AHSS. In Figure 20, the possible routes to produce dual-phase steels, such as banite-martensite, and martensite-austenite, as well as martensitic steels, are demonstrated [95-97]. These transformation results are due to controlled cooling after elevated temperature holding/processing, as demonstrated in Figure 20 [2]. Details can be read from references provided.

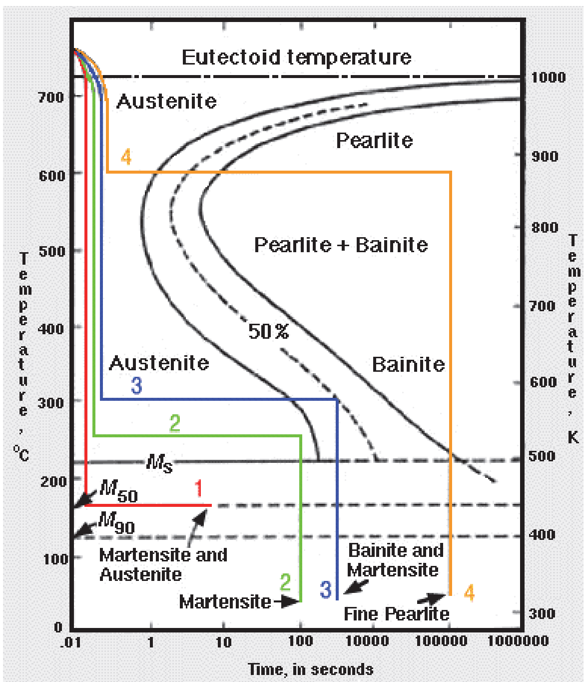

Figure 20: Processing routes to produce 1st Generation of AHSS [2].

The processing cycle for TRIP steels of this category is rather complex. It starts with bringing down the temperature of the material to a stable ferritic range. At this stage, a significant amount of carbon (~0.4%) enters austenite. After 50-60% ferrite has precipitated, the material is cooled to bainite stable temperature (Figure 21) [98]. Due to the nucleation of bainite, the carbon concentration in austenite further raised to 1.2%. The austenite phase formed after this treatment amount to 10-15% which later accounts for the TRIP phenomenon during plastic deformation [98].

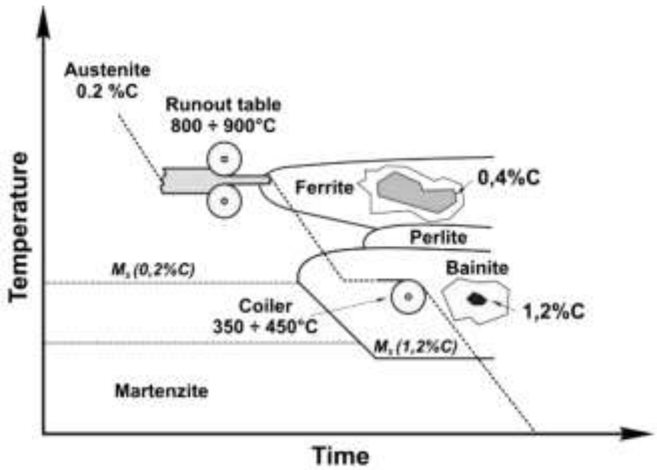

Figure 21: Cooling procedure in the production of the TRIP plates [98].

2.16. Development of austenite-based 2nd and 3rd generation of AHSS

Hua et al [99] investigated the mechanical properties and microstructure of high manganese steel of the following chemical compositions manganese (15-30 wt.%), aluminum (2.7-3.0 wt.%), silicon (3 wt.%) and carbon (0.0006 wt.%). These steels are fully austenitic at room temperature, after quenching, from an elevated temperature holding of one hour as shown in Figure 22. They showed that when these steels are plastically deformed at ambient temperature, the austenite phase transformed into epsilon martensite/deformation twins as shown in Figures 23 and 24. The tensile strength achieved was ~700 MPa with total elongation of 80% [99].

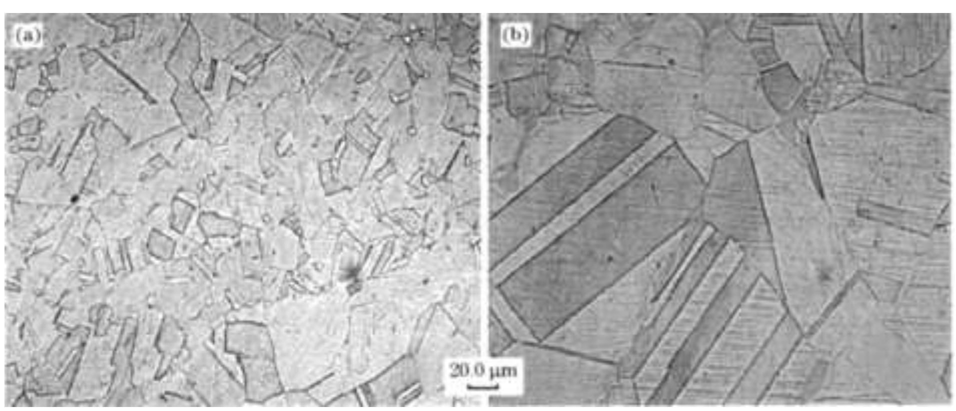

Figure 22: Microstructures of high Mn steel before cold deformation showing annealing twins (a) 24 wt.% manganese, 2.7 wt.% aluminum, 3 wt.% silicon, and 0.0006 wt.% carbon, (b) 33 wt.% manganese, 2.7 wt.% aluminum, 3 wt.% silicon, and 0.0006 wt.% carbon [99].

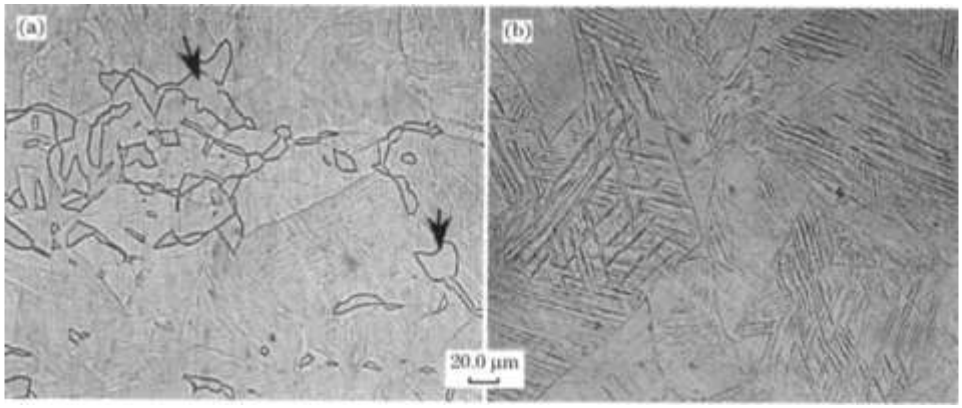

Figure 23: Microstructures of high Mn steel after cold deformation showing transformed martensite/deformation twins (a) 24 wt.% manganese, 2.7 wt.% aluminum, 3 wt.% silicon, and 0.0006 wt.% carbon, (b) 33 wt.% manganese, 2.7 wt.% aluminum, 3 wt.% silicon, and 0.0006 wt.% carbon [99].

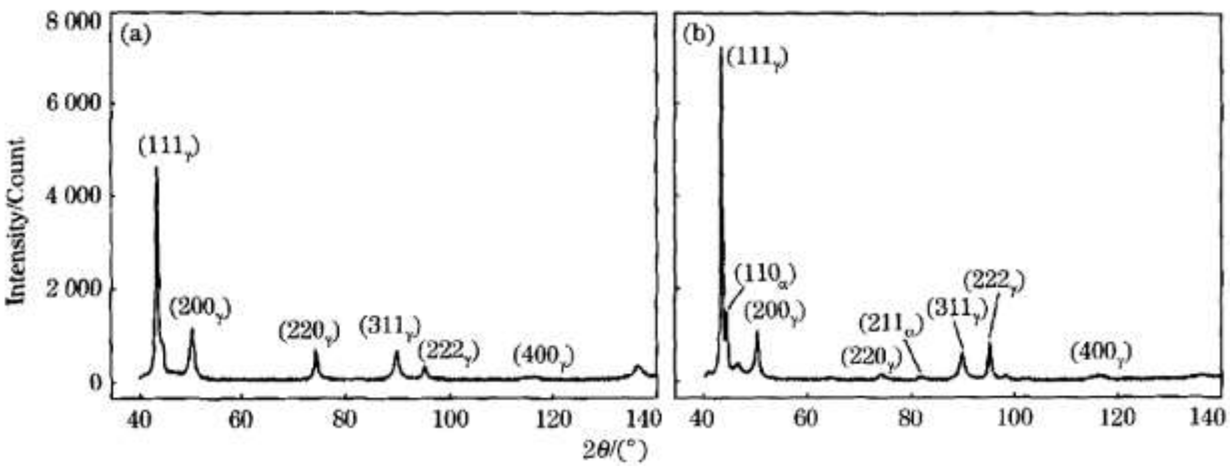

Figure 24: XRD pattern of 24 wt.% manganese, 2.7 wt.% aluminum, 3 wt.% silicon, and 0.0006 wt.% carbon (a) Undeformed sample (100% austenite), (b) Deformed samples (austenite and bcc martensite) [99].

In other research conducted by Grassel et al [100], they studied the mechanical properties of high Mn steel containing aluminum and silicon. Various alloys were produced in which the Mn content was varied from 15-30 wt.%, whereas silicon and aluminum were added in the range of 1.8-4.3wt.% and 1.8-3.9 wt.%, respectively. An almost similar production method, as implemented by Hao, was applied to produce fully austenitic steel. After casting, the sample was hot deformed

(77%), and solution treated, in order to obtain 100% austenite phase. The plastic deformations were carried out at room temperature. The austenite (γ) was observed to transform into, α and ε martensite, as well as twins, during plastic deformation. The resulting transformation increases the tensile strength of the steel up to 1100MPa, with a corresponding increase in the elongation (60-95%), as shown in Figures 25 and 26 [100].

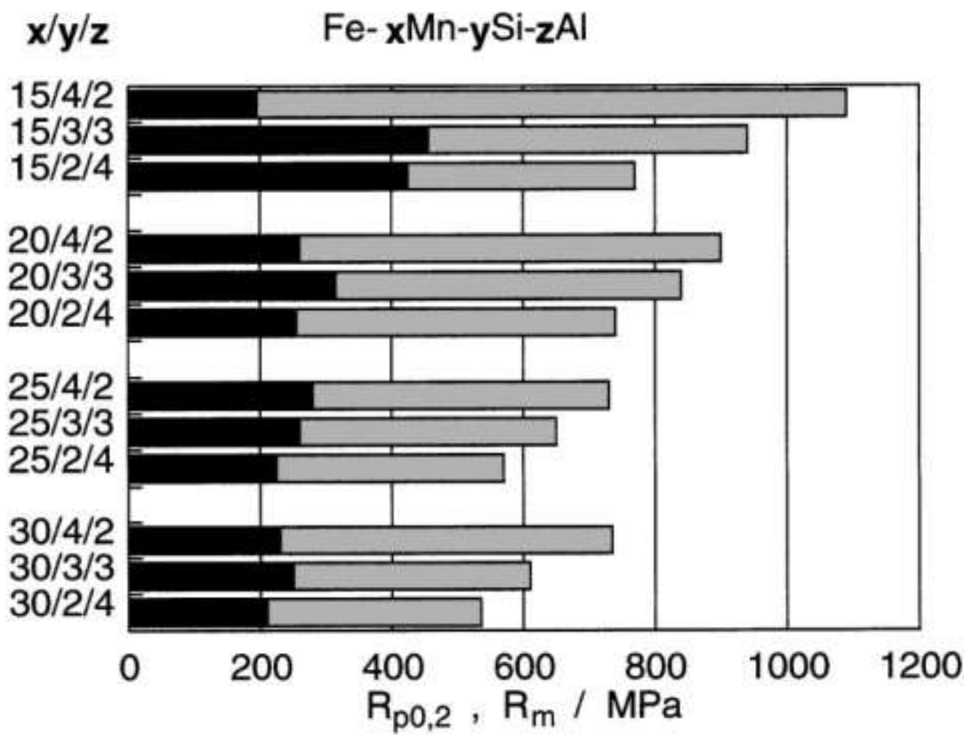

Figure 25: Yield strength (dark), Ultimate tensile strength (grey) of high manganese steels, tested at room temperature, strain rate $\varepsilon = 10^{-4}s^{-1}$ [100].

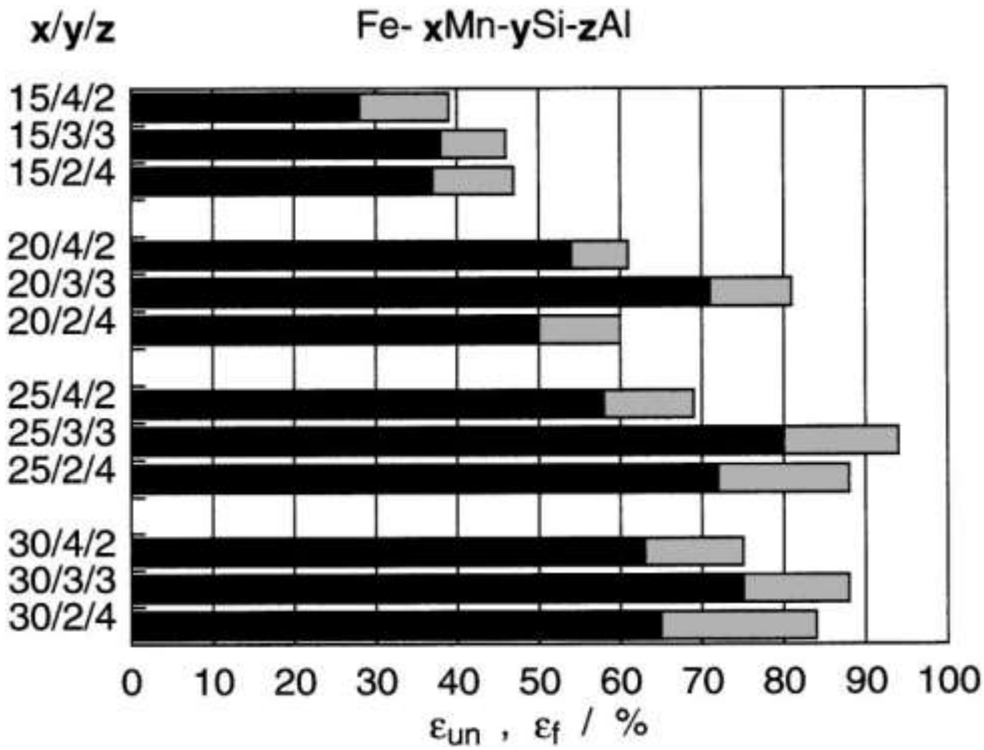

Figure 26: Uniform elongation (dark), Total elongation (grey) of high Mn steels, tested at room temperature, strain rate strain rate $\varepsilon = 10^{-4}s^{-1}$ [100].

Similarly, other research conducted by Ueji et al [101], proposed a very similar steel composition as presented above i.e. 17-30 wt.% manganese, 3wt.% aluminum, 3wt.% silicon, as well as production process, to obtain a fully austenitic phase at room temperature. The mean grain size of the TWIP steel was controlled by cold deformation and subsequent annealing treatment, followed by air cooling. Three different austenite grain sizes were obtained i.e. 1.8, 7.2, and 49.6 µm. Tensile testing at ambient temperature was performed and the maximum tensile strength of 800 MPa was achieved for fine grained steel (1.8µm), as shown in Figure 27. Additionally, it was determined that the fine grained structure inhibits the deformation twinning mechanism. Details can be read in reference [101].

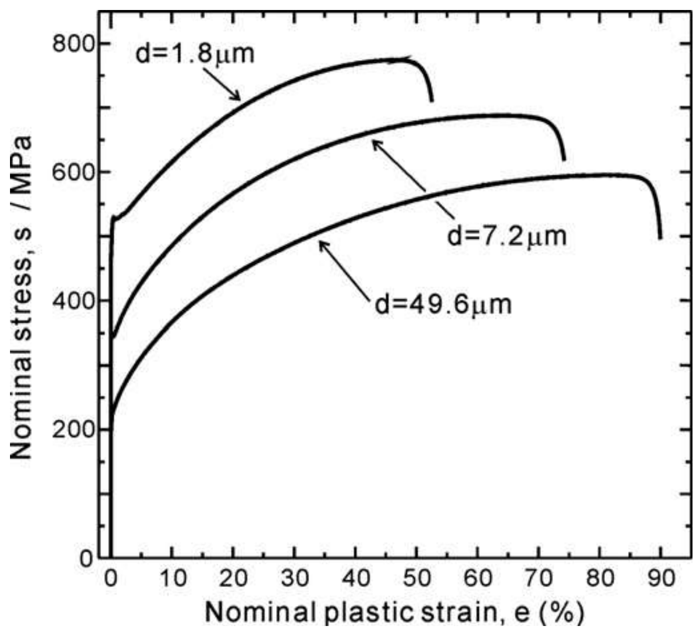

Figure 27: Tensile strength of high manganese steel (31wt.% manganese, 3wt.% aluminum, 3wt.% silicon), processed in such a way as to achieve different grain sizes i.e., d=1.8μm, d=7.2μm, d=49.6μm [101].

2.17. Deformation Twin

Twinning is regarded as one of the principle modes of deformation, observed in various FCC, BCC and HCP metals and alloys. Twins typically activate when plastic deformation through slip mechanism is not possible, i.e. when slip systems required to satisfy the Von Mises criterion are missing [102].

Unlike body centered cubic (BCC) crystals, in which a twin forms within the elastic region, in FCC metals and alloys, plastic deformation is required to form twins. The twinning mechanism is also very sensitive to temperature and strain rate. The generation of twins increases with a reduction in the temperature or by increasing the strain rate [102]. This will be discussed in later paragraphs.

In order to form a twin, the parent and twin lattices must be related to each other either by a reflection in some plane (mirror symmetry) or by a 180° rotation about an axis. They may form during nucleation, phase transformation, recrystallization or plastic deformation. Some literature suggests that deformation twins have an imperfect structure with high stacking fault energy, which is the result of a highly coordinated motion of individual atoms. This is unlike deformation through a slipping mechanism, where the entire motion of the atoms is chaotic and irregular [102, 103].

2.17.1. Stages of Twin Formation

Twins formed under the application of plastic deformation exhibit two stages i.e. nucleation and growth. The nucleation stage is further classified into homogenous and heterogenous nucleation [104]. Homogenous nucleation is generally observed in near perfect crystals, whereas heterogenous nucleation is generally facilitated by some crystal defects. There is no experimental evidence that support homogenous nucleation. However, several models have been formulated to explain heterogenous nucleation, and these were supported by experimental work. All these models were based on the dissociation of dislocation configurations into single, and multilayered, stacking faults, serving as a twin nucleus. This nucleus then grows in an orderly process, to form a deformation twin [103].

They have been described as follows: Cottrell and Bilby, in 1951, first proposed a mechanism for the formation of deformation twins in BCC crystals, as schematically represented in Figure 28 [105]. As shown, a portion (OB) of a perfect dislocation line AOBC, having a burger vector 1/2[111], lying in a (112) plane, in which it cannot glide, dissociates into 1/3[112] and 1/6[111] partials, with nodes at O and B. The burger vector 1/6[111] further cross slips onto $(\bar{1}21)$, resulting in a fault that is bounded by partials OF and FE, as shown in Figure 28. The twinning dislocation can further climb onto a consecutive $(\bar{1}21)$ planes through an imitated rotation around the dislocation OB (a pole dislocation). This results in the node at O, moving towards B, resulting in the formation of a macroscopic twin [103, 105].

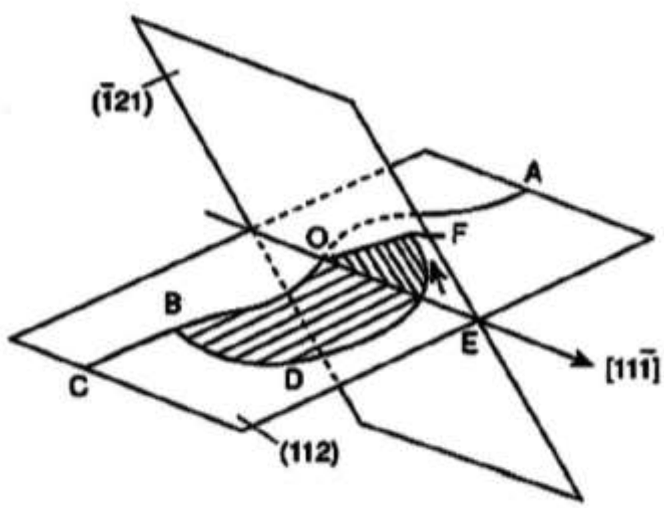

Figure 28. The Cottrell-Bilby pole mechanism for twinning in a BCC crystal. The lengths of the lattice dislocation is represented as AO and BO of burger vector 1/2 [111], BO represents the sessile partial dislocation (a pole dislocation) with burger vector 1/3 [112], whereas BDEFO represents a glissile dislocation with burger vector 1/6 [111]. OE does not have any dislocation line [105].

In later years, Sleeswyk (1963) proposed another method for the formation of a deformation twin. According to Sleeswyk, the 1/2$< 11\bar{1} >$ screw dislocation has three-fold symmetry i.e., a three-dimensional core with a 1/6$< 11\bar{1} >$ partial on each of the intersecting {112} planes. Under plastic deformation, this configuration will become unstable, resulting in a rearrangement of partials to form a three-layered twin on the most highly stressed {112} planes [106]. The dislocation reaction is presented as follows: ½ [111] screws →3 x 1/6[111] screws.

Additionally, Sleeswyk assumed that deformation twin growth also occurred by spiraling of 1/6 [111] twinning partials around a suitable pole dislocation. The Sleeswyk model was experimentally validated by Mahajan (1972a, 1975b) and co workers (1980) [107, 108]. Details can be read from the references provided.

2.18. Deformation in FCC Metals

Cottrell and Bilby also proposed a mechanism for the formation of deformation twins in FCC metals and alloys that was later modified by Venables in 1961[109]. This model was explained using the notation of the Thompson Tetrahedron, in which a Burgers vector AC is considered lying in plane b as shown in Figure 29. On the other hand, a long jog N1N2 was considered to lie in plane “a” as shown in Figure 29a. Assume that a part of the dislocation in plane a now dissociates into a Shockley and a Frank-Read Partial. AC→Aα + αC. During plastic deformation, the glissile Shockley partial αC moves away from the sessile Frank partial Aα on a plane, leaving an intrinsic fault as shown in Figure 29b. The αC winds around N1 and N2 to reach a new position as shown in Figure 29c. The αC dislocation are at one interplanar distance along RS. Since these two parts of αC are in opposite directions, large stress is required to move them further away from each other. Venables believed that the process continued to take place in another plane which leads to the generation of a microscopic twin [109], as schematically illustrated in Figure 29(c-f).

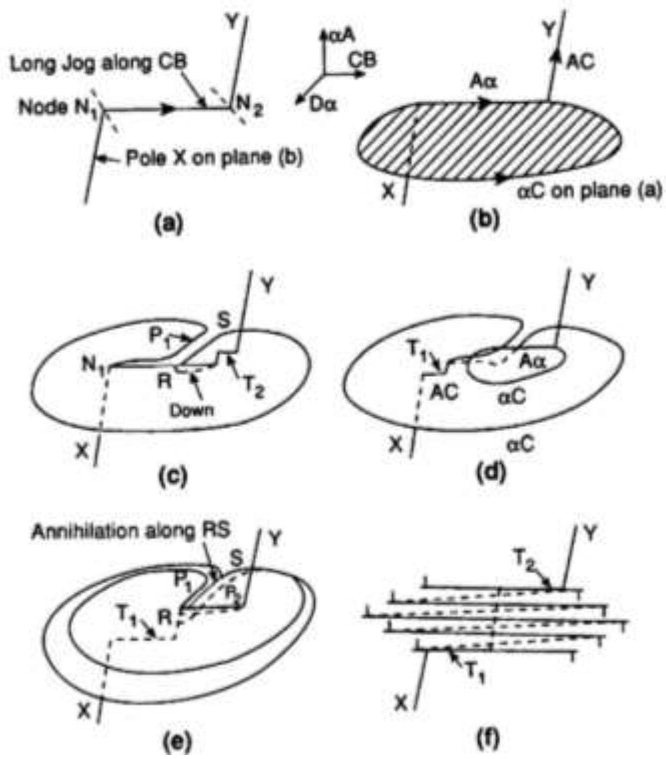

Figure 29. Prismatic glide mechanism for twinning [109].

In addition to the theoretical models presented above, several theories were formulated that were based on experimental results [110]. According to these models, twinning can only take place after slip is successfully activated on at least two systems. The reaction between dislocations of the primary system with Burger vector BC and of the co-planar system with vector DC to form three

Shockley Partials is presented as BC+DC→ 3αC, which can then be rearranged on a consecutive plane to form a three-layered fault as represented in Figure 30. For further information, please refer to reference [110].

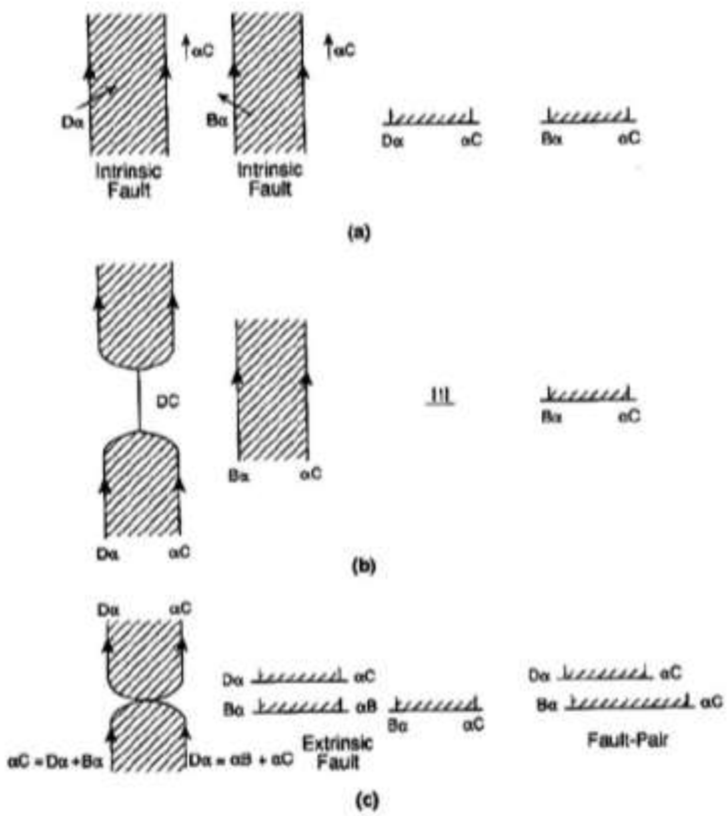

Figure 30. Various steps involved in the formation of fault pair in FCC crystal [109].

2.19. Influence of Material Variables on Twinning

The twinning phenomenon is dependent on many factors such as strain rate, temperature, prestrain etc. However, it is out of the scope of the present literature, to discuss each of them in detail. As such, only the effects of temperature and strain rate over the formation of twins are explained in the next section.

2.19.1. Temperature

The tendency for FCC, BCC and HCP metals to form twins upon plastic deformation, increases with decreasing temperature. In FCC metals and alloys, the temperature governs whether twins or slip will form during plastic deformation. Additionally, the type of the deformation twin that results due to plastic deformation is also dependant on temperature. For example, alloys with very low fault energies generally form very fine deformation twins at low temperatures, as opposed to metals with high fault energies that form large deformation twins when deformed at high temperatures [110, 111, 112].

2.19.2. Strain Rate

Strain rate has a dominant effect on the formation of deformation twins. In fact, all metals, under severe shock loading conditions, irrespective of their crystal structure, i.e. BCC, FCC, and HCP, deform entirely via twinning. The typical mechanism through which twins form at a high strain rate, is now presented. After severe plastic deformation, the microstructure will be consisting mostly of long screw dislocations. These are generally immobile, unlike tangled dislocation structures formed after room temperature deformation. Due to their restricted mobility, they prefer to dissociate, and to form deformation twin embryos, as explained above.

At sufficiently low temperatures, the incidence of double cross slip is reduced with a subsequent increase in the interaction between co-planar dislocation interaction. As a result, thin twins will form [102, 103].

2.20. Annealing Twins

Annealing twins are generally observed in FCC metals and alloys and are characterized by many straight-sided crystals, having mirror symmetry with its neighbouring crystals [113]. Annealing twins have been extensively researched over the last 90 years ever since they were first observed. Especially in the last 20 years, when the focus shifted to achieve high strength polycrystalline material via grain boundary engineering (GBE) [113]. Additionally, the origin and growth of the annealing twins by direct and indirect methods were investigated. A direct observation is the method in which the formation of annealing twins is analyzed in-situ [114, 115, 116], as opposed to indirect observation. This involves quantitative analysis of annealing twins and its influence on processing and other microstructural factors [117, 118]. Additionally, various models have been proposed, to explain the general mechanism for the formation of annealing twins in FCC metal and alloys. These models were based on the following phenomena (1) growth accident, (2) nucleation via stacking fault, (3) immobile boundary decomposition and (4) Annealing twin boundaries interactions related to boundary migration [119].

There is a mutual consensus between researchers that annealing twins generally form during recrystallization and grain growth, primarily during the recrystallization phase. Additionally, the nucleation and growth of an annealing twin is not associated with a reduction of interfacial energy, unlike grain boundary orientation phenomenon or partial dislocation emission. Instead, the formation of twins is related to the grain boundary mobility and migration velocity. For further details please refer to the appropriate literature [119].

2.20.1. Crystallographic Description of a Twin in FCC

The twins formed in a FCC crystal structure have a different stacking sequence as compared to their neighbouring crystals, as shown in Figure 31c. The stacking sequence is inverted from ABC to CBA at the twin plane. As a result, the twin plane and the ones surrounding it (ABA), have the characteristics of a hexagonal close-packed (HCP) structure, with the free energy of a FCC structure. Additionally, the twins lie in [111] plane are inherently coherent, otherwise they are in-coherent (See Figure 31a) [114].

2.20.2. Annealing Twin Morphologies

There are many different types of twin morphologies, broadly classified into two and three-dimensions, as shown in Figure 31b, 32. The morphologies of two-dimensional twins were first explained by Mahajan et al in 1997 [120]. According to them, the annealing twin could have four different morphologies as shown in Figure 31b. Twin A appears to be located at the very corner of the grain as opposed to B and C which are located almost in the middle. Twin B spans throughout the grain whereas Twin C terminates within the grain. The last twin is embedded entirely inside the grain. It has been determined that the two-dimensional morphologies cannot describe the real three-dimensional nature of the annealing twin, therefore a three-dimensional system of designation was devised later by Bystrzycki et al as [121] shown in Figure 32a. He showed that a typical three-dimensional annealing twin can exhibit different types of two-dimensional morphologies which were later proved by carrying out the serial sectioning experiments represented in Figure 32b.

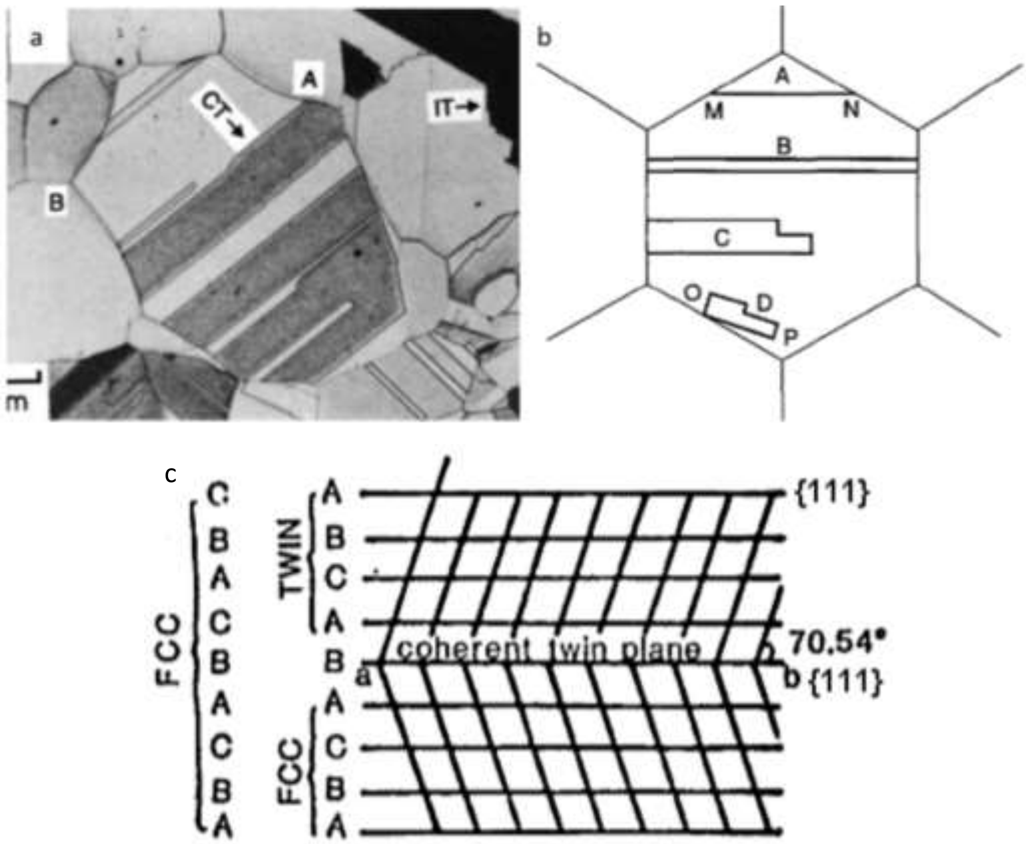

Figure 31. (a) Showing coherent and incoherent twin boundaries in a 70:30 brass, (b) Schematic of two-dimensional morphologies of annealing twins observed in F.C.C. crystals [119], (c) Stacking sequence of FCC crystal and annealing twin [114].

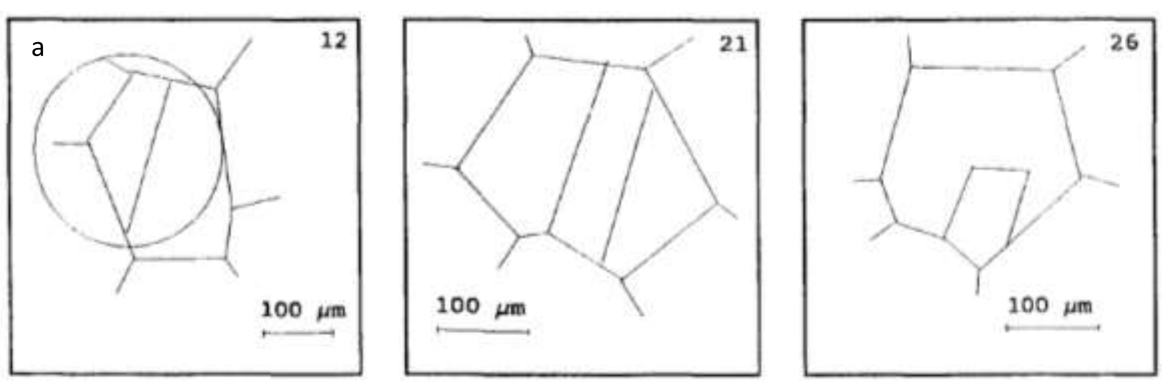

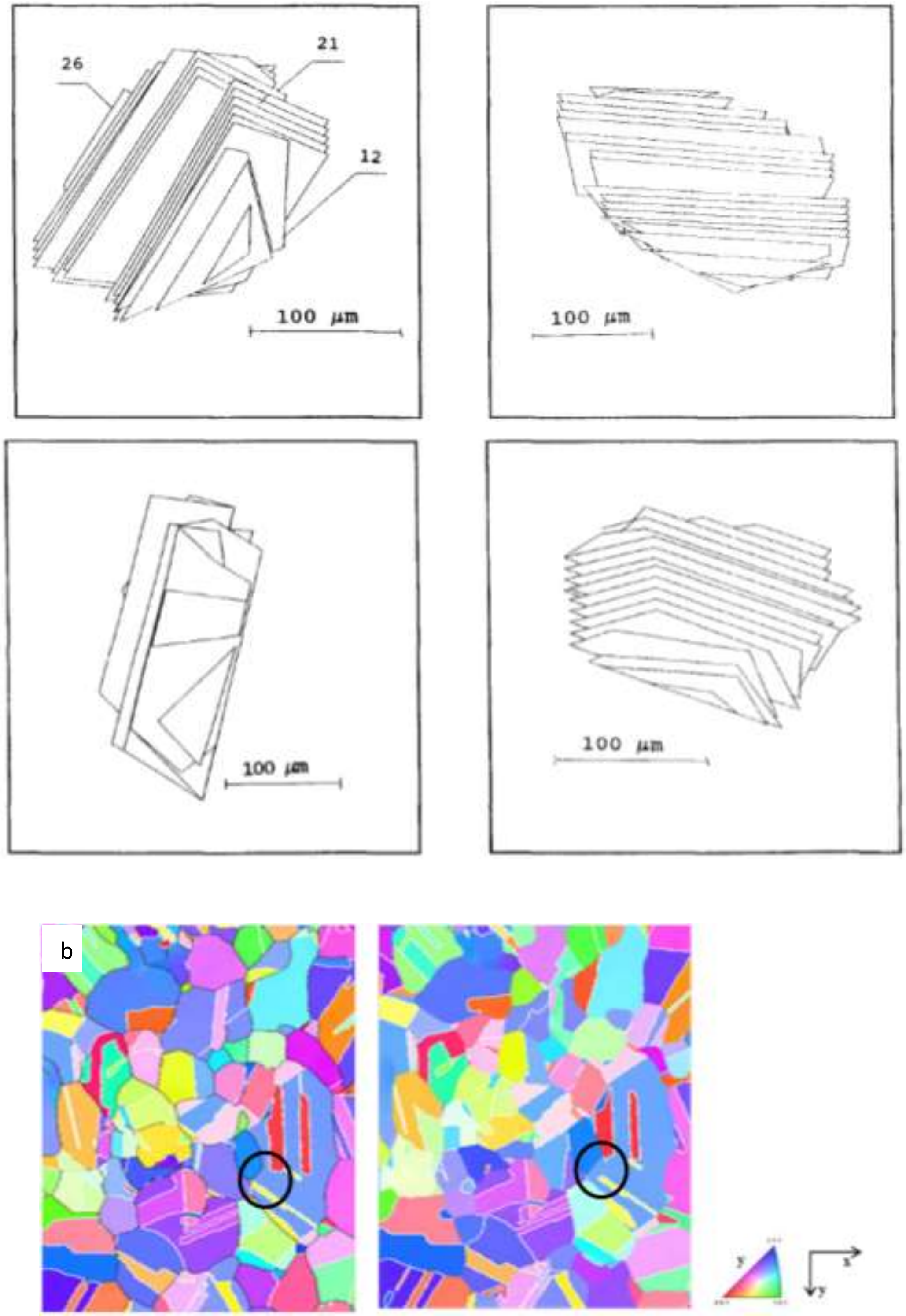

Figure 32. (a) Three dimensional morphologies of annealing twins (serial sections) [122], (b) Micrograph taken at two different planes, proving three-dimensional morphology of annealing twins [114].

2.21. Horizontal Single Belt Casting (HSBC) Process

2.21.1. Introduction

The ferrous/non-ferrous industries are struggling to bring down the overall cost of production, whilst conforming to increasingly stringent environmental regulations imposed by governmental bodies. Near Net Shape Casting (NNSC) processes offer an efficient, cost-effective and environmentally sustainable path to produce ferrous/non-ferrous strips [123]. In NNSC processes, the cast products dimension is close to that of the final product. As such, only a few deformation passes are required to achieve the desired sheet thickness, without the need for intermediate reheating [124]. These factors bring significant economic and environmental benefits, that are virtually impossible to achieve through conventional Continuous Casting (CC)/Direct Chill Casting (DSC) of ferrous/non-ferrous strips. Two most commonly practiced NNSC processes are Horizontal Single Belt Casting (HSBC) and Twin Roll Casting (TRC) [123, 124].

2.21.2. Brief History of Near Net Shape Casting Processes

Henry Bessemer, in early 1846, conceived the idea of producing the metal strip directly from molten metal [125]. In 1865, he patented his twin roll caster design for casting iron and steel strips [126, 127]. The design of the Bessemer's twin-roll caster is shown in Figure 33a. He later identified some fundamental problems such as the feeding of the molten metal into the revolving rolls, edge containment, and poor strip quality, which forced him to abandon his idea of casting steel strip via the TRC method [128].

Edwin Norton, in 1890 pursued Henri Bessemer's twin-roll casting concept by taking it to the level where he successfully produced 3-5 mm thick strip [125, 129, 130]. However, he also identified several mechanical problems associated with the TRC design which stopped him moving further ahead with this project [125, 130, 131].

1920 was the year when the TRC project was again picked up by Western Countries and the USSR. Several research programs were initiated; among the most noticeable was that by Clarence W. Hazelett [129, 132]. However, when he failed to resolve the problems associated with strip thickness variability, cast quality, and edge containment, he switched to design the Single Roll Caster (SRC) [125, 129, 132]. SRC also failed to overcome the problems associated with steel strip manufacturing mentioned above. As a result, Hazelett abandoned the development of single/twin roll casters for casting steel and concentrated on the development of a Twin Belt Casting (TBC) process [125].

After 1930 onwards, or more precisely, in between 1934 to 1950, various programs were initiated in the USSR to produce strips via NNSC processes, particularly for roofing applications [127]. However, these research and development efforts were discontinued in 1940 due to various technical difficulties such as low "as-cast" quality, low productivity, variable solidification structures, and poor mechanical properties [129, 131, 133].

The first commercialized Twin-Roll caster was developed by Hunter and Pechiney in the year 1954. This utilizes upward-vertical twin roll design to produce aluminum alloy strip [134]. Later, in 1962, a horizontal twin roll design was also developed, as shown in Figure 32. In 1970, a little modification was applied in the existing design via lifting the front end of the caster up to 15 degrees as shown schematically in Figure 33b. In following years, considerable advancements in the design/development of the TRC have been observed such as Hunter's Super Speed Caster and Pechiney's Jumbo3C (~1975), Hunter's Speed Caster/Speed Caster Plus, Pechiney's Jumbo 3CM, and Davy FastCast (~1992). For further information, please refer to the suggested references [134].

a

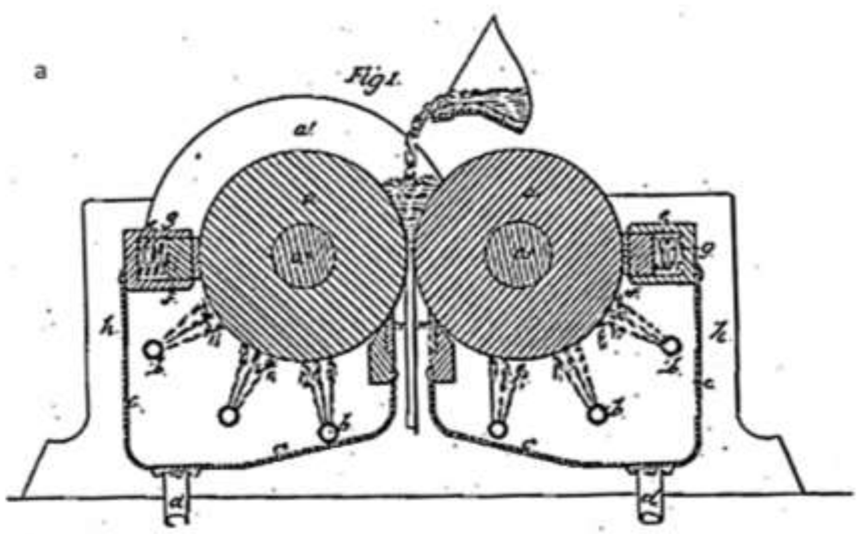

Figure 33: (a) Bessemer's twin-roll caster design for steel (1865) [126].

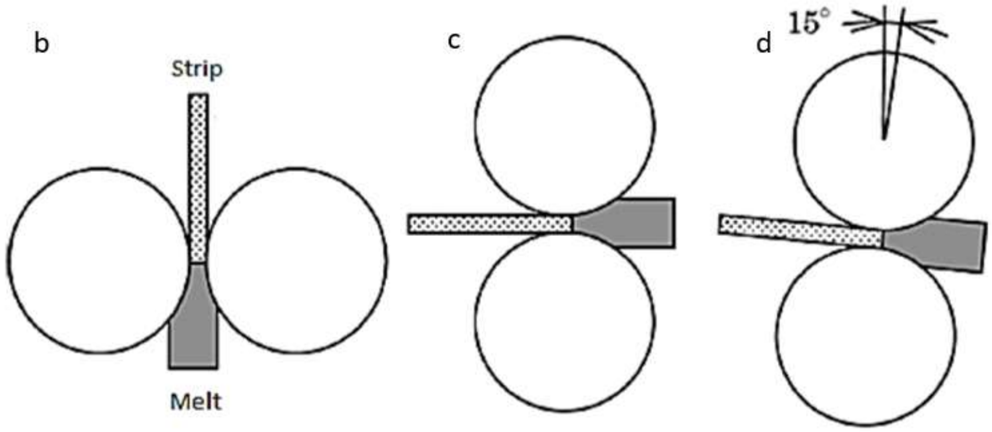

Figure 33: (b) Twin-Roll caster for aluminum alloys, the upward-vertical design (1954), (c) Twin Roll caster for aluminum alloys, the horizontal design (1962), and (d) Twin-Roll caster for aluminum alloys, the tilted design (1970) [134].

In between 1975-1985, over an hundred R&D initiatives were made by steel manufacturers, aiming to improve continuous casting processes [135, 136]. Many previously studied processes were taken into the consideration. These included Bessemer Twin-Roll and Hazelett Twin Belt caster designs [125]. The Hazelett twin belt caster was given special attention, owing to its inherent potential for producing high-quality metal strips [129]. The technical difficulties associated with this process were revisited, analyzed and believed not to be inherent to the caster [125].

Over these years, steel manufacturers emphasized the development of Hazelett style Twin Belt caster (TBC) [137]. However, when the Thin Slab Caster (TSC) process was commercialized in 1989 by Nucor, the development of TBC process again became unnecessary since TSC could produce steel strip within the same thickness ranges [135]. This lead to the termination of the majority of R&D efforts to develop TBC for steel [125].

Inspired by the potential advantages that the strip casting process could bring to steel manufacturers, Allegheny Ludlum started developing a single roll caster for specialty steels [136]. Later, in 1988, Allegheny collaborated with VAI [138], the US-based Austrian machine builder. VAI, at that time was actively performing research studies on the development of single and twin roll casters to produce steel strips [125]. In 1990, Allegheny announced that they had started pilot casting experiments at Lockport site [139]. However, they stopped their casting R&D in 1994 [125]. Over a similar time period i.e. in between 1983-1988, Armco (US-based Company) started developing Single Roll Casters. They were actively involved in this strip casting project until 1993, when they finally sold their carbon steel division and announced their termination of the project [125]. Armco also collaborated with Hazelett to develop a single roll caster. However, they believed that TRC was a better strip casting design as opposed to SRC [125].

R&D efforts continued afterward, when IMI began R&D efforts in 1987, motivated by Dofasco, Ipsco, Ispat-Sidbec, Ivaco, Stelco, and Algoma, a consortium of six steel making companies in Canada, which wanted to develop the TRC process. They named this project "Project Bessemer" [139, 140] and in 1992, a machine was produced by Hatch and Associates, a Canadian engineering consultancy firm. From 1989 to 1992, a research program was started, which was financially supported by the Canadian National Research Council [125, 140], in an effort to produce less expensive, and good quality carbon steel strip. The Project Bessemer turned into a considerable success as it was able to successfully produce carbon steel strip (2-5 mm thick and 100-200 mm wide) [136, 139]. Despite the huge amount of investment into this project, 40 million Canadian dollars coupled with 10 years of R&D efforts that had been devoted to this project, project Bessemer was finally terminated in 1988 [139]. The reasons were a lack of interest from Canadian steel makers owing to the fact that the Castrip process for carbon steel had been successfully commercialized. Canadian steelmakers had already invested in the Thin Slab Casting (TSC) process and above all, the cost of building/manufacturing industrial-scale caster was approximately 100 million Canadian dollars, coupled with the lack of investment from financial institutions [125, 139].

Other noticeable R&D efforts were carried out by Allegheny Ludlum and Armco. Bethlehem Steel began developing TRC in 1981[125, 136]. At the same time, Weirton and Inland Steel, and Argonne National Laboratory were given the task of solving the edge containment problems in the TRC process [129]. These companies were funded by the US Department of Energy (DOE) [136]. However, despite considerable research efforts, the answer to the existing question could not be found. As a result, by 1994, all the major strip casting R&D efforts in the United States were terminated [125, 136].

Another prominent contribution in the development of Twin Roll Casting was observed when Carnegie Mellon University (CMU) and the American Iron and Steel Institute (AISI) started a three years research program 'Industries of the Future' [125, 140, 141]. Several international institutions have participated including AK Steel (US), Max Planck Institution (Germany), British Steel R&D lab (UK), Dofasco (Canada), LTV Steel Company (US), USX- US Steel Company, National Steel Corporation (US), and SMS-Demag (Germany- US). This research ended with some useful conclusions, explaining the great potential and economic advantages that strip casting processes could bring to the steel manufacturing industries [129, 141].

Another breakthrough in the development of TRC was observed when the Institut de Recherches de la Siderurgie (IRSID) started R&D efforts from 1986 to 1990 [136]. This research program was funded by the European Community on Steel and Coal (ECSC)'s, Thyssen (German Steel manufacturers), Aachen Institute of Technology (RWTH) [125, 133]. The lab-scale hot model was manufactured and TRC was identified as the most feasible design to produce steel strip [142, 143].

During these years, another project 'Myosotis' was started aiming to produce 865 mm wide, 2-4 mm thick stainless-steel strips [144]. This project was financially backed by Usinor (a stainless-steel plant in Isbergues) and Thyssen [139, 145]. The Myosotis resulted in reaching industrial-scale operation when merged with Euro strip project in the 2000's [144, 146].

Nippon Steel Corporation, in 1980, began to investigate the Twin-Roll casting for stainless steel. This research project was a joint venture of Nippon Steel and Krupp Stahl AG. Their proposed design was slightly different to the conventional twin roll caster designs explored previously, since the casting rolls were of different diameters [136]. By 1987, the caster was able to produce 1-4 mm thick SS strip [147].

1986 was the year when British Steel initiated R&D efforts at its Teesside Technology Center [136]. The lab-scale model was developed for the casting of carbon and stainless-steel grades which was later upgraded in 1990 [125, 139]. The new caster could produce 2-6 mm thick and 400 mm wide strip. Nonetheless, all these efforts were abandoned in favor of conventional techniques [136].

Japanese machine builders began exploring the TRC process since 1981. Later, they collaborated with Pacific Metals, a stainless steel company located in Japan at the time, to develop a pilot caster, which was fully operational in 1990 [125]. Later US-steelmaker Inland became involved and an agreement was signed between Hitachi and Inland to implement the electromagnetic edge dam concept on the Hachinohe pilot caster. Despite satisfactory results, this project finally ended in the early 2000s [136, 148].

Strip casting research and development paved its way to the next millennium where frequent mergers and industrial synergies were seen. The most noticeable advancement in this regard is the Eurostrip project [145] started in September 1999 and via a consortium of VAI, ThyssenKrupp, with the support of AST (Acciai Speciali Terni), CSM, (Centro Sviluppo Materiali) and Usinor-Sacilor (later merged in 2001 into Arcelor and ArcelorMittal in 2006). VAI became the plant builder for the Eurostrip project [149].

In a similar year, another TRC named the Terni strip caster was developed, and was fully operational in December 1999 [125]. The caster could produce 1.4-4.5 mm thick and 1430 mm wide stainless-steel strip, with an annual production capacity of 100,000 ton [145, 149-151]. This project was funded by ThyssenKrupp and Krupp Thyssen Nirosta which was an established joint stainless-steel producer at that time. In 2003, several modifications were applied, resulting in an increase in the production capacity of the caster up to 400,000 ton/yr [151]. An inline four-high hot rolling stand and an inclined inductive heating system were also added in the existing setup [150]. The schematic of the pre-industrial scale caster is shown in Figure 34a.

The Terni caster was later utilized for the strip casting of low carbon as well as electrical steels [149-152]. An inline four-high hot rolling stand was added to the Terni caster, so as to achieve in line thickness reduction of up to 40% [150]. The layout of the Terni strip caster is shown in Figure 34b.

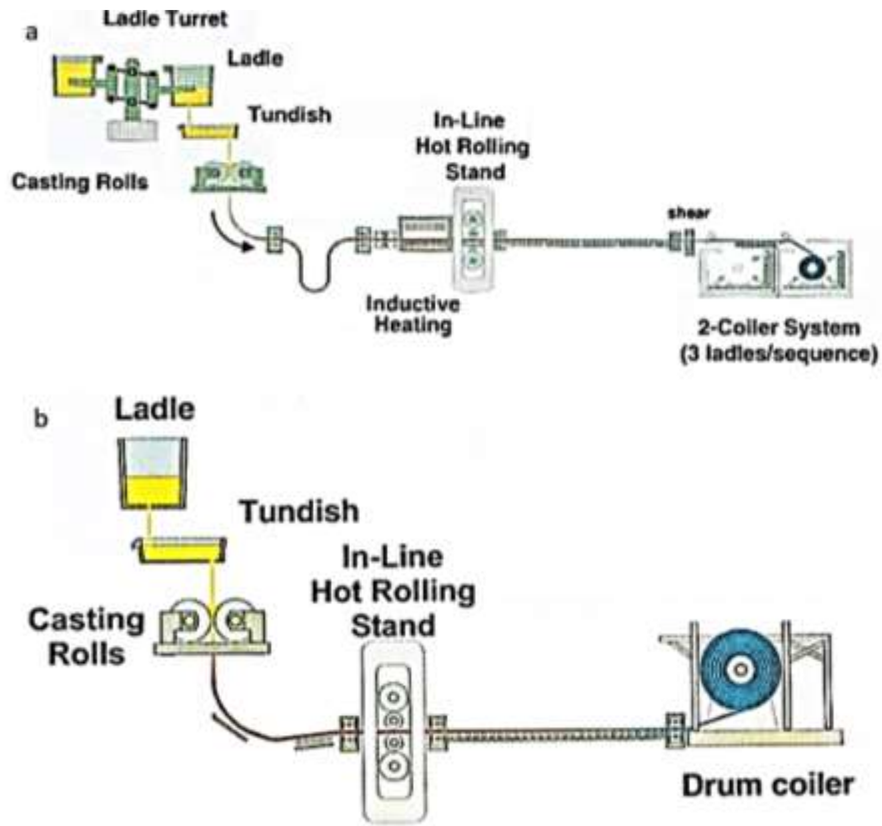

Figure 34: (a) Schematic of the industrial scale caster built at Krefeld, Germany [150], (b) Schematic of Eurostrip's Twin-Roll strip caster at Terni [150].

Both Terni and Krefeld casters were a commercial success in the early 2000s. Euro strip was another industrialized strip casting setup, available at that time [127]. However, the Euro strip project was not able to reach commercial viability, which resulted in the project termination in the mid-2000s for unknown reasons [153].

The Horizontal Single Belt Casting (HSBC) process, independently conceived by Herbertson, Guthrie [154], Reichelt, and Schwerdtfeger, et al [155], emerged from a joint effort of BHP (Australia), McGill University (Canada) and the Hazelett Strip Casting Corporation (USA). This process is like the Pilkington float glass technology, in which the molten glass is continuously poured over a bath of molten tin where it solidifies into continuous glass sheet [156]. The HSBC method involves the feeding molten metal at a pre-selected flow rate on to a chilled moving belt, where it solidifies and forms a strip of thickness up to 10 mm, as shown in Figure 35 [157, 158].

Afterward, the strip is guided through a pinch roll and a hot rolling strand, where it is reduced to the desired dimensions, as shown in Figures 36 [157, 158].

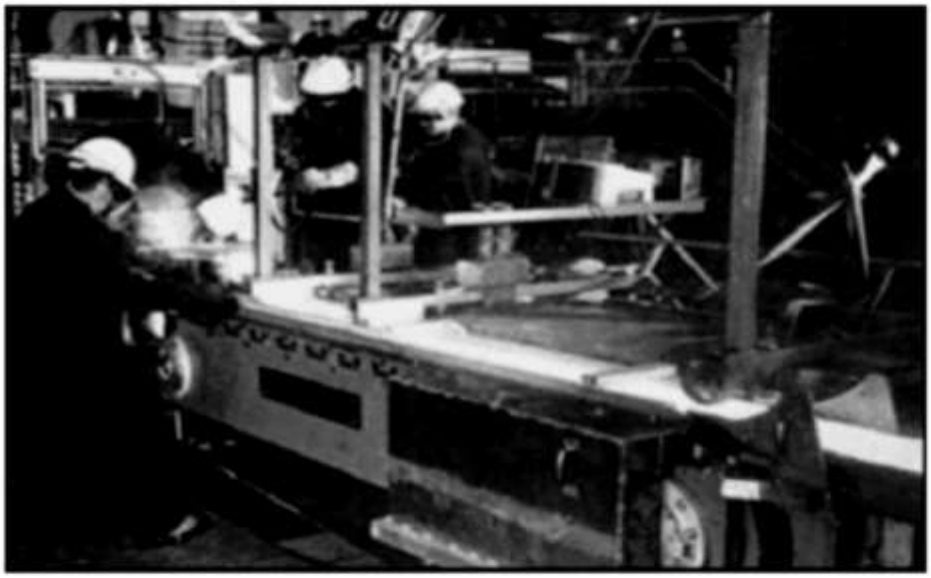

Figure 35: The Hazelett HSBC caster operating at BHP's laboratory in Australia [157, 158].

The Pilot-scale Horizontal Single Belt caster operating at the McGill Metals Processing Centre, between 1998 and 2012 was initially manufactured in 1989 for BHP's Clayton Research Laboratories by Hazelett, in order to explore the feasibility of the HSBC process to cast 7mm thick steel strips [157, 158]. The casting trials were stopped in 1995 when BHP turned its focus to the Twin Roll Casting (TRC) process [156]. Afterwards the caster was transported to McGill Metals Processing Center (MMPC) where it received several modifications. These included the design of a new alumina refractory nozzle slot, increases to the cooling capability of the moving steel belt needed to completely solidify the molten aluminum before it exits the moving belt, and enlarging the strip guidance system, so as to accommodate the wider strip exiting the caster. The new HSBC pilot-scale system also included an extension of the length of the run-out table. Details can be read from the appropriate literature [158, 159]. The HSBC pilot scale machine was relocated to the MetSim Inc. laboratories, in 2012.

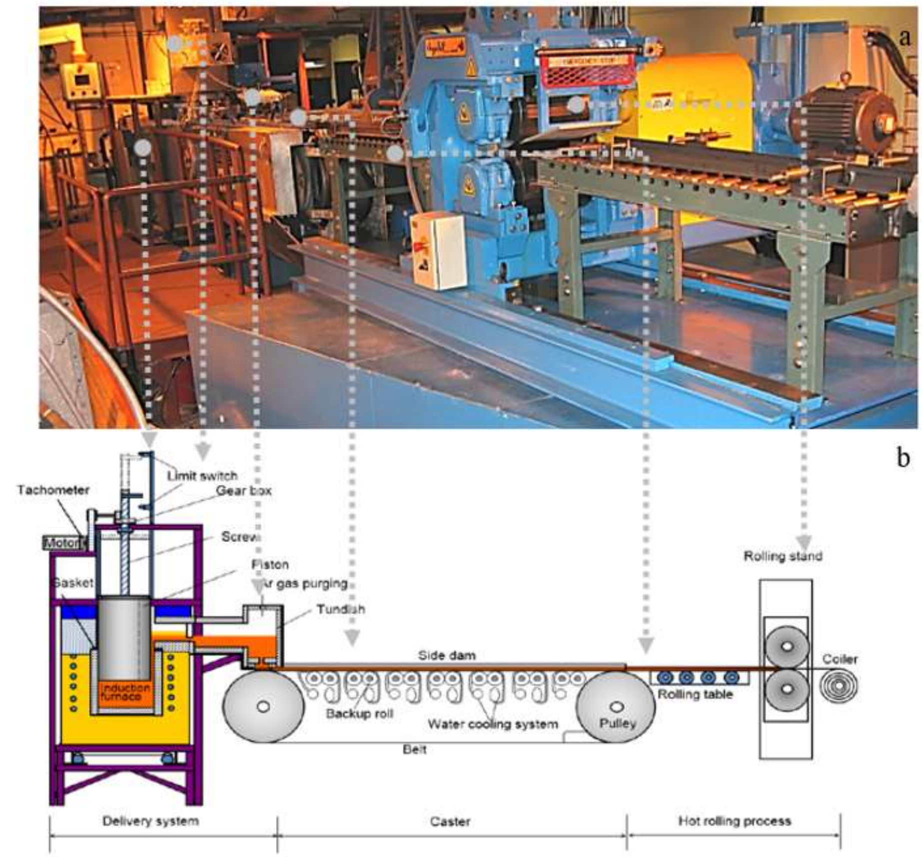

Figure 36: (a) A photograph of the HSBC pilot-scale plant, and b) a schematic of the HSBC pilot-scale machine in operation at MetSim Inc's, High Temperature, Melting and Casting Laboratory, Quebec, Canada [123, 159].

Since September 2010, the first commercial-scale HSBC plant, named Belt Casting Technology (BCT) was commissioned by SMS Siemag AG, previously Mannesmann Demag Metallurgy (MDM), and is operational in Salzgitter, Germany. It is similar in principle to the HSBC process. Historically, the first pilot plant was built in 1988 in Belo Horizonte, Brazil, capable of producing 5-10 mm thick, 450 mm wide strip [136, 160]. Later, Technical University of Clausthal (TU Clausthal) showed interest and a joint R&D effort was started which lead to the production of 10 mm thick, 170 mm wide steel strips [136]. The first casting trial was conducted in 1989. In the late 1990's, MEFOS, a Swedish research institute decided to collaborate with TU Clausthal since the single belt casting process has a production rate approximately five times higher than a typical Twin Roll Caster operation [160]. Consecutively, MDM, Daido Steel (Japan) and Vitcovice Steel (Czech Republic) joined this research initiative and in 1992, the first casting trial at the MEFOS facility took place, and a 5-10 mm thick, 450 mm wide steel strip was produced [136, 160, 161]. The caster featured a low-pressure system (LPS) and the tube feeding system (TFS). The schematic of single belt caster proposed by MEFOS is shown in Figure 37 [136].

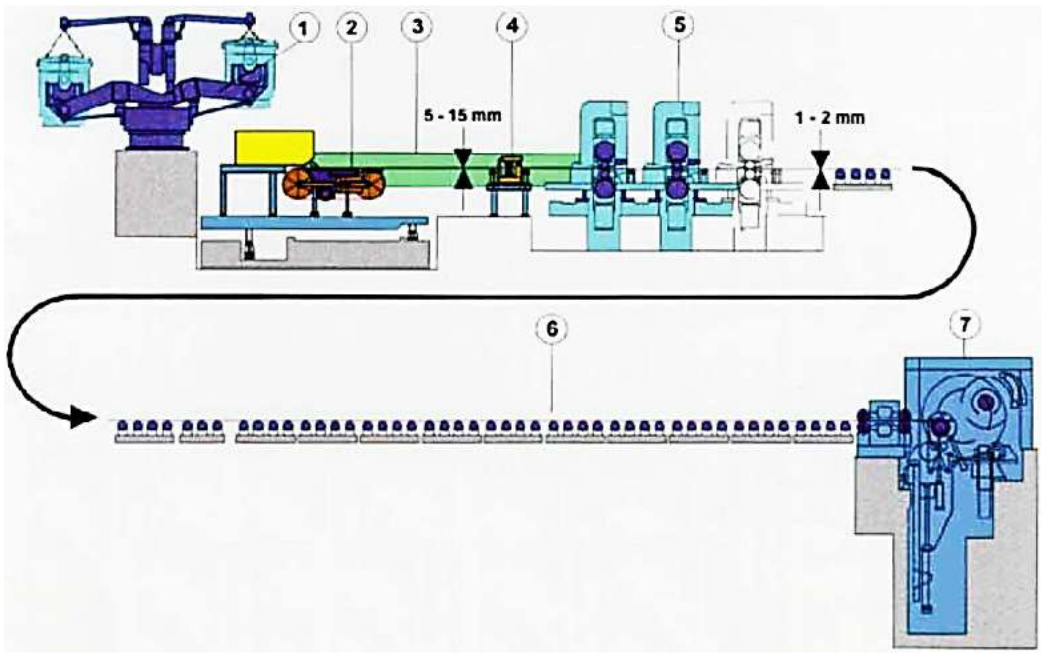

Figure 37: Schematic of a Horizontal Single Belt Caster operated by MEFOS, showing (1) Ladle, (2) Caster, (3) Shrouding, (4) Withdrawal machine, (5) Rolling mill, (6) Laminar strip cooling section, and (7) Coiler, adapted from [160].

In recent years, we have seen the European Community on Steel and Coal (ECSC), putting their efforts in developing BCT. The first ECSC project, led by both TU Clausthal and MEFOS was started in 1995 to demonstrate the high productivity achievable by BCT, followed by a second ECSC project that was started in 1997 which showed the potential of BCT to cast 900 mm wide steel strips [160]. The third ECSC project took place in 1998 with the intention of obtaining data for building a demo-caster. R&D effort continued, emphasizing on improving the liquid steel feeding system, studying the phenomenon of heat transfer, etc. Seeing these advancements urged Salzgitter AG and ThyssenKrupp to invest in BCT [160, 162]. By 2006, there were three pilot casters, fully operational and progressing towards commercialization [163, 164]. Finally, in September 2010, a contract was signed between Salzgitter AG and SMS Siemag to build an industrial scale BCT pilot caster which was later commissioned at Salzgitter AG in Peine, Germany, BCT® in between 2012- 2013. This plant has a production capacity of 25,000 ton/year. [165]. The design of the HSBC pilot caster at Clausthal and BCT caster at Peine strip casting plant are shown in Figure 38 and Figure 39 [165].

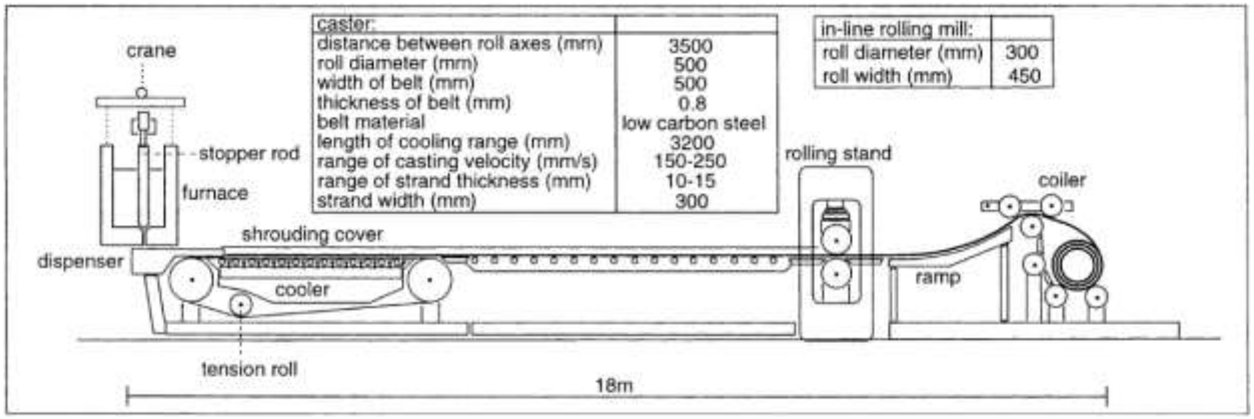

Figure 38: Scheme of the BCT pilot caster at Clausthal [162].

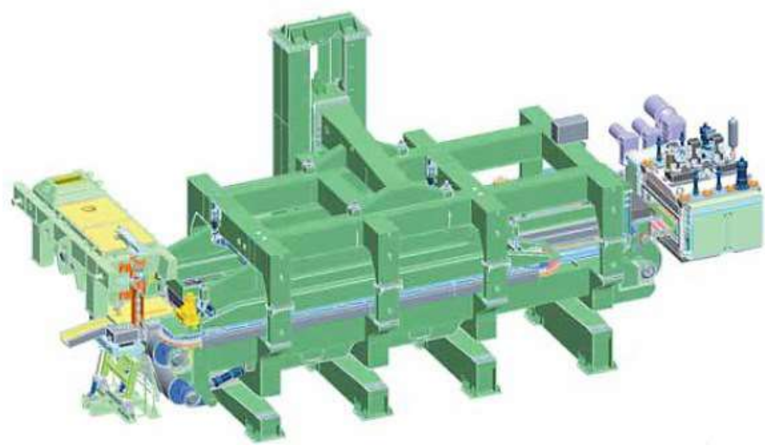

Figure 39: BCT caster installed at the Peine strip casting plant [165].

In 1985, Mitsubishi Heavy Industries (MHI), a Japanese machine builder developed a TRC system [166]. It could produce 600 mm wide strip employing a 600 mm wide and 600 mm Φ rolls. Later it was modified after Nippon steel decided to invest on TRC project for producing stainless steel strip [167]. A 1-ton, 800 mm wide, lab-scale model was manufactured in 1986 which was further upgraded to a 10-ton pilot caster in 1989 [167]. The plant was installed at Hikari works, comprising of 800 mm wide, and 1200 mm diameter rolls [166-168]. The schematic of Hikari TRC is shown in Figure 40. Further modifications were applied in later years, so as to increase the width of the as-cast strip. The pilot caster could produce 1.6-5.0 mm thick steel strips at 20-130 m/min casting speed, as was fully operational by 1993 [168].

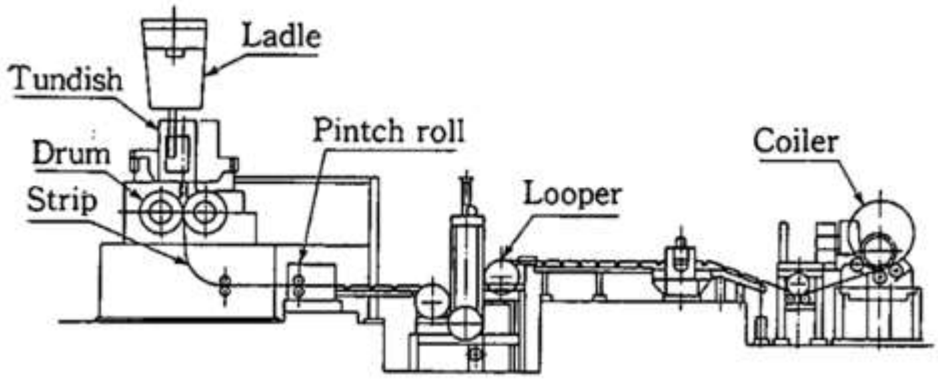

Figure 40: Schematic of Nippon Steel's 10t pilot twin-roll caster at Hikari, Japan [168].

In 1996, the construction of the world’s first commercial TRC began and approximately after two years, the commercial production of stainless steel strip was started in September 1998, after successive casting trials [167].

The Hikari caster was successfully utilized to produce stainless steel strip which reached the production capacity of 20,000 ton/month in 1998 [125,127, 167, 169]. The strip was hot rolled in line, employing a four-high, hot rolling stand. The as-cast thickness was 2-5 mm, whereas the width of the strip was 1330 mm [167]. The caster operated with 60-ton heat with a casting rate of 90 m/min [167]. A schematic of the Nippon Steel-MHI strip caster is shown in Figure 41.

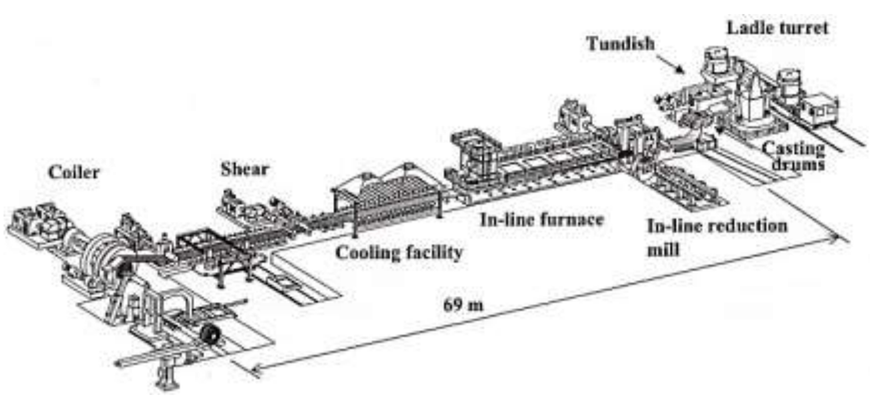

Figure 41: Schematic of Nippon Steel’s industrial-scale strip caster [127].

In 1982, Broken Hill Proprietary (BHP) and IHI agreed to develop a TRC (Castrip process) that can produce stainless and carbon steel strip for the construction industry [149]. A 5-tonne pilot caster was installed at Unanderra, Australia, in 1990 [125, 170, 171]. In 1993, steel strips, 2 mm thick and 1300 mm wide were successfully produced [171, 172]. Later in 1994, the construction of a full-scale strip caster was completed which became fully operational in February 1995.The material produced was successfully processed and were utilized by the construction industries [125, 171]. The schematic of the plant at Port Kembla is shown in Figure 42

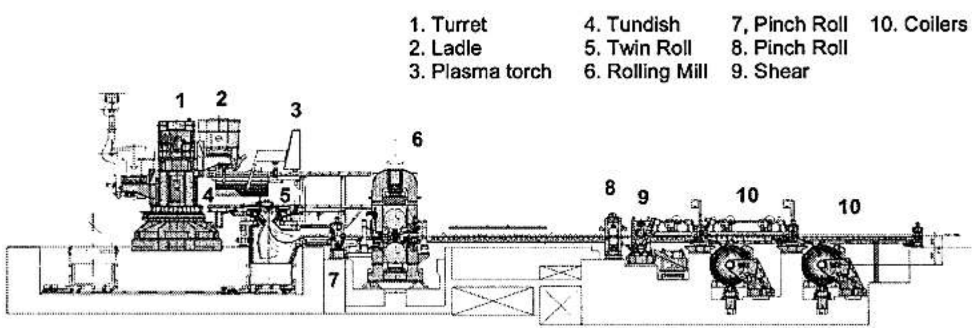

Figure 42: Schematic of the Port Kembla plant [172].

The production capacity of Castrip process was gradually increased up to 540,000 ton/yr by 2008 when it was operated by Nucor steel in between 2002-2004 [173, 174]. Products were sold to the potential buyers and the success of the Crawfordsville urged Nucor to build another TRC facility at Blytheville, in Arkansas [173, 174]. To date, two Castrip plants are fully operational in US, each capable of producing over 500,000 ton/yr steel strips [175].

In August 2000, MAIN AG and MTAG Marti-Technologie AG (MTA) collaborated with SMS Siemag for the construction of an industrial-scale TRC to produce both stainless steel and carbon steel strip [176]. The caster was supposed to produce 1360 mm wide, 1.9-3.1 mm thick strip, with a production capacity of 300,000-800,000 ton/yr, at casting speed of 40-100m/min [127, 176, 177].

Later CFD modeling work was also conducted by Lucerne University of Applied Sciences and Arts (HTA Lucerne, Switzerland), in order to determine the optimum casting parameters [178]. The casting trials were started on a TRC operated by Corus Research, Development, and Technology (Corus RD&T) and Teesside Technology Center (TTC), originally used in British

Steel's TRC project. It was reported in 2005 that hollow sections can be directly processed through TRC without intermediate rolling. The MAINSTRIP process is still struggling to reach an industrial scale testing phase [179]. The schematic of MAINSTRIP twin roll caster is shown in Figure 43.

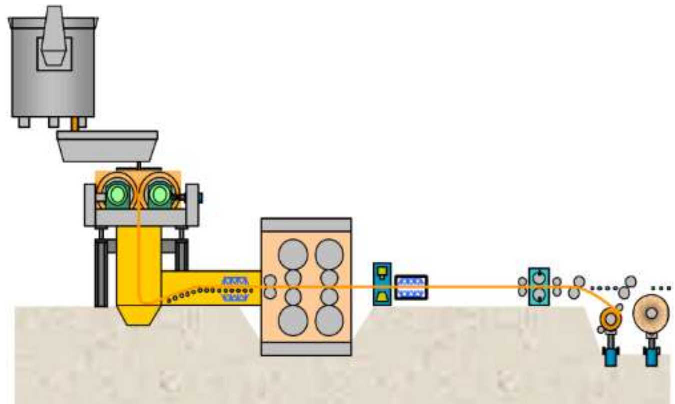

Figure 43: Schematic of a MAINSTRIP-type twin roll caster and process line. [179].

Apart from the considerable R&D efforts by North American and European countries to develop strip casting processes, Pohang Iron and Steel Company (POSCO), South Korea started developing twin roll casters in 1989 with Research Institute of Industrial Science and Technology (RIST) [180, 181]. The first Pilot caster was built in 1994 which became fully operational in 1995 [169, 180]. The pilot plant features 1,250 mm diameter rolls, 1,300 mm wide. Casting speeds were in between 50-130 m/min, and the as-cast strip thickness varied from 1.8-5 mm [127, 182].

After going through several upgrades/modifications [183], POSCO was able to build an industrial scale demonstration caster (designated poStrip), capable of producing 600,000 ton/year of steel strips. The construction work began in June 2004 at Pohang Works and was finished in June 2006. The schematic of the caster is shown in Figure 44 [125, 184]. An inline hot reduction setup is also shown in Figure 44. It was added later in 2007 into the existing TRC set up in order to produce 1.3 mm thick TRC strip [185].

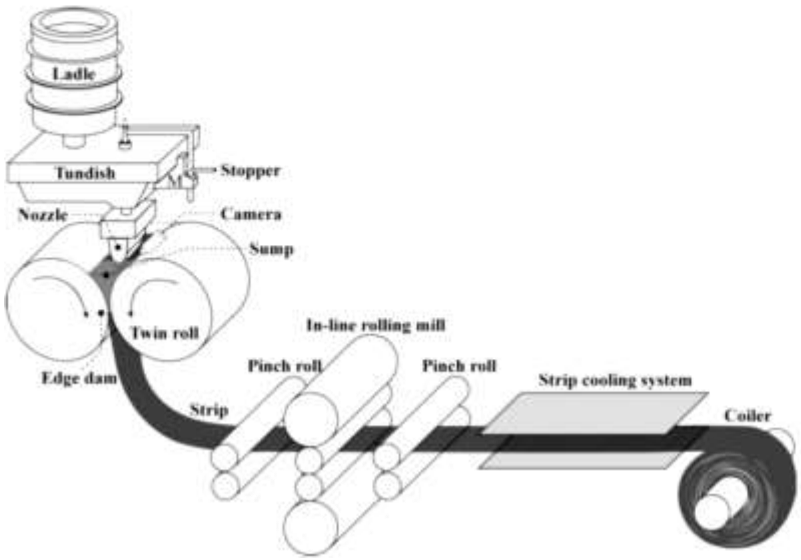

Figure 44: Schematic of POSCO's commercial-scale Twin Roll Caster [186].

Bao steel, a steel manufacturing company in China soon realized the potential of strip casting processes and decided to invest in building a TRC [187]. The project was officially started in November 2001, and after two years, in 2003, a pilot-scale caster was completed and commissioned [187]. Trial castings of stainless, carbon and silicon steels were conducted in 2004, 2005 and 2006 [187, 188]. By February 2008, the TRC received many upgrades and was turned into a full-scale test caster. An inline hot mill was also added [188]. The Boastrip caster was able to produce 2-5 mm thick, 1,350 mm wide steel strips at 110 m/min casting speed, as shown in Figure 45 [188].

Figure 45: Baostrip full-scale test caster [188].

2.22. Technical and Design Overview of the Horizontal Single Belt Caster (HSBC) System.

The HSBC strip casting technology, potentially, in many ways, is superior to Thin Slab Casting (TSB) and Continuous Casting (CC) processes. Unlike CC and TSB, the strip can be processed into finish gauge thickness with minimal reduction, since the as-cast thickness is closed to the desired final thickness. This leads to a considerable amount of energy savings, coupled with much lower carbon dioxide emissions. Additionally, strip casters are comparatively compact in shape and size, as compared to CC and TSC [189].

2.22.1. Operation and Machine Layouts of the HSBC Systems installed at McGill MMPC & TU Clausthal

The details related to the layout and operation of pilot Horizontal Single Belt Caster (HSBC), installed at McGill Metal Processing Centre (MMPC) is discussed in Chapter 3. The specific features of TU Clausthal caster is presented as follows.

The pilot HSBC installed in TU Clausthal features a tundish with an opening at its bottom through which the molten metal is delivered on to a moving belt [189]. A weir system is installed inside the launder/delivery system. Its purpose is to block the slag entering the tundish [189]. A pressure of ~ 0.7 atm is used to keep the belt stretched in order to reduce its distortion. During the casting, the molten metal is shielded with argon gas for oxidation prevention [189]. The solidified strip runs to the homogenization zone, where it is exposed to a suitable temperature for temperature homogenization, or stress relief annealing. The strip is hot deformed in a finishing line which consists of a set of three reduction rolls, in which the last one is a smoothing roll set. After the desired thickness reduction is achieved, the strip passes through the cooling zone and is subsequently coiled [189].

The caster is equipped with argon gas rakes. Their purpose is to decelerate the molten metal as it reaches the belt. In this way, an even distribution of molten metal can be ensured [164]. A schematic of the TU Clausthal Caster is shown in Figure 46.

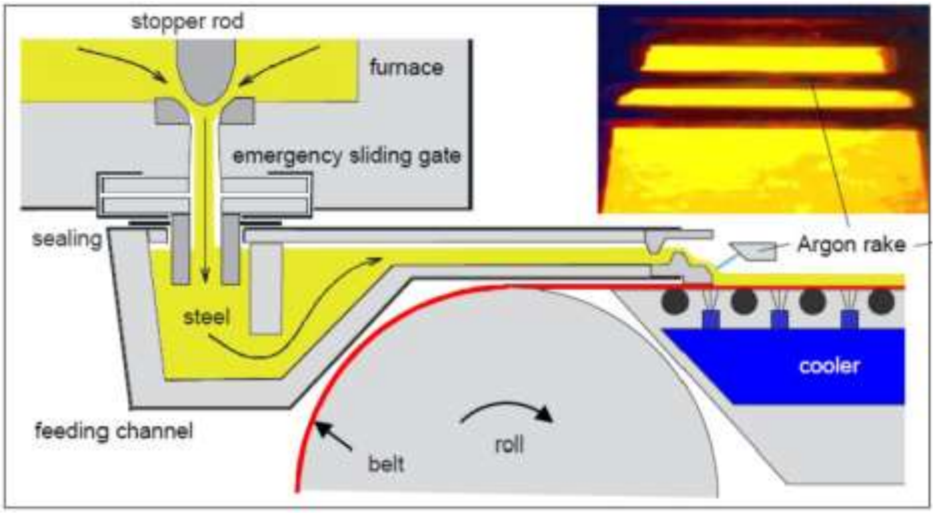

Figure 46: Schematic of the feeding system of TU Clausthal Belt caster [190].

A very distinctive feature of the TU Clausthal caster is the electromagnetic braking system, installed just behind the argon rakes [164]. Its purpose is to create a powerful magnetic field in order to minimize the relative velocity of the molten steel with respect to moving belt, thereby increasing the uniformity and smoothness of the flow [164].

Care must be exercised, controlling the upward motion (bulging) of the belt while it moves, considering the molten metal flow could become inconsistent over the belt, which would lead to a poor surface quality. In order to counteract this problem, the caster is equipped with a series of support rollers with staggered support joints. The belt is pulled against the support rollers via applying negative pressure (~ 0.3 bar). In this way, an unavoidable large deflection/distortion can be divided into many small portions along the belt, thereby limiting the overall belt movement to below 0.1 mm [190]. Additionally, a textured belt (containing raised dimples/grooves, or many small burls) is used to prevent large scale bulging. The design of the Clausthal's roll support system is shown in Figure 47 [190].

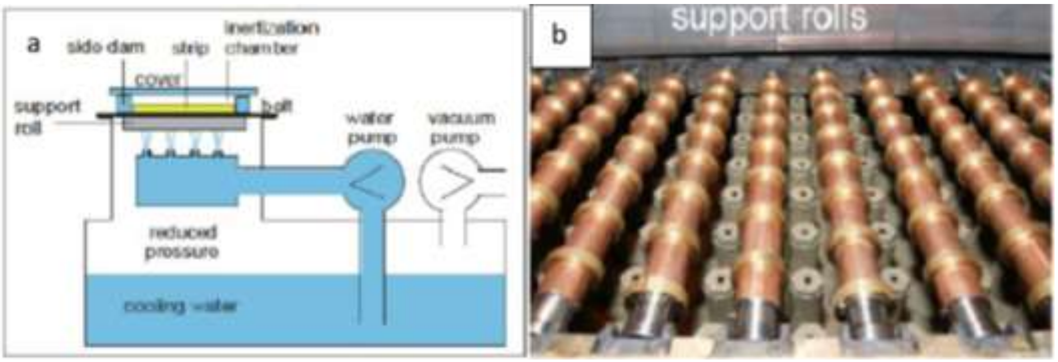

Figure 47: (a) Schematic and (b) Picture of the belt support system for the Clausthal Belt Caster [190].

Another important feature of the HSBC is the side dams. They help in lateral confinement of the molten metal, especially when thicker strip is produced (> 7mm) [164]. Figure 48 is showing a moving side dam system used in Clausthal's strip caster which consists of revolving copper blocks attached via tubes made of high strength and temperature resistant material, to form a continuous dam. Through these tubes the water could flow to maintain the side dam's temperature to the specified value.

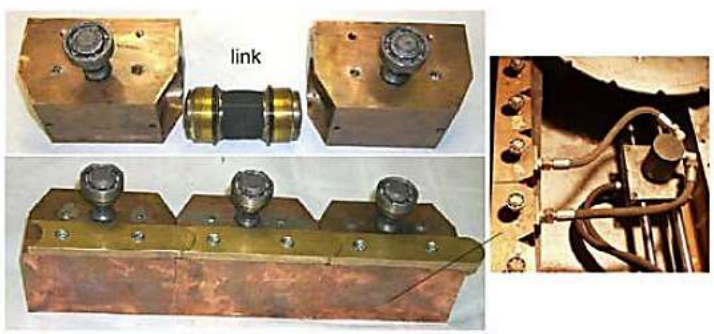

Figure 48: Different components of the moving side dam system at TU Clausthal [190].

As mentioned above, argon gas is used to protect the molten metal from oxidation, this considerably reduces the emissivity of the hot metal, resulting in a decrease in the overall rate of heat removal from the surface [164]. On the other hand, the heat removal at the bottom surface of the strip is considerably intense since the hot metal is in contact with intensively cooled belt which means that final solidification will take place close to the surface of the melt leaving a porous upper strip surface. In order to counteract this issue, CO_2 gas is added with argon. Its purpose is to decarburize the top surface of the melt thereby raising its freezing temperature. As a result, during cooling, the solidified layer readily forms on the surface due to heterogeneous nucleation which tends to increase the steel's surface emissivity. Higher emissivity leads to greater heat extraction from the top surface. Hence, the solidification of steel flow terminates approximately halfway through the strip thickness i.e. approximately at the middle of the strip. Any potential micro-porosity can then be sealed during subsequent in-line hot rolling [164].

Since the flow in the HSBC process is gravity driven, the thickness of the cast strip is heavily dependent on the quantity of the metal present in the tundish. In the TU Clausthal caster, this level is typically maintained by a ladle stopper rod mechanism, like the one used in the CC process to regulate the flow of the molten metal from tundish to the copper mold. The caster is also equipped with an in-line hot rolling and coiling system, which must be precisely synchronized with the caster speed. This synchronization is typically obtained by using speedometers, installed before and after the rolls. Rolling/coiling speed is then adjusted with the casting speed considering strip shrinkage during cooling [164].

The first commercial-scale HSBC machine was built by SMS Siemag. It was installed at Salzgitter Flachstahl GmbH in Peine, Germany and was fully operational in 2012 [165, 191]. The plant shares all the features that were previously mentioned for the TU Clausthal caster. The schematic (Figure 49) shows different components present in the caster. The caster has an 80-ton ladle and is capable of casting 1,000 mm wide strip. The entire process line is 60 m long. The maximum attainable casting speed is 30m/min [191].

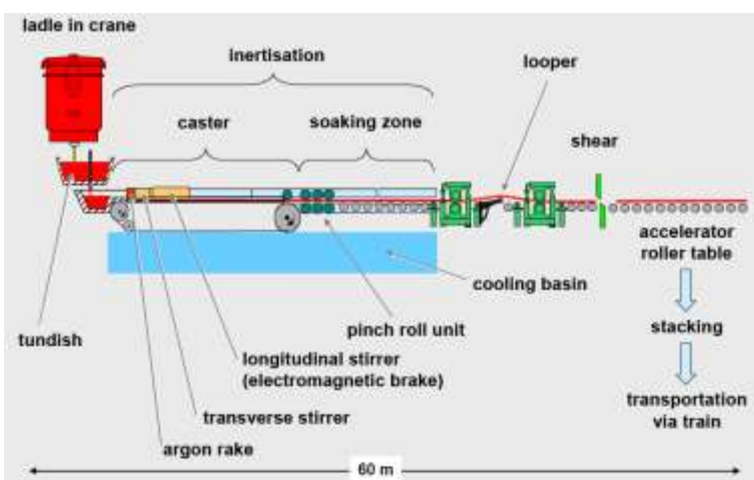

Figure 49: Schematic of the commercial-scale HSBC caster at Peine, Germany [192].

2.23. Mathematical and Physical Modelling Work Related to Thin Slab Casting (TSC) and Twin Roll Casting (TRC) Processes

Computational fluid dynamics modelling has proved itself to be extremely beneficial for design/ development and process optimization applications. A considerable amount of available literature on this subject reflects its wide applicability in the field of science and engineering. Especially the contributions of MMPC, in terms of providing technical assistance, to a number of metallurgical industries is highly appreciated. For Example, in 1990, two different designs of Submerged Entry Nozzle (SEN) were investigated at MMPC. It was demonstrated that the flow of the molten metal through the vertical slot nozzle is many times superior to the bifurcated one. Similarly, widening the TRC nozzle to the entire width of the caster leads to a much uniform solidification profile as shown in Figure 50 [193, 194].

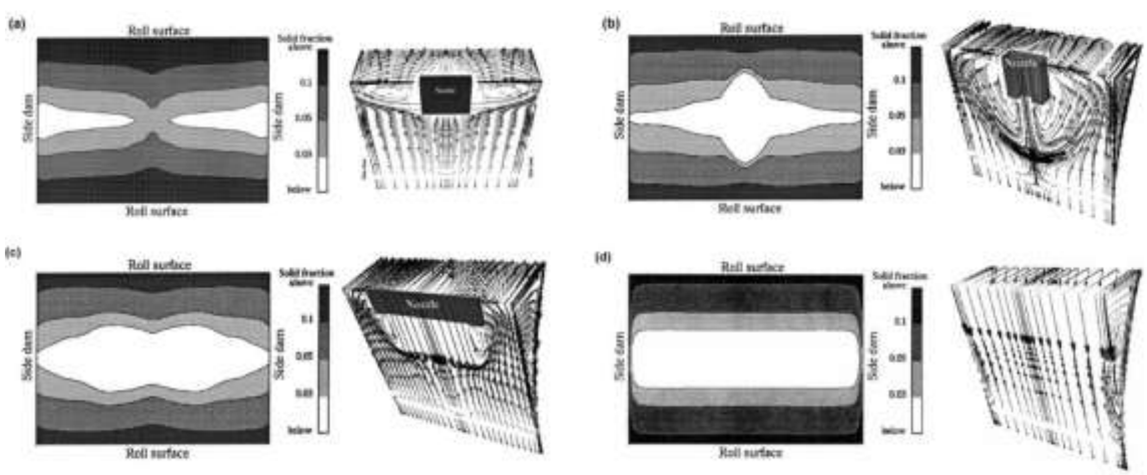

Figure 50: Predicted solid fraction profiles at horizontal plane 100 mm below molten melt/air interface and molten metal velocity fields generated by different slot nozzle configurations, a) Tubular nozzle with double horizontal ports, b) Vertical, tubular nozzle, c) Slot nozzle length is half of the roll length and d) Slot nozzle length equals the roll length [193, 194, 195].

Furthermore, MMPC researchers studied the dynamics of solidification under different casting conditions, i.e. slow and fast cooling. They particularly focused on the effect of interfacial heat fluxes obtained under different casting speeds, the mechanism of the formation of a central equiaxed region in twin-roll cast strip, and lastly the phenomenon of the double heat flux peaks obtained at higher casting speeds [196].

They showed that a cast structure of thick strip is composed entirely of columnar dendrites without any equiaxed region in the centre as opposed to thin strip in which a central region is largely equiaxed as shown in Figure 51. Furthermore, for thicker strip, the dendrites are broken or bend, marked by arrows in Figure 51. This is due to the intersection of two columnar dendrites growing from two opposite sides. For thick strip, the dendritic structure is coarse with a large secondary dendritic arm spacing (SDAS), as compared to thin strip [196].

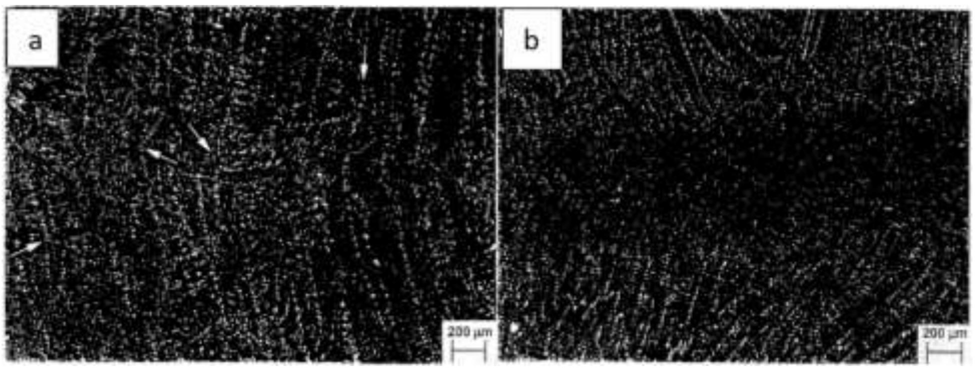

Figure 51: Cast structure of carbon steel strips produced via the TRC method under different casting conditions, (a) 6 mm thick strip produced at 4 m/min, and (b) 3.5 mm thick strip produced at 7.5 m/min. [11].

The mechanism for the formation of equi-axed grains in the center of the strip, produced via the twin-roll casting process was also explained by Tavares, Isac, and Guthrie [197]. This has resulted due to melt recirculation and plastic deformation, allowing heterogeneous nucleation of solid at the center of the strip (on dendrites tips) before it left the rolls. [197].

Furthermore, the equiaxed zone was observed to be impurities deficient. This was due to the squeezing of interdendritic liquid, full of impurities, away from the center, by the action of rolls, during semi-solid state reduction, at the kissing point. The micrographs were obtained using Oberhoffer's reagent, (Figure 51) which reveals impurity-rich regions as white, and impurities depleted region as black. As can be seen in Figure 51, the center region of a thin strip, appeared to be black, i.e. depleted of impurities.

Further physical modeling work illustrated the development of large grains formed when thicker strips were produced. This is due to the lower heat flux through the moving rolls. The metal there remained at higher temperature for an appreciable time, thereby allowing grains to grow [196].

It is important to mention that the MMPC was also actively involved in the execution of Project Bessemer described earlier in this chapter. Heat fluxes were determined under slow and fast casting speeds, using the Inverse Heat Conduction Problem (IHCP) method [197]. This program uses the time-temperature data, obtained from two thermocouples inserted into the copper substrate at different depths, 0.55 mm and 3.70 mm below the top surface, respectively. At a slow casting speed (~4m/min), a single heat flux peak was observed, as opposed to at a high casting speed (~ 7.5 m/min), in which two peaks were identified. The mechanism was explained by Guthrie, Isac, Kim, and Tavares, by taking into account various factors such as formation of a solidified shell adjacent to each moving mold, the thermal expansion of the moving rolls due to transfer of heat of the molten metal to them, shrinkage of the solid metal in contact with moving rolls, and rolling of the solidified strip [197]. These phenomena are schematically represented in Figure 52 and 53.

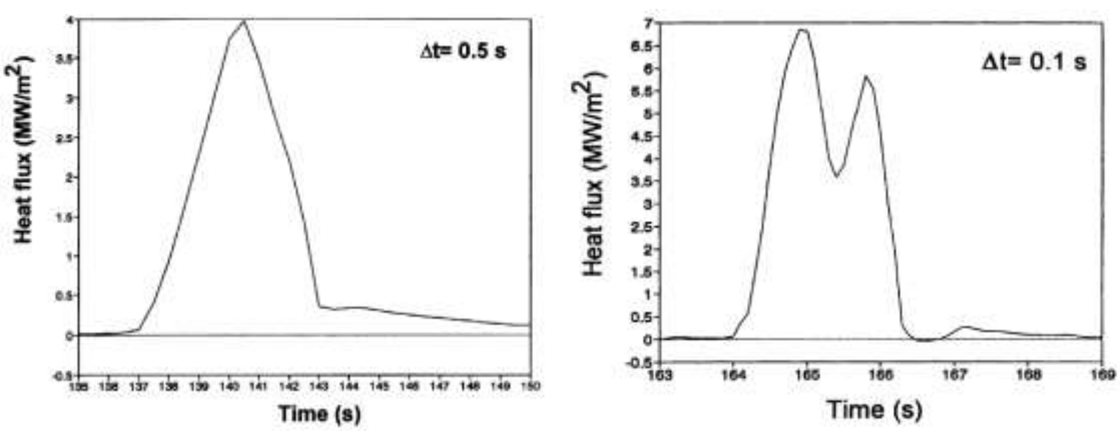

Figure 52: Interfacial heat fluxes vs contact time, for (a) Slow casting speed (4 m/min) and (b) “Higher” casting speed (7-8 m/min) [197].

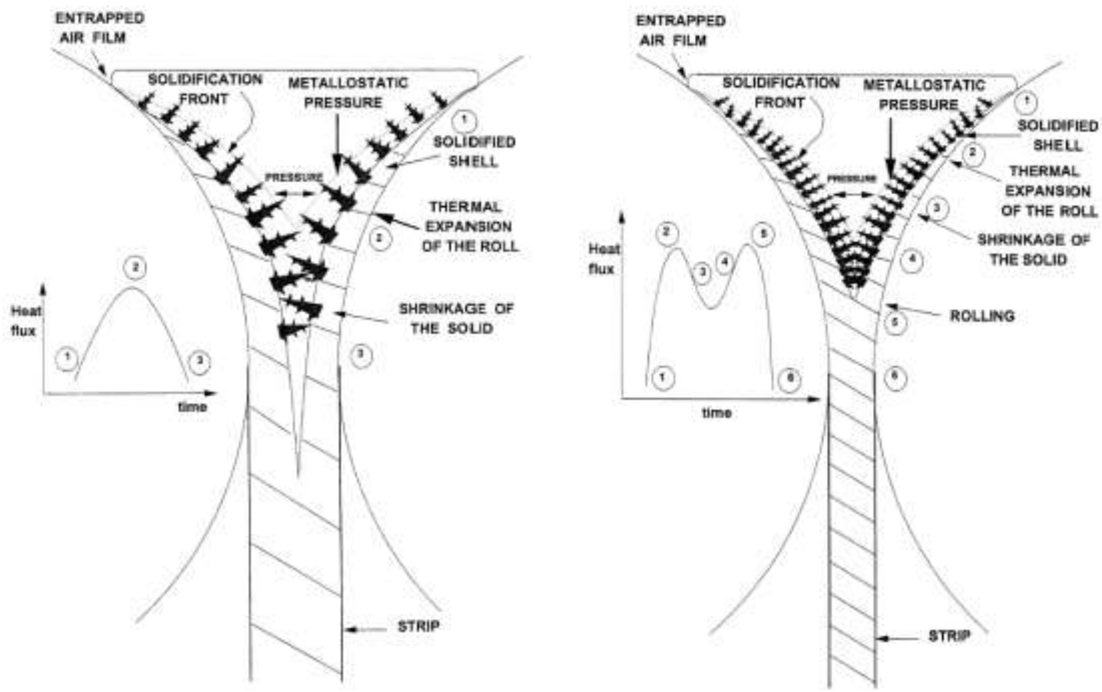

Figure 53: (a) Heat flux curve with a single peak obtained at slow casting speed, (b) Heat flux curve with double peaks obtained at higher casting speeds [197].

2.24. Mathematical and Physical Modelling Work Related to Horizontal Single Belt Casting Process (HSBC)

The success of the HSBC process rests heavily on the method through which molten metal is delivered to a cooling substrate. Two different kinds of the delivery system were numerically and experimentally tested in this thesis. They were classified into two major groups, i.e. single impingement, and double impingement, depending on how many times the falling stream of molten metal, encounters obstacles [198]. Numerical modelling was utilized, coupled with the experiments, to determine the correlation between various operating parameters against the stability of the meniscus at a triple point, a point where the molten metal-free stream, air, and moving substrate, all meet each other, as shown in Figure 54, 55 [198]. It was determined that a highly fluctuating meniscus tends to drag air into the strip thereby affecting its bulk quality. Similarly, the fluctuation of the melt/air interface, up the inclined refractory plane was numerically investigated and was considered as a primary reason for disturbances being transferred downstream to the entire length of the aluminum strip, thereby deteriorating the surface quality of the as-cast product as shown in Figure 55 [198].

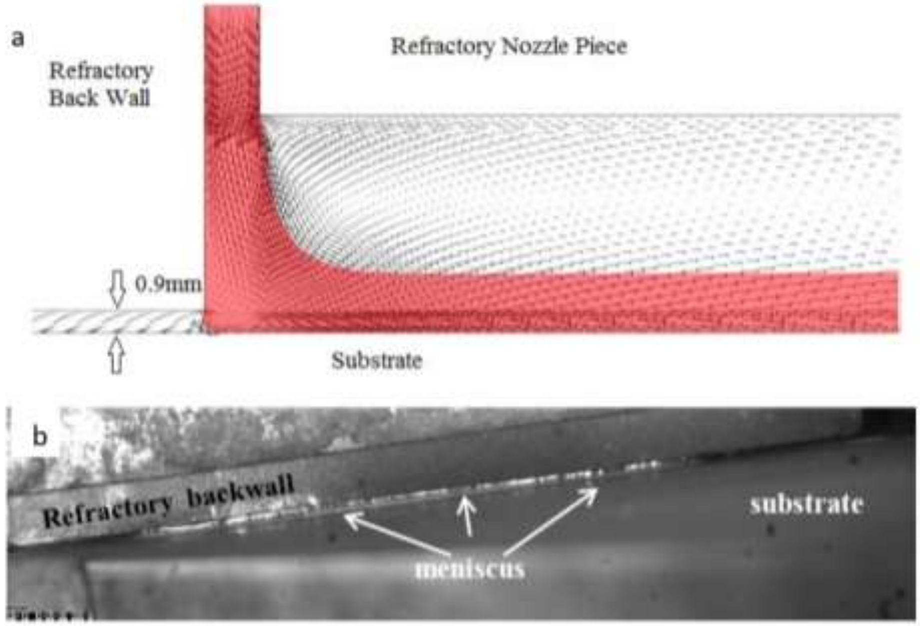

Figure 54:(a) The predicted and (b) experimental molten aluminum flow, at triple point in a HSBC process [6].

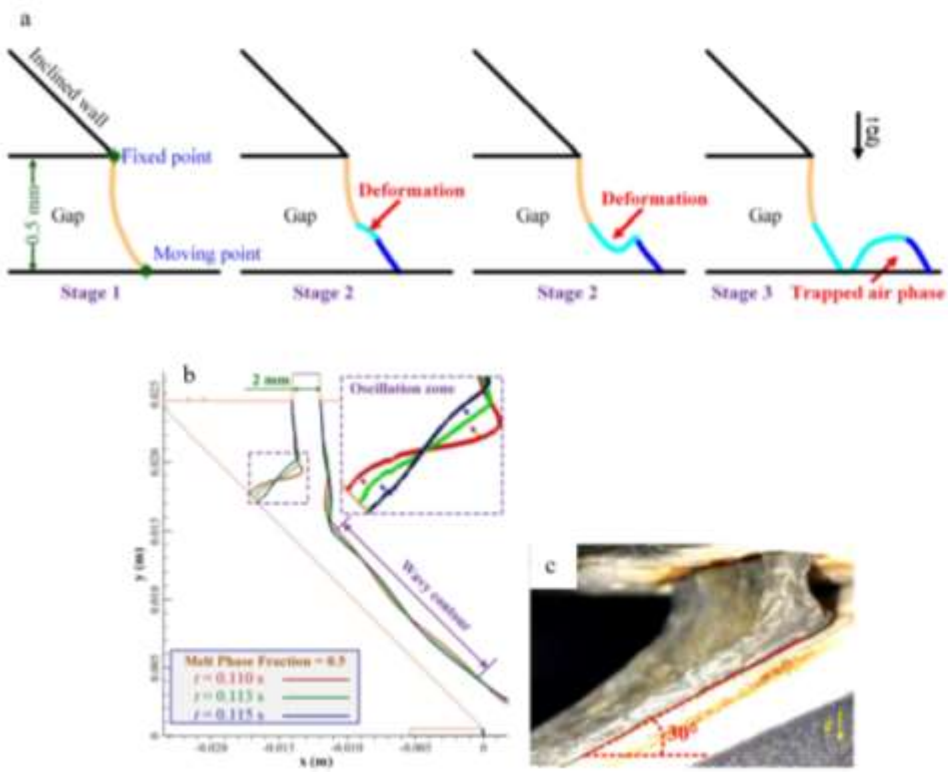

Figure 55: (a) Deformation/instability of molten metal/air interface at triple point, (b) Fluctuation of molten metal/air interface over inclined refractory plane [198].

Additionally, considerable R&D efforts were made, in order to understand the cooling capability of the chilled substrate as a function of its surface roughness. *Ab-initio* predictions of interfacial heat fluxes were used for detailed numerical studies [157]. It was determined that air entrapped within the crevices of the chilled substrate, can significantly reduce the heat flux and greatly affect the bottom surface quality of the cast strip. Since these crevices on the substrate are filled with air, the air is instantaneously heated up, and expanded, when coming into contact with the hot, molten, metal. These localized thermal expansions can lead to the formation of dimples at the bottom surface of the strip, as shown schematically in Figure 56 [157]. These projections/dimples limit heat transfer owing to the loss of contact between, copper substrate and the molten metal which results in an overall reduction in interfacial heat flux value [199].

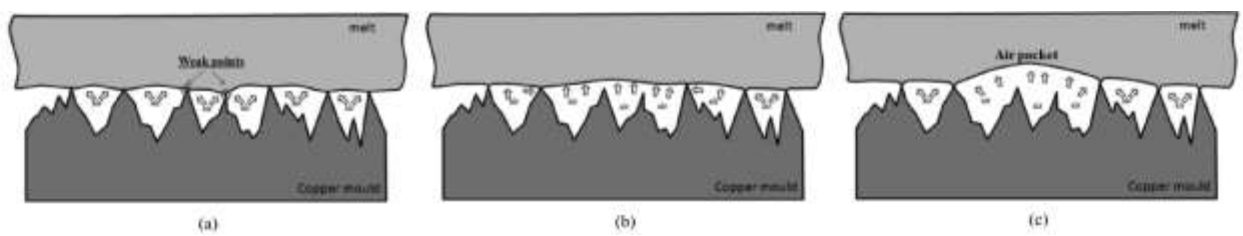

Figure 56: Proposed mechanism for air pocket formation, a) Expansion of entrapped air, b) Molten melt loses contact with the substrate at various points and c) Air pocket formation and growth [157].

2.25. Solidification of Molten Metal in the HSBC Process

As explained above, the HSBC process involves feeding molten metal onto an intensively cooled moving belt. The strip microstructure (grain size and SDAS) is relatively finer than those in conventional cast products obtained through (Direct Chill (DC) Casting/Continuous Casting (CC) process. This is the result of the high cooling rate of molten metal in the HSBC process [6].

To explain this phenomenon better, a 3D multi-phase ab-initio thermal model was developed by the MMPC researchers that helped to accurately predict transient molten metal/substrate interfacial heat flux, as the characteristics of the microstructure are heavily dependent on the value of the heat flux. The effect of the air-gap evolution onto the interfacial heat flux and substrate roughness was also investigated [199]. Details related to the said model are represented in Figure 57.

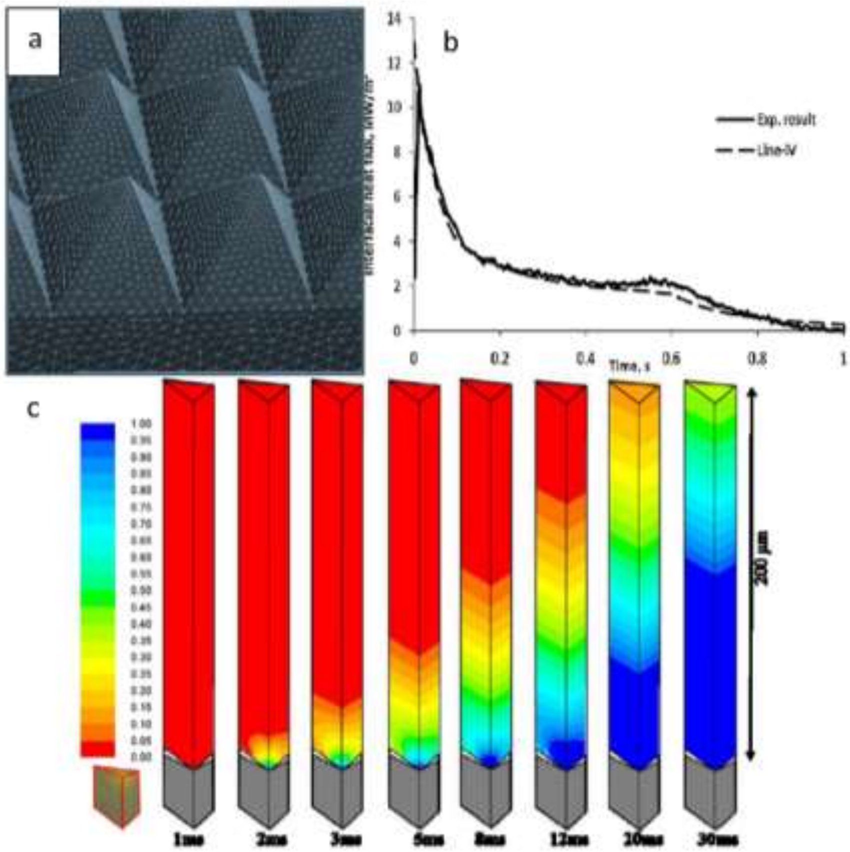

Figure 57: 3D ab-initio HSBC model developed by MMPC researchers, (a) Showing the 3D mesh design of the substrate, (b) The predicted vs. measured interfacial heat flux, and (c) The predicted transient melt solidification behavior [178].

Furthermore findings show that increasing the substrate roughness can be very advantageous towards achieving high interfacial heat flux, i.e. from 1.7- 3.5 MW/m^2 (without sandblasting), to 12.8-13.3 MW/m^2 (with a sandblasted copper substrate). This result is due to an increase in the density of the microscopic projections, or more appropriately, the contact points between the molten metal and copper substrate [178].

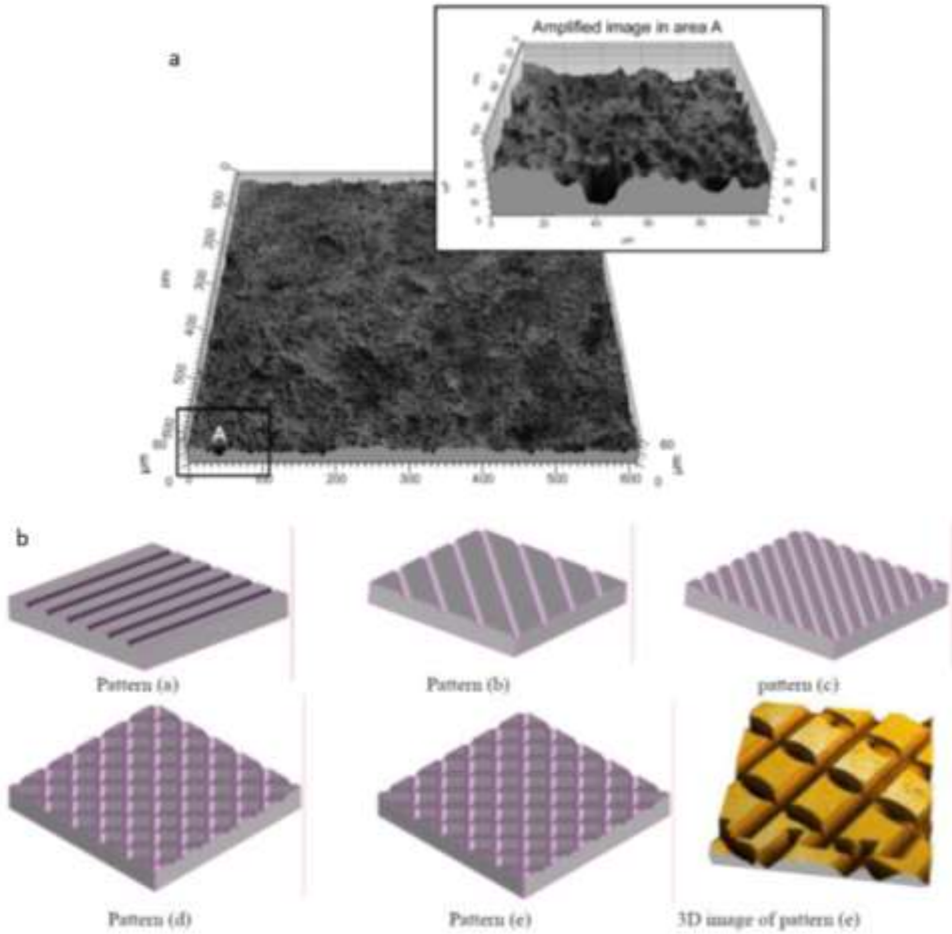

Figure 58: (a) Sand blasted substrate, (b) Different substrate textures. [200].

Additionally, different macroscopically textured copper substrates were tested. For example, patterns d and e were identified to be very effective towards increasing the as-cast surface quality of AA6111 strip along with a reduction in average grain size, resulting in increasing the mechanical properties of the cast strip, as shown in Figure 58 [200].

The grain size and secondary dendrite arm spacing were measured for a 3.5 mm thick AA6111 strip produced on a textured and sandblasted copper substrate, coated with graphite. SDAS resulted in a textured substrate was finer than the sandblasted, and graphite coated. This was due to rapid heat extraction from molten metal to the moving belt which otherwise is reduced on the application of a graphite coating. The microstructure of the HSBC strips of AA6111 consists in equiaxed grains with uniform distribution of Al_3Cu_4MgSi, $Al_{12}CuMgSi_3$, and $Al_{12}Cu_2MgSi_3$ inter-metallics within the grains, and $Al_{13}Cu_4MgSi$ and $Al_{12}CuMg_2Si_3$ phases precipitated along the grain boundaries [6].

It is well known that the mechanical properties of metals are highly dependent on their microstructures, or more appropriately, on grain size and on SDAS, respectively. Therefore, it is important to understand the relationship between SDAS and cooling rates This concept has been studied and explained in Figure 59 by measuring the SDAS for AA6111, under different cooling rates i.e. 0-10 K/s observed in DC casting, versus 10-100 K/s for HSBC process. As expected, the SDAS was observed to decrease from 74.7 μm to 10 μm, when the cooling rates were increased from 1K/s to 95 K/s. The decrease in SDAS results in increasing the mechanical properties of the cast alloy structure. The relationship between SDAS and cooling rate was mathematically represented by SDAS= $11.5(t_f)^{0.43}$, where t_f represents the solidification time of the melt [6].

Based on the information presented above, it is quite evident that the HSBC cast product microstructure is superior in comparison to conventional cast products. Additionally, in DC cast products, the alloying elements tend to segregate along the surface. This occurs because the molten metal of higher concentration is sucked back into the inter-dendritic channels during the solidification process, involving shrinkage. The phenomenon is termed “Inverse Segregation”. The segregation at the cast surface/subsurface lead to problems during subsequent processing such as rolling, extrusion, etc. and must be removed from the DC cast product, prior to rolling. This process is known as “scalping”. Scalping is considered an extra process that requires capital investment and time. However, HSBC strip does not require any surface scalping, since the alloying elements are homogenously spread throughout the strip thickness, owing to the high cooling rates of molten metal, and its mode of freezing, in the HSBC process [6].

Additionally, centerline segregation is also observed in DC cast products. This is attributed to the solute convection in which small particles of lower solute concentration detach from the initial solidified layer, and settle at the center of the cast product.

Almost similar results were obtained for M2 tool steel produced through slab/continuous casting process. The average grain sizes in continuous cast products are smaller than sand cast products i.e. 50.54 µm and 69.4 µm respectively. Furthermore, the grain size at the center of continuous cast products is 2.12 times that at the edges. An almost similar nonlinear relationship was obtained for steel casting, as observed for aluminum casting, as shown in Figure 59b. Moreover, the SDAS was 21.14 µm for continuously cast products versus 37.34 µm obtained for sand mold casting. The reduction in SDAS is due to the high cooling rate of molten metal in the continuous casting process as compared to sand mold casting. A similar analysis can be expected for HSBC products since the cooling rates of molten metal exceed continuous casting and sand-casting processes [206].

$\mathrm{L} = 92.3\left(\frac{\mathrm{dT}}{\mathrm{dt}}\right)^{-0.318}$, where L is the grain size, $\frac{\mathrm{dT}}{\mathrm{dt}}$ is the cooling rate.

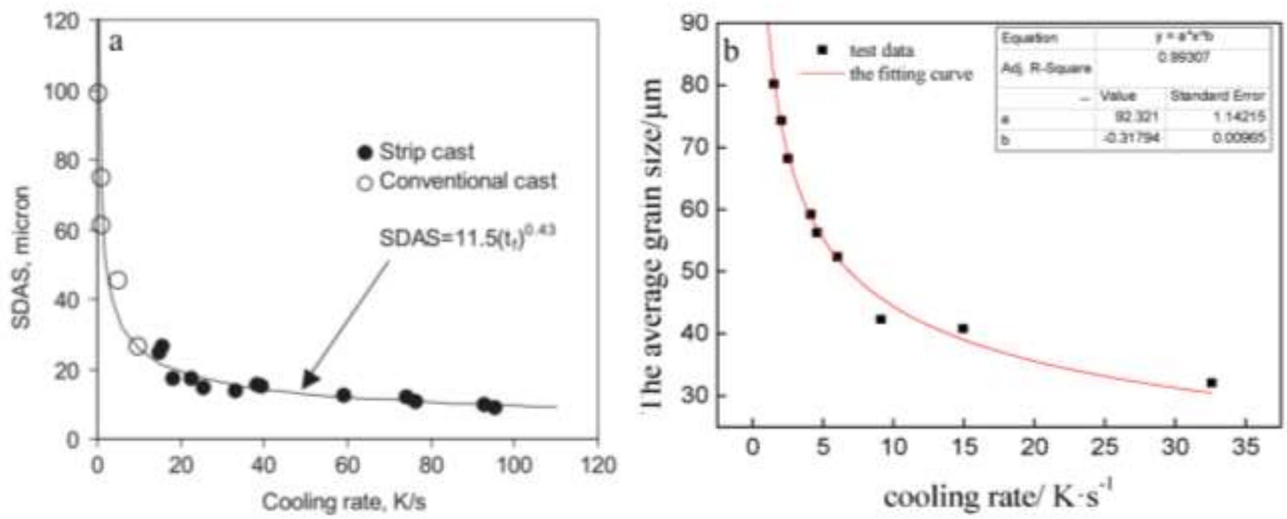

Figure 59: (a) Relationship between SDAS (microns) and cooling rate (K/s) in the HSBC process for aluminum [6], (b) The relation between grain size and cooling rate of an M2 high-speed steel during solidification [206].

In addition to the grain size and SDAS, the cooling rates in conventional casting processes are highly variable across the thickness of the product, since different sections of the casting solidify under different cooling conditions, and this is reflected in their cast structure, which is a combination of columnar and equiaxed grains. By contrast, for the HSBC process, the cooling rate is both fast, and uniform across the thickness of the product, resulting in a uniform microstructure with reduced grain sizes, and absent macro-segregation [15].

2.26. Final Remarks

Horizontal Single Belt Casting (HSBC) is regarded as a potential substitute for the Conventional Continuous Casting method (CCC), and also for the Thin Slab Casting (TSC) method, used in the production of metallic strips. Apart from its low energy requirements and promising productivity, the technology is capable of producing green and near-net-shape alloy strips, with cooling rates of up to, as much as, 500°C/sec. Therefore, HSBC can be exploited to cast ferrous and nonferrous metals, with reduced grain size and absent segregation, with uniform microstructure across cast product, and with better mechanical properties.

The following Chapter focuses on the production of Advanced High Strength Steels (AHSS) and AA6111 aluminum alloy via the HSBC process. AHSS grades are lighter than regular steels, and have unique combinations of mechanical strength and formability characteristics, making them a candidate material for automotive applications. On the other hand, AA6111 aluminum alloy has always remained at the forefront to produce automotive components, since they are lighter and stronger than other aluminium alloys. AA6111 generally strengthen by work hardening or precipitation strengthening (natural or artificial aging) phenomena, or a combination of both. Aging heat treatment consists of heating the sample to 520ºC - 550ºC, followed by water quenching. The quenching process produces the supersaturated solid-solution, which when exposed to elevated temperatures, below the GP zones solvus temperature, results in the precipitation of metastable, or transition phases such as, hexagonal $\beta^{//}$, $\beta^{/}(Mg_2Si)$. These precipitates are coherent with the matrix. In general, 6xxx alloys are processed through the following production route; solution treatment, pre-aging, deformation, and final aging.

On the other hand, the AHSS has complex phase structures and includes Dual Phase (DP), Transformation Induced Plasticity (TRIP), Complex Phase (CP), Twinning Induced Plasticity (TWIP), and Martensitic Steels. Each has unique microstructural features, alloying additions, processing requirements, and therefore, has unique applications. The practical usefulness of AHSS is significant. They are lighter, due to increased content of aluminum, and silicon. These additions are also relatively less expensive alloying elements, as compared to chromium, nickel and molybdenum. The weight reduction comes without sacrificing the mechanical properties and therefore, these steels have increased tensile strength, as well as total elongations. The

Transformation Induced Plasticity (TRIP), and Twinning Induced Plasticity (TWIP), phenomena are the main reasons explaining their improved properties.

The HSBC process features a compact design, and could provide a far better economic production process, as compared to a Thin Slab Casting (TSC). Commercial HSBC caster can produce strip up to a thickness of 15 mm and a width as large as 1000 mm, or more, thereby providing substantial energy saving options by directly hot rolling without intermediate reheating. As per the literature, the minimum as-cast thickness is approximately 50 mm to 70 mm in TSC production, and multiple hot rolling passes followed by cold rolling have to be carried out, in order to produce the desired thickness sheet. This, in comparison to the HSBC process, undoubtedly, requires far more expenditure, in terms of capital costs, running costs, as well as personnel costs, steel yield's, and environmental benefits.

Chapter 3

3.0. Experimental Procedures/Methods

3.1. Introduction

In this chapter, experimental procedures related to the production/casting of AHSS and AA6111 strips via the Horizontal Single Belt Casting (HSBC) process are discussed. The procedures related to setting up the fluid flow model using Ansys Fluent Software and the calculation of the Stacking Fault Energy (SFE) model via the Olson-Cohen modelling approach are presented in Chapter 4.

TRIP/TWIP steels demonstrate exceptional ductility and good strength and are therefore largely employed by automotive industries for the manufacturing of various body parts [2]. In this research study, two different AHSS grades were selected i.e. Fe-21%Mn-2.5%Al-2.8%Si-0.08 %C wt.%, and Fe-17%Mn-4%Al-3%Si-0.45%C wt.%. The microstructures of these steels at room temperature are predominantly austenitic, which later transforms into epsilon martensite, and deformation twins upon plastic deformation [99-101].

Apart from the TRIP and TWIP steels discussed above, AA6111 (aluminum alloy) was also selected for HSBC casting experiments. AA6111 is lighter and possesses unique combinations of mechanical strength and formability characteristics, making it a candidate alloy material for automotive applications [26-28, 31].

3.2. Detailed Experimental Procedure regarding the Production, Casting, and Characterization of AA6111 Aluminum Alloy

AA6111 alloy was produced by first melting pure aluminum in a pre-heated induction furnace (Inductotherm, 150 KVA) under a protective argon atmosphere, followed by the addition of Al-Mg, and Al-Mn master alloys (the chemical composition is mentioned in Table 7). Good melt stirring was ensured to completely dissolve/mix the alloy additives into the pure aluminum. During the entire melting/alloying processes, argon gas was continuously injected into the melt through a graphite pipe. The melt was then de-gassed for 20 minutes, and Al-5% Ti-1%B grain refiner was added, in the conventional way, just before the start of the casting. These grain refiners form TiB_2, $(TiAl)B_2$, and TiC, particles within the melt, which provide nucleation sites for new grains, resulting in a solidification microstructure with more grains and smaller sizes (refined microstructure).

The temperature of the molten metal was accurately measured using appropriate-type thermocouples (Type k), to determine melt superheat. The molten AA6111 was cast into thin strips with width between 100 to 250 mm, ~ 6 mm thickness, using the HSBC pilot caster. Details are presented in subsequent paragraphs. The strip's microstructure was determined using an Optical/SEM microscope. The surface roughness of the cast strip was determined using the Nanovea 3D profilometer. Details are presented in the following paragraphs. The chemical composition of the alloys strips was determined via Spark OES and Energy Dispersive Spectroscopy (EDS) methods. Details are presented in subsequent paragraphs.

Table 7: Additives used in the production of AA6111.

Materials Used	**Chemical Composition (Supplied by the manufacturers)**
Pure aluminum	99.9 % Pure
Al-Mg Alloy	75% Al-25% Mg
Al-Mn Alloy	75 %Al-25% Mn

3.3. Detailed Experimental Procedure regarding the Production, Casting and Characterization of AHSS Alloy

AHSS alloys were produced by first melting plain steel in a pre-heated induction furnace (Inductotherm, 150 KVA) under a protective argon atmosphere, followed by the addition of iron-manganese, iron-silicon, and manganese-aluminum master alloys (the chemical composition is mentioned in Table 8). Good stirring was used to ensure complete dissolution/mixing in of the alloy additives in the plain carbon steel melt. Thin strips were produced afterwards, employing HSBC simulator caster. Its operation is mentioned in the following paragraphs.

Hot deformation was applied to the cast strip. The general purpose of the hot deformation was to increase the mechanical strength of the alloy via the transformation of a coarse dendritic structure into fine equiaxed grains [202]. Also, the micro/macro segregation, as well as the other casting related defects are appreciably reduced/welded, after the hot deformation [203] (for further details, refer to Chapters 5 & 6). The hot deformed strips were also heat treated. The microstructures of the cast and heat-treated steel strips were analyzed using Optical/SEM microscopes. The mechanical properties were determined via the Shear Punch Test method. Surface roughness of the cast strip was determined using the Nanovea 3D profilometer. The chemical composition of the alloys strips was determined using Spark OES and Energy Dispersive Spectroscopy (EDS) methods. Details are presented in subsequent paragraphs.

The hot deformation/heat treatment procedures of AHSS's, for both grades: Fe-21%Mn-2.5%Al-2.8%Si-0.08 %C (in wt.%), and Fe-17%Mn-4%Al-3%Si-0.45%C wt.%, were formulated in such a way as to get an average grain size of 40 micrometer, so as to achieve high strength and elongation [99-101]. The SFE of the strip produced was calculated using the Olson-Cohen thermodynamic model. The ($\Delta G_{ex}^{\gamma\rightarrow\varepsilon}$) term, which is the contribution of grain size towards $\Delta G^{\gamma\rightarrow\varepsilon}$ [83], was estimated assuming a 40 micrometers grain size (for further details refer to Chapter 4). The samples, after heat treatment, were cold deformed. This was done in order to observe the generation of epsilon martensite and deformation twins against cold plastic deformation, so as to validate Olson-Cohen thermodynamic modeling predictions [83]. Details are presented in Chapters 5 and 6.

Table 8: Additives used in the production of AHSS

Materials Used	**Chemical Composition (Supplied by the manufacturers)**
Plain Carbon Steel	0.4Mn-0.20C-0.001Si-0.001P-Balance Fe
Fe-Mn Alloy	78.40Mn-1.47C-0.60Si-0.17P-Balance Fe
Fe-Si Alloy	76.50Si-0.10C-1.50Al-0.25Ti-0.04P-Balance Fe
Mn-Al Alloy	75Al-25Mn

All experiments were carried out at the Met Sim Inc, Stinson Laboratories. There the HSBC pilot-scale systems, as well as HSBC simulator system, were installed and are operational since 2012. The specifics of the two HSBC systems, and their operation, are explained below:

3.4. Pilot-Scale Horizontal Single Belt Casting (HSBC) System operational at the Met Sim Inc., Stinson Laboratory

The Horizontal Single Belt pilot-scale Caster at the off-campus laboratory (MetSim Inc), features a low head metal delivery system, a 2.6-meter-long, endlessly moving belt, and an in-line hot deformation pinch-roll mini-mill set-up. The lateral movement of the belt can be set as low as 0.1 m/s to as high as 1.5 m/s. The belt is continuously cooled from the bottom via a system of spray nozzles, delivering water jets horizontally to the moving belt. During casting, the belt is always kept under tension, in order to eliminate the chances of belt distortion and warpage due to the high temperature of the hot metal alloys cast on it. Additionally, the belt is supported by magnetic back-up rolls, in the upstream region, where the melt first contacts the belt. All these measures ensure belt flatness during strip casting [6, 11, 12].

The liquid metal delivery system of HSBC pilot caster consists of a refractory piston, and a tundish, inter connected with a channel/trough, as shown in Figure 36. The schematic of the tundish is presented in Figure 36 [6, 11, 12]. The tunidsh and trough is lined with METAL KAST 90, capable of withstanding temperatures up to 1800°C. The tundish is supplied with a refractory nozzle slot at its bottom. In recent times, the HSBC pilot caster has received several modifications such as the design of a new alumina refractory nozzle slot, increasing the cooling capability under the moving steel belt, and enlarging the strip guidance system, in order to accommodate casting wider strips. These modifications were performed in order to produce up-to 250mm wide strips. The new HSBC pilot scale system also includes a 42 feet extension of the length of the run-out table, as shown in Figure 36.

3.5. Pilot-scale Caster Operation

Before performing melting and casting operations, the entire delivery system of the HSBC pilot-scale system, is routinely preheated to approximately 500-550°C, using resistance heaters. This needs to be done to avoid any premature freezing of the molten metal inside the trough and tundish. Since the tundish has a refractory nozzle slot that opens right above the moving belt, the radiating heat from preheaters could exit the nozzle slot opening, causing the heat up the magnetic backup rolls located underneath the belt. At higher temperatures, the magnetic back-up rolls lose their magnetic properties, so they have to be kept close to room temperature. In order to counteract this problem, the water pump of the pilot caster is turned on at regular intervals, assuring the belt continued cooling, and ensuring that magnetic roller temperature always remained at ambient temperature, respectively [11, 12]. Prior to casting, the belt is sprayed with graphite powder, and then dried using a resistive heater. Compressed air can also be blown over the belt to remove moisture, if present.

Once the metal is ready to cast and the entire delivery system had been preheated, the induction furnace is brought to the caster station, and firmly attached to the metal delivery system. The refractory piston then slowly entered the induction furnace at a pre-selected speed, thereby displacing molten metal into the trough. Once the appropriate metal head within the tundish was reached, the stopper rod, initially blocking the nozzle slot opening, is rapidly withdrawn. Thermocouples are installed at various locations in the delivery system i.e. adjacent to refractory cylinder and nozzle slot outlet. These thermocouples were used to measure melt superheat prior to casting.

A weir and dam were used to prevent slag from entering the nozzle slot, as well as to minimize turbulence in the molten metal. Rotating side dams were also used in some casting experiments. Their purpose was to contain the molten metal pool after it leaves the nozzle slot, and to give it a nice straight/smooth edge as it solidifies on the moving belt. After that, the solidified strip is guided to the rolling stand. This rolling stand can either acts as a pinch roll to withdraw the strip from the caster, or the punch roll/mini-mill, where the thickness of strip can be reduced by up to 20 % (for steel rolling)[11]. After the casting process is finished, the cast strip is allowed to cool on the belt caters run-out table.

3.6. Design and Operation Specifics of the HSBC Simulator, Located at Met Sim Inc, Stinson Laboratory

A schematic of the HSBC simulator is given in Figure 60. It comprises a stationary, refractory-lined vessel (tundish), to contain the molten metal. The tundish is provided with a slot at its bottom, which remains closed, and is only opened once casting commences. The simulator is equipped with a compression spring system, which when activated, propels the chilling copper substrate, located beneath the tundish, in the positive x direction. Metal pours through the slot nozzle, and onto the moving cooling substrate. This substrate uses high purity copper (99.99 %), is 800 mm long,110 mm wide, and 12.7 mm thick [8].

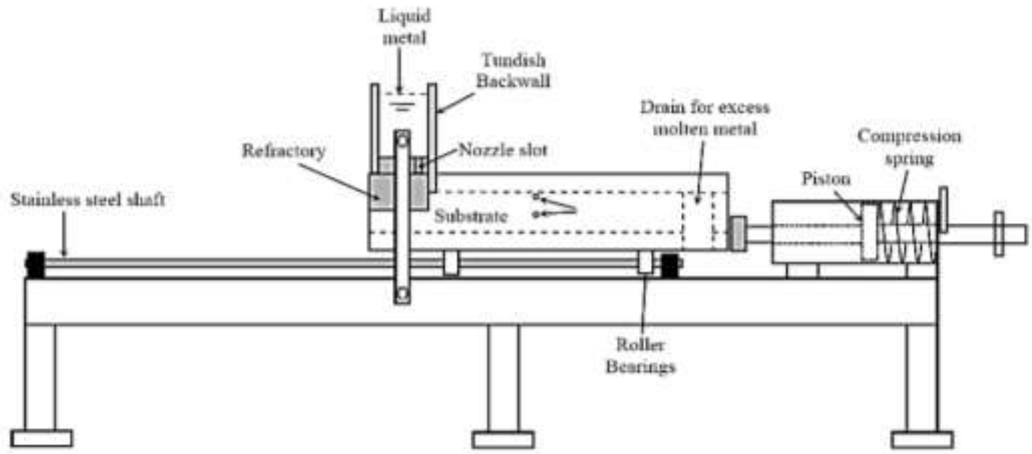

Figure 60: Schematic of the HSBC simulator system operated at MetSim Inc Laboratory [8].

3.7. Operation Details of Horizontal Single Belt Caster Simulator

The entire simulation process starts with the production of the ferrous, or non-ferrous, alloy to be studied, using a 30 kW, Ajax Tocco induction furnace. Following melting the molten alloy is poured into the tundish, where it stays for few seconds to dissipate the kinetic energy of turbulence. The compressed spring is then released, so as to push the chilled substrate, at a pre-selected speed (0.4, or 0.8 m/s). The melt flows through the nozzle slot, and solidifies over the moving substrate, under an argon (or other) gaseous environment. When a substrate velocity is pre-selected at 0.8 m/s, the experiment was completed within a second! However, before the start of an experiment, the tundish and the inclined refractory plane were heated to approximately 500-800°C using an air/methane gas mixture, so as to preheat the refractory and to avoid any premature freezing of the molten metal inside the tundish, or over the inclined refractory plane. To measure the heat flux through the molten metal during the solidification, two K-type thermocouples were used. These thermocouples are embedded inside the copper substrate, one very close to the surface, the other vertically underneath, to record the local temperature-time data during the entire casting process.

3.8. Heat Treatment of Advanced High Strength Steels (AHSS)

Heat treatment procedures were devised for two AHSS grades, as mentioned above. For both grades, prior to heat treatment, the cast steel strips were hot forged (~60%) using a 100-ton hydraulic press, installed at the MetSim Inc. laboratories, as shown in Figure 61. The as-cast strip thickness was 4-5mm, and this was reduced to ~1-1.5mm after a hot reduction/treatment, compensating for oxidation losses for these steels. The hot deformation/forging was carried out at 1,150°C i.e., above the ferrite nucleation temperature, in the austenite region. The hot deformation was applied in order to transform the dendritic structure into fine equiaxed grains, and to allow the diffusion of the alloying elements homogenously throughout the material. These were micro-segregated in the cast structure within the inter-dendritic regions [202]. Another purpose of hot reduction was to squash/weld any pores, if present, in the cast strip, so as to improve its mechanical properties [203].

After hot deformation, the samples were again heated to 1,150 °C for ~ 10 minutes. This is an added procedure and was done because during hot forging, the temperature of the sample had dropped to ~750°C, which was the temperature for ferrite nucleation, determined through Fact Sage software. If ferrite had nucleated, it would have affected the SFE value of the austenite [83]. After holding the samples for 10 minutes at 1,150° C, the sample was quenched in water in order to obtain a fully austenitic microstructure. This was verified via Optical/SEM microscopy analysis.

(Note: The nucleation of ferrite is not desirable as it can alter the SFE of the austenite, by changing the concentration of alloying elements present in it. This will change the deformation behaviour of the austenite, which greatly affects the alloy's strength and ductility [83]).

Figure 61: 100 tonne hydraulic press, installed in the MetSim Inc. Stinson Laboratory.

3.8.1. Heat Treatment Procedure for TWIP Steel (17%Mn-4%Al-3%Si-0.45%C wt.%)

The step by step procedure for the heat treatment of 17%Mn-4%Al-3%Si-0.45%C (wt.%) was as follows.

1. The samples, ~ 20 mm x 20 mm were sectioned from the strip, and introduced into a resistive heating furnace.
2. The temperature of the samples was raised to 1,150°C where they were held for different durations. This temperature was determined via Fact Sage assessments, as described above.
3. The samples were hot forged to approximately 60% in a single step using the100 ton hydraulic press. In this way, the dendritic structure of the samples was completely broken down and transformed into equiaxed austenite grains, as shown in Figure 64. Afterwards, the samples were water quenched. The hot deformation step was omitted for some samples, as explained below.

4. By passing the hot plastic deformation step, and directly quenching the sample after holding it at 1,150°C for up to three hours, this was insufficient a time to fully transform the dendritic structure into equiaxed grains. In this case, the dendritic structure was not fully broken-up and homogenized, as it was, when hot working was done prior to the heat treatment. (Figure 62).

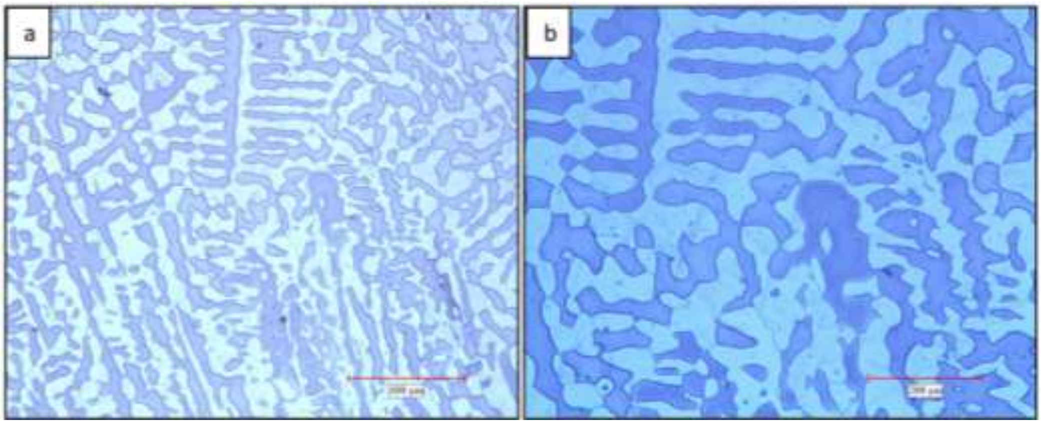

Figure 62: (a) (50 X) & (b) (100 X): Fe-17%Mn-4%Al-3%Si-0.45%C (wt.%), Soaked for 2 hours at 1,150° C followed by water quenching. The sample was not hot deformed prior to heat treatment.

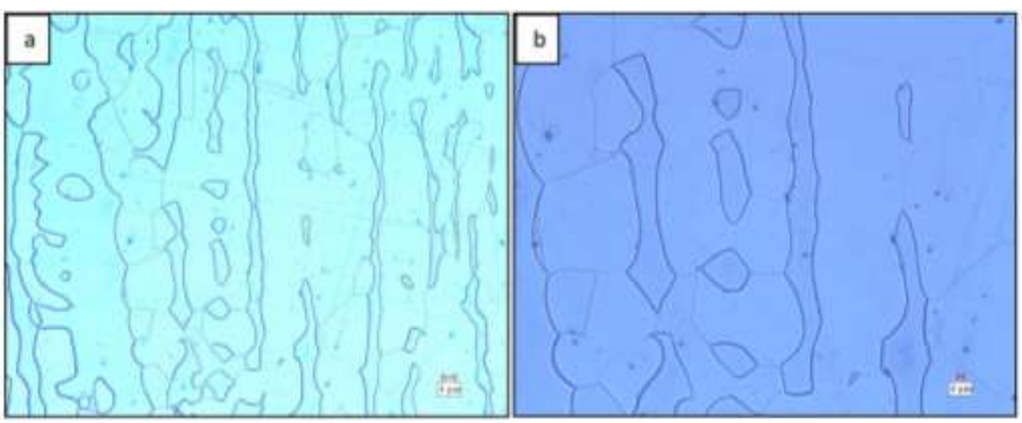

Figure 63: (a) (100 X) & (b) (200 X): Fe-17%Mn-4%Al-3%Si-0.45%C (wt.%), Soaked for 2 hours 45 min at 1150° C followed by water quenching. The sample was not hot deformed prior to heat treatment.

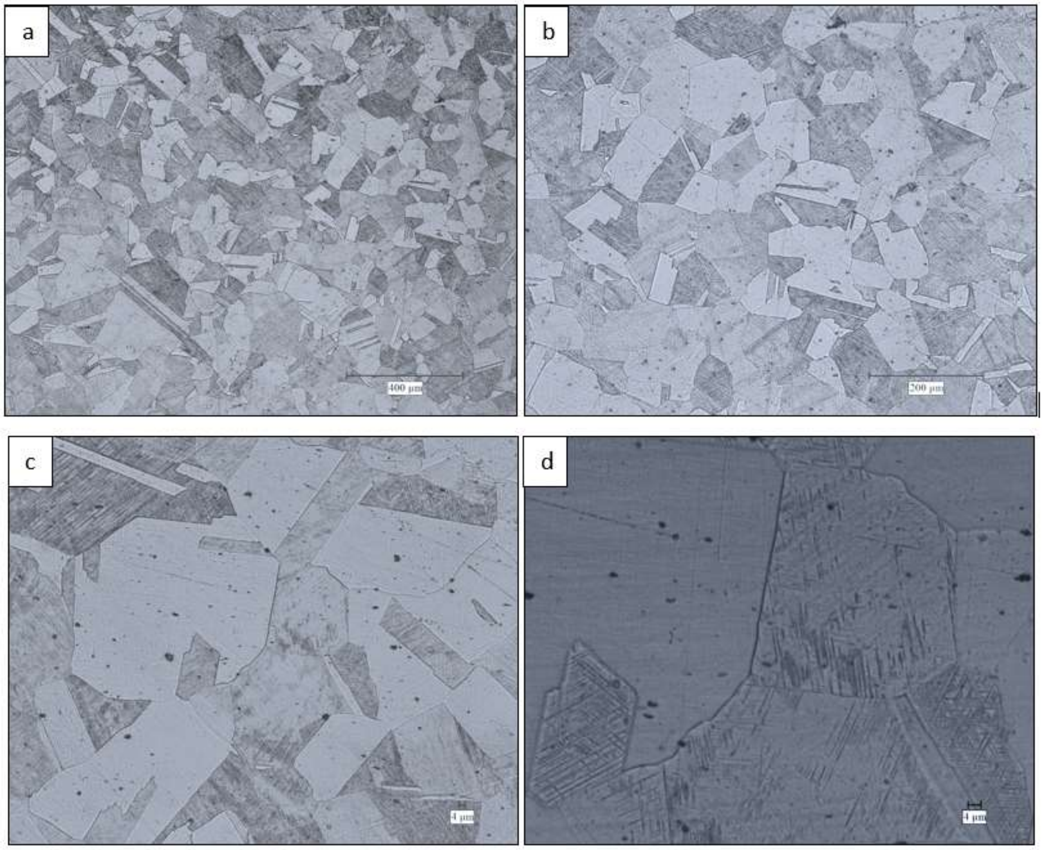

Figures 64: (a) (50 X), (b) (100 X), (c) (200 X), (d) (500X): Fe-17%Mn-4%Al-3%Si-0.45%C (wt.%), soaked for 2 hours 45 min at 1,150° C, followed by plastic deformation (60 %). After plastic deformation, the samples were water quenched.

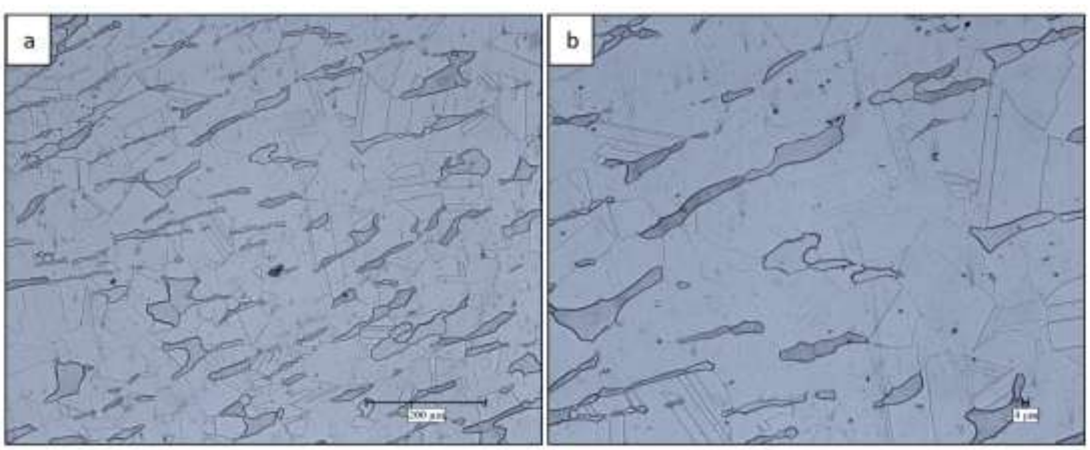

Figure 65: (a) (100 X), (b) (200 X): Fe-17%Mn-4%Al-3%Si-0.45%C (wt.%), Soaked for 1 hours 30 min at 1150° C followed by plastic deformation (60 %). After plastic deformation, the samples were water quenched.

3.8.2. Heat Treatment Procedure for TRIP/TWIP Steel (Fe-21%Mn-2.5%Al-2.8%Si-0.08 %C wt.%)

The step by step procedure for the heat treatment of Fe-21%Mn-2.5%Al-2.8%Si-0.08 %C (wt.%) grade was as follows:

1. The samples, ~20 mm x 20 mm, were sectioned from the strip, and introduced into a resistive heating furnace.
2. The temperature of the samples was raised to 1,150°C where they were held for different durations of time. This temperature was determined via Fact Sage, described above.
5. The samples were hot forged to approximately 60% in a single reduction step using the 100 tonne hydraulic press. In this way, the dendritic structure was completely broken down and transformed into equiaxed austenite grains, as shown in Figure 66. Afterwards, the samples were water quenched.
3. It has been determined that holding the sample for a longer time at 1,150°C, prior to hot deformation, results in grain coarsening, as shown in Figure 67.

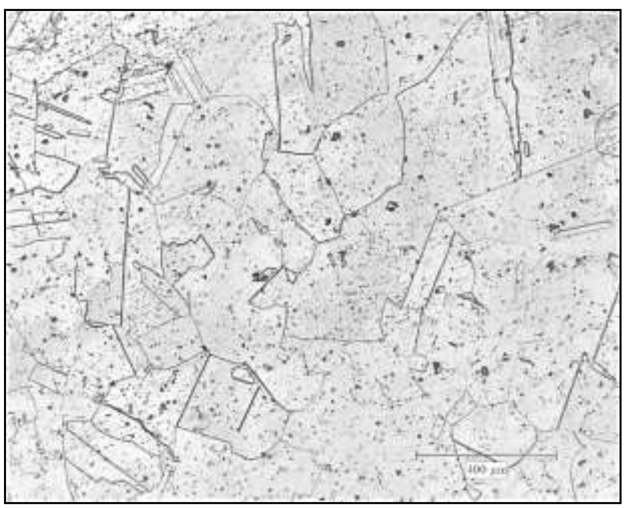

Figures 66: (50 X): Fe-21%Mn-2.5%Al-2.8%Si-0.08 %C (wt.%), Soaked for 50 min at 1150° C followed by plastic deformation (60 %). After plastic deformation, the sample was water quenched.

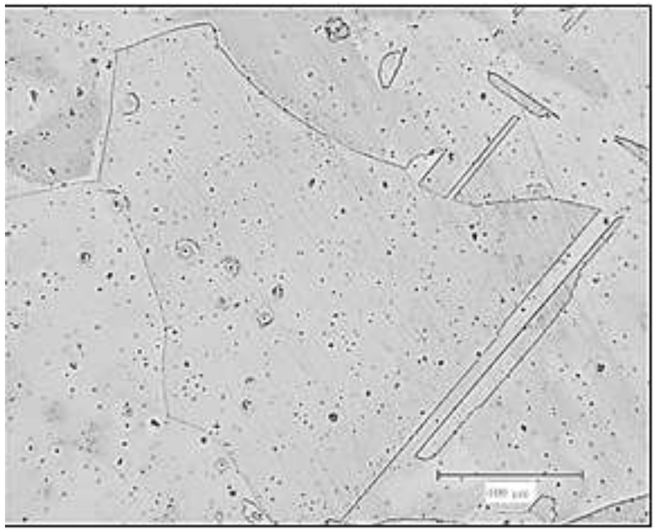

Figures 67: (50 X): Fe-21%Mn-2.5%Al-2.8%Si-0.08 %C (wt.%), Soaked for 1.5 hours at 1150° C followed by plastic deformation (60 %). After plastic deformation, the sample was water quenched.

3.9. Characterization of the Cast/Heat-Treated Strips

After the casting, the strip was macro-analysed for the detection of any surface defects such as roughness, cracks, foreign particle entrapments, surface blowholes, scratches, etc. Micro analyses was used to detect the possible bulk defects such as of porosities, internal cracks, non-metallic inclusions, shrinkage cavities, etc. Microstructures of the cast and heat-treated strip were determined using optical and Scanning Electron Microscopy (SEM). For chemical composition analysis, Spark Optical Emission Spectroscopy (Spark-OES), and Energy Dispersive Spectroscopy (EDS) analyses, were performed. The mechanical properties of the cast/heat treated AHSS strip were determined using the Shear Punch Testing (SPT) equipment, whilst the surface roughness was measured using the Nanovea 3D Profilometer. Shear punch testing was employed due to sample size limitations. Details related to the shear punch test and the 3D surface roughness measurement using Nanovea 3D profilometer are presented below.

3.10. Shear Punch Test (SPT)

The Shear Punch Test (SPT) is a technique widely used for evaluating the mechanical properties of ferrous/non-ferrous alloys. The test works on the principle of blanking operations, common to sheet metal forming processes, and calculate the applied load versus displacement curves. This information can then be further correlated to normal stress/strain data, using the well documented linear correlation theory. In this way, mechanical properties such as the yield and ultimate strength can be easily calculated using SPT data. Additionally, SPT has the inherent ability to determine the mechanical properties of localized zones or for cases where material availability is an issue [204].

Figure 68 shows the set-up used for the shear punch test in the present research work. The assembly consisted of a punch with a flat cylindrical head, 1mm in diameter, mounted on a hydraulic press (MTS model Alliance RF/200) with a 10 kN load cell. The samples, 20mm long and 600 μm thick, were securely placed inside the fixture, and deformed, using a punch speed of 0.1mm/min.

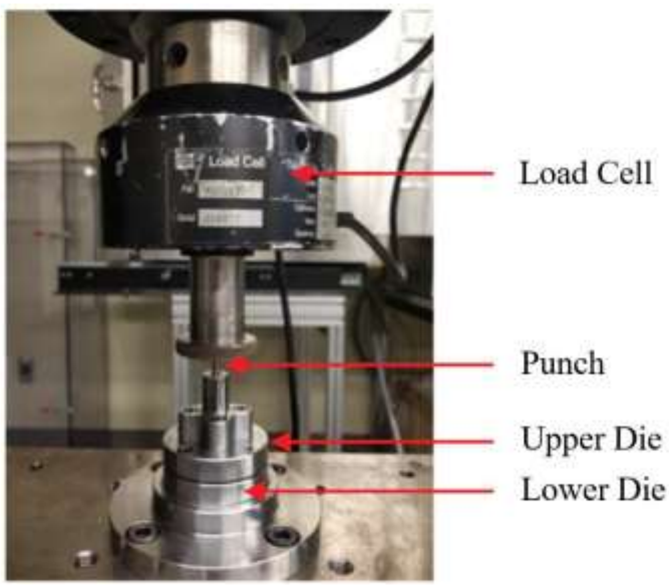

Figure 68: Shear punch test setup.

The shear stress, τ, was calculated using equation 1

$$\tau = \frac{P}{2\pi r_{avg} t} \tag{1}$$

where P is the applied load, $r_{avg} = \frac{r_{punch}+r_{die}}{2}$, is average radius of the die and the punch, and t is the specimen thickness. The normalized displacement, ε_{eff}, was calculated by dividing the displacement by the specimen thickness.

$$\varepsilon_{eff} = \frac{d_t}{t} \tag{2}$$

The yield shear stress τ_{ys} and ultimate shear stress τ_{us} were obtained from the shear stress versus the normalized displacement curve. The yield tensile stress σ_{ys} and ultimate tensile stress σ_{us} were respectively calculated using the following two relations.

$$\sigma_{ys} = 1.77\tau_{ys}, \quad \text{and} \quad \sigma_{us} = 1.8\,\tau_{us} \tag{3}$$

It was not possible to determine the tensile strength of Fe-21%Mn-2.5%Al-2.8%Si-0.08 %C wt.%, and Fe-17%Mn-4%Al-3%Si-0.45%C wt.% via the standard tensile testing method due to the unavailability of the material as discussed above. Furthermore, the thickness of the forged and heat treated sample was variable. To obtain a uniform thickness, the samples were manually ground and polished. However, in doing so, the final thickness of the samples was decreased to ~ 600 micrometers.

Since SPT allows the testing of sample with width as short as few millimeters and thickness of the order of few hundred of micrometers, the SPT test was performed for determining the tensile strength of the AHSS samples.

3.11. Surface Roughness Measurements

The surface waviness of the top/bottom sides of the strip was determined using a Nanovea 3D Profilometer. This technique works on the principle of measuring the physical wavelength of light and directly relating it to a specific height. This ensures accurate measurement of surface roughness/finish [205]. The scan length for all the measurements was 5mm whereas the scan speed was 0.1mm/s. Ten random locations were selected for surface roughness measurements. These locations were largely selected from all over the strip. The surface profiles are almost identical to each other. The results are presented in Chapters 5, 6, and 7.

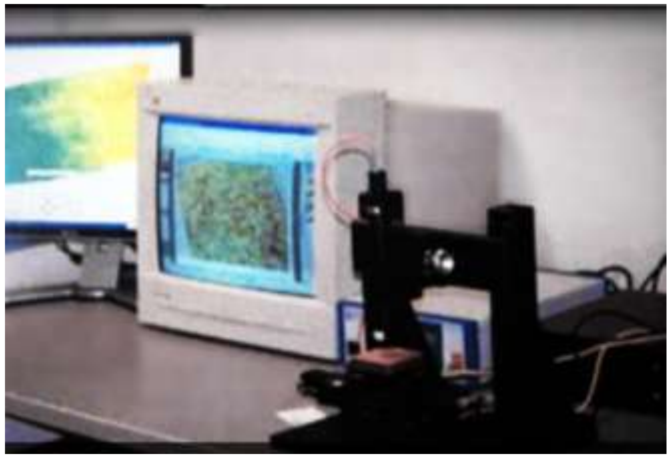

Figure 69: 3D Profilometer by Nanovea for measuring surface roughness.

3.12. Conclusions

In this chapter, the experimental procedure related to the production of two AHSS grades and AA6111 aluminum alloy strips via Horizontal Single Belt Casting (HSBC) process has been presented. Two different AHSS grades were selected for this research study. The first one is in the category of a TRIP-TWIP steel, of the following composition Fe-21%Mn-2.5%Al-2.8%Si-0.08 %C wt.%. The second one was a Fe-17%Mn-4%Al-3%Si-0.45%C wt.% AHSS grade, which lies in the category of a TWIP steel. Horizontal single belt pilot-scale system, as well as the HSBC simulator system were used to produce the thin strips. After casting, the strips were hot deformed (~ 60 %) at 1,150°C (above the ferrite nucleation temperature). The general purpose of the hot deformation was to increase the mechanical strength of the alloy via the transformation of a coarse dendritic cast structure into fine, equiaxed, grains. Also, micro/macro segregation, as well as other casting related defects, were appreciably reduced after hot deformation. The hot deformation was carried out within the stable austenite region (750°C-1,300°C). At this temperature range, all the other secondary phases should dissolve in austenite. After applying hot deformation, the samples were quenched in water, so as to obtain the austenite phase, rich in aluminum, silicon, manganese and carbon. The cast/heat treated steels were characterized for microstructure, chemical composition, surface roughness, and mechanical properties.

Chapter 4

4.0. Details of the Mathematical Modeling

4.1. Introduction

All ferrous and non-ferrous melting and casting processes involve complex transport phenomena (fluid flow, heat and mass transfer). These includes the entrainment of slag and gas in liquid metal, the addition of alloying elements and their mixing into the bath's molten metal, molten metal temperature losses due to conduction, convection and/or radiation, the movement and flotation of inclusions, etc. Numerical modeling, therefore, allows metallurgists not only to deepen the understanding of these complex metallurgical phenomena, but also help in optimizing their operational configurations [207-209]. Additionally, CFD modeling also contributes to the development of new processes, or incorporating design improvements into existing systems. This is particularly true for the HSBC process, in which the molten metal flow is dependent on many factors, such as, the belt speed and its temperature, the slant angle of the refractory plane, the metal head within the tundish, etc [198]. Determining the influence of each operating parameter on the quality of the strip is not only experimentally difficult, but is also time-consuming.

On the basis of the above discussion, it can be emphasized that CFD has become a very versatile tool for modeling ferrous/nonferrous metal production processes. Starting from the metallurgical furnace, right up to casting and freezing the metal, and beyond; CFD has a role to play! All these advances in CFD are possible, due to the immense improvements in computer power and the remarkable development in numerical techniques, all now incorporated in commercial CFD packages, readily available to engineers working in either research institutions or in industry [210].

4.2. Essentials of a CFD Study

It is essential to understand the basics of a CFD study before it can be executed effectively. Therefore, in this section, details related to CFD modeling are presented. It starts with selecting an appropriate commercial software such as ANSYS Fluent, COMSOL, FLOW 3D, CFX, ABAQUS, PHOENICS, etc., or by writing your own CFD code [211-214]. Regardless of the numerical methods used in different software, the following steps are identical for all of them [211-214];

1. The first step is to select an appropriate calculation domain i.e., the region where the governing partial differential equations are to be solved. In this research study, the simulation domain was chosen to simulate the interaction of the molten metal with the inclined refractory plane and the moving belt, and to study the solidification behavior of the metal in the HSBC process. Details are presented in subsequent chapters:

2. The second step is known as “meshing” and involves the discretization of the simulation domain into small areas (for 2-dimensional flows), and volumes (for 3-dimensional flows). The types and dimensions of these meshes are critically important to obtain reasonable results. However, increasing the mesh density beyond a certain point only increases computational times, without increasing the solution’s accuracy. In this research study, the simulation domain was discretized using quadrilateral and hexahedral meshes, so as to achieve the results desired. For more details, please refer to Chapters 5, 6 and 7.

3. Afterward, the appropriate boundary conditions are defined for solving the partial differential equations (PDE), followed by their conversion into equivalent algebraic terms using a suitable numerical technique. These algebraic equations are solved iteratively to generate data which can be further visualized by suitable post-processing software, such as FLUENT-ANSYS post-processing.

4.3. Conservative Forms of the Governing Equations

The conservative form of all equations incorporating the flow of fluids can usefully be written in the following generalized form:

$$\left(\frac{\partial \rho \Phi}{\partial t}\right) + \mathrm{div}(\rho \Phi u) = \mathrm{div}(\Gamma_{\Phi} \mathrm{grad}\Phi) + S_{\Phi} \quad (1)$$

or, in word format,

Rate of increase of Φ of fluid element + Net rate of flow of Φ out of fluid elements (convection) = Rate of increase of Φ due to diffusion + Rate of increase of Φ due to source terms

In CFD, this set of conservation laws, can involve the mass continuity equation, the conservation of momentum (i.e. the Navier-Stokes, or turbulent N-S equations), the species continuity equation, and the energy equations, plus an extra equation linking the pressure to the Continuity and Navier-Stokes equations, so as to satisfy the two, simultaneously. Finally, we have partial differential equations for describing the generation of turbulence kinetic energy, and its destruction through viscous flow phenomena. As there are significant similarities between the various equations, a general variable "Φ" is used to represent different quantities [213] as mentioned below in Table 9, for substitution of "Φ" in equation 1.

Table 9: Values of $\Phi, \Gamma_{\Phi}, S_{\Phi}$ for continuity, momentum, energy and species transport equations [213].

Quantity	Φ	Γ_{Φ}	S_{Φ}	Governing Equation
Continuity	1	0	0	$\left(\frac{\partial \rho}{\partial t}\right) + \mathrm{div}(\rho u) = 0$
x-momentum	u	μ	$-\frac{\partial P}{\partial x} + S_{Mx}$	$\left(\frac{\partial \rho u}{\partial t}\right) + \mathrm{div}(\rho \bar{u} u) = -\frac{\partial p}{\partial x} + \mathrm{div}(\mu \mathrm{grad}(u)) + S_{Mx}$
y-momentum	v	μ	$-\frac{\partial P}{\partial y} + S_{My}$	$\left(\frac{\partial \rho v}{\partial t}\right) + \mathrm{div}(\rho \bar{u} v) = -\frac{\partial p}{\partial y} + \mathrm{div}(\mu \mathrm{grad}(v)) + S_{My}$
z-momentum	w	μ	$-\frac{\partial P}{\partial z} + S_{Mz}$	$\left(\frac{\partial \rho w}{\partial t}\right) + \mathrm{div}(\rho \bar{u} w) = -\frac{\partial p}{\partial y} + \mathrm{div}(\mu \mathrm{grad}(v)) + S_{Mz}$
Energy	T	k/C_p	S_T/C_p	$\left(\frac{\partial \rho T}{\partial t}\right) + \mathrm{div}(\rho \bar{u} T) = \mathrm{div}\left({}^{k}/_{C_p}\, \mathrm{grad}(T)\right) + {}^{S_T}/_{C_p}$
Species	m_i	ρD_i	S_s	$\left(\frac{\partial \rho m_i}{\partial t}\right) + \mathrm{div}(\rho \bar{u} m_i) = \mathrm{div}(\rho D_i \mathrm{grad}(m_i)) + S_s$

4.4. Numerical Models and Methods

The term Numerical Model is defined as a mathematical representation of physical behavior based on simplifying assumptions. For example, k-ε, and k-ω, are the two most commonly used numerical models to simulate the turbulent fluid flow in the HSBC process. Numerical methods, on the other hand, are applied to express a model in a discrete form, so as to generate and solve a system of algebraic equations that approximates this model. Finite difference, finite elements and finite volume, approaches, etc., are some of the most commonly used numerical methods available to the CFD modeler. All the numerical methods theoretically converge to a single result, or prediction, provided the discretization is progressively refined; this means that the numerical method should have no impact on the physical meaning of the solution. However, a numerical method defines the accuracy to which the numerical model can be approximated. The choice of the method also has an impact on the computation times needed in obtaining a solution [213].

It is beyond the scope of this document to provide full details of the numerical models and methods. These can be found in appropriate literature [211 - 215]. However, the approach used in modeling "turbulence" will be discussed in this section. The details related to multiphase modeling will be presented in Chapters 5.

4.4.1. Numerical Models

4.4.1.1. Details of the Turbulence Modeling

Turbulence is a chaotic phenomenon, present in a wide range of natural and industrial flows. Turbulent flows are inherently random/unsteady and possess rotational flow structures, known as eddies or vortices. It is known that the higher the Reynolds number, the wider will be its eddy spectrum. In order to capture these eddies from the largest to the smallest, the numerical solution of the full Navier-Stokes equations is required. This is the approach used in DNS (Direct Numerical Simulation) modeling. DNS is a computationally expensive model and a very fine mesh is required to capture the full details of turbulent structures; as such, its application is restricted to simple geometries and low to moderate Reynolds number flows [215, 216].

In general, engineers are interested in computing average values rather than capturing the full details of turbulence structures and this is the modeling approach used in the Statistical Turbulence Modeling (STM) approach. These models decompose the flow variables such as velocity, pressure, temperature into mean and fluctuating parts. Because STM is not computing all the eddy sizes, the mesh required is significantly coarser than the one needed in DNS modeling [216-217].

There is an alternative route of turbulence modeling, which lies in between DNS and STM. This model is known as Large Eddy Simulation (LES) [217]. The LES involves the direct simulation of large-scale turbulence motions (large eddies), whereas the effect of small eddies is modeled using a method similar to the STM approach. LES model is computationally expensive at high Reynolds number and requires substantially refined meshes, as compared to the STM approach [218].

As mentioned earlier, there is no need to determine instantaneous values, if average values are all that is required. It is outside the scope of the present text to discuss the details of STM modeling. It can be read from the available literature [217]. Only the k-ε, and some of its variants, as well as the k-ω turbulence modeling approaches, are discussed in the following paragraphs since these models are used to simulate the flow of the molten metal in the HSBC process [6, 8, 198].

4.4.1.2. k-ε Turbulence Modeling

The k-ε model was first proposed by Launder and Spalding in 1974 [218]. It is composed of the transport equations for k (turbulent kinetic energy), and ε (the rate of dissipation of turbulent kinetic energy). The turbulence model mentioned below represents the standard version, generally known as the high Reynolds k-ε turbulent model [216].

$$\frac{\partial}{\partial t}(\rho k) + \frac{\partial}{\partial x_i}(\rho k u_i) = \frac{\partial}{\partial x_i}\left[\left(\mu + \frac{\mu_t}{\sigma_k}\right)\frac{\partial k}{\partial x_i}\right] + G_k - \rho\varepsilon \tag{2}$$

$$\frac{\partial}{\partial t}(\rho \varepsilon) + \frac{\partial}{\partial x_i}(\rho \varepsilon u_i) = \frac{\partial}{\partial x_i}\left[\left(\mu + \frac{\mu_t}{\sigma_\varepsilon}\right)\frac{\partial \varepsilon}{\partial x_i}\right] + G_{1\varepsilon}\frac{\varepsilon}{k}(G_k) - \rho C_{2\varepsilon}\left(\frac{\varepsilon^2}{k}\right) \tag{3}$$

The velocity scale is determined by the square root of the turbulent kinetic energy i.e., $V_t = \sqrt{k}$, whereas the turbulent length scale is expressed as $l = \frac{k^{\frac{3}{2}}}{\varepsilon}$.

Additionally, the turbulent viscosity can be calculated by the following equation $\mu_t = \rho C_\mu \frac{k^2}{\varepsilon}$. Here C_μ is a dimensionless constant. Other constants for the standard k-ε turbulent model are given in Table 2.

Table 10: Constants used in the k-ε turbulent model [218]

Constant	C_{μ}	σ_{κ}	σ_{ε}	$C_{1\varepsilon}$	$C_{2\varepsilon}$
Value	0.09	1.00	1.30	1.44	1.92

The limitation and drawback of using the standard k-ε are that the mean velocity and turbulence quantities at near-wall regions, more particularly in the viscous sublayer, are predicted by wall functions, and not by the k-ε model itself. Also, the standard k-ε model only gives accurate predictions when simulating relatively simple flows. This means that flows involving large strains or swirling/rotational motions cannot be modeled accurately, using the standard k-ε model.

There has been a large amount of research conducted, not to only to overcome the limitations of the k-ε model, discussed above, but also to accurately predict fluid flow behavior near walls, with greater accuracy. For example, the RNG k-ε (Re-Normalisation Group) is a modified version of standard k-ε model [219]. This model greatly improves the accuracy in predicting rotational flows by the addition of a source term into the ε transport equation. However, like the standard k-ε model, the RNG k-ε model has a limitation in predicting vortex evolution. The Realizable k-ε is a result of the further advancement in modeling turbulent flows and is even more precise in terms of predicting swirls/rotations within the flows [220].

In order to avoid the use of the wall function method, the k-ω turbulent model evolved, in which the transport equation for the rate of dissipation of turbulent kinetic energy is replaced with the specific dissipation rate. The following section is dedicated to describing the k-ω turbulence model in detail, as this model was used in the present research study [216].

4.4.1.3. The k-ω Turbulence Model

The k-ω turbulence model was originally proposed by Wilcox in 1988 [221]. It is composed of the transport equations for k (turbulence kinetic energy) and ω (the specific dissipation rate). It is represented, as follows:

$$\frac{\partial}{\partial t}(\rho k) + \frac{\partial}{\partial x_i}(\rho k u_i) = \frac{\partial}{\partial x_j}\left[\Gamma_k \frac{\partial k}{\partial x_j}\right] + G_k - Y_k + S_k \tag{4}$$

$$\frac{\partial}{\partial t}(\rho\omega) + \frac{\partial}{\partial x_i}(\rho\omega u_i) = \frac{\partial}{\partial x_j}\left[\Gamma_\omega \frac{\partial\omega}{\partial x_j}\right] + G_\omega - Y_\omega + S_\omega \tag{5}$$

In the above-mentioned equation, Gk, Gω represent the generation of turbulence kinetic energy due to mean velocity gradient and the generation of the specific dissipation rate respectively, Yk, Yω represents the dissipation term and Sk, Sω represent the source terms.

The effective diffusivities are calculated by the following equations, in which the σ terms represent turbulent Prandtl numbers and, μt is the turbulent viscosity:

$$\Gamma_k = \mu + \frac{\mu_t}{\sigma_k};\ \Gamma_\omega = \mu + \frac{\mu_t}{\sigma_\omega} \tag{6}$$

$$\mu_t = \alpha^* \frac{\rho k}{\omega} \tag{7}$$

$\alpha*$ is known as a dimensionless coefficient, this is used to dampen μt. It is calculated by the following equation

$$\alpha^* = \alpha^*_\infty \left(\frac{\alpha^*_o + \frac{Re_t}{R_K}}{1 + \frac{Re_t}{R_k}}\right) \tag{8}$$

The constant used in the standard k-ω model is, $\alpha^*_\infty = 1, \alpha_\infty = 0.52, \alpha_o = \frac{1}{9}$, $\beta^\circ_\infty = 0.09, \beta_i = 0.072, R_\beta = 8, R_k = 6, R_\omega = 2.95, M_{t0} = 0.25, \xi^* = 1.5, \sigma_k = \ \sigma_\omega = 2.0$.

The advantages of the k-ω model are that it can be applied throughout the boundary layer without the need for wall functions, which are otherwise required in the k-ε model, as discussed above. However, this model is not very accurate in predicting values of ω in the free stream region. A variation of the k-ω model is the Shear-Stress Transport (SST) k-ω model. That was proposed by Menter in 1993 [216]. SST k-ω is a blend of k-ω, applied near the wall, and k-ε model, utilized in the far-field regions. The model has the following formulation:

$$\frac{\partial}{\partial t}(\rho k) + \frac{\partial}{\partial x_i}(\rho k u_i) = \frac{\partial}{\partial x_j}\left[\Gamma_k \frac{\partial k}{\partial x_j}\right] + \widetilde{G}_k - Y_k + S_k \tag{9}$$

$$\frac{\partial}{\partial t}(\rho\omega)+\frac{\partial}{\partial x_i}(\rho\omega u_i)=\frac{\partial}{\partial x_j}\left[\Gamma_\omega\frac{\partial\omega}{\partial x_j}\right]+G_\omega-Y_\omega+D_\omega+S_\omega \tag{10}$$

Here $\tilde{G}_k$ and G_ω represents the generation of turbulence kinetic energy and the specific dissipation rate respectively. The dissipation of k and ω is represented by Y_k and Y_ω. The D_ω in the above equation is the cross-diffusion term.

Γ_k and Γ_ω are the effective diffusivity and related to σ_ω, σ_k, the turbulent Prandtl numbers and μ_t the turbulent viscosity by the following relation.

$$\Gamma_k=\mu+\frac{\mu_t}{\sigma_k};\ \Gamma_\omega=\mu+\frac{\mu_t}{\sigma_\omega} \tag{11}$$

Here

$$\mu_t=\frac{\rho k}{\omega}\frac{1}{\max\left[\frac{1}{\alpha^*},\frac{SF_2}{a_{1\omega}}\right]} \tag{12}$$

$$\sigma_k=\frac{1}{\frac{F1}{\sigma_{k,1}}+\frac{(1-F_1)}{\sigma_{k,2}}} \tag{13}$$

$$\sigma_\omega=\frac{1}{\frac{F1}{\sigma_{\omega,1}}+\frac{(1-F_1)}{\sigma_{\omega,2}}} \tag{14}$$

The F_1, F_2 are the blending function

$$F_1=\tanh(\Phi_1^4) \tag{15}$$

$$\Phi_1=\min\left[\max\left(\frac{\sqrt{k}}{0.09\,\omega y},\frac{500\mu}{\rho y^2\omega}\right),\frac{4\rho k}{\sigma_{\omega,2}D_\omega^+y^2}\right] \tag{16}$$

$$D_\omega^+=\max\left[2\rho\frac{1}{\sigma_{\omega,2}}\frac{1}{\omega}\frac{\partial k}{\partial x_j}\frac{\partial\omega}{\partial x_j},10^{-10}\right] \tag{17}$$

$$F_2=\tanh(\Phi_2^2) \tag{18}$$

$$\Phi_2=\max\left(2\frac{\sqrt{k}}{0.09\,\omega y},\frac{500\mu}{\rho y^2\omega}\right) \tag{19}$$

Where y is the distance to the next surface and D_{ω}^{+} is the positive portion of the cross-diffusion term

$$\widetilde{G}_k = \min(G_k, 10\rho\beta^* k\omega) \tag{20}$$

$$G_{\omega} = \frac{\alpha}{v_t} G_k \tag{21}$$

4.4.2. Numerical Method

To numerically solve the governing equations, which in the present case are, continuity, momentum, energy or temperature, and those from the turbulence model, one needs to select a suitable numerical technique. Among the techniques available in the literature, the most widely used are the Finite Difference, Finite Element, and Finite Volume. In the present research study, the Integral Finite Volume method is used to discretize the governing equations. Additionally, several numerical schemes can be used to determine the pressure field, leading to the prediction of velocities for simultaneously satisfying the continuity and N-S equations. The most common are the Semi-Implicit Method for Pressure Linked Equations (SIMPLE), and the Pressure Implicit with Splitting of Operators (PISO) [222, 223]. In this research study, the PISO scheme was used, but details are not presented here as it can be read from the appropriate literature [216, 219].

4.5. Thermodynamic Modeling

In this research study, the Olson-Cohen modeling approach was used to determine the Stacking Fault Energy (SFE). This is the energy associated with an interruption in the normal stacking sequence of atomic planes in a closed-packed crystal structure [84, 88, 224]. The SFE plays a dominant role in controlling the active deformation mechanism in Advanced High Strength Steels (AHSS), as described in the previous chapter, and can be calculated using equation 22 [90]. In this section, details related to the calculation of SFE are presented. Additionally, FactSage software was used to determine the liquidus, solidus, and nucleation temperatures of the primary and secondary phases observed in high Mn steel, under macroscopic equilibrium and non-equilibrium, cooling conditions.

$$\mathrm{SFE} = n\rho[\Delta G^{\gamma\to\varepsilon}] + 2\sigma^{\gamma/\varepsilon} \tag{22}$$

Here ρ is the density of the atoms present in the {111} plane of γ, and can be evaluated through

$$\rho = \frac{4}{\sqrt{3}}\frac{1}{a^2 N} \tag{23}$$

N represents Avogadro's number, whilst "a" is the lattice parameter of the austenite. "a" is calculated using the composition-dependent equation 24, proposed by Charles et al [90]. The effect of the temperature on the lattice parameter calculation is neglected in these calculations.

$$a_{(FCC)} = 3.594 + 0.00125(\%Mn - 20) + 0.00594\ (\%Al) + 0.0272\ (\%C) \tag{24}$$

$\sigma^{\gamma/\varepsilon}$ is the interfacial energy between γ and ε equal to $10\,\frac{mJ}{m^2}$

$\Delta G^{\gamma\rightarrow\varepsilon}$ is the chemical Gibbs free energy difference of the γ→ε transformation, computed by the regular solution modeling approach. This is explained as follows:

4.5.1. Calculation of $\Delta G^{\gamma\rightarrow\varepsilon}$

The Gibbs free energy difference of a binary solid solution (in this case γ, ε) can be approached using the regular solution law, given as follows:

$$\Delta G^{\gamma\rightarrow\varepsilon} = \Delta G^{\gamma\rightarrow\varepsilon}_{chem} + \Delta G^{\gamma\rightarrow\varepsilon}_{mag} + \Delta G^{\gamma\rightarrow\varepsilon}_{seg} + \Delta G_{ex} \tag{25}$$

Where ($\Delta G^{\gamma\rightarrow\varepsilon}_{chem}$) is the molar thermochemical Gibbs free energy difference between γ and ε. $\Delta G^{\gamma\rightarrow\varepsilon}_{mg}$ = Change in the Gibbs free energy due to the Neel transition of each phase i.e. paramagnetic to anti-ferromagnetic transition, evaluated using the Indian-Hillert-Jarl (IHJ) model [90] expressed by

$$\Delta G^{\varphi}_{mag} = RT\ln\left(1 + \frac{\beta^{\varphi}}{\mu\beta}\right) f\left(\frac{T}{T^{\varphi}_{N}}\right), \varphi = \gamma, \varepsilon \tag{26}$$

where R, T, β^{φ}, f, T_N^{φ}, μβ are the universal gas constant, temperature in kelvin, magnetic moment, polynomial function, the Neel temperature of the phase φ and the Bohr magneton, respectively. T_N^{φ} is a function of chemical composition (at. %), and is presented as follows, and (was) used in the present investigation. The other parameters used are expressed by the following equations [90, 226];

$$T_N^{\gamma} = 0.00001x_{Mn}^3 + 0.08984x_{Mn}^2 + 11.76x_{Mn} - 19.92x_C - 12.72x_{Si} - 6.61x_{Si} + 152.4 \quad (27)$$

$$T_N^{\varepsilon} = 580x_{Mn} \quad (28)$$

$$\frac{\beta^{\gamma}}{\mu\beta} = 0.7x_{Fe} + 0.62x_{Mn} - 0.64x_{Fe}x_{Mn} - 4x_C \quad (29)$$

$$\frac{\beta^{\varepsilon}}{\mu\beta} = 0.62x_{Mn} - 4x_C \quad (30)$$

$$\text{If } \tau \geq 1,\ \tau = \left(\frac{T}{T_N^{\varphi}}\right), \quad (31)$$

$$f = 1 - \frac{\left\{\left[\frac{79\tau^{-1}}{140p} + \frac{474}{497}\left[\frac{1}{p} - 1\right]\left[\frac{\tau^3}{6} + \frac{\tau^9}{135} + \frac{\tau^{15}}{600}\right]\right]\right\}}{D} \quad (32)$$

$$\text{If } \tau \leq 1,\ \tau = \left(\frac{T}{T_N^{\varphi}}\right) \quad (33)$$

$$f = \frac{\left\{\left[\frac{\tau^{-5}}{10} + \frac{\tau^{-15}}{315} + \frac{\tau^{-25}}{1500}\right]\right\}}{D} \quad (33)$$

f is the polynomial function of the following form, p=0.28, D ≈ 2.3424 for FCC and HCP phase. ($\Delta G_{seg}^{\gamma\rightarrow\varepsilon}$) is the free energy difference due to the Suzuki effect between γ and ε, or more appropriately, it represents the effect on the SFE value when the solute concentration at the stacking fault differs from the bulk concentration (Neglected in the present calculation due to its negligible effect on the overall SFE value. ($\Delta G_{ex}^{\gamma\rightarrow\varepsilon}$) is the free energy difference due to the grain size of γ and ε and is considered in the present calculation. Its value can be determined using the following expression [224]:

$$\Delta G_{ex} = 170.06 \exp\left(\frac{-d}{18.55}\right) \tag{34}$$

where d is the austenite grain size in μm, taken as 40 μm in the present calculation.

The molar thermochemical Gibbs free energy difference $\Delta G_{chem}^{\gamma\rightarrow\varepsilon}$ can be evaluated by considering the following terms

$$\Delta G_{chem}^{\gamma\rightarrow\varepsilon} = \sum_i x_i \, \Delta G_i^{\gamma\rightarrow\varepsilon} + \sum_{it} x_i x_j \Delta\Omega_{it}^{\gamma\rightarrow\varepsilon} \tag{35}$$

where $x_i =$ the mole fraction of each constituent, i, accounting for alloying elements added in the system i.e. Fe, Mn, Al, Si & C.

$\Delta G_i^{\gamma\rightarrow\varepsilon}$ Gibbs free molar energy change associated with the addition of alloying elements, $\Delta\Omega_{it}^{\gamma\rightarrow\varepsilon}, \Delta\Omega_{it}^{\gamma\rightarrow\alpha}$ = Interaction parameter determining the interaction of different alloying elements with iron and the associated change in the free energy between γ and ε [72].

The other parameters used in this work are summarized in Table 11 [72].

Parameters	Expression/Value
$\Delta G_{Fe}^{\gamma\rightarrow\varepsilon}$	-1828.4 + 4.686T $\left(K, \frac{J}{mol}\right)$
$\Delta G_{Mn}^{\gamma\rightarrow\varepsilon}$	3970 – 1.6667 T $\left(K, \frac{J}{mol}\right)$
$\Delta G_{Al}^{\gamma\rightarrow\varepsilon}$	5481.04 – 1.79912 T $\left(K, \frac{J}{mol}\right)$
$\Delta G_{Si}^{\gamma\rightarrow\varepsilon}$	–560 – 8T $\left(K, \frac{J}{mol}\right)$
$\Delta G_{C}^{\gamma\rightarrow\varepsilon}$	–22,166 $\left(K, \frac{J}{mol}\right)$
$\Delta \Omega_{FeMn}^{\gamma\rightarrow\varepsilon}$	-9135.5 + 15,282.1XMn $\left(\frac{J}{mol}\right)$
$\Delta \Omega_{FeAl}^{\gamma\rightarrow\varepsilon}$	3326.28 $\left(\frac{J}{mol}\right)$
$\Delta \Omega_{FeSi}^{\gamma\rightarrow\varepsilon}$	1780 $\left(\frac{J}{mol}\right)$
$\Delta \Omega_{FeC}^{\gamma\rightarrow\varepsilon}$	42,500 $\left(\frac{J}{mol}\right)$
R	8.314 $\left(\frac{J}{Kmol}\right)$

4.6. Assumptions/Simplifications Incorporated in the Current Modeling Work

Following assumptions/simplifications were considered for the Fluid Flow/Thermal modeling:

1. The liquid steel was assumed to be incompressible and a newtonian fluid.
2. Physical properties of the fluid (molten metal), most particularly density, viscosity and surface tension, were all assumed constant throughout the simulation. These physical properties are highly dependent on temperature, which may vary during the process. However, any slight variations in density, viscosity and surface tension due to the change in temperature were ignored.
3. Constant boundary conditions were applied in the present numerical simulations. These included constant velocity of the molten metal at the nozzle slot outlet which in general depends on the molten metal head inside the tundish. The slight variation of molten metal head within the tundish, if they existed during the process, were ignored.
4. The temperature of the molten metal at the nozzle slot outlet was assumed constant. This is indicative of a molten metal/alloy's superheat before the start of the process. During

experiments, one could expect the molten metal's temperature to be constantly decreasing with time, instead of remaining constant. However, these little changes in temperature were ignored.

5. Solidification of molten metal was modeled considering perfect contact of molten metal with the moving belt. In the real situation, there is an air gap in between solidified shell and the moving belt which can significantly reduce the heat flux through the belt.
6. Any mass transfer from molten metal to the air, and vice-versa, were considered zero, since these fluids were considered immiscible, insoluble, and non-inter-penetrating. Also, the source was considered zero, since there was no creation or destruction of any presumed phase. In reality, the molten aluminum is reacting with air in AA6111 alloy, and formed a thin oxide layer, which means that the source term was not zero. However, the formation of a thin oxide was assumed to hardly influence the bulk flow of liquid metal, and was therefore ignored for the present computations.

Following assumptions/simplifications were considered for the FactSage Thermodynamic modeling:

1. The diffusion within the solidified metal was assumed to be zero.
2. Infinitely fast diffusion occurs within the molten metal at all temperatures.
3. An equilibrium at the solid-liquid interface is assumed, therefore the compositions from the phase diagram are valid.
4. Solidus and liquidus are straight segments.

4.7. Final Remarks

This chapter has discussed the basics of the CFD and the Thermodynamics modeling approaches employed in this research study. The CFD modeling was used to simulate the molten metal flow in the HSBC process, whereas the thermodynamics modeling (Olson-Cohen and FactSage assessments) were used to determine the types, amounts, and stability of the phases in AHSS. Additionally, in this chapter, details related to the use of the numerical models and methods have been presented. Furthermore, the procedure to solve the governing equations are explained, in which the first step is to select the computational domain i.e., a region bounded by edges (2-Dimensional) or faces (3-Dimensional), followed by its discretization into tiny imaginary cells, called meshing. In the second stage, the initial and boundary conditions are defined for each of the governing equations and numerical models and methods are implemented to solve them. In the third step, the governing equations are iteratively solved, until the relative residuals reach predefined values, in the order of 10^{-6} or even less. Residuals quantify the error in the solution of the system of equations or in other words it measures the local imbalance of a conserved variable in each control volume. Finally, the detailed procedure to calculate the Stacking Fault Energy (SFE) with a special focus on measuring a Gibbs free energy of transformation via the Regular Solution Modeling approach has been presented.

Chapter 5

5.0. Numerical Modeling of Transport Phenomena in the Horizontal Single Belt Casting (HSBC) Process, for AA6111 Alloy Strip

This chapter discusses the casting of AA6111 aluminum alloy strip, 250 mm wide, and 6 mm thick using the Horizontal Single Belt pilot-scale Caster. In this study, a three-dimensional CFD model was developed, to examine the flow of the molten AA6111 alloy in the HSBC process. The phenomenon behind the formation of center shrinkage defect is explained and remedial measures to prevent its occurrence are proposed. The experimental findings are in accord with the model predictions. The microstructures of the strip produced were evaluated using optical and Scanning Electron Microscopy. Surface roughness was measured using the Nanovea 3D optical profilometer. The research presented below made the object of the publication entitled: "Numerical Modeling of Transport Phenomena in the Horizontal Single Belt Casting (HSBC) Process for the Production of AA6111 Aluminum Alloy Strip", Usman Niaz, Mihaiela M. Isac & Roderick I. L. Guthrie, publisher MPDI, in the Journal "Processes", 2020, Volume 8, pp: 529 - 538.

5.1. Synopsis

In this research study, numerical modelling and experimental casting of AA6111 strips, 250 mm wide, 6mm thick was conducted. The velocity of the molten AA6111 at the nozzle slot outlet was raised to 2m/s, whilst the belt speed was kept at 0.3m/s. The numerical model demonstrates considerable turbulence/fluctuations in the flow of the molten AA6111 alloy in the HSBC process, rendering its free surface highly non-uniform and uneven. These discontinuites in the flow resulted from the sudden impact of molten metal onto the inclined refractory plane and then onto slow moving belt. However, it has been determined that these surface variations are rapidly damped, and as such are not detrimental to final strip surface quality. Any surface perturbations remaining can be easily eliminated via hot plastic deformation. The experimental findings are in accordance with the model predictions. Furthermore, at high metal heads inside the tundish, the molten metal was observed to be flowing inwards towards the center of the strip, thereby filling the centre depression region, formed otherwise. The model predictions were validated against experimental findings. Additionally, the physical properties of the as-cast strip were determined which confirmed that strip produced under the above-mentioned conditions had a high surface quality. A microstructural analysis was also conducted to determine the quality of the as-cast strip which revealed a fine grain microstructure, with no columnar zone.

Key Words

Horizontal Single Belt Casting Process (HSBC), Computational Fluid Dynamics (CFD), Double Impingement Feeding System.

5.2. Introduction

The Horizontal Single Belt Casting (HSBC) process can be used to produce superior quality ferrous/non-ferrous strips of thicknesses up to 15 mm [1-4]. Apart from its low energy requirements and promising productivity, the technology is capable of producing near net shape metallic products which have a homogenous microstructure and a fine grain size [1-4]. Also, all inverse macro-segregation occurring with the DC slab casting route is eliminated, since the cooling rate of metal in the HSBC process is significantly higher. i.e. up to 500°K/second [5].

In a simplistic way, the HSBC process involves feeding molten metal, on to an intensively cooled, moving belt, which acts as the mold. Depending on the metal head inside the tundish, the velocity of the molten metal issuing from the nozzle slot can be easily adjusted [3]. However, the force of gravity is also equally responsible in further accelerating the molten metal before it contacts the moving belt, on which it solidifies [3]. The material produced via the HSBC process can then be processed downstream, by hot rolling followed by cold rolling as shown in Figure 1 [3, 4].

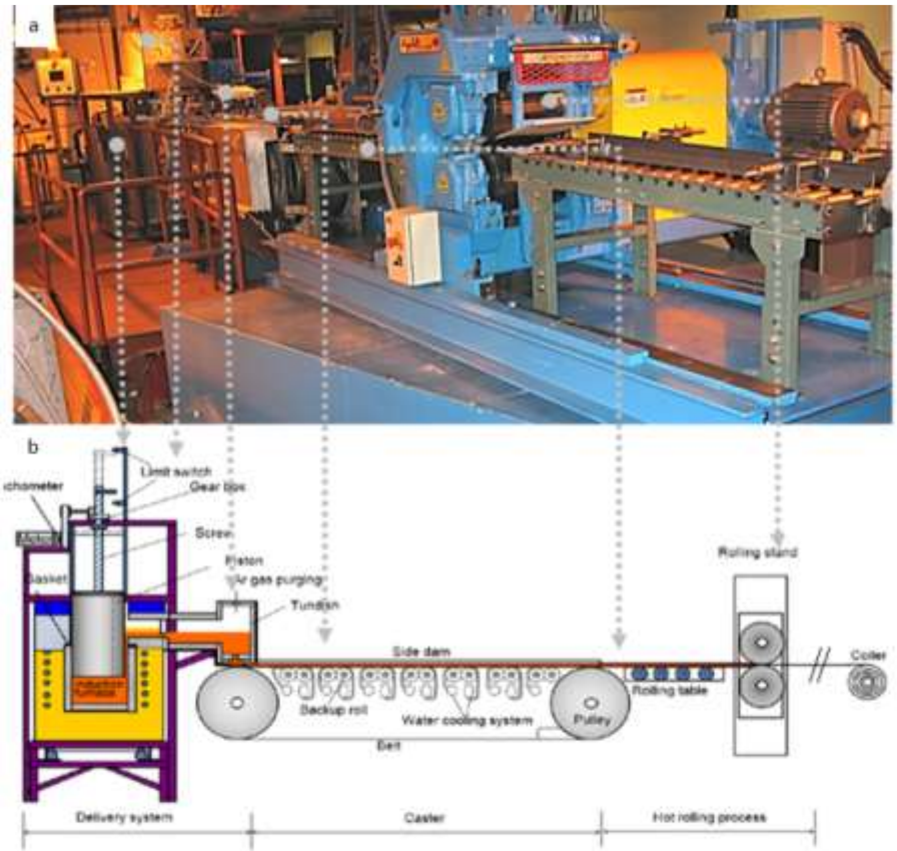

Figures 1: (a) A photograph of the HSBC pilot-scale plant, and b) a schematic of the HSBC pilot scale machine located at MetSim Inc's, High Temperature, Melting and Casting Laboratory, Quebec, Canada [1].

The HSBC process avoids the hot deformation required in the Direct Chill (DC) cast material, together with intermediate annealing steps, whilst producing the desired final thickness of the sheet product. As such, a large amount of energy can be saved [3, 5]. The HSBC process features a compact design and provides for a better economic production of both ferrous/non-ferrous metallic products. The production of Advanced High Strength Steel (AHSS) strips, 10 mm thick, via the HSBC process at Salzgitter Group Steelworks, Germany, is an example which makes use of the advantages that the HSBC process offers, versus conventional strip manufacturing processes [6, 7].

5.3. Feeding System & Important Parameters of the HSBC Process

Many variants of the feeding system have been investigated by researchers at McGill University. They can be classified into two types of metal delivery system; single impingement and multi-impingement, based on the number of times the molten metal encounters obstacles before reaching the cooling substrate [2]. In the present research study, a double impingement feeding system was used for the production of 250 mm wide AA6111 strip, as shown in Figure 3. In the double impingement feeding system, the molten metal first interacts with the inclined refractory plane (45°), followed by its second interaction with the moving belt [2]. The strip quality is highly dependent on these two important interactions, as they can lead to instabilities in the molten metal flow, and can result in longitudinal thickness variations during upward freezing of the cast strip [2]. Other operating parameters, such as melt fluidity i.e. super-heating, nozzle slot dimensions, and belt velocity, are critical to cast product quality [1-5]. Lastly, the gap between the refractory inclined plane and the moving belt is also important, as it dominates the meniscus behavior at the quadruple point, or more precisely at the quadruple region where melt-refractory-air-belt coexist [1-5]. This vertical distance must be a little less than the critical gap necessary to prevent extensive back-flow of metal, that may lead to skull formation, thereby curtailing further casting [4]. The entire process is carried out under atmospheric pressure and therefore the operating parameters of the process discussed above and their effective control, is the key towards obtaining perfectly flat and uniform upper & bottom surfaces of the cast sheet material [2].

5.4. Aluminum Alloy AA6111 used in the Present Research

Keeping in mind the suitability of the HSBC process to cast both ferrous and non-ferrous alloys and knowing the use of AA6111 aluminum alloy in the production of the lightweight body in white (BIW) automotive structures, AA6111 was selected for HSBC strip production. AA6111 is an alloy of Al-Mg-Si (Cu). AA6111 possess higher mechanical strength (i.e., 400 MPa), high formability, and good corrosion resistance. The main mechanism behind AA6111's increased strength is precipitation hardening, along with solid solution and work strengthening [8, 9]. The alloying elements present in AA6111 are as shown in Table 1.

The casting of AA6111 strip via the HSBC process is comparatively new, and is presently in its development stages. It is therefore hoped that this paper will add fundamental knowledge to the information already existing on this subject, and help industries realize the versatility of the HSBC process to cast AA6111 aluminum alloy strips. Its chemical composition is presented in Table 1.

5.5. Details of the Experimental Procedure

AA6111 alloy was produced by first melting pure aluminum in a pre-heated induction furnace under a protective argon atmosphere, followed by the addition of Al-Mg, and Al-Mn alloys, etc. Good melt stirring was ensured to completely dissolve/mix the alloy additives into the pure aluminum. The melt was then de-gassed, and Ti-B grain refiner was added, in the conventional way. The AA6111 melt was then cast using the HSBC system. The step by step operation of the HSBC pilot caster is presented as follows.

The process started with the production of AA6111 alloy using the 600 lb induction melting furnace. Afterwards, the furnace was moved to the casting station, where it was locked with the liquid metal delivery system, consisted of a refractory cylinder (regulated by a servo motor) and a launder, as shown in Figure 1. Once, the tight seal between induction furnace and delivery system was ensured, the refractory cylinder was allowed to enter into the induction furnace at a pre-selected speed, thereby displacing the molten metal into the launder. Once molten metal reached the desired level inside the launder, the stopper bar blocking the nozzle outlet was rapidly withdrawn, and liquid metal began to pour onto the belt. A weir and a dam were used to help prevent Al_2O_3 oxide skin from entering the nozzle slot, as well as to help in minimizing turbulence present within the flowing molten metal. The moving belt could also be equipped with two rotating side dams. Their purpose is to contain the molten metal once it leaves the nozzle slot and to provide a straight/smooth edge before it enters the minimill for hot reduction. To avoid any premature freezing, the entire delivery system and the refractory piston were preheated to approximately 500-550°C, using resistive heating systems.

To evaluate the bulk, as well as the surface, quality of the cast strips, samples were sectioned from the strip. All samples were polished and prepared for metallographic observations and analyzed under the Leica DM IRM Optical and Hitachi TM3030 Scanning Electron Microscope. The surface roughness was measured using 3D Nanovea Profilometer. Results will be presented in later paragraphs.

Table 1: Chemical composition of the AA6111 strip produced vis HSBC process, determined using spark OES technique.

Alloying Elements Wt. %								
Cu	Fe	Mg	Mn	Cr	Si	Ti	Zn	Al
0.5-0.9	> 0.4	0.5 – 1.0	0.1 – 0.45	< 0.1	0.6 – 1.1	< 0.1	< 0.15	Remaining

5.6. Details of the Model Setup

For CFD studies, the three-dimensional, transient state, turbulent fluid flow was modeled using Ansys Fluent 14.5 software. The code is based on the Finite Volume Method (FVM) [10]. The simulation domain chosen to carry out this research study had the following dimensions, length (0.195 m), height (0.016 m), width (0.05 m) as shown in Figure 2. The semi-implicit method for pressure linked equations (SIMPLE) was used for coupling pressure and velocity in the governing equations. More details can be found in the literature [10]. To improve on the accuracy, the advection terms were discretized using a 2nd order upwind scheme over the entire simulation domain, whereas the diffusion term was approximated by the central differencing scheme. To stabilize the interactive process, an under-relaxation factor of 0.7 for the velocity and 0.3 for the pressure, were used. The solution process was reiterated until the residuals of governing equations reduced to $1\text{x}10^{-7}$. Different grids were tested until mesh-independent results were achieved. Finally, 2867541 hexahedral cells were identified as being an accurate but less computationally intensive, exercise for obtaining the desired results. The molten metal was treated as a Newtonian, incompressible fluid, and all the physical properties were assumed to be constant (Table 2 and 3).

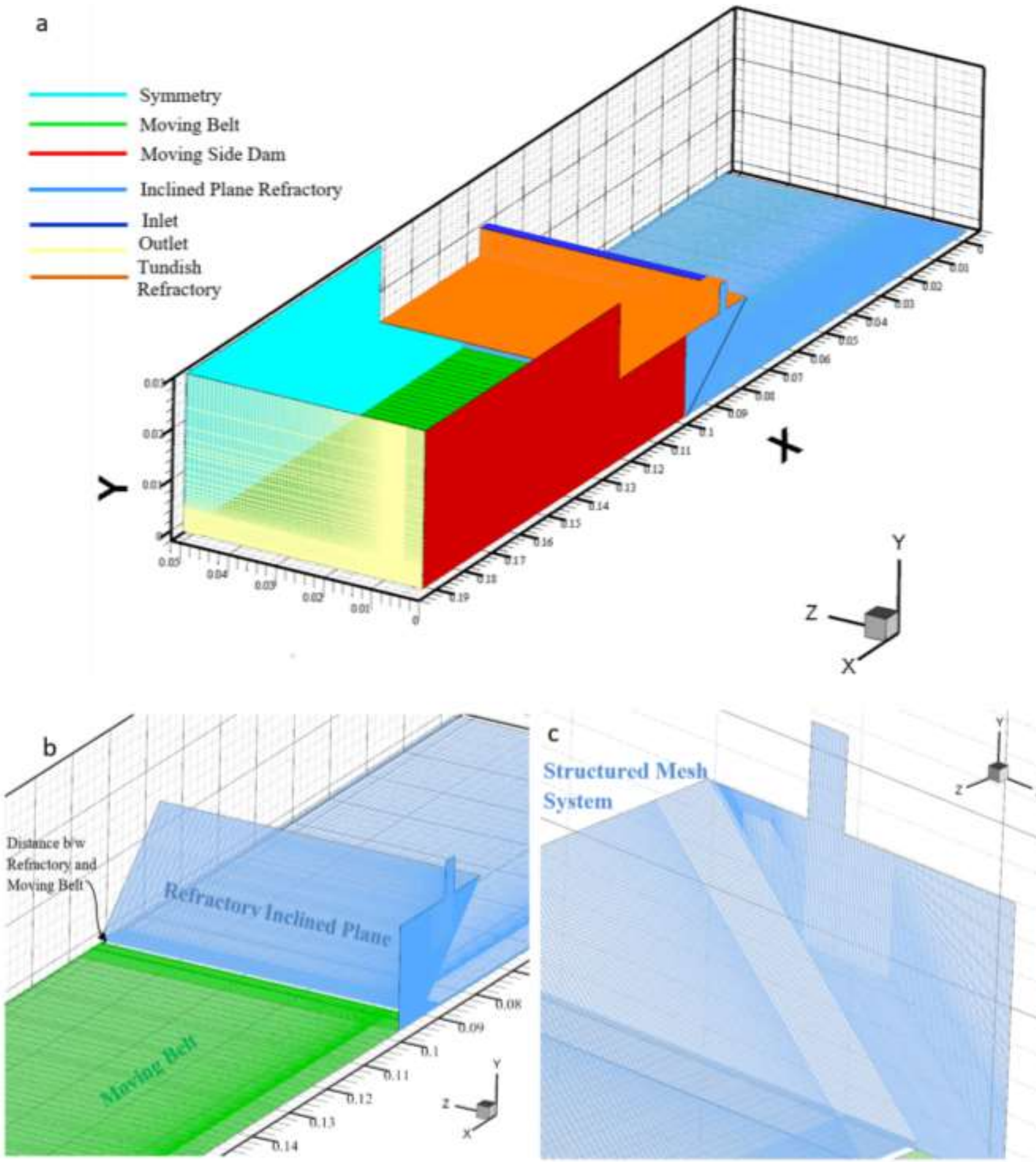

Figures 2: (a) Simulation domain containing hexahedral meshes (3D), (b) Mesh refinement at the nozzle outlet and triple point

Table 2: Physical Properties of the Phases used in the Model.

Operating Parameters/Assumptions	**Value**
Slot Nozzle Dimension	3 x 250 mm
Inlet Velocity	2 m/s
Surface Tension of the Melt in Air	0.914 N/m [10]
Copper Substrate Longitudinal speed	0.3 m/s
Turbulence Model	SST k-ω
Contact Angle Between Melt and Alumina Refractory	135° [2,11]
Contact Angle Between Melt and Copper Substrate	105° [2, 11]
Distance Between Stationary Inclined Refractory Plane and Moving Belt	0.4 mm
Solidus Temperature (K)	858.15 [11]
Liquidus Temperature (K)	923.15 [11]

Table 3: Operating Parameters and Assumptions Made in the Model [2, 11]

Property	**AA6111**	**Air**
Density, $\rho(\frac{\mathrm{Kg}}{\mathrm{m}^3})$	2300	1.225
Specific Heat Capacity, $C_p\left(\frac{\mathrm{KJ}}{\mathrm{KgK}}\right)$	1.177	1.006
Thermal Conductivity, $K\left(\frac{\mathrm{W}}{\mathrm{mK}}\right)$	104	0.0242
Viscosity, $\mu\left(\frac{\mathrm{Kg}}{\mathrm{ms}}\right)$	0.001338	1.75×10^{-5}
Molecular Weight, $\left(\frac{\mathrm{Kg}}{\mathrm{kmol}}\right)$	26.98	28.97
Standard State Enthalpy $\left(\frac{\mathrm{J}}{\mathrm{kgmol}}\right)$	$1.100493\mathrm{x}10^{7}$	-
Reference Temperature (K)	298.15	298.15
Initial Temperature (K)	1000	300
Latent Heat $\left(\frac{\mathrm{J}}{\mathrm{kg}}\right)$	387000	-

5.7. The Volume of the Fluid (VOF) Multiphase Model [12]

The volume of the Fluid (VOF) multiphase model is applied to a fixed Eulerian mesh for solving a single set of the momentum equations. In this way, the volume fraction of each fluid $(\alpha_{metal}, \alpha_{air})$ in all the computational cells, could be determined, so as to track the melt-air interface. The VOF method solves a continuity and momentum equation.

$$\frac{1}{\rho_q}\left[\frac{\partial}{\partial t}\left(\alpha_q \rho_q\right) + \nabla\left(\alpha_q \rho_q \dot{u}_q\right) = S_{\alpha q} + \left(\dot{m}_{pq} - \dot{m}_{qp}\right)\right], \text{Where } \alpha_{metal} + \alpha_{air} = 1 \quad (1)$$

where ρ is the density, t is the time, α is the volume fraction, $\bar{u}$ is the velocity and the subscript q represents phase (melt or air). $\dot{m}_{pq}$ is the mass transfer from phase q to phase p and vice versa for $\dot{m}_{qp}$. Both terms are zero here, since molten metal and air are immiscible, insoluble and non-inter-penetrating. Also, the source term, here designated as $S_{\alpha q}$, is zero, since there is no creation or destruction of any phase.

Explicit time discretization is used to solve the VOF equation for this transient 3D model as represented in equation 2

$$\frac{\alpha_q^{n+1}\rho_q^n - \alpha_q^n \rho_q^n}{\Delta t} V + \sum_f \left(\rho_q U_f^n \alpha_{q,f}^n\right) = \left[\left(\dot{m}_{pq} - \dot{m}_{qp}\right) + S_{\alpha_q}\right] V \quad (2)$$

Here n and n+1 are the time step indices of the variables, $\alpha_{q,f}$ is the computed face value of the volume fraction of phase q. U_f is the volumetric flux through a specific face, based on the normal velocity, and V is the cell volume.

5.8. Momentum Conservation Equation [10]

The general form of the momentum conservation equation is represented in equation 3.

$$\frac{\partial(\rho\bar{u})}{\partial t} + \nabla.(\rho\bar{u}\bar{u}) = -\nabla p + \nabla.\left[\mu\left(\nabla\bar{u} + \nabla\bar{u}^T\right)\right] + \rho\bar{g} + \bar{F}_\sigma \quad (3)$$

p is the static pressure, μ is the dynamic viscosity, $\bar{g}$ is acceleration due to gravity and $\bar{F}_\sigma$ is the surface tension force. The momentum equation shown above is dependent on the volume fraction of the phases in each control volume through the properties ρ and μ, which are approximated using the two equations below.

$$\rho = \alpha_{melt}\,\rho_{melt} + \alpha_{air}\rho_{air}, \tag{4}$$

$$\mu = \alpha_{melt}\rho_{melt}\eta_{melt} + \alpha_{air}\rho_{air}\eta_{air} \tag{5}$$

In this study, an explicit time marching scheme was used, to discretize and solve the transient VOF equation and Geometric Reconstruction Scheme (GRS) was selected to reconstruct the interface between the melt and air, using a Piecewise Linear Interphase Method. GRS assumes a linear slope of the fluids interface within each computational cell and uses this linear slope to evaluate the advection of the fluid through the cell phases [2].

Also, surface tension effects, along with the melt-air interface, was studied by incorporating the continuum surface force (CSF) model. The CSF model adds a source term in the momentum equation which can be calculated as per equation 6.

$$\vec{F}_\alpha = \sigma k \vec{n} \tag{6}$$

where σ is the surface tension coefficient, k is the free surface curvature and $\vec{n}$ is the interface normal vector.

5.9. Shear-Stress Transport (SST) k-ω Model [10]

The Shear-Stress Transport (SST) k-ω model was employed in this research study. This model is a blend of k-ω, applied near the wall, and k-ε model, utilized in the far field regions as represented in equation 7 and 8.

$$\frac{\partial}{\partial t}(\rho k) + \frac{\partial}{\partial x_i}(\rho k u_i) = \frac{\partial}{\partial x_j}\left[\Gamma_k \frac{\partial k}{\partial x_j}\right] + \widetilde{G}_k - Y_k + S_k \tag{7}$$

$$\frac{\partial}{\partial t}(\rho \omega) + \frac{\partial}{\partial x_i}(\rho \omega u_i) = \frac{\partial}{\partial x_j}\left[\Gamma_\omega \frac{\partial \omega}{\partial x_j}\right] + G_\omega - Y_\omega + D_\omega + S_\omega \tag{8}$$

Additionally, $\tilde{G}_k$ and G_ω represent the generation of turbulence kinetic energy and the specific dissipation rate respectively. The dissipation of k and ω is represented by Y_k and Y_ω. The D_ω in the above equation is the cross-diffusion term.

Γ_k and Γ_ω are the effective diffusivity and related to σ_ω, σ_k, the turbulent Prandtl numbers, and μ_t the turbulent viscosity as represented in equation 9.

$$\Gamma_k = \mu + \frac{\mu_t}{\sigma_k};\ \Gamma_\omega = \mu + \frac{\mu_t}{\sigma_\omega} \tag{9}$$

Here

$$\mu_t = \frac{\rho k}{\omega}\frac{1}{\max\left[\frac{1}{\alpha^*}, \frac{SF_2}{a_{1\omega}}\right]} \tag{10}$$

$$\sigma_k = \frac{1}{\frac{F1}{\sigma_{k,1}} + \frac{(1-F_1)}{\sigma_{k,2}}} \tag{11}$$

$$\sigma_\omega = \frac{1}{\frac{F1}{\sigma_{\omega,1}} + \frac{(1-F_1)}{\sigma_{\omega,2}}} \tag{12}$$

The F_1, F_2 are the blending functions

$$F_1 = \tanh(\Phi_1^4) \tag{13}$$

$$\Phi_1 = \min\left[\max\left(\frac{\sqrt{k}}{0.09\ \omega y}, \frac{500\mu}{\rho y^2 \omega}\right), \frac{4\rho k}{\sigma_{\omega,2} D_\omega^+ y^2}\right] \tag{14}$$

$$D_\omega^+ = \max\left[2\rho \frac{1}{\sigma_{\omega,2}} \frac{1}{\omega} \frac{\partial k}{\partial x_j} \frac{\partial \omega}{\partial x_j}, 10^{-10}\right] \tag{15}$$

$$F_2 = \tanh(\Phi_2^2) \tag{16}$$

$$\Phi_2 = \max\left(2 \frac{\sqrt{k}}{0.09\ \omega y}, \frac{500\mu}{\rho y^2 \omega}\right) \tag{17}$$

where y is the distance to the next surface and D_ω^+ is the positive portion of the cross-diffusion term

$$\tilde{G}_k = \min(G_k, 10\rho\beta^* k\omega) \tag{18}$$

$$G_\omega = \frac{\alpha}{v_t} G_k \tag{19}$$

5.10. Objectives of the Present Research Study

The following objectives are supposed to be achieved through this study:

1. Is it possible to cast high surface quality strip under non isokinetic feeding conditions (i.e. the molten metal velocity at the nozzle slot outlet is 2m/s, with the belt running at 0.3m/s).
2. Since the pilot caster belt is only 2.6 meters long, will the molten metal solidify under the above mentioned operating condition.
3. Are the surface discontinuites/distrubances, formed under above mentioned non-isokinetic feeding condition, inhiliated before the molten metal solidifies within 2.6 meters.
4. To investigate the phenomenon of molten metal's inward flow.

In order to achieve the above-mentioned objectives, several modifications to the existing pilot caster at the McGill Metals Processing Center (MMPC) were carried out. These include, the design of a new alumina refractory nozzle slot, increasing the cooling capability of the moving steel belt needed to completely solidify 250 mm wide, ~ 4-6 mm thick molten AA6111 strip, before it exits the moving belt. Additionally, the caster modifications include enlarging the strip guidance system, and lastly the extension of the length and width of the run-out table so as to accommodate the wider strip exiting the caster.

5.11. Results & Discussion of Numerical Simulations

5.11.1. Method to Eradicate Center Cavity Defects

It was observed through numerical simulation studies that in HSBC process, the molten metal tends to contract, while exiting through the nozzle slot outlet, as shown in Figures 3a and b. Due to this lateral contraction, the weight of the molten metal around the edges considerably increases as compared to the center. The heavier section accelerates downwards under the influence of gravitational force, eventually reaching a high terminal speed. As a result, the amount of the molten metal, delivered towards the edges, is considerably more as compared to the center as shown in Figures 3a and b.

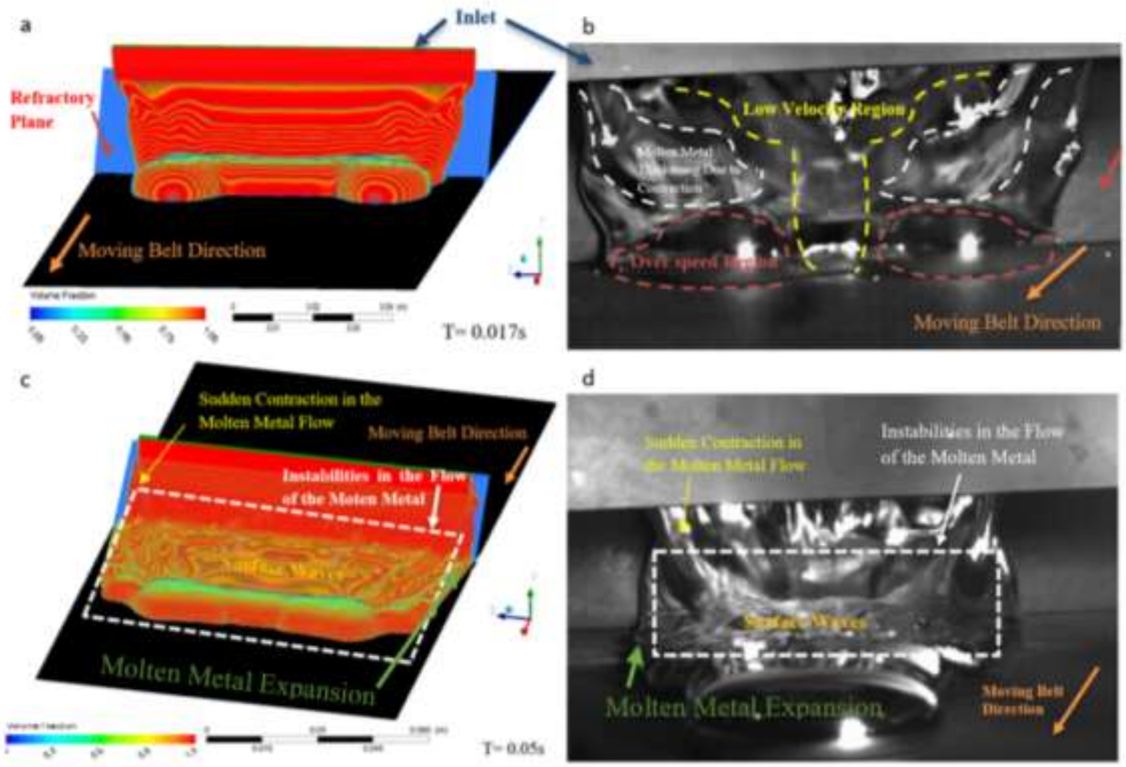

Figures 3: Molten AA6111 flow in HSBC process, (a & c) Simulated AA6111 flow showing metal's contraction after leaving the nozzle slot, and (b & d) Actual Molten AA6111 flow in HSBC process.

If the metal head inside the tundish is below 50 mm, the molten metal delivered over the moving belt will proportionally be lower according to equation 20 [2]. Keeping in view the heat extraction rate of the molten metal over the moving belt of the pilot horizontal single belt caster which is of the order of 500 k/sec [5] and since the quantity of the molten metal over the belt is low, it tends to solidify almost immediately. The molten metal under these operating conditions, will not have enough time to settle down before solidification. This results in a strip with a thicker edge and a comparatively thinner center. The opposite is true for high metalhead inside the tundish i.e. (>50mm), in this case, the quantity of the molten metal delivered to the moving belt is high. For a constant heat extraction rate of the moving belt as described above, this would allow molten metal to settle down before the completion of solidification, resulting in a high-quality strip with uniform thickness throughout the thickness as observed experimentally.

$$V = C_D\sqrt{2gh} \tag{20}$$

v is the melt velocity, h is the molten metal head inside the tundish

Increasing the depth of molten metal in the tundish, results into a corresponding rise in its exit velocity at the nozzle slot outlet. This proportionally increases the lateral inward flow of the molten metal, shown in Figure 4.

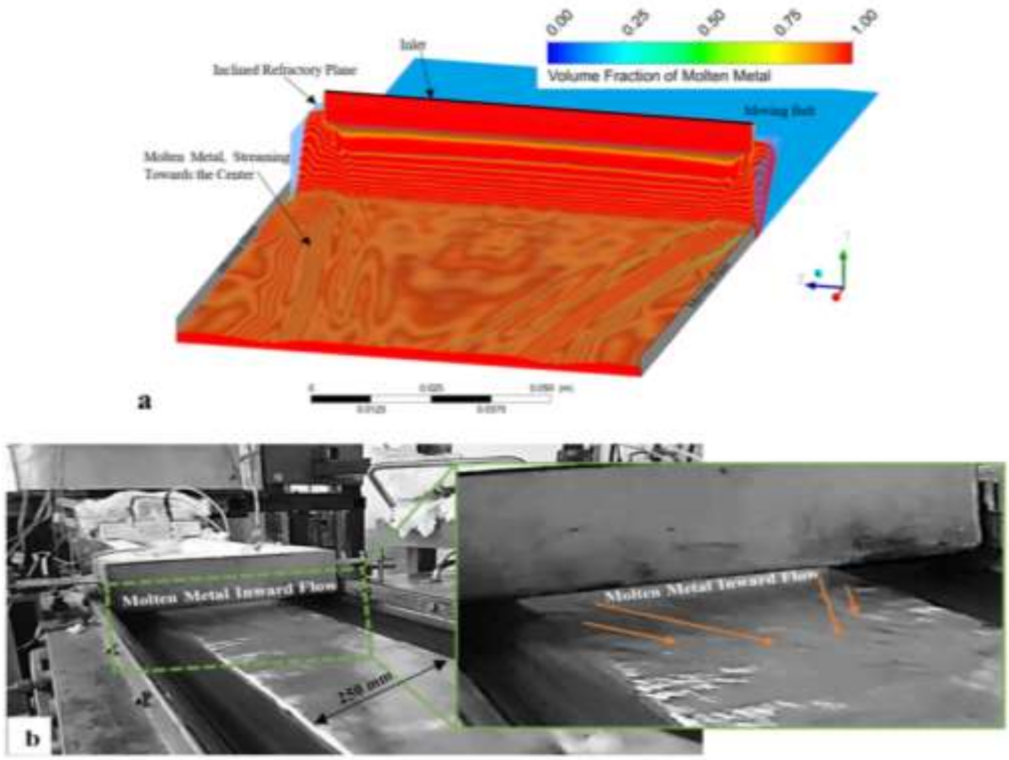

Figures 4: The inward flow of the molten metal over the moving belt (a) Simulated (b) Actual.

5.11.2. Iso-Surfaces of Z-Component of Velocities

Since, the velocity vector can be resolved into three components i.e., x, y, and z in which z-velocity component represents a net inward flow of the molten metal. For these reasons, the iso-surfaces of z-component of velocities were evaluated and are represented in Figure 5.

As expected, the z-component of the velocity vector is maximum during the first instants of molten metal contact with the moving belt, owing to the fact that molten metal, while flowing over an inclined plane, continously accelerates, under the force of gravity. Furthermore, the z-component of velocity was observed to be high adjacent to the molten metal/air interface and zero near the moving belt. However, further downstream, over the belt, the z-component of velocity was observed to be decreasing with distance.This is essentially true, as there is no driving force that could help molten metal to further accelerate over horizontal moving belt.

The similar concept was explained by plotting z-component of velocity along the lines, marked as 1 and 2 in Figure 6. These lines are 12 mm in length and are originating from the moving edge dam, in the positive z-direction, ending at the symmetry plane. Line 1 was located over the inclined refractory plane where as Line 2 was placed over the moving belt, adjacent to quodruple point. As expected the peak velocity recorded over the inclined refractory plane was approximately 0.5 m/s as opposed to 0.6 m/s, documented over the moving belt, near the quodruple region. However after 12mm in the positive z axis, the z-component velocity was zero. This clearly proves that the turning effect of the molten metal is only concentrated around the edges of free molten-metal stream.

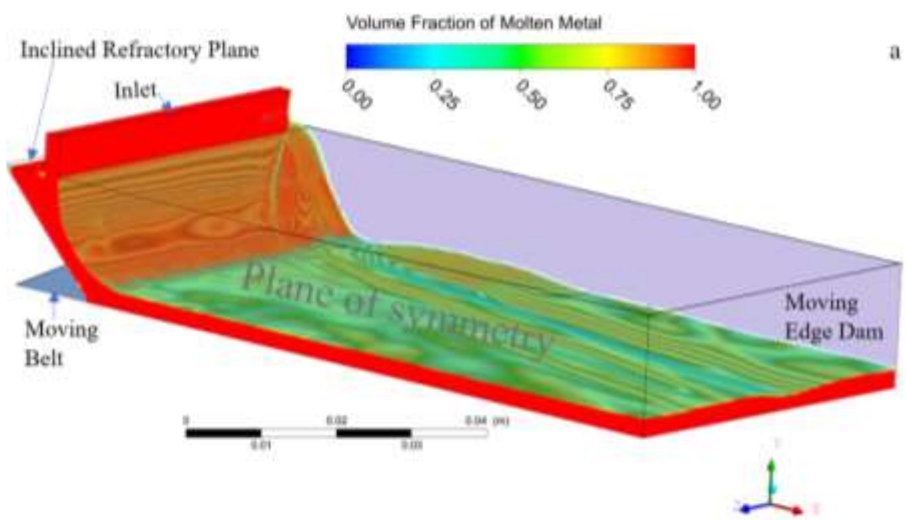

Figures 5: (a) Molten metal flow in HSBC process.

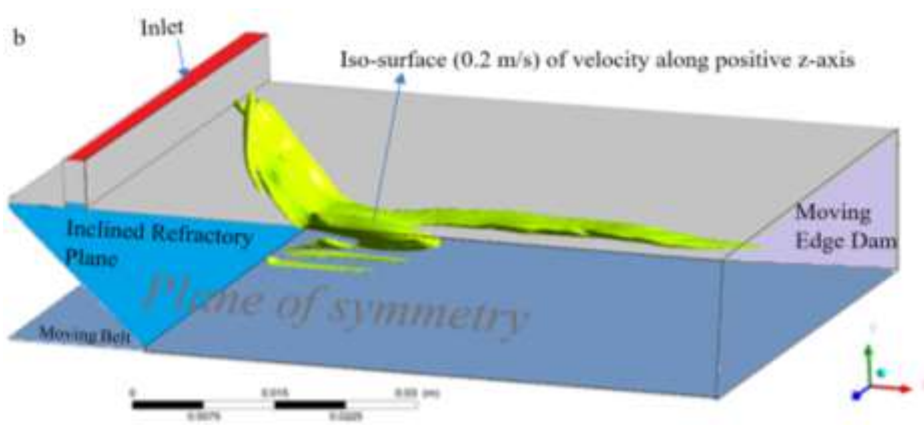

Figures 5: (b) Iso-velocity (0.2 m/s) along + z-direction.

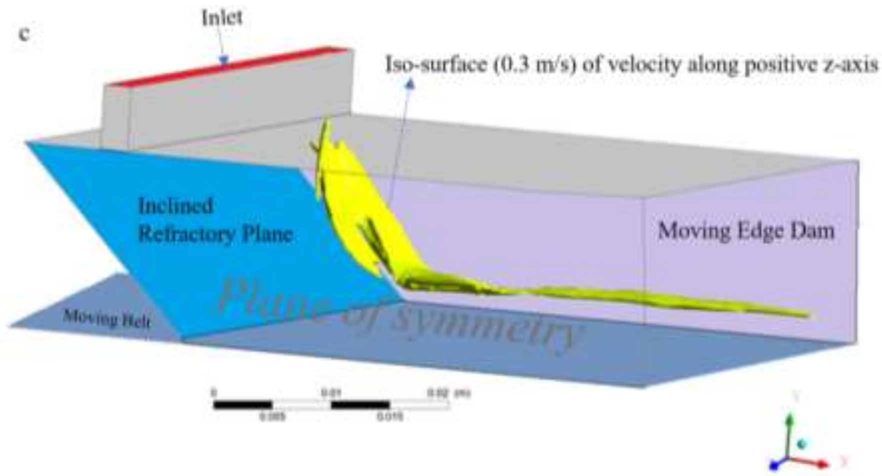

Figures 5: (c) Iso-velocity (0.3 m/s) along + z-direction.

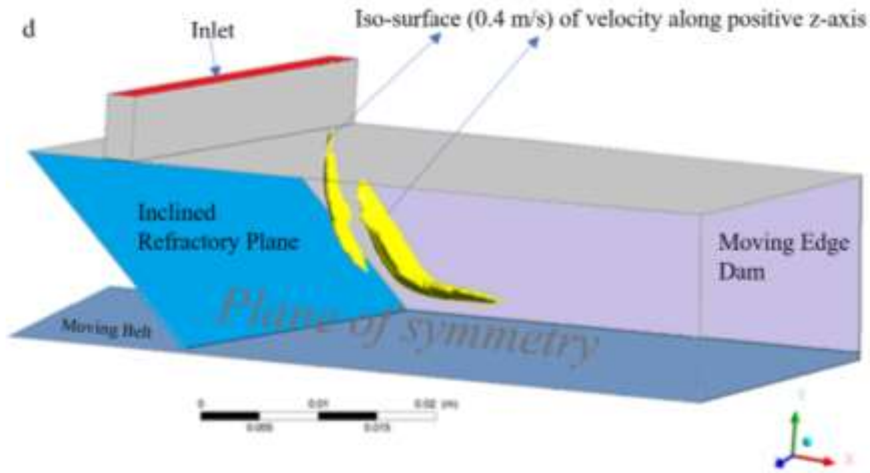

Figures 5: (d) Iso-velocity (0.4 m/s) along + z-direction.

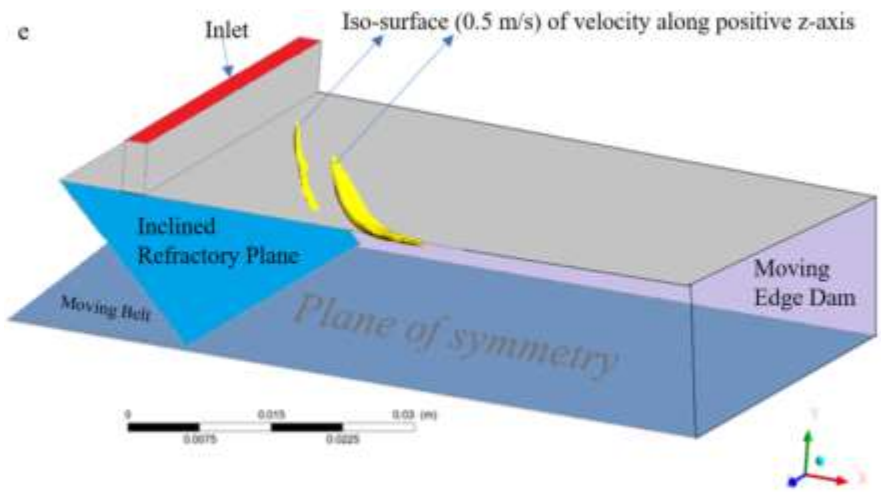

Figures 5: (e) Iso-velocity (0.5 m/s) along + z-direction.

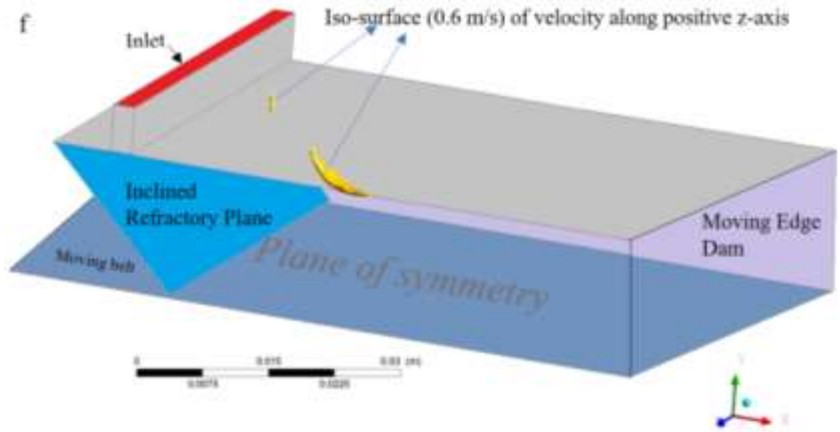

Figures 5: (f) Iso-velocity (0.6 m/s) along + z-direction.

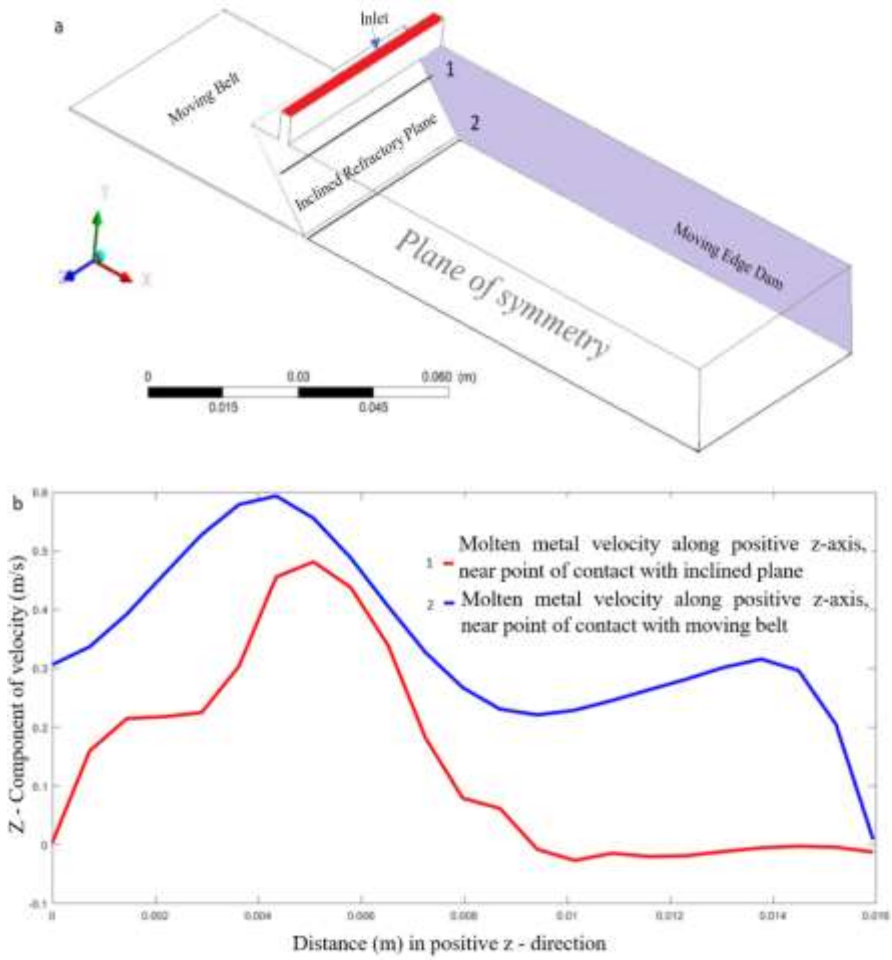

Figures 6: (a) Simulation domain showing the line at which the velocity profile is plotted, (b) a plot of z-component of velocity along a line 1 and line 2 vs Distance (m) from moving edge dam.

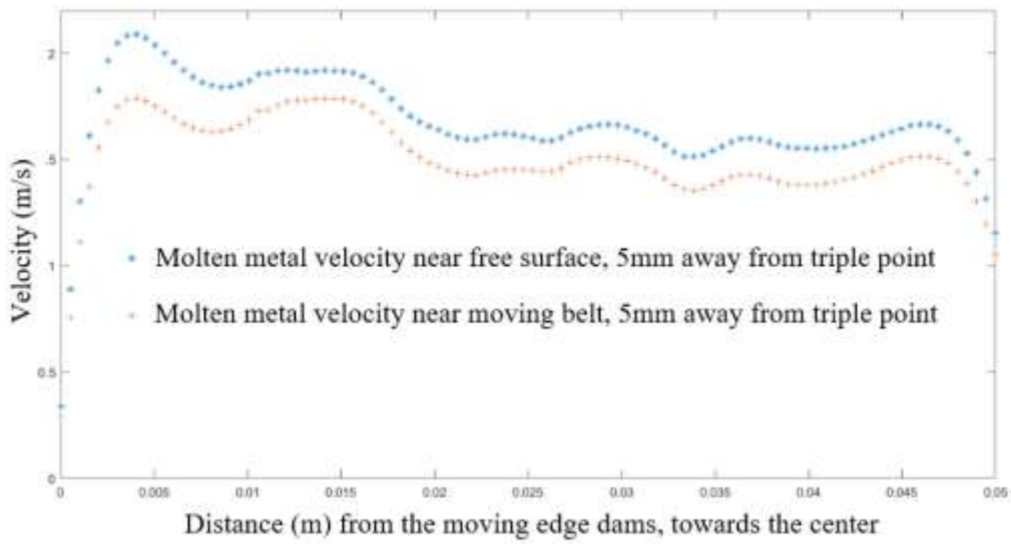

Figure 7: A plot of predicted velocity vs Distance (m) from moving edge dam.

5.11.3. Casting of AA6111 without the Use of Side Dams

The friction imposed by a slow moving belt fairly reduces the speed of the molten metal. As a result, the molten metal tends to spread outwards, as shown in Figure 3c and d. However, adjacent to the free interface, the flow of the molten metal is directed towards the center, as is evident from the z-component of velocity iso-therms presented above. Depending on the relative magnitude of these two opposite effects, the molten metal can either flow towards the center or outwards.

However, by looking into Figure 4, it can be clearly seen that the molten metal is flowing towards the center. This is very beneficial, as it eliminates the need of side dams to control the outward flow of the molten metal. The successful casting of AA6111 strip (Figure 15c), without the aid of side dams (See Figure 4), experimentally verifed these numerical modelling predictions.

5.11.4. Pressure Distribution of Molten Metal and the Generation of a Vortex Near the Triple Point

It is observed via the numerical simulation that the inclined refractory plane has the tendency to lessen, or moderate, the final impact of the molten metal on to the moving belt, by converting a part of molten metal's kinetic energy into static pressure, as presented in Figure 8b.

Additionally, the numerical simulation has predicted considerably high absolute pressure (low velocity) near the triple point (Figure 8b) due to sudden decrease in velocity of the molten metal by a slow-moving belt, thereby resulting in the part of the molten metal climbing upwards, forming a vortex as shown in Figure 9. Furthermore, the dynamic pressure i.e., $\frac{1}{2}\rho u^2$ is observed to be high adjacent to molten melt/air interface. This result is due to high velocity of the molten metal near free surface as shown in Figure 8a.

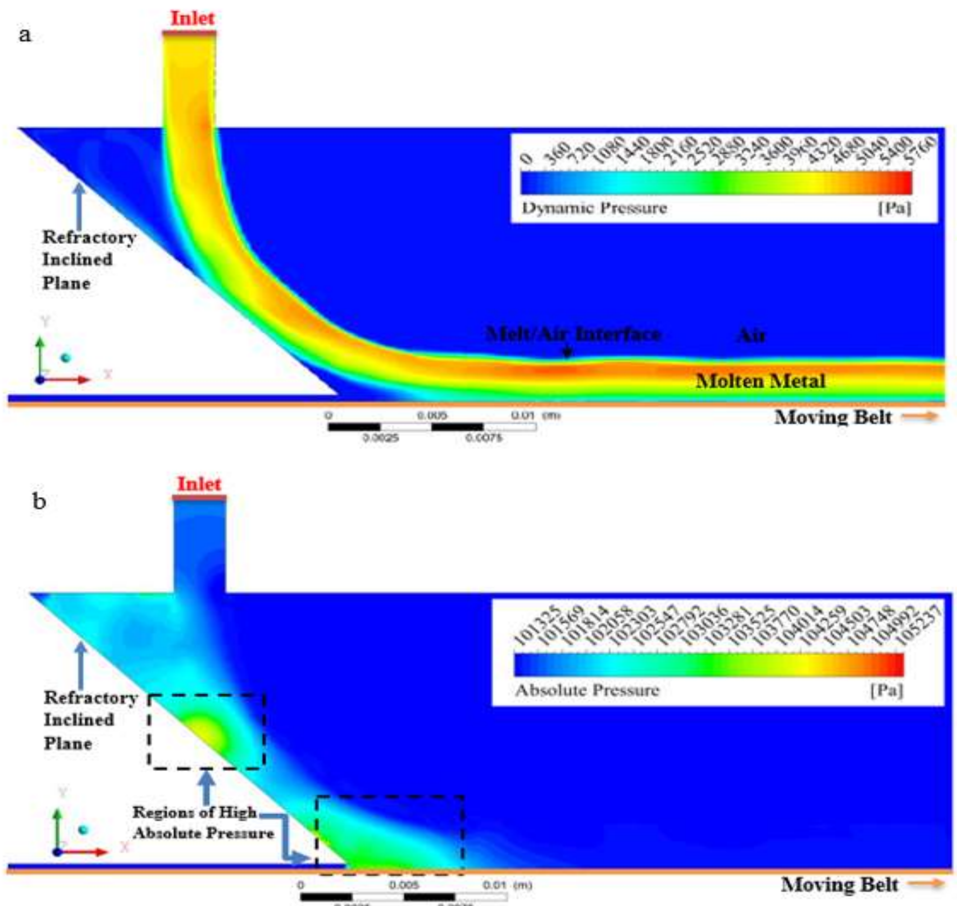

Figures 8: (a) Dynamic Pressure, $P_{dyn} = 0.5\rho\sum u_i^2$, where ρ is the density, u is the velocity, (b) Absolute pressure (103281 Pa).

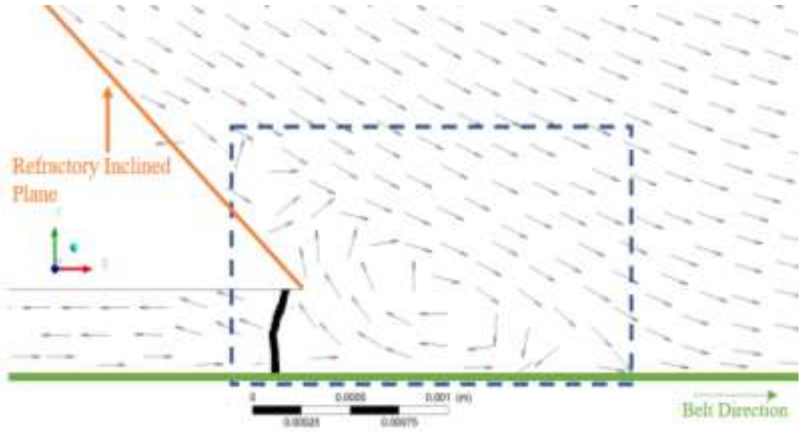

Figure 9: The swirling motion of the molten metal at the triple point after the second impingement.

5.11.5. The Temperature of the Molten Metal at the Melt/Air Interface

The hydraulic jump at the inclined refractory plane could substantially degrade the surface quality of the cast product owing to the generation of free surface waves/discontinuities [13]. As per the numerical simulation, the temperature over of the melt/air interface is above liquidus for a considerable distance as shown in Figures 10, considering perfect contact of molten metal with the moving belt. The experimental casting of AA6111 strip was in accord with predictions from the numerical simulation, in which the melt/air interface was observed to be in a liquid state for approximately the first meter of the moving belt. In this way, molten metal surface discontinuities had enough time to settled down by the damping forces generated, before solidification, as shown in Figure 15c.

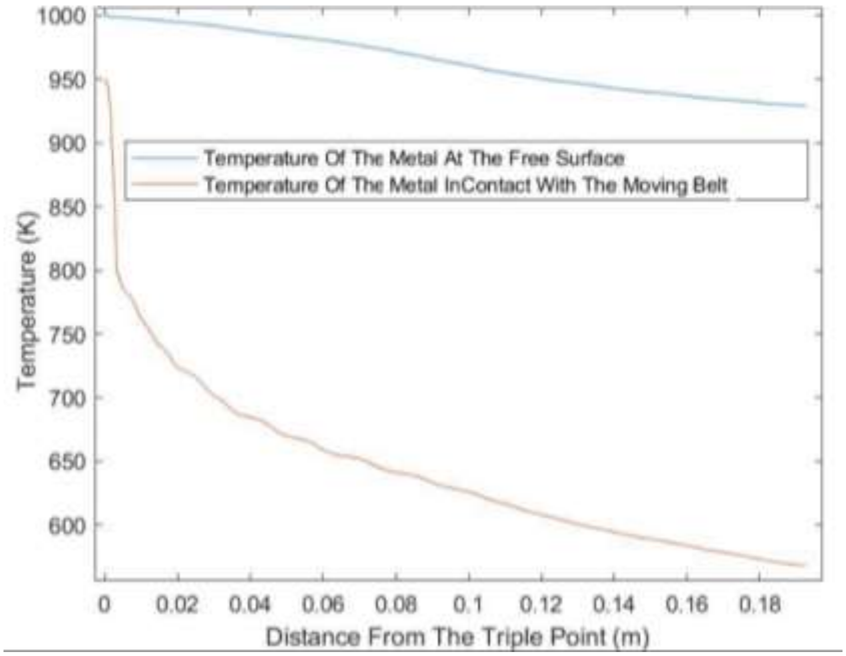

Figure 10: The predicted temperature distribution along the top and bottom faces of the strip along the casting direction.

5.11.6. Characterization of the AA6111 Alloy Cast Strip

A microstructural study has been carried out to analyze the quality of the cast strips as shown in Figure 11. The samples for optical microscopy were ground down to 1200 grid, and then electropolished/etched using 2% Perchloric acid ($HClO_4$) in alcohol. Micro images were taken using a Leica DM IRM optical microscope and a Hitachi TM3030 (Scanning Electron Microscope). The microstructure consisted of fine equi-axed grains throughout the thickness of the strips (see Figure 12). The microstructure also contains porosities at various locations within the cast strip, very similar to DC cast product. The average grain size of the strip was determined to be 46 µm. A very similar grain size i.e. 42 µm, was reported by Donghui Li for the casting of AA6111 strip via the HSBC process [4]. The surface quality of the cast strip was also found satisfactory (Figures 15c).

The inter-metallics are also observed to be distributed inside the grains, as well as at the grain boundaries of the cast microstructure, as shown in Figure 12c. X-Ray micro-analyses revealed that inter-metallics dispersed throughout the cast structure have the following stoichiometry: $Al_{17}Cu_2Mg_3Si_3$, $Al_{20}Cu_2Mg_{2.5}Si_5$, whereas the elongated inter-metallics distributed at the grain boundaries are in the category of $Al_{17}(CuMg)_2(FeMn)Si_2$, or $Al_{25}(CuMg)_{4.5}(FeMn)Si_5$ [8]. These phases are clearly observed in the Figure (12c) at higher magnification of 500X.

Figure 11: Transverse section of the cast strip.

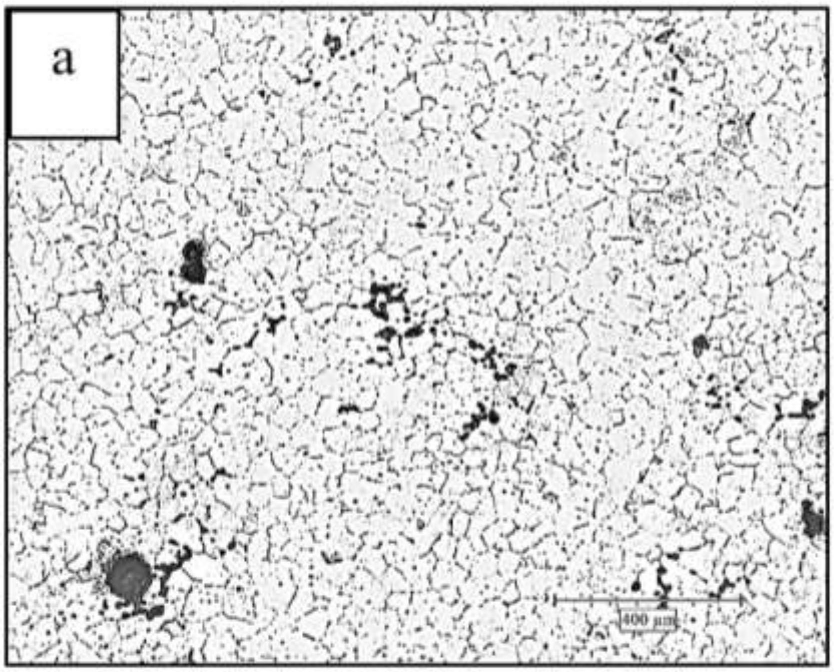

Figures 12: (a) Microstructure at the center of the AA6111 strip (50X).

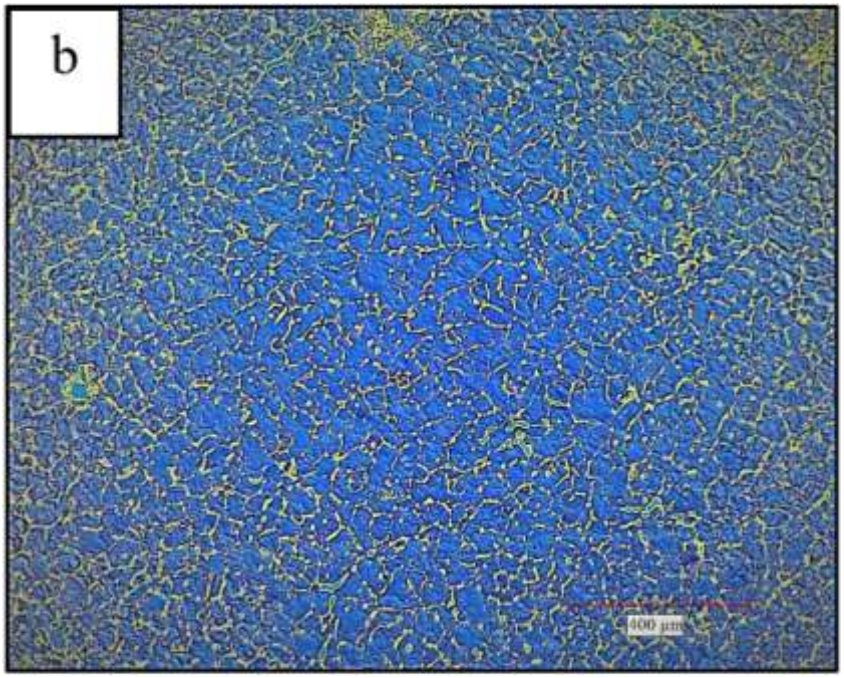

Figures 12: (b) Polarized micrograph at the center of the AA6111 strip (50 X).

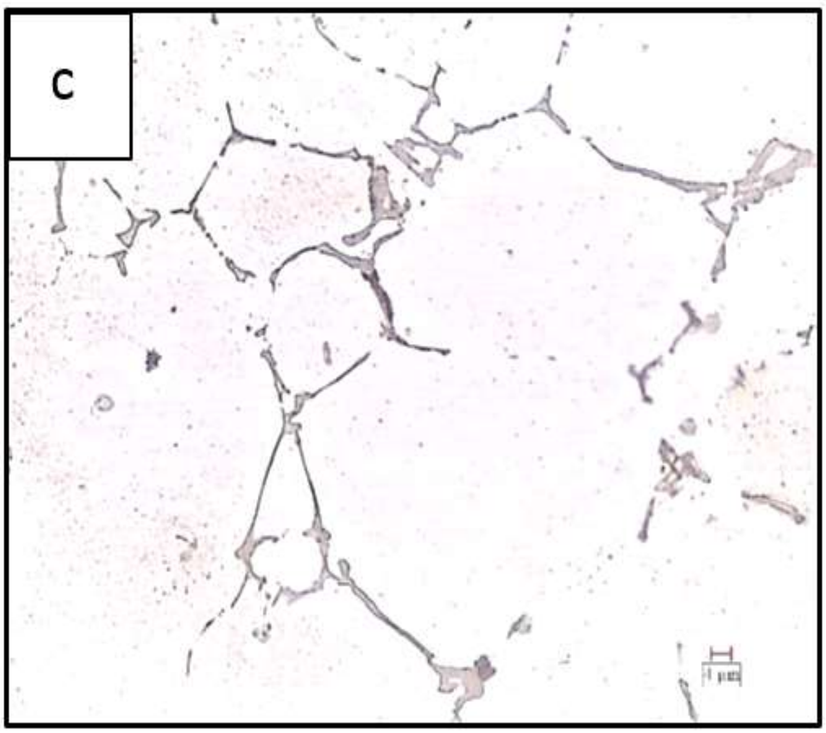

Figures 12: (c) Intermetallics observed at the grain boundaries and inside the grains (500 X).

5.11.7. Energy Dispersive Spectroscopy (EDX) Analysis of the Cast AA6111 Alloy

Energy Dispersive Spectroscopy (EDX) analysis confirmed the presence of Al, Cu, Mg, and Si, in AA6111 alloy as shown in Figure 13. Furthermore, there is negligible macro-segregation of alloying element in the cast strip, as shown in the chemical element's maps, obtained at 15KV excitation voltage. This is caused by the rapid solidification of molten AA6111 alloy in the HSBC process, which resulted in a homogenous microstructure with fine equiaxed grain. Additionally, the element maps provide us the details of the chemical nature of the secondary phases. EDX analyses revealed that inter-metallics dispersed throughout the cast structure are rich in Cu and Mg. whereas the elongated inter-metallics found at the grain boundaries are concentrated in Si, Cu and Mg.

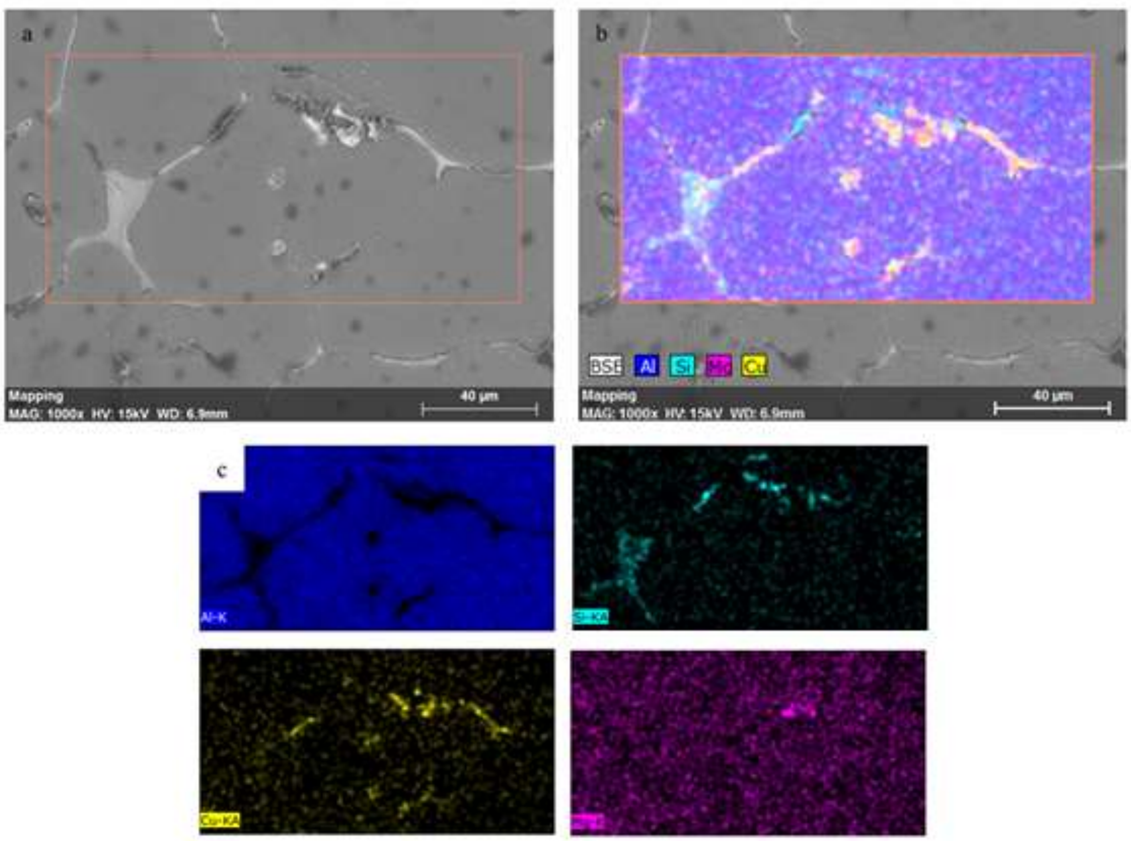

Figures 13: (a) Intermetallics distributed within grains and at grain boundaries (1000X), (b & c) Elemental maps showing the chemical content of the intermetallics.

5.11.8. Surface Roughness Measurement

The surface waviness of the top/bottom sides of the strip were determined using a Nanovea 3D profilometer. This technique works on the principle of measuring the physical wavelength of light and directly relating it to a specific height. This ensures accurate measurement of surface roughness/finish [14]. The scan length for all the measurements was 3mm whereas the scan speed was 0.1mm/s. Ten random locations were selected for surface roughness measurements. These locations were randomly selected from all over the strip. The surface profiles are almost identical to each other

The upper surface roughness lies within the 20 μm (0.02 mm) range, as shown in Figure 14a which is considerably smaller than continuous cast product roughness i.e., 0.05 mm for AA1050 and 0.45 mm for AA5182 aluminum alloy (Figure 15a and b) [15]. Additionally, pin holes/blow holes were not detected on the surface of the cast strip, unlike continuously cast products, which possessed defects on their surfaces, and require surface grinding prior to hot rolling [16].

The strip bottom surface roughness was also measured, and lay in the 10μm range. As evidenced by the results of the line scans, the bottom surface quality is much superior to the top surface. This fact is credited to the fact that the molten metal is in direct contact with the moving belt, and conforms to its shape during the solidification process. On the other hand, the top surface of the cast strip is exposed to the atmosphere and is affected by disturbances in the flows of the molten metal.

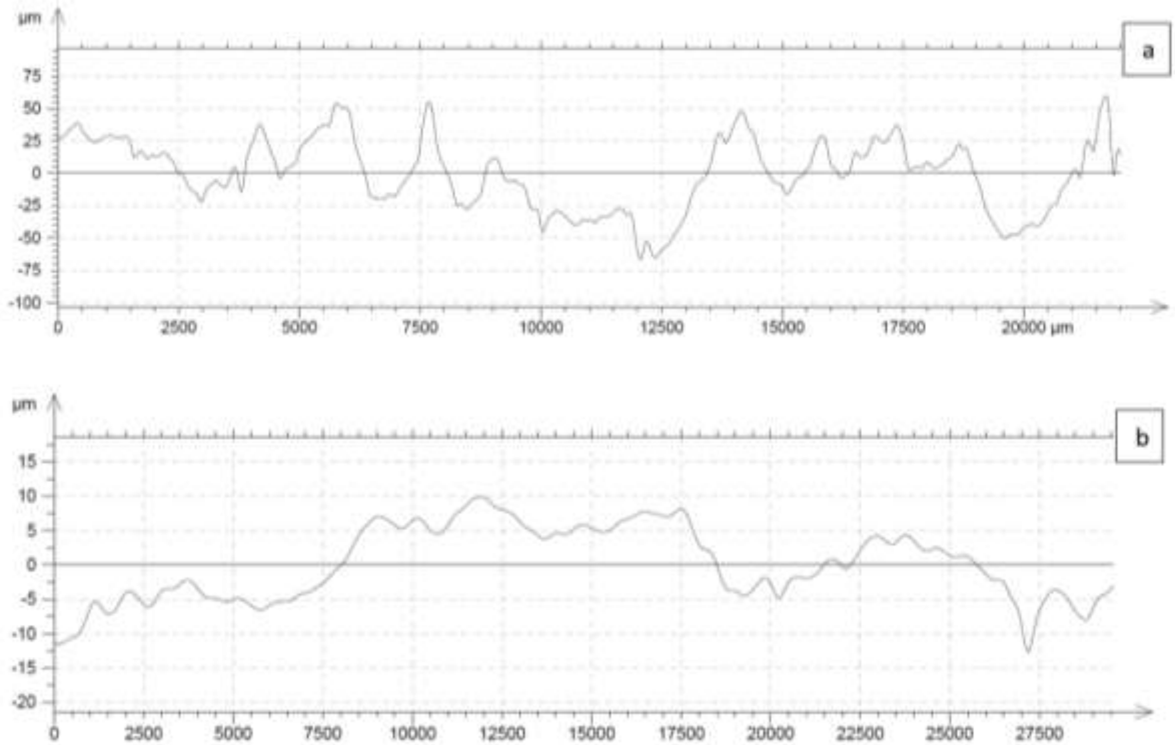

Figures 14: 3D profilometry results, a) strip top surface roughness and b) strip bottom surface roughness.

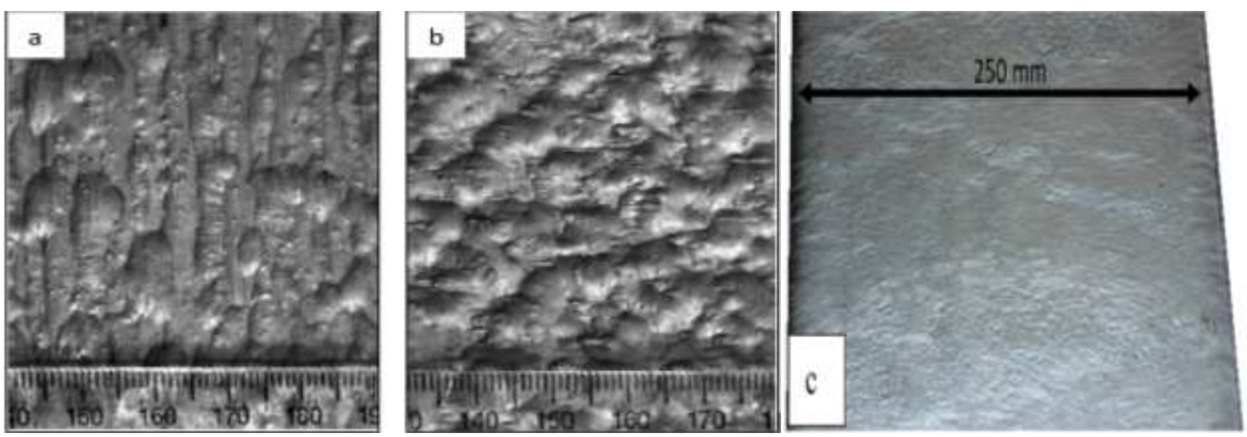

Figures 15: Strand surface morphologies of direct chill of (a) AA3004 (Al-1%Mn-1%Mg), (b) AA5182 (Al-4.5%Mg) [15], (c) HSBC surface of the AA6111 (Al-1.1% Si-1%Mg-0.45%Mn) cast strip.

5.12. Conclusions

This present paper discusses the casting conditions and analyses results on AA6111 strips, 250 mm wide and 6 mm thick, produced via the HSBC process. Computational Fluid Dynamics (CFD) analyses were performed to examine molten AA6111 flows in the HSBC process, so as to achieve uniform thickness and good surface finish of the cast strip.

The following conclusions were drawn, for the double impingement, no side dams metal feeding system.

1. Under non-isokinetic feeding, the surface quality of the cast AA6111 alloy strip is not compromised by the generation of surface disturbances.
2. The AA6111 alloy molten stream shrinks from its two edges. This build up of the mass around the edges, or corners, eventually reach a higher terminal velocity, vs the centre flow region. A net inward flow of the molten metal resulted, which filled in the center shrinkage depressions.
3. It was also determined that the inclined refractory plane of the double impingement metal feeding system has the tendency to lessen, or moderate, the final impact of molten metal with the moving belt compared vs a single impingement metal feeding system, where the molten metal encountered an abrupt change in direction with the presence of a moving belt.
4. The swirling flow of the molten metal in the immediate vicinity of the triple point is due to the sudden vertical deceleration of the molten metal caused by the horizontally moving belt. However, the meniscus at the triple point was still observed to be stable and non-fluctuating.
5. The temperature of the molten metal within the immediate vicinity of the free surface, along the entire length of the simulation domain, remains above the liquidus temperature. As a result, any molten metal discontinuities (waves) formed at the free molten metal/air interface thus had enough time to damped prior to final solidification of the strip.

5.13. Acknowledgments

The authors would like to acknowledge the financial support received from the Natural Sciences and Engineering Research Council of Canada (NSERC), and the International Advisory Board of supporting companies of the McGill Metals Processing Centre (MMPC), in carrying out this research. The authors would also like to acknowledge the support received from ANSYS Inc. for software licensing to facilitate this research.

5.14. References

1. M. Celikin, D.H. Li, M. Isac and R.I.L. Guthrie: Light Metals 2013., (2016),1037.
2. M. Xu, M. Isac, R.I.L. Guthrie: Metallurgical and Materials Transactions B., (2018), 1003.
3. S. Ge, S. Chang, T. Wang: Metal and Material Transaction B., 47(2016), 1893.
4. R.I.L. Guthrie and M. Isac: Steel Research International., 85(2014), 1291.
5. G. Sa, M. Isac and R. I. L. Guthrie: ISIJ Int., 52(2013), 2109.
6. K.H. Spitzer, F. Ruppel and R. Viscorova: Steel Research International., 74(2016), 724.
7. J. Wans, C. Geerkens, H. Cremers, U. Grethe, P. Juchmann and R.S. Jurgensen: International part of the ABM week, (2015), 111.
8. D. Li, S.G. Shabestari, M. Isac, R.I.L. Guthrie :TMS., (2006), 851.
9. P. Mukhopadhyay, ISRN Metallurgy., 2012.
10. FLUENT 14.5 Manual, ANSYS Inc., 10 Cavendish Court, Lebanon, NH, USA.
11. G. Sa, K. Chattopadhyay and R.I.L. Guthrie: 5th International Congress on the Science and Technology of Steelmaking, (2012).
12. C.W. Hirt, B.D. Nichols, Volume of Fluid (VOF) Method for the Dynamics of Free Boundaries, Journal of Computational Physics., 39(1981), 201.
13. U. Niaz, M. Isac, R.I.L. Gurthrie: Material Science and Technology., (2018), 945.
14. Surface roughness determination using 3D Nanovea profilometer, Available https://nanovea.com/profilometry-roughness-finish.
15. J. Sengupta, B.G. Thomas, M.A. Wells: Metallurgical and Materials Transactions A., 36(2005), 187.
16. A.B. Sychkov, M.A. Zhigarev, A.V. Perchatkin, S.N. Mazanov, V.S. Zenin: Metallurgist., 50(2006), 83.

Chapter 6

6.0. The Production of Thin Strips of a TRIP-TWIP Steel (Fe-21%Mn-2.5%Al-2.8%Si-0.08 %C wt.%) Using an HSBC Simulator

The previous chapter discusses the casting of AA6111 aluminum alloy strip via a horizontal single belt pilot caster. It was determined that the molten metal tends to flow inward towards the center of the strip thereby helping to fill any center shrinkage cavity defect. Additionally, the molten metal level inside the tundish must be sufficient enough to trigger a strong inward flow; otherwise center shrinkage cavity defect will occur.

In this chapter, the flow of molten Fe-21%Mn-2.5%Al-2.8%Si-0.08 %C wt.% steel in the HSBC process is modeled. The velocity of the molten metal at the nozzle slot outlet and that of the belt is fixed at 0.8 m/s, unlike in the previous chapter in which the simulations were performed under non-isokinetic feeding conditions i.e. the speed of the belt and molten metal velocity at nozzle slot outlet was 0.3 m/s and 2m/s respectively. Additionally, the phenomenon of the molten metal/air interface fluctuations over an inclined refractory plane is also illustrated, which increases when the inclination angle of the refractory plane, is decreased. It is important to minimize these fluctuations, as they travel further downstream, thereby affecting the surface quality of the cast strip. Additionally, the oscillatory flow of molten metal, upstream of the inclined refractory plane can significantly reduce the bulk quality of the cast strip, and may lead to air entrapment within the strip. These concepts are explained in light of the CFD numerical modeling results. The Stacking Fault Energy (SFE) of the alloy is determined using the Olson-Cohen modeling approach, whereas FactSage software was used to predict the liquidus and solidus temperatures, as well as the types and amounts of the solid phases present, under the relevant, rapid (Scheil)-cooling conditions. Mechanical properties of the hot deformed and heat-treated strip were evaluated via the Shear Punch Test (SPT) technique, while surface roughness was measured using the Nanovea 3D optical profilometer.

The research presented below made the object of the publication entitled: ”Horizontal Single Belt Casting (HSBC) of Thin Strips of an Advanced High Strength Steel (Fe-21%Mn-2.5%Al-

2.8%Si-0.08 %C wt. %)", Usman Niaz, Mihaiela M. Isac & Roderick I.L. Guthrie submitted to the Journal of "Steel Research International", presently under peer review.

6.1. Introduction

The Horizontal Single Belt Casting (HSBC) of strips is a Near-Net-Shape-Casting (NNSC), continuous process. It appears to be the most obvious way of producing good quality ferrous/non-ferrous strips [1-4]. Apart from its low energy requirements and promising productivity, this "green" technology is capable of producing near net shape metallic products which have a homogenous microstructure, and a small final grain size [1-4]. Micro-segregation is negligible compared to that encountered in typical commercial slab casting processes, given the higher cooling rates of up to 500°K/second [5] achieved in the HSBC process.

The basic process, for both pilot caster and small-scale HSBC simulator, is shown in Figures 1 and 2, respectively. There, molten metal passes through a slot nozzle from a low-head metal delivery system, and is further accelerated by gravity, and delivered onto a moving, water-cooled belt or substrate, onto which it solidifies [3]. The material produced through the HSBC process can then be processed downstream, with in-line hot rolling, and cold rolling [2,3]. As such, the HSBC process features a compact NNSC (Near Net Shape Casting) design, which provides optimum economic production capabilities for both ferrous, and non-ferrous, metallic sheet products [2]. The length of a belt, its speed of casting, plus the slot width, determine caster productivity and product dimensions [4].

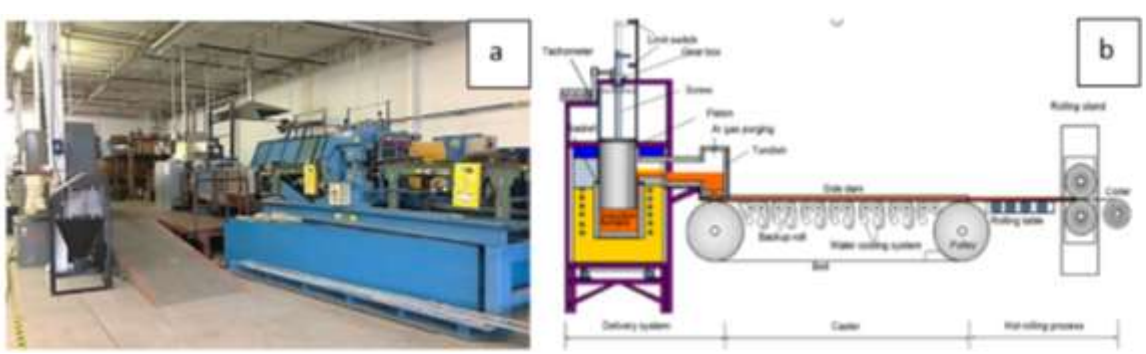

Figure 1: (a) Photograph of the HSBC pilot-scale caster located at MetSim Inc's, High Temperature Laboratory, Montreal, Canada, and (b) A schematic of an HSBC pilot scale caster [2, 4].

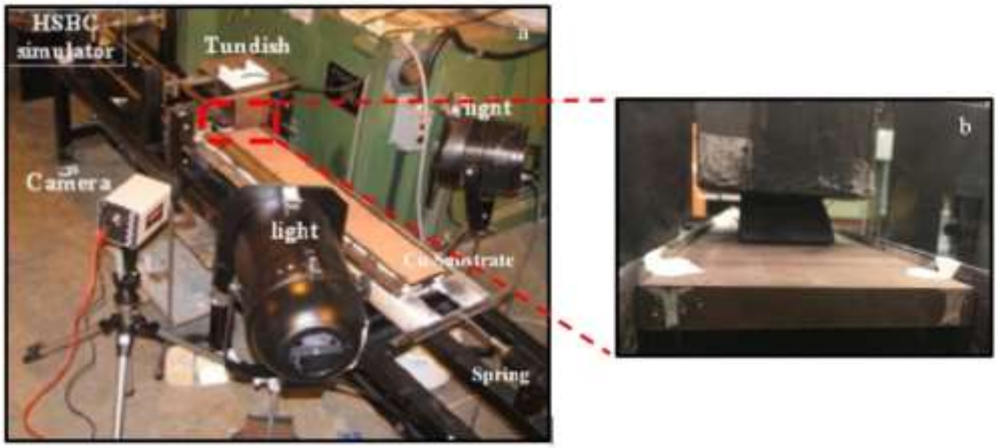

Figure 2: (a) HSBC simulator (b) Double impingement feeding system for it [1, 3].

6.2. A Brief Review of the Previous Studies & Objectives of the Present Research

Research previously conducted by other members of our research group [2, 6], showed how the molten metal/air interface fluctuates over an inclined refractory plane (a component of a double impingement feeding system). According to them, these vibrations/fluctuations are inherent in HSBC process and could considerably affect the surface quality of the cast strip. They suggested that the success of the HSBC process depend on how effectively molten metal/air interface fluctuations over an inclined refractory plane can be controlled, as these fluctuations could travel downstream and affect the upper surface quality of the cast product. Furthermore, they also explained how instability of molten metal flows, in the HSBC process, could lead to the phenomenon of air entrapment within the forming strip. In their studies, AA6111 metal was selected for HSBC casting trials, and they standardized the angle of inclination of the refractory plane at 45° [2, 6].

The present research study has the following objectives;

1. To investigate possible reasons for the instability of the molten metal stream after its interaction with the inclined refractory plane and determine ways to minimize this instability.
2. The possible reasons for the generation of waves on the free surface of the molten metal due to the phenomenon of a hydraulic jump.

6.3. Experimental Procedure

A AHSS containing Fe-21%Mn-2.5%Al-2.8%Si-0.08%C (wt.%) was produced by first melting plain carbon steel in a pre-heated induction furnace, under a protective argon atmosphere, followed by the addition of Fe-Mn, Fe-Si, and Mn-Al alloy additions. Good agitation was ensured, so as to completely dissolve/mix the alloy additives into the melted plain carbon steel. The steel was then poured into the HSBC simulator tundish, and subsequently cast into a thin strip. Afterwards, the specimens were sectioned from the as-cast, as well as heat treated, strip, they were prepared for metallographic analysis, using grinding and polishing operations. Polishing was performed using 1μm diamond paste contained in an alcohol-based lubricating fluid. This was followed by etching in Nital (5wt% Nitric acid in alcohol) solution in order to reveal the microstructure.

6.4. Details of the Mathematical Modeling & Solution Procedures

A two-dimensional, transient state, turbulent flow was modeled using ANSYS FLUENT 14.5 software. This code is based on the Finite Volume Method (FVM). The volume of the Fluid (VOF) multiphase model was applied to a fixed Eulerian mesh, to solve a single set of the momentum equations. In this way, the volume fraction of each fluid ($\alpha_{metal}, \alpha_{air}$) in all computational cells could be determined, and the melt-air interface tracked [7]. The VOF method solves a continuity equation of the following form:

$$\frac{\partial}{\partial t}\left(\alpha_q \rho_q\right) + \nabla\left(\alpha_q \rho_q \dot{u}_q\right) = S_{\alpha q} + \left(\dot{m}_{pq} - \dot{m}_{qp}\right) \tag{1}$$

where $\alpha_{metal} + \alpha_{air} = 1$. Here ρ represents density, t is the time, α is the volume fraction, $\bar{u}$ is the mean velocity, whilst subscript q represents the phase (melt or air), $\dot{m}_{pq}$ is the mass transfer from phase q to phase p and vice versa for $\dot{m}_{qp}$. Both terms are zero here, since molten metal and air are immiscible, insoluble and non-interpenetrating. Also, the source term, here designated as $S_{\alpha q}$ is zero, since there is no creation or destruction of any phase.

The relevant momentum equation is;

$$\frac{\partial(\rho\bar{u})}{\partial t} + \nabla.(\rho\bar{u}\bar{u}) = -\nabla p + \nabla.[\mu(\nabla\bar{u} + \nabla\bar{u}^T)] + \rho\bar{g} + \bar{F}_\sigma \tag{2}$$

where p represents the static pressure, μ is the dynamic viscosity, $\overline{g}$ is acceleration due to gravity and $\overline{F}_\sigma$ is the surface tension force. This momentum equation depends on the volume fractions of the phases in each control volume, through the properties ρ and μ evaluated by the following two equations;

$$\rho = \alpha_{melt}\,\rho_{melt} + \alpha_{air}\rho_{air},\ \ \mu = \alpha_{melt}\mu_{melt} + \ \alpha_{air}\mu_{air} \tag{3}$$

where the primary and secondary phases for this study are air, and metal, respectively. An explicit time marching scheme was used to discretize and solve the transient VOF equations. The geometric reconstruction scheme (GRS) was selected to reconstruct the interface between the melt and air, using the Piecewise Linear Interphase Method. GRS assumes a linear slope of the fluids interface within each computational cell and uses this linear slope to evaluate the advection of the fluid through the cell phases [8].

For turbulence modeling, an additional single set of transport equations also needs to be solved. Turbulence variables are shared by the phases throughout the computational domain. In this study, the 2D turbulent molten metal flow is modeled using the SST k-w turbulence model. Details regarding turbulence modeling are not given here but can be found in the literature [8].

Also, surface tension effects, along the melt-air interface, was studied by incorporating the continuum surface force (CSF) model. The CSF model adds a source term in the momentum equations which can be calculated as per the following equation [8].

$$\vec{F}_\alpha = \sigma k \vec{n} \tag{4}$$

where σ is the surface tension coefficient, k is the free surface curvature described in terms of the divergence of the unit normal $\hat{n}$, mathematically represented as $k = -\nabla . \hat{n} = -\nabla\left(\frac{\nabla\alpha_q}{|\nabla\alpha_q|}\right)$ and $\vec{n}$ is the interface normal vector defined as the gradient of αq, the volume fraction of the qth phase i.e. $\vec{n} = \nabla\alpha_q$, $\hat{n} = \frac{n}{|n|} = \frac{\nabla\alpha_q}{|\nabla\alpha_q|}$.

The Pressure-Implicit with Splitting of Operators (PISO) algorithm was used for coupling pressure and velocity in the governing equations. More details can be found in the available literature [8]. The advection term was discretized using a 2nd order upwind scheme over the entire simulation domain as shown in Figure 3, whereas the diffusion term was approximated using the central differencing scheme. To stabilize the iterative operations during the simultaneous solution of all the PDE's, under-relaxation factors of 0.7 for the velocity, and 0.3 for the pressure, were used. The solution process was re-iterated until the residual relative errors on continuity, momentum, and turbulence governing equations were reduced to $1\text{x}10^{-7}$. Different grids were tested, until mesh-independent results were achieved. Finally, a 688,656 computational grids were identified as the most accurate/dense, and least computationally intensive, number of grid points needed for obtaining the desired results. The molten metal was treated as an incompressible, Newtonian liquid, and all the physical properties were assumed to be constant. The operating parameters and some of the assumptions of the numerical model are presented in Tables 1 & 2.

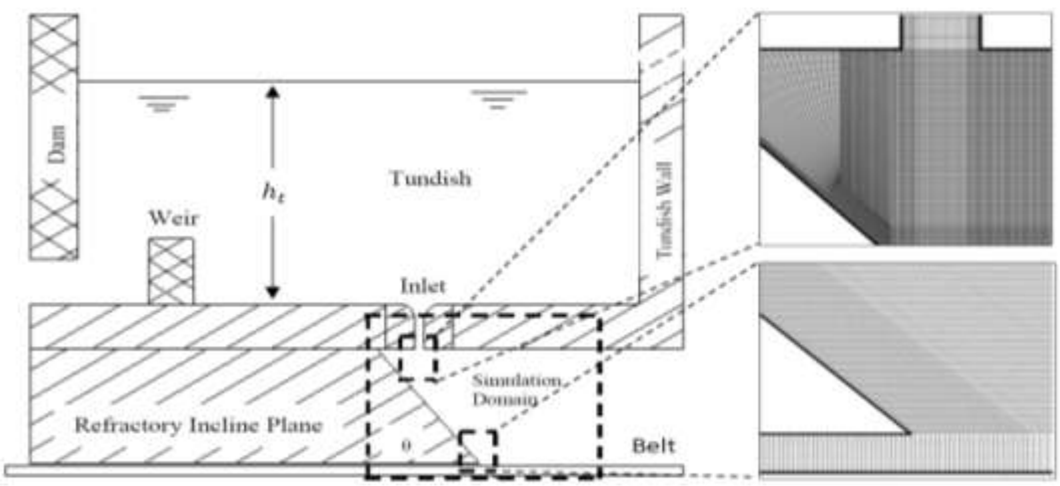

Figure 3: Simulation domain and structural mesh at the nozzle outlet and triple point.

Table 1: Physical Properties of the Phases modelled.

Operating Parameters/Assumptions	**Value**
Slot Nozzle Thickness.	3 mm
Inlet Velocity.	0.8 m/s
Surface Tension of the Melt in Air.	1.5 N/m [9]
Copper Substrate Longitudinal speed.	0.8 m/s
Turbulence Model.	SST k-ω
Contact Angle between melt, and sand-blasted, copper substrate.	105° [3]
Contact Angle between melt and alumina refractory	135° [3]
Gap between stationary inclined refractory plane and moving belt.	0.4 mm

Table 2: Operating Parameters and Assumptions made in the model [3, 9].

Property	TWIP Steel	Air	Substrate (Pure Cu)
Density, $\rho, (\frac{\mathrm{kg}}{\mathrm{m}^3})$	6950	1.225	8978
Specific Heat Capacity, $C_p, \left(\frac{\mathrm{J}}{\mathrm{kg\ K}}\right)$	720	1006	381
Thermal Conductivity, $k, \left(\frac{\mathrm{W}}{\mathrm{m\ K}}\right)$	30.5	0.0242	387.6
Viscosity, $\mu, \left(\frac{\mathrm{kg}}{\mathrm{m\ s}}\right)$	0.0063	1.75×10^{-5}	--
Molecular Weight, $\left(\frac{\mathrm{kg}}{\mathrm{kmol}}\right)$	55.8	28.97	63.55

Simulations were carried out, keeping the velocity of the molten metal constant at 0.8 m/s at the nozzle slot outlet, while the belt substrate was fixed at 0.8m/s, in order to approach iso-kinetic feeding (a condition in which the belt speed closely approaches molten metal velocities). Heat transfer to the cooling belt was not considered in this research study, since only the first 10 cm of the moving belt was simulated. During this first contact with the belt, any solidified metal layer formed would be extremely thin (~ 20 micron), and therefore not expected to influence the initial flows of liquid metal over it [2, 3]. Numerical predictions were validated against experimental findings. The results are presented in the following section.

6.5. Results & Discussion

6.5.1. Fluctuations of the Molten Metal over an Inclined Refractory plane leading to Wavy Molten Metal/Air Interface, and Air Entrainment in the Forming Strip

As described above, the balance of forces acting on the melt in the HSBC process are confined to gravity and friction. It was determined that at a sufficiently low angle of inclination i.e. 30°, the molten metal has the tendency to climb/flow up, the inclined refractory slope, but later gravity forces draw it back (down) to merge with the molten metal, flowing downwards. In doing so, the molten metal free stream becomes unstable and distorted, and was found to oscillate over a distance of 3.5mm, as shown in Figure 4a. Due to these fluctuations, the entire flow of the molten metal over the inclined refractory plane become unstable and non-uniform.

However, at a sufficiently high angle ($\geq$45°), the downward force of gravity prevents molten metal from climbing/ascending up much of the inclined refractory plane. As a result, the molten metal free stream is confined to oscillating over a shorter length i.e. 2mm for 45° as shown in Figure 4b. Increasing the inclination up to 60° further reduces the instability of the falling free stream which significantly reduces the molten metal/air interface fluctuations, further downstream, as represented in Figure 4c. Additionally, increasing the molten metal free stream stability results in avoiding air entrapment in forming strip, as discussed by coworkers for the casting of molten AA6111 via the HSBC process [2, 6]. A similar behaviour was observed for molten AHSS flowing over a 45° inclined refractory plane, as represented in Figure 5.

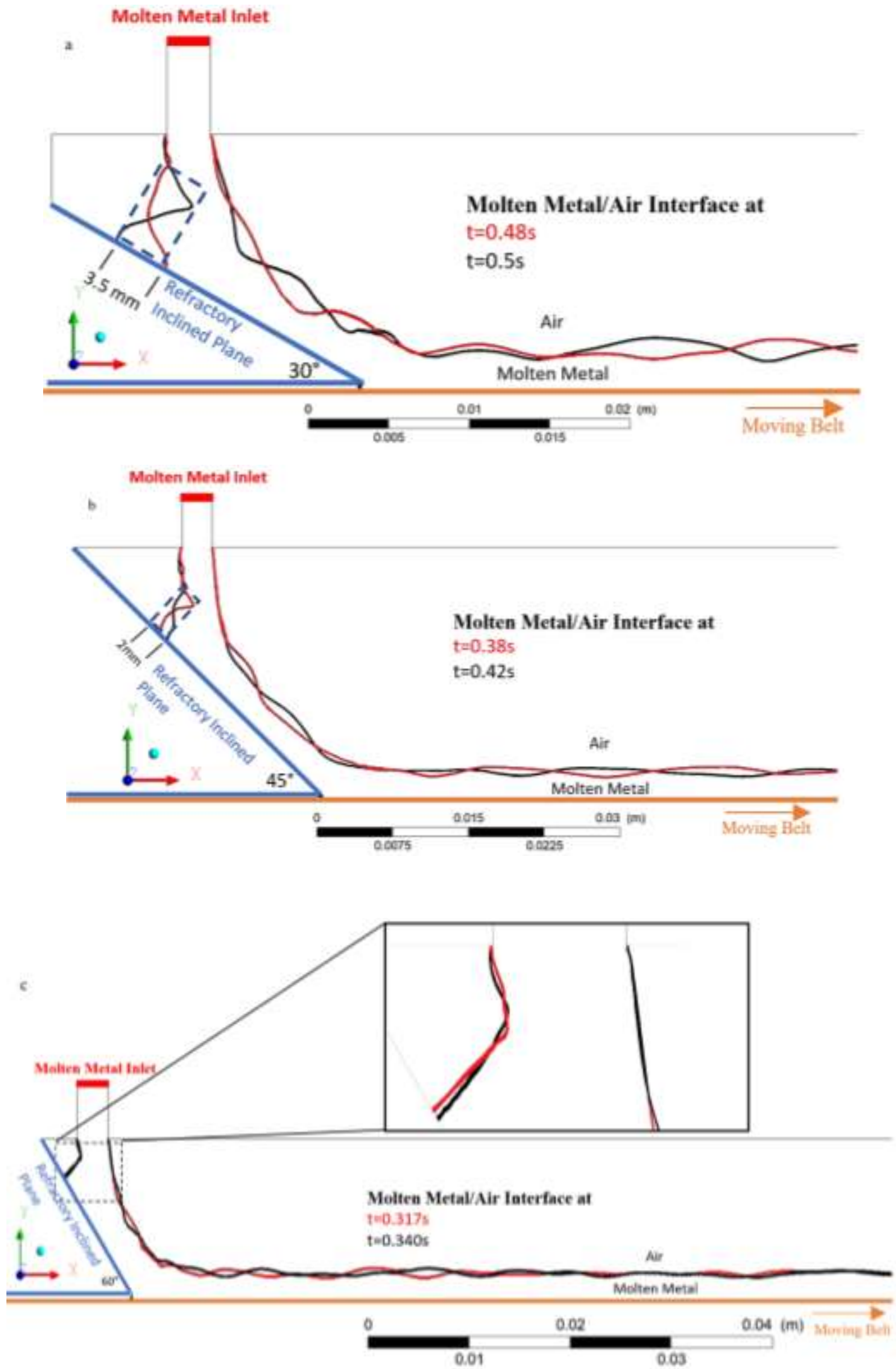

Figure 4: Molten metal jump in the molten metal down an inclined refractory plane, (a) 30°, (b) 45°, (c) 60°. Instabilities in the flow of the molten metal flowing over inclined refractory plane.

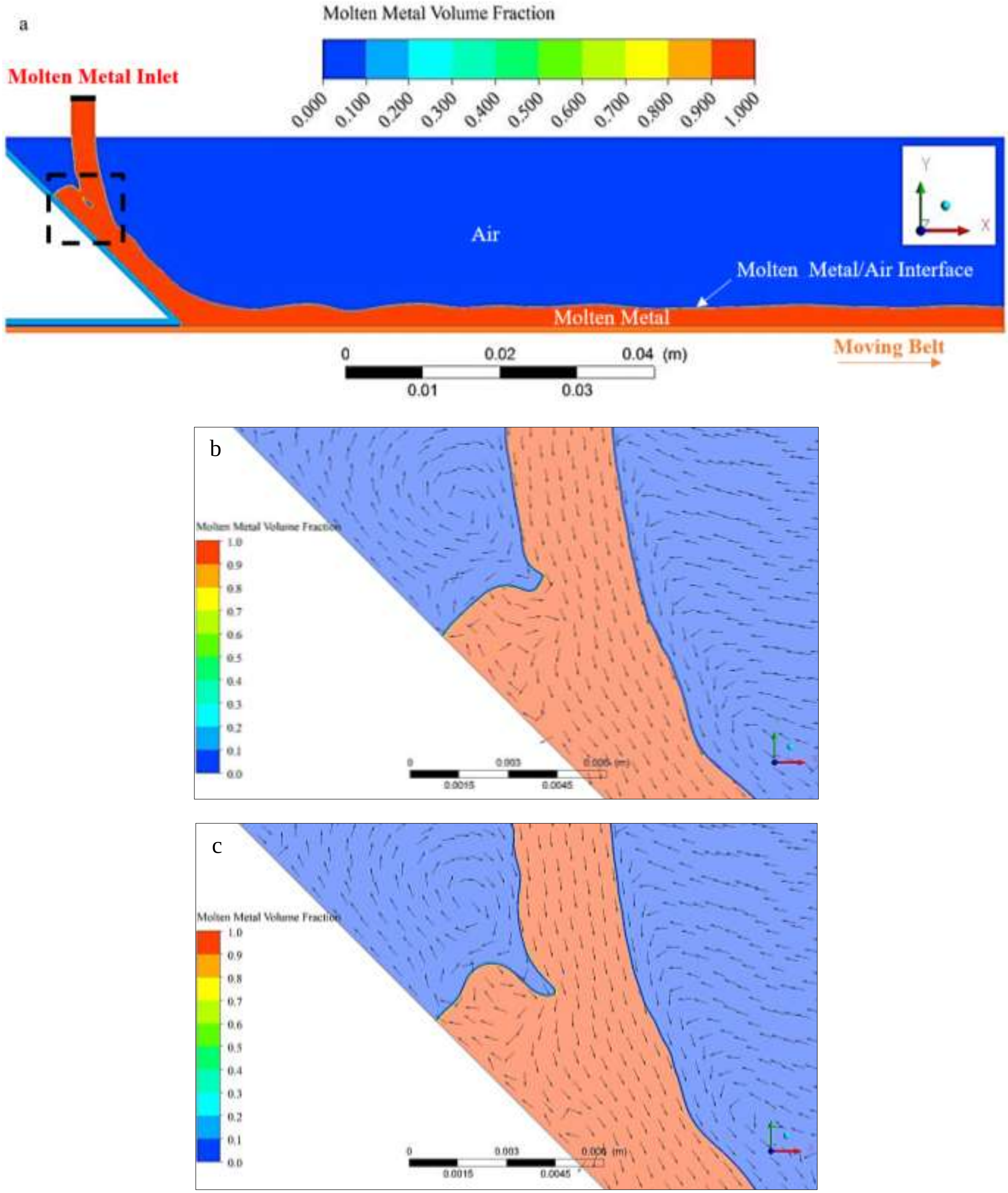
a
Molten Metal Volume Fraction
0.000
0.100
0.200
0.300
0.400
0.500
0.600
0.700
0.800
0.900
1.000
Molten Metal Inlet
Air
Molten Metal/Air Interface
Molten Metal
Moving Belt
0
0.02
0.04 (m)
0.01
0.03
b
Molten Metal Volume Fraction
c
Molten Metal Volume Fraction

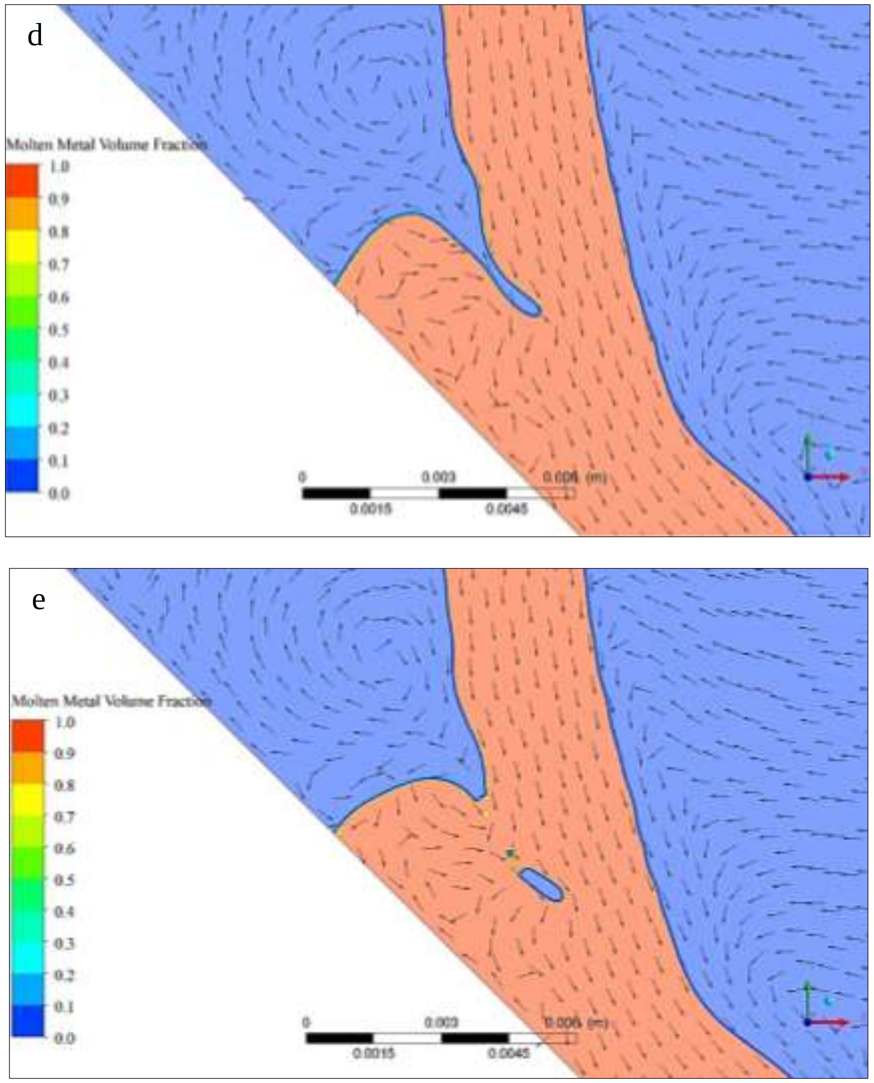

Figure 5: (a) Predicted fluctuations at the melt/air interface can give rise to air entrapment, (b, c d, e, f) Showing different stages of molten metal/air interface fluctuation leading to air entrapment.

Additionally, looking upstream into the plane of an inclined refractory plane, a swirling/rotational flow of the molten metal was observed, as represented in Figure 6a. The possible reasons for this rotational motion of the molten metal are still not very clear. This will be analyzed in our future publications, as it could also introduce instabilities in the flow.

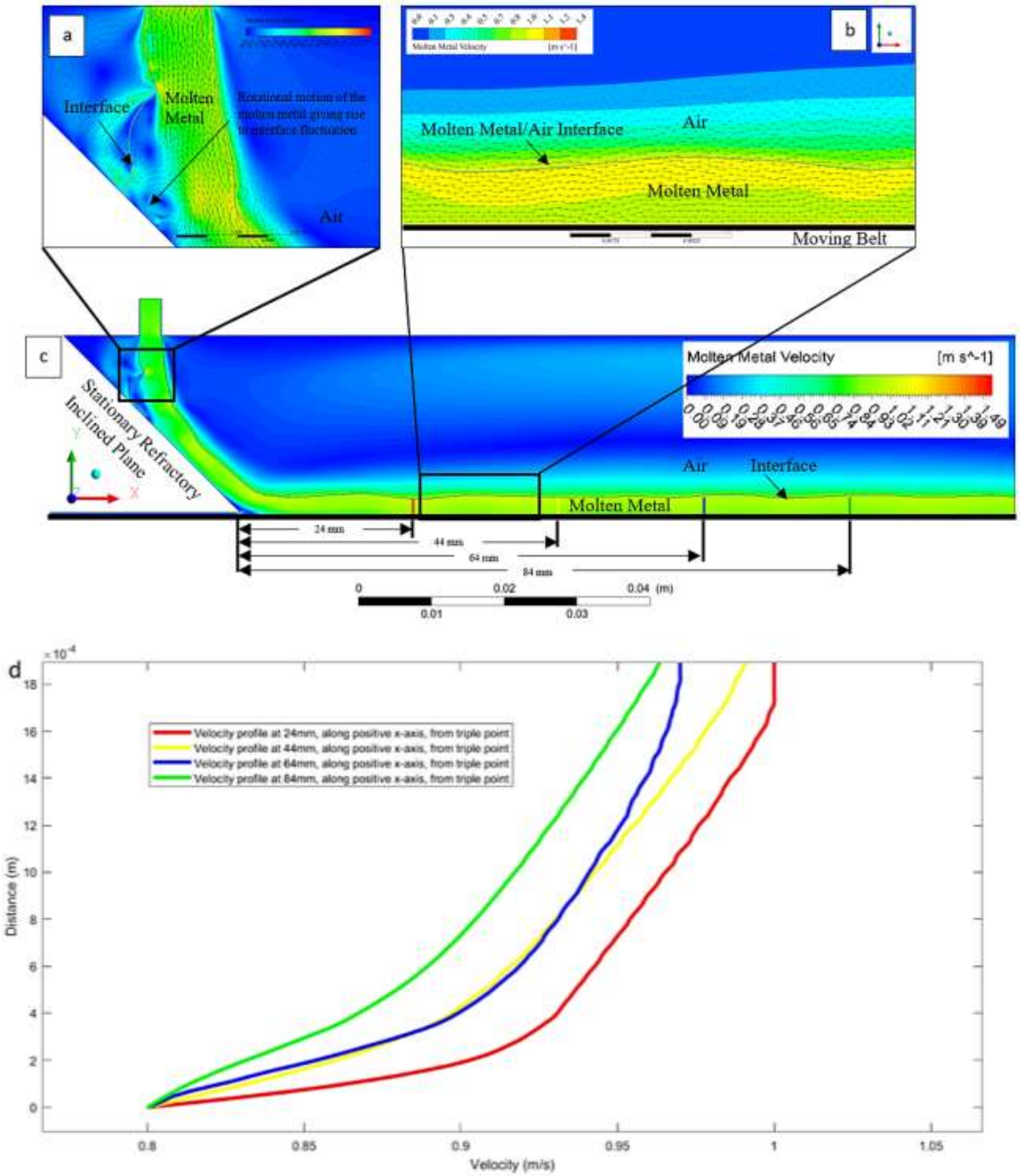

Figure 6: (a) Rotational motion of the molten metal giving rise to interface fluctuations (b) Velocity of molten metal adjacent to molten metal/air interface (c) Variation in velocity over the thickness of the strip, (d) The velocity profile at different locations over moving belt.

Another important point to consider is the phenomenon of a hydraulic jump of the molten metal over an inclined refractory plane, as this could also induce instabilities in the flow as explained below.

6.5.2. Fluctuations of the Molten Metal over Inclined Refractory Plane Leading to Hydraulic Jump

Literature is available on the hydraulic jump of water that forms, when flowing over an inclined plane. This suggests that for a fixed Froude number, the hydraulic jump increases with an increase in the inclination of the refractory plane. Also, by increasing the inlet Froude number $\left(\mathrm{Fr} = \frac{\mathrm{V}^2}{\mathrm{gh}}\right)$, for a fixed angle of inclination, the hydraulic jump increases [10-18]. Similar behaviour can be expected for molten metal, since the kinematic viscosity of molten steel and water ensure similarity in their fluid flow behavior, provided it meets other similarity criteria [19]. Therefore, it can be concluded that the two most important parameters that could lead to the generation of molten metal surface waves, are the molten metal's velocity at the nozzle slot outlet, and the inclination angle of the refractory plane. In this research study, only the inclination of the refractory plane was varied, and numerical simulations were carried to analyse that.

6.5.3. General Mechanism for the Formation of Free Surface Waves in HSBC Process Employing Double Impingnment Feeding System

The phenomenon of hydraulic jump is explained for 45° inclined refractory plane, however similar analysis can be concluded for 30° and 60° planes also. It is determined that when molten metal exits the nozzle slot, it accelerates from 0.8 m/s to 0.93 m/s down an inclined refractory plane. This acceleration is due to the y-component of the gravity force acting on the fluid body. However, further downstream, it slows down to 0.7m/s (due to the friction of the inclined surface/plane), through a set of shock wave, termed hydraulic jump as shown in Figure 7a, Figure 7b, and Figure 7c. This jump results in the formation of waves running down an inclined refractory slope, and further travelling downwards along the entire length of the strip, as shown in the Figure 7d.

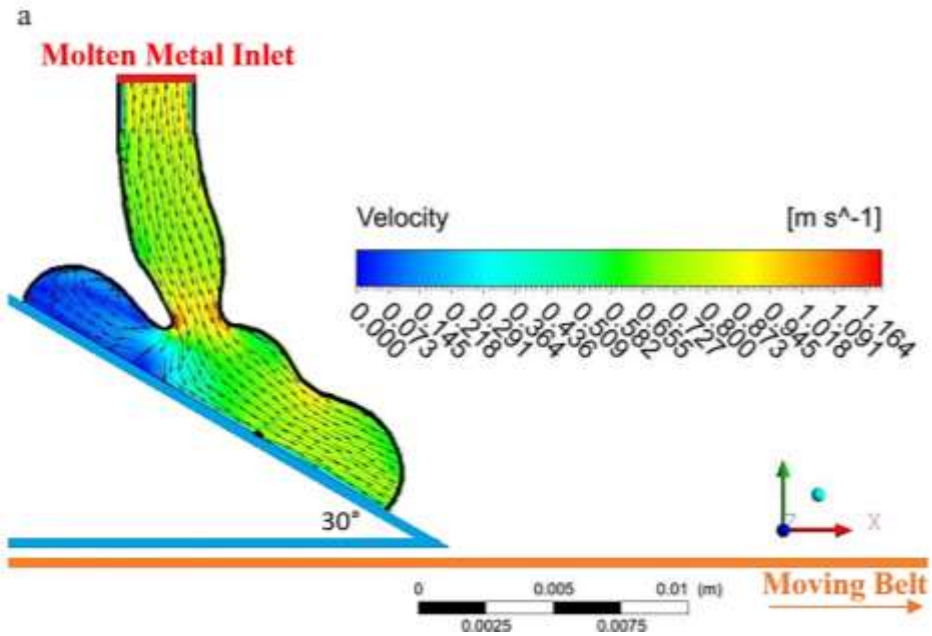
a
Molten Metal Inlet
Velocity
[m s^-1]
0.000 0.073 0.145 0.218 0.291 0.364 0.436 0.509 0.582 0.655 0.727 0.800 0.873 0.945 1.018 1.091 1.164
30°
X
0
0.005
0.01 (m)
0.0025
0.0075
Moving Belt

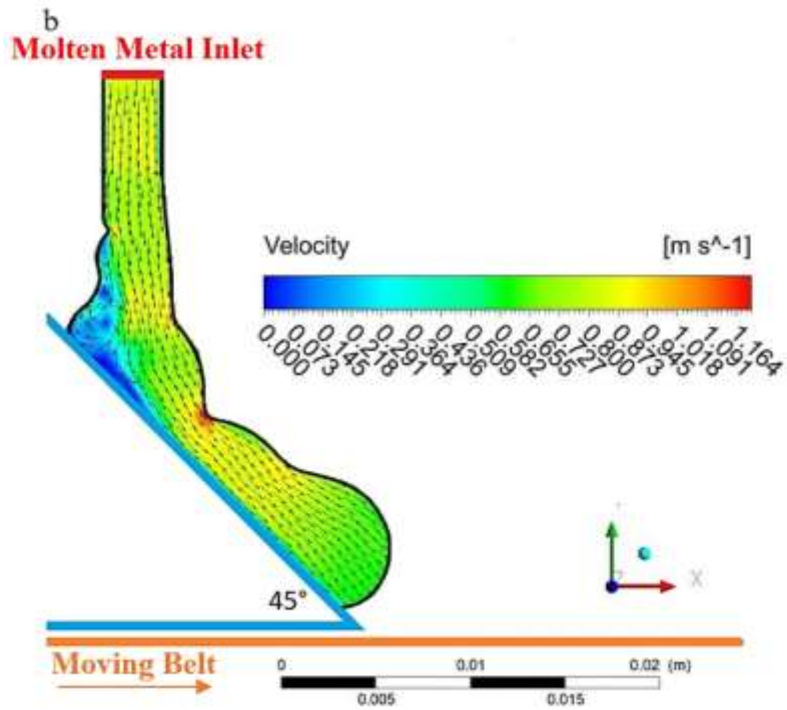
b
Molten Metal Inlet
Velocity
[m s^-1]
0.000 0.073 0.145 0.218 0.291 0.364 0.436 0.509 0.582 0.655 0.727 0.800 0.873 0.945 1.018 1.091 1.164
45°
X
Moving Belt
0
0.01
0.02 (m)
0.005
0.015

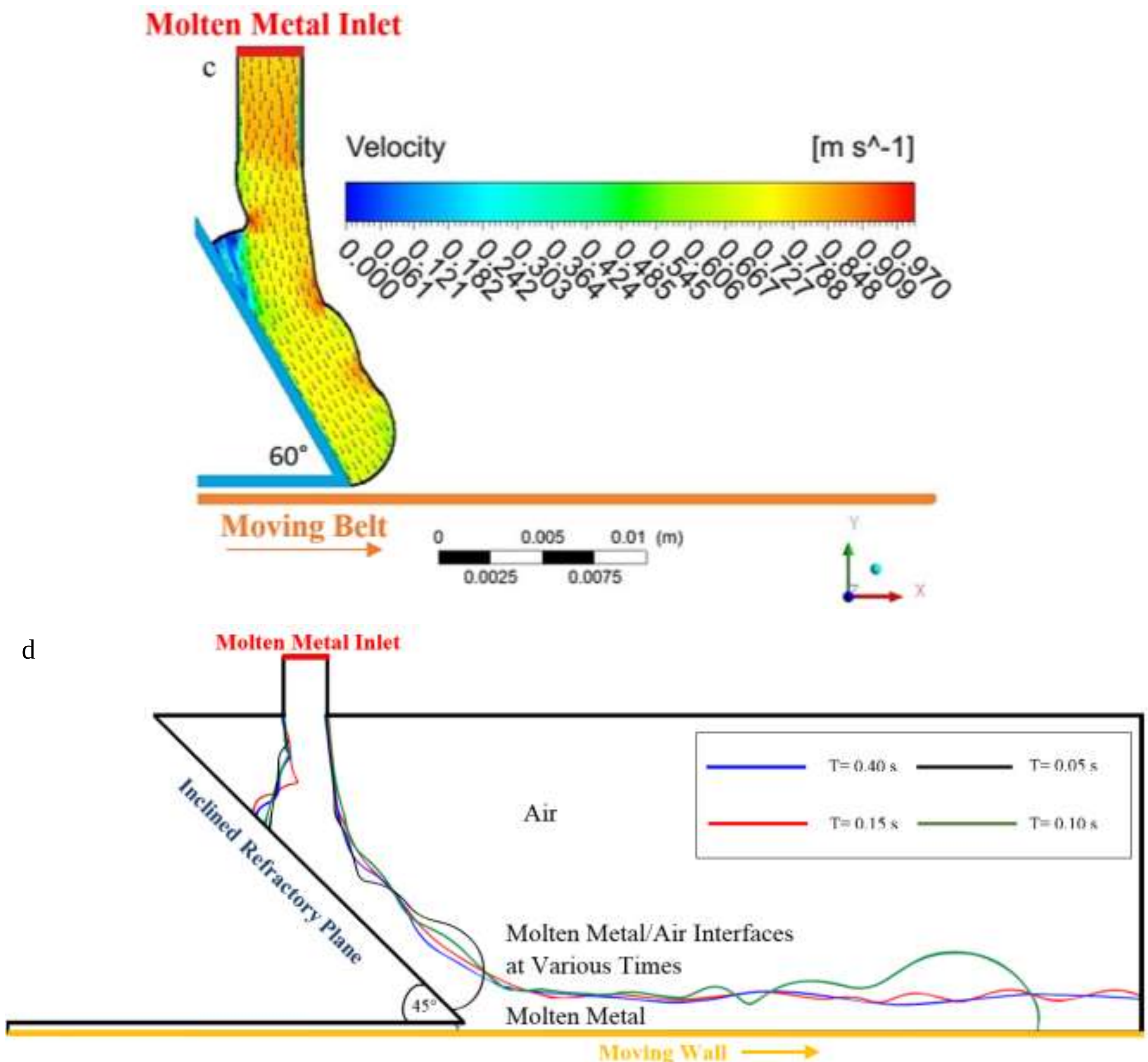

Figure 7: Velocity contour of molten metal flowing over (a) 30°, (b) 45°, (c) 60° inclined refractory plane, (d) A representation of computed surface profiles caused by fluctuations in the molten metal air interface, during initial flows of steel onto the 45° (at several different time steps overlaid on each other).

The intensity and amplitude of these free surface waves are high, near the triple point, but decrease further downstream until becoming almost flat. The experimental findings are in accord with the model prediction in which a nearly flat solidified strip was produced without any upper surface irregularities. These simulations/experimental results for AHSS casting are in close agreement with the results published for light metal castings, in which a similar, non-uniform flow, down a 45° inclined refractory plane, and over a moving belt, was observed.

6.5.4. Optimum Conditions for Casting of AHSS via HSBC Process

As discussed above, the suppression of free surface discontinuities of molten metal in HSBC, is crtically important towards achieving high quality strips. This is best obtained by incorporating a $\geq$45° inclined refractory plane in the feeding system. Furthermore, the incoming velocity of the molten metal should match that of the moving belt speed, for iso-kinetic feeding [1-3].

It is important to understand that gravity, viscosity, and surface tension are the forces responsible for restoring these surface waves to complete flatness. Heat extraction rates, belt temperature, and cast thickness would need to be adjusted (as important variables to ensure the production of high-quality strip), in such a way as to allow these surface waves to settle down, before the completion of molten metal solidification [1-4, 7].

6.5.5. Molten Metal Velocity Contours/Profile over Moving Belt

In this section, the velocity profile of the molten metal over the moving belt is examined. As per numerical simulations, the velocity of the molten metal at the free surface was observed to be slightly higher than the belt velocity, as shown in Figure 6b and Figure 6c. However, with distance, 84mm from triple point, this difference reduces to only 0.17 m/s, represented in Figure 6d. Therefore, the flow can be considered as near iso-kinetic since the belt speed is almost equivalent to the molten metal velocity.

6.5.6. Behavior of Fe-21%Mn-2.5%Al-2.8%Si-0.08%C Steel under Plastic Deformation, using the Olson-Cohen Thermodynamic Modeling Approach, and the FactSage Assessment

As per the Olson-Cohen thermodynamic modeling approach and literature, Fe-21%Mn-2.5%Al-2.8%Si-0.08%C Wt.% steel demonstrates both TRIP and TWIP behavior, during plastic deformation [20-27]. This is due to the fact that the SFE (~18 $\frac{\mathrm{mJ}}{\mathrm{mole}}$) lies in a region where both symmetric twin and epsilon martensite can form simultaneously, during plastic deformation [27]. Our experimental results are in agreement with this thermodynamic model prediction, and the archival literature. Given the evidence of annealing twins before plastic deformation (See Figure

8b), and deformation twins and epsilon martensite (See Figure 8c) after pressing/deforming the sample, to approximately ~ 60% at room temperature, using 100-ton hydraulic press.

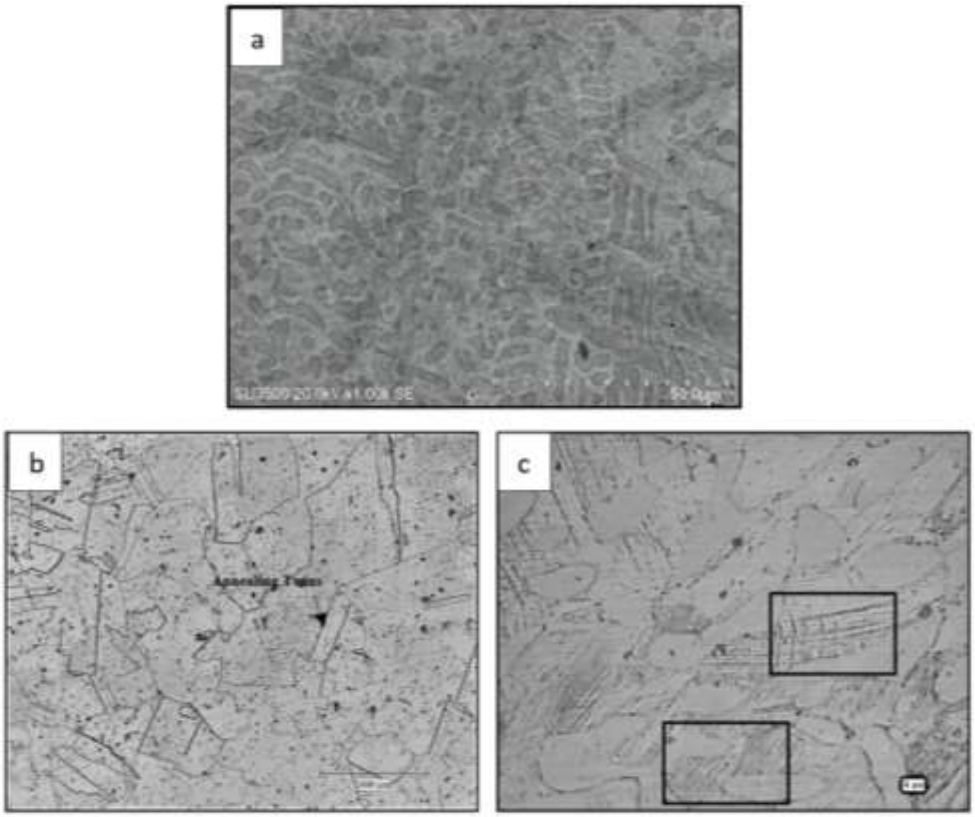

Figure 8: (a) Dendritic structure of the cast strip (Fe-21%Mn-2.5%Al-2.8%Si-0.08 %C wt.%), (b) Fe-21%Mn-2.5%Al-2.8%Si-0.08%C wt.%, soaked for 50 min at 1150° C followed by water quenching (for avoiding secondary particles precipitation), showing annealing twins, (100 X), (c) Plastically deformed (60 %) at room temperature, showing the evidence of mechanical twins, as well as epsilon martensite (500 X).

The liquidus and solidus temperatures of Fe-21%Mn-2.5%Al-2.8%Si-0.08%C wt.%, as calculated through FactSage, were found to be approximately 1,420℃ and 1,320℃, respectively. The nucleation temperatures of different phases are shown in Figure 9. Under Scheil (non-equilibrium/rapid cooling) the microstructure, predicted by FactSage for the AHSS: Fe-21%Mn-2.5%Al-2.8%Si-0.08%C wt.%, is 100 % austenite with no kappa phase precipitation.

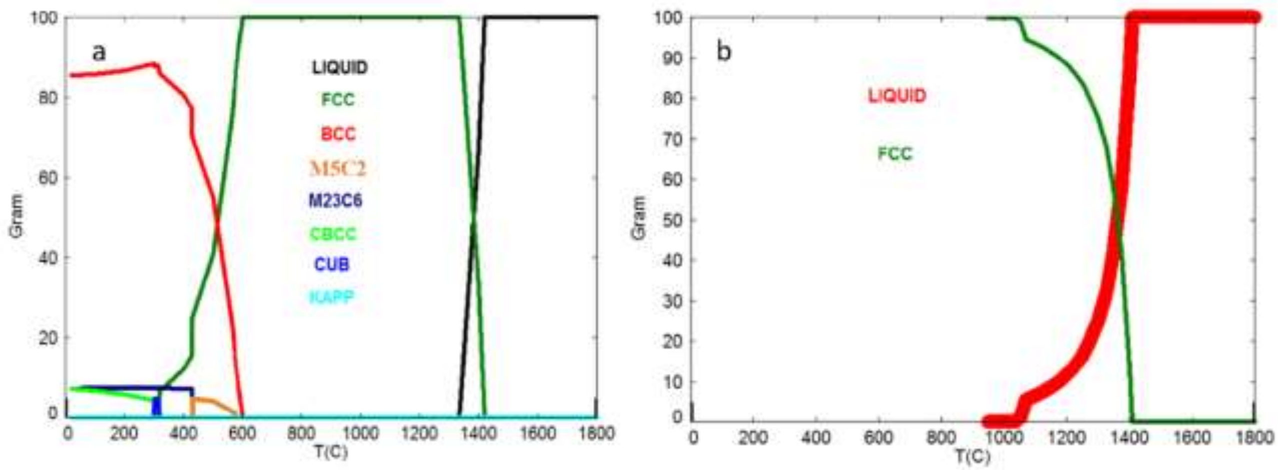

Figure 9: (a) FactSage analysis results: Phases formed due to Equilibrium Cooling, and (b) Non-Equilibrium Cooling.

6.5.7. Downstream Processing and Mechanical Properties achieved in Strips products of Fe-21%Mn-2.5%Al-2.8%Si-0.08%C wt.% Steel

Heat treatment procedures were devised for the Fe-21%Mn-2.5%Al-2.8%Si-0.08%C (wt.%) steel. Prior to heat treatment, the cast steel strip was hot forged (~60%). The hot deformation/forging was carried out at 1,150°C i.e., above ferrite nucleation temperature, using a 100-ton hydraulic press. The hot deformation was applied in order to transform the cast dendritic structure into fine equiaxed grains, and to spread the alloying elements homogenously throughout the material. These had been segregated in the cast structure [28]. Another purpose of hot reduction was to squash/weld any pores, if present, in the cast strip, so as to increase its mechanical properties [28].

After hot deformation, the samples were heated again to 1150 °C, for ~ 10 minutes. This is an added procedure and was done because during hot forging, the temperature of the sample had dropped to 750°C, which is the ferrite nucleation temperature, determined through Fact Sage software. If ferrite had nucleated, it will affect the SFE value of austenite [21-27]. After holding the samples for 10 minutes at 1150° C, the sample was quenched in water in order to obtain a fully austenitic microstructure, verified via optical/SEM microscopy analysis (See Figure 8b and Figure 10a).

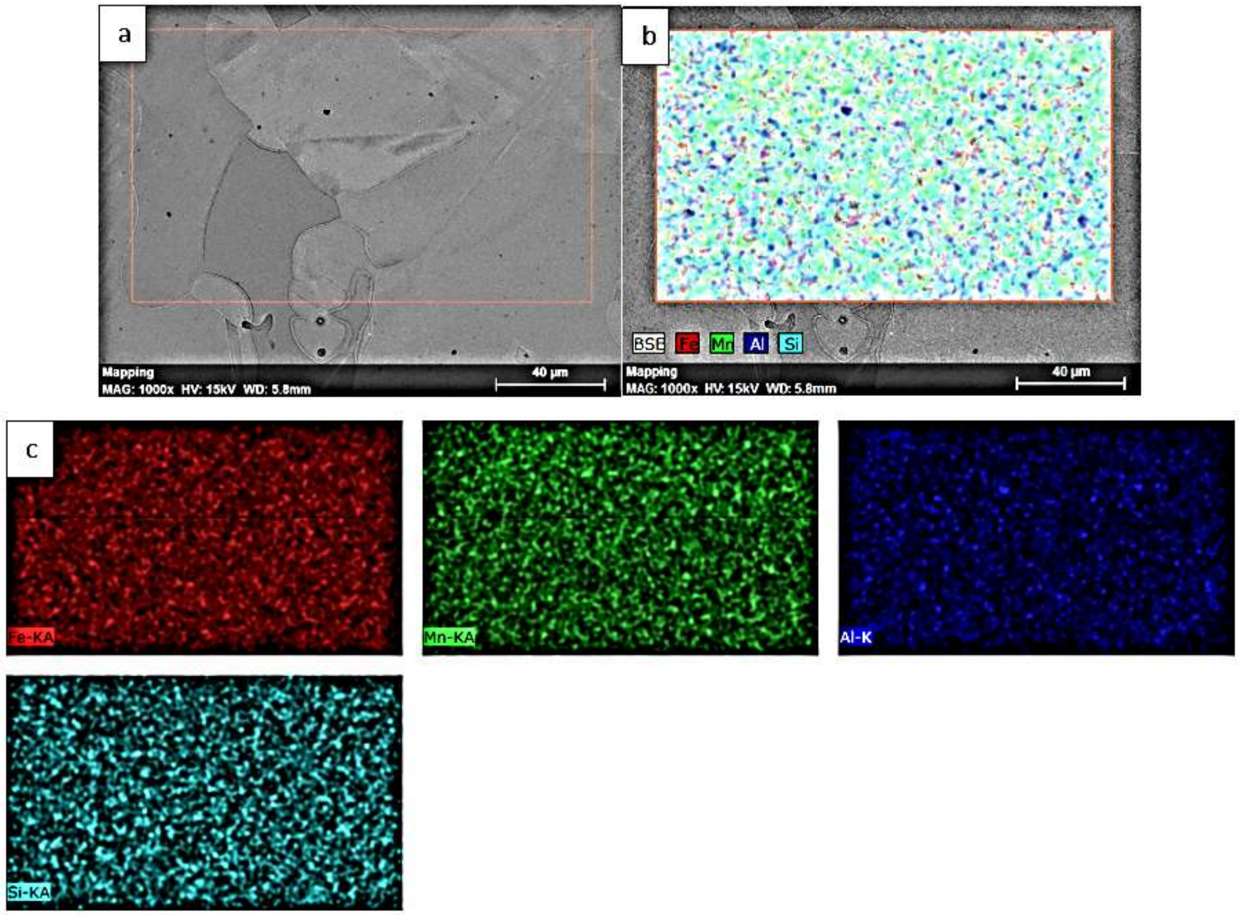

Figure 10: (a) Elemental map showing the homogenous distribution of alloying elements in the microstructure (1000X).

6.5.8. Characterization of the As-Cast and Heat-Treated Strip

The microstructural analysis of the as-cast, and heat-treated, strip was carried out using optical, and scanning electron microscopy, as shown in Figures 8a and Figure 8b. The microstructure revealed equiaxed grains with average size of 200µm. Spark Optical Emission Spectroscopy (S-OES) and Energy Dispersive Spectroscopy (EDS) analyses were performed to determine the chemical composition of the strip (See Table 3). Both OES/EDX confirmed the presence of Al, Si, Mn and Fe. Furthermore, no elemental segregation of the alloying element in the heat-treated sample was observed as shown in Figure 10b and Figure 10c.

Table 3: Chemical composition (wt.%.) determination through Spark OES.

Mn	Al	Si	C	Fe
21	2.5	2.8	0.08	Remaining

The yield (σ_{ys}) and ultimate tensile (σ_{us}) strengths of hot deformed-heat-treated strip have been determined using MTS model Alliance RF/200) shear testing machine, shown in Figure 11[30].

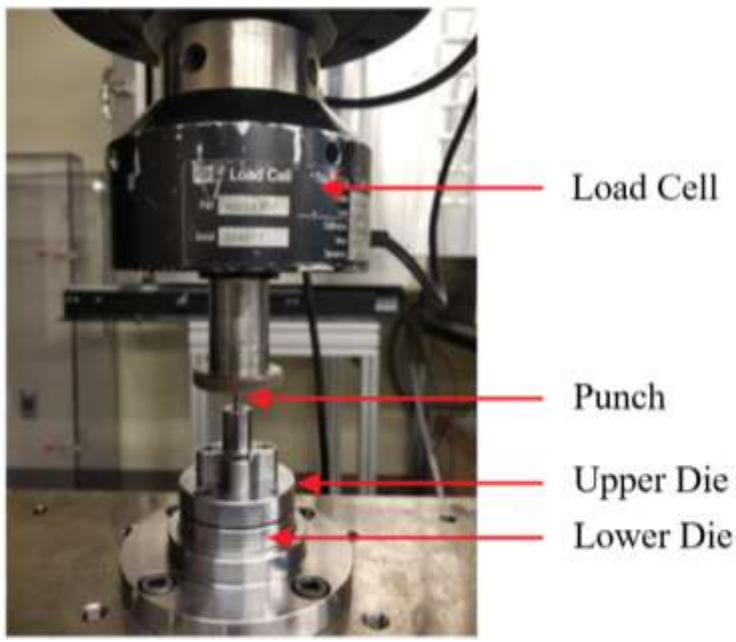

Figure 11: Shear punch test setup.

For each sample, the Shear Punch Test (SPT) were performed at five different locations and an average value was used to document the tensile strength of the strip. These average values were found to be approximately 610 MPa and 950 MPa, respectively (See Table 4). The shear stress (τ) vs shear strain (γ) curve obtained from SPT is shown in Figure 12.

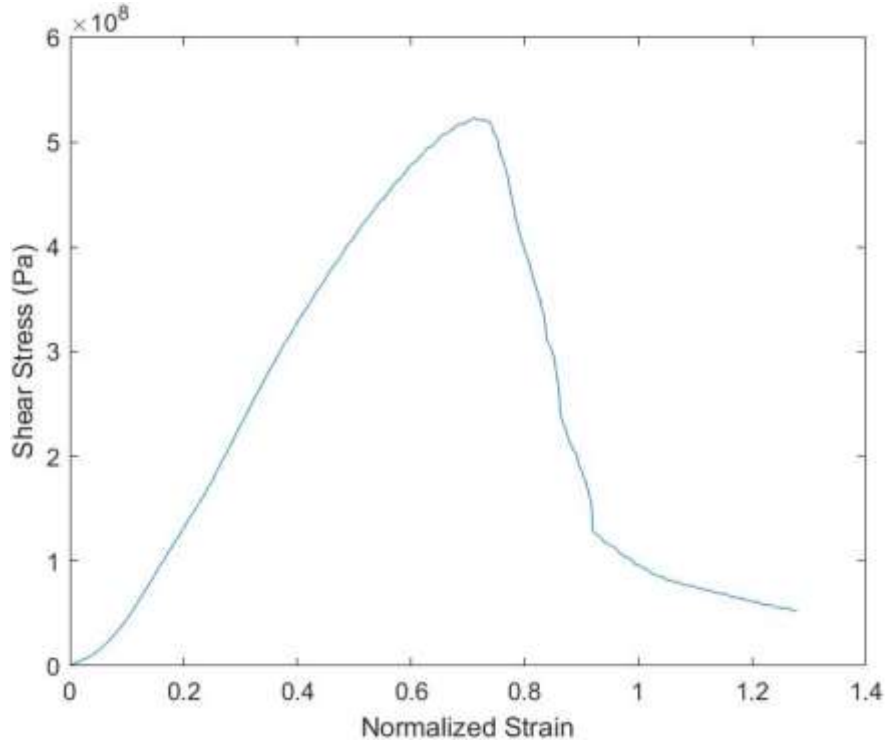

Figure 12: Shear stress vs shear strain graph of AHSS.

Table 4: Shear Punch Test Results.

Sample	**Tensile Strength (MPa)**
Sample 1	952
Sample 2	973
Sample 3	943
Sample 4	968
Sample 5	920
Average	**951**

As per the literature, steels that have tensile strength beyond 780 MPa are regarded as Advanced High Strength Steels (AHSS) [27]. Based on this definition, of Fe-21%Mn-2.5%Al-2.8%Si-0.08 %C wt.%, steel can be regarded as AHSS since it's fulfilling the mechanical properties criterion specified for AHSS [27].

The surface waviness of the top/bottom sides of the strip were determined using a Nanovea 3D profilometer. This technique works on the principle of measuring the physical wavelength of light, and directly relating it to a specific height. This ensures accurate measurement of surface roughness/finish [31]. The scan length for all the measurements was 30mm, whereas the scan speed was 0.1mm/s. Ten random locations were selected for surface roughness measurements. These locations were largely selected from all over the strip. The longitudinal surface profiles are almost identical to each other.

In the HSBC process, the top surface of the cast strip is exposed to the atmosphere and is affected by the disturbances in the flow of the molten metal. As per the numerical simulations, for a feeding system employing a 30° inclined refractory plane, the molten metal free surface variations formed over the moving belt is comparatively higher than those for 45° or 60° inclined refractory planes. The possible reasons have already been explained in previous paragraphs. Furthermore, the free surface discontinuities were damped with distance, as can be seen in Figure 13.

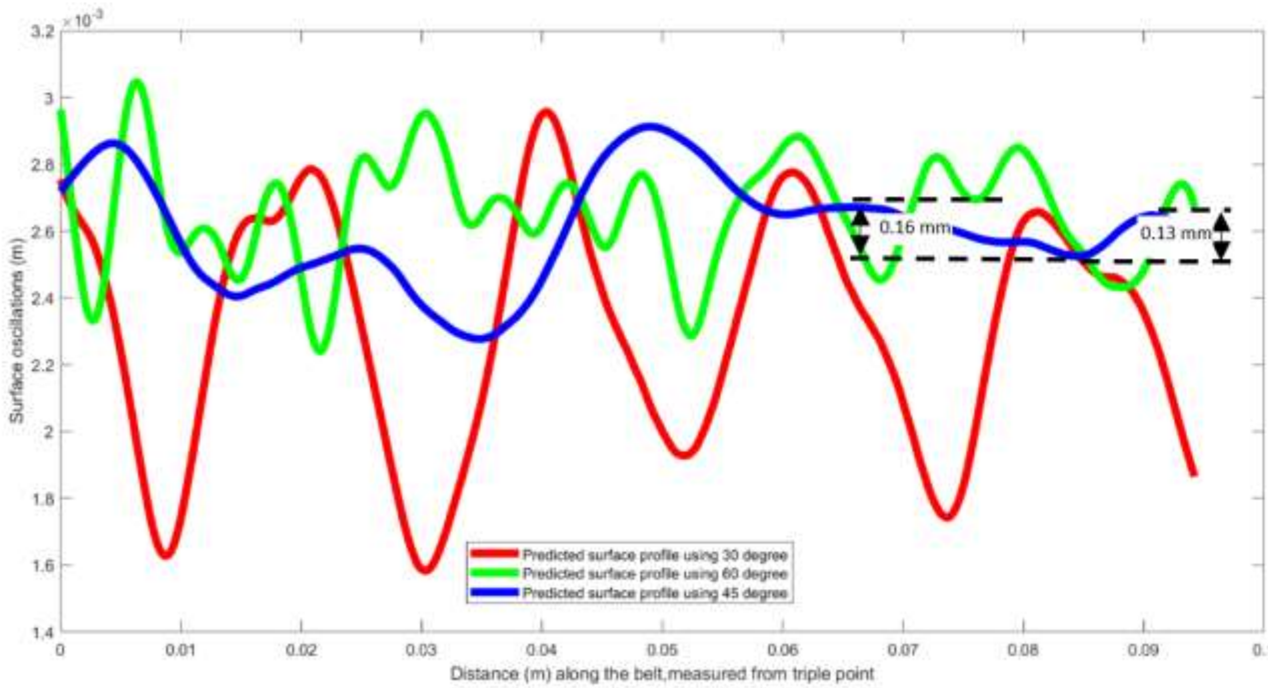

Figure 13: Predicted surface profile of molten metal over the moving belt considering different inclined refractory plane.

In the present research study, the 45° inclined refractory plane was incorporated in the design of the feeding system to produce AHSS strip, owing to its inherent advantage to supress free surface waves. The numerically computed top surface waviness of the molten metal, using the 45°inclined plane, lies in the range of 0.13 - 0.16 mm, as measured by considering the last 23 mm of the computational casting length studied as shown in Figure 13. This is in accord with the experimentally determined surface roughness of the strip i.e. 0.125 mm, obtained using 45° inclined refractory plane as shown in Figure 14a. Additionally, the surface roughness of continuous cast products is generally of the order of 0.25 mm for low/high-carbon steels and 0.65 mm for peritectic grades as shown in Figure 15a and Figure 15b [32]. By simple comparison, the cast surface quality of HSBC products is superior than continuous cast products.

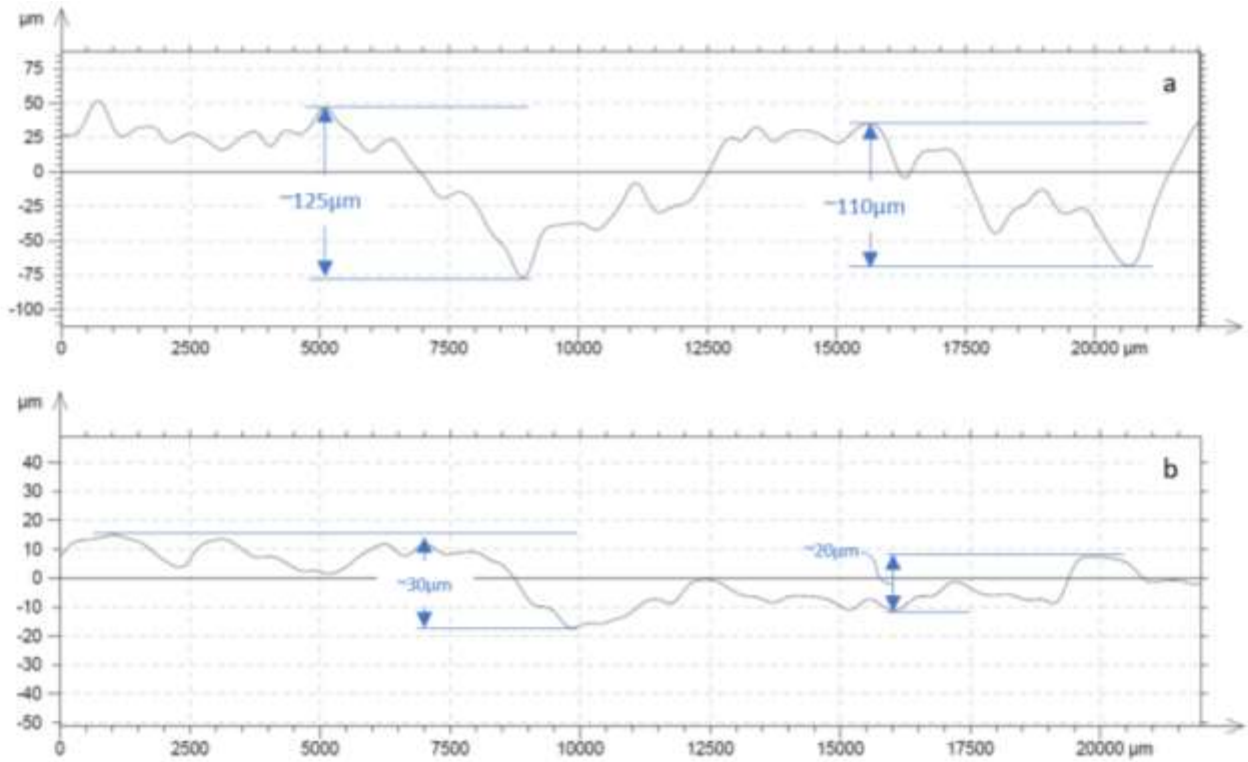

Figure 14: (a) Measured top surface roughness, and (b) Measured bottom surface roughness.

Additionally, pin holes/blow holes and oscillation marks are not detected on the surface of the cast strip (Figure 15c), unlike for continuously cast products, which possess several defects on their surface, and can require surface grinding prior to hot rolling. The strip bottom surface roughness was also measured and lies within 40 range, as shown in Figure 14b. These measurements prove that the bottom surface quality is far superior as compared to the top surface. This occurrence can be credited to the fact that the molten metal is in direct contact with the moving belt, and conforms to its shape during the solidification.

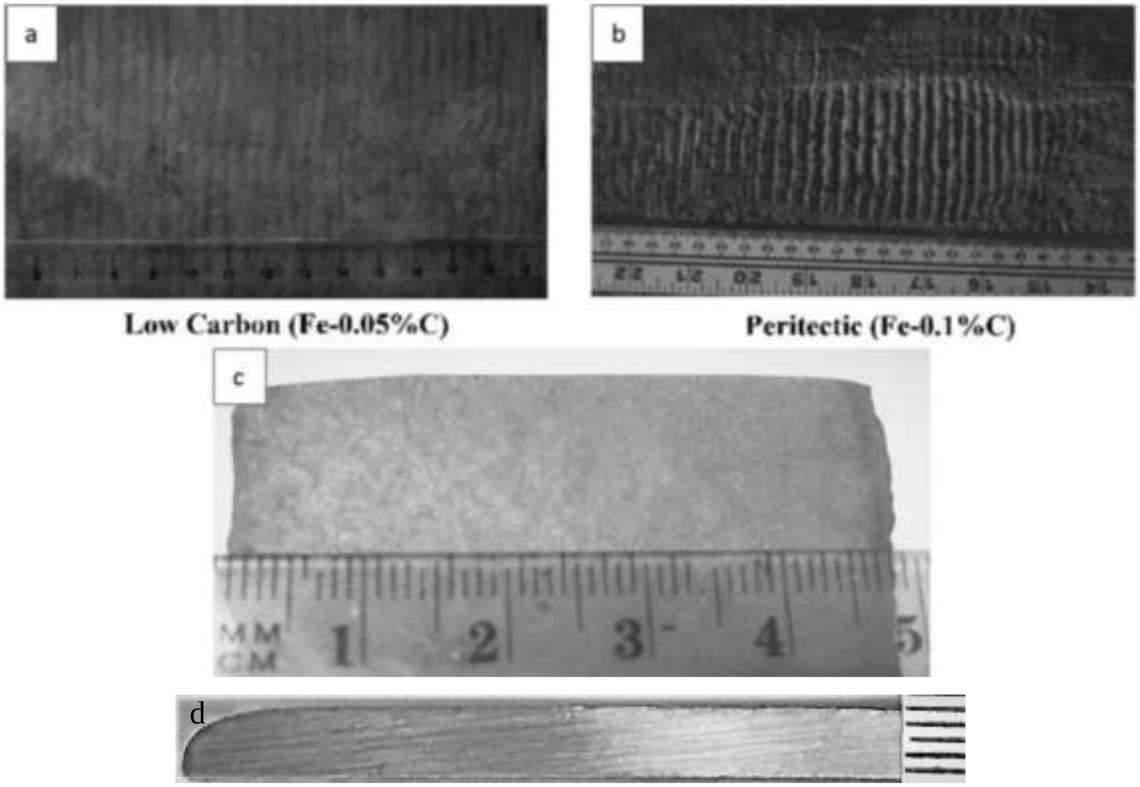

Figure 15: Continuous cast products (a) low carbon (Fe-0.05% C), (b) Peritectic (Fe-0.1%C), (c) The smooth surface finish of Fe-21%Mn-2.5%Al-2.8%Si-0.08 %C wt.% strip produced using the HSBC simulator, in which the belt velocity approximates the incoming molten metal velocity (d) Cross-section of the produced strip.

6.6. Conclusions

The present research has focused on the capability of the HSBC technology to produce thin strips of advanced high strength steels, of composition Fe-21%Mn-2.5%Al-2.8%Si-0.08%C wt.%. Ansys Fluent 14.5 software was used to analyze the dynamics of fluid flow from the liquid metal delivery system onto the moving belt. It has been determined that the vibrations/fluctuations of molten metal/air interface are inherent in the HSBC process and could affect the surface quality of the cast strip, if not closely managed. At a sufficiently low angle of inclination i.e. 30° of the refractory plane of the metal delivery system, the molten metal-free stream becomes distorted/deformed and triggers instabilities in the flow of the molten metal. However, at a sufficiently high angle (≥45°), the molten metal stream was observed to be uniform and less fluctuating which in result reduces these instabilities. Additionally, the phenomenon of a hydraulic jump is also explained which also contributes towards the generation of free surface waves running down an inclined refractory plane and moving belt. It was determined that any discontinuities in the flow of the molten metal will not affect the surface quality provided the metal remains liquid for an appreciable time, thereby allowing these surface waves to settle down before solidification. The surface roughness and microstructure of the produced strip were also evaluated which was observed to be superior to conventional cast products.

6.7. References

17. M. Celikin, D. Li, L. Calzado, M. Isac, R.I. Guthrie, Light Metals 2013, 2016, 1037.
18. M. Xu, M. Isac, R.I. Guthrie, Metallurgical and Materials Transactions B, 2018, 49, 1003.
19. S. Ge, S. Chang, T. Wang, L.E. Calzado, M. Isac, J. Kozinski, R.I. Guthrie, Metallurgical and Materials Transactions B, 2016, 47, 1893.
20. R.I. Guthrie, M. Isac, Steel Research International, 2014, 85, 1291.
21. S. Ge, M. Isac, R.I. Guthrie, ISIJ international, 2013, 53, 729.
22. M. Xu, M. Isac, R.I. Guthrie, Ironmaking & Steelmaking, 2018, 45, 878.
23. C.W Hirt, B.D. Nichols, Journal of computational physics, 1981, 39, 201.
24. FLUENT 14.5 Manual, ANSYS Inc., 10 Cavendish Court, Lebanon, NH, USA.
25. T. Le Hoai, J. Lee, Metallurgical & Materials Transactions B, 2011, 42.
26. G.L. Richard, S.L. Gavrilyuk, Journal of Fluid Mechanics, 2012, 698, 374.
27. W.H. Hager, Energy dissipators and hydraulic jump, Springer Science & Business Media, 2013, 8, Zirich, Switzerland, 1992.
28. H.M. Chaudhry, Open-Channel Flow, Springer Science & Business Media, Carolina, 2008.
29. N. Rajaratnam, Hydraulic jumps, Advances in hydroscience,1967, 4,197.
30. R.F. Dressler, Communications on Pure and Applied Mathematics,1949,149.
31. H. Chanson, European Journal of Mechanics-B/Fluids, 2009, 28, 191.
32. M. Kumar, A.S. Lodhi, ISH Journal of Hydraulic Engineering, 2016, 22, 127.
33. P. Parastoo, F. Davoud, H.Z.D. Ali, A. Akram, J.N.E. Mohammad, ISH Journal of Hydraulic Engineering, 2017, 301.
34. S. Chippada, B. Ramaswamy, M.F. Wheeler, International Journal for Numerical Methods in Engineering, 1994, 3,1381.
35. D. Mazumdar, J.W Evans, Modeling of steelmaking processes, CRC Press, 2009.

36. M. Hillert, M. Jarl, Calphad, 1978, 2, 227.
37. O.A. Zambrano, Journal of Engineering Materials and Technology, 2016, 4, 138.
38. W. Bleck, K. Phiu-On, Microstructure and Texture in Steels, 2009, 145.
39. N.I. Medvedeva, M.S. Park, D.C. Van Aken, J.E. Medvedeva, Journal of Alloys and Compounds, 2014, 582, 475.
40. S.J. Lee, Y.K Lee, A. Soon, Applied surface science, 2012, 258, 9977.
41. S. Allain, J.P. Chateau, O. Bouaziz, S. Migot, N. Guelton, Materials Science and Engineering A, 2004, 387, 158.
42. G. Dini, A. Najafizadeh, S.M. Monir-Vaghefi, R. Ueji, Journal of Materials Science & Technology, 2010, 26, 181.
43. G. Frommeyer, U. Brüx, P. Neumann, ISIJ international, 2003, 43, 438.
44. L.Z. Zhuang, E.W. Langer, Journal of materials science,1989, 24, 381.
45. A. Wang, P.F. Thomson, P.D. Hodgson, Journal of Materials Processing Technology, 1996, 60, 95.
46. A. Fall, H. Monajati, A. Khodabandeh, M.H. Fesharaki, H. Champliaud, M. Jahazi, Materials Science and Engineering A, 2019, 749, 166.
47. Surface roughness determination using 3D Nanovea profilometer, Available https://nanovea.com/profilometry-roughness-finish.
48. J. Sengupta, B.G. Thomas, M.A. Wells, Metallurgical and Materials Transactions A, 2005, 36, 187.

Chapter 7

7.0. The Production of Thin Strips of a (17%Mn-4%Al-3%Si-0.45%C wt.%) TWIP Steel Using HSBC Simulator

In the previous Chapter, the flow of molten Fe-21%Mn-2.5%Al-2.8%Si-0.08%C wt.% in the HSBC process was modeled and the phenomenon of molten metal/air interface fluctuations over the inclined refractory plane was explained. It was determined that by decreasing the refractory inclination angle, the molten metal tends to climb up the inclined refractory plane, and on its way down, being subjected to constant gravity force, became distorted and non-uniform. This backflow upstream of the inclined refractory plane can be prevented by increasing the inclination angle of the refractory plane.

This Chapter presents optimum operating parameters for the production of thin strips of 50 mm wide, ~ 4 mm thick of Fe-17%Mn-4%Al-3%Si-0.45%C wt.% TWIP steel using a HSBC process. A two-dimensional model was developed to examine the flow of molten metal in the HSBC process, primarily focusing on investigating the instabilities/turbulence that arises when molten metal encounters the moving belt. the molten metal velocity at the nozzle slot outlet is fixed at 0.8 m/s whereas the belt velocity is varied from 0.4 m/s to 1.2 m/s unlike in the previous study where the belt speed was fixed at 0.8 m/s. The significance of iso-kinetic feeding of molten metal over the moving belt in the HSBC process is explained in the light of numerical modeling predictions. FactSage software was used to predict the liquidus and solidus temperatures, as well as the types and amounts of the solid phases present, under the relevant, rapid (Scheil)-cooling conditions. Mechanical properties of the hot deformed and heat-treated strip were evaluated via the Shear Punch Test (SPT) technique, whereas surface roughness was measured using the Nanovea 3D optical profilometer.

The research presented below made the object of the publication entitled: “Numerical Modeling and Experimental Casting of 17%Mn–4%Al–3%Si–0.45%C wt. % TWIP Steel via the Horizontal Single Belt Casting (HSBC) Process”, : Usman Niaz, Mihaiela M. Isac & Roderick I. L. Guthrie, “publisher Taylor & Francis, in the Journal of “Ironmaking & Steelmaking”, 13 March 2020, pp: 1-14.

7.1. Abstract

This paper presents optimum operating parameters for the production of thin strips of 50 mm wide, ~ 4 mm thick of Fe-17%Mn-4%Al-3%Si-0.45%C wt.% TWIP steel using a HSBC process. A two-dimensional model was developed to examine the flow of molten metal in the HSBC process, primarily focusing on investigating the instabilities/turbulence that arise when molten metal encounters the moving belt. For CFD modeling, three belt speeds were tested i.e., 0.4, 0.8, and 1.2 (m/s), against a constant molten metal velocity of 0.8 m/s at nozzle slot outlet. It was observed that the molten metal/air interface fluctuations were appreciably suppressed/reduced when the belt and molten metal velocities approached each other. The fluctuations formed, are damped further downstream, and any remaining surface perturbations can be eliminated via hot plastic deformation. An appropriate heat treatment was also designed for the TWIP steel strips, in order to achieve the desired microstructure and mechanical properties.

Key words: Computational Fluid Dynamics (CFD), Thermodynamics, Horizontal Single Belt Casting (HSBC) Process. Advanced High Strength Steel (AHSS).

7.2. Introduction

The Horizontal Single Belt Casting (HSBC) process can be used to produce superior quality ferrous/non-ferrous strips [1-4]. Apart from its low energy requirements and promising productivity, the technology is capable of producing Near Net Shape metallic products [1-4]. Elemental segregation is negligible versus the commercially proven slab casting process, given that the cooling rates for the HSBC process can reach up to about 500°K/second [5].

The HSBC process, shown in the Figure 1a, and 1b, involves feeding molten metal, iso-kinetically, onto an intensively cooled, moving belt, which acts as the mold. Passing through a slot nozzle from a low-head metal delivery system, the liquid steel further accelerates onto the moving, water-cooled belt, onto which it solidifies [3]. The material produced through the HSBC process is then processed in line, using hot and cold rolling steps [2-3].

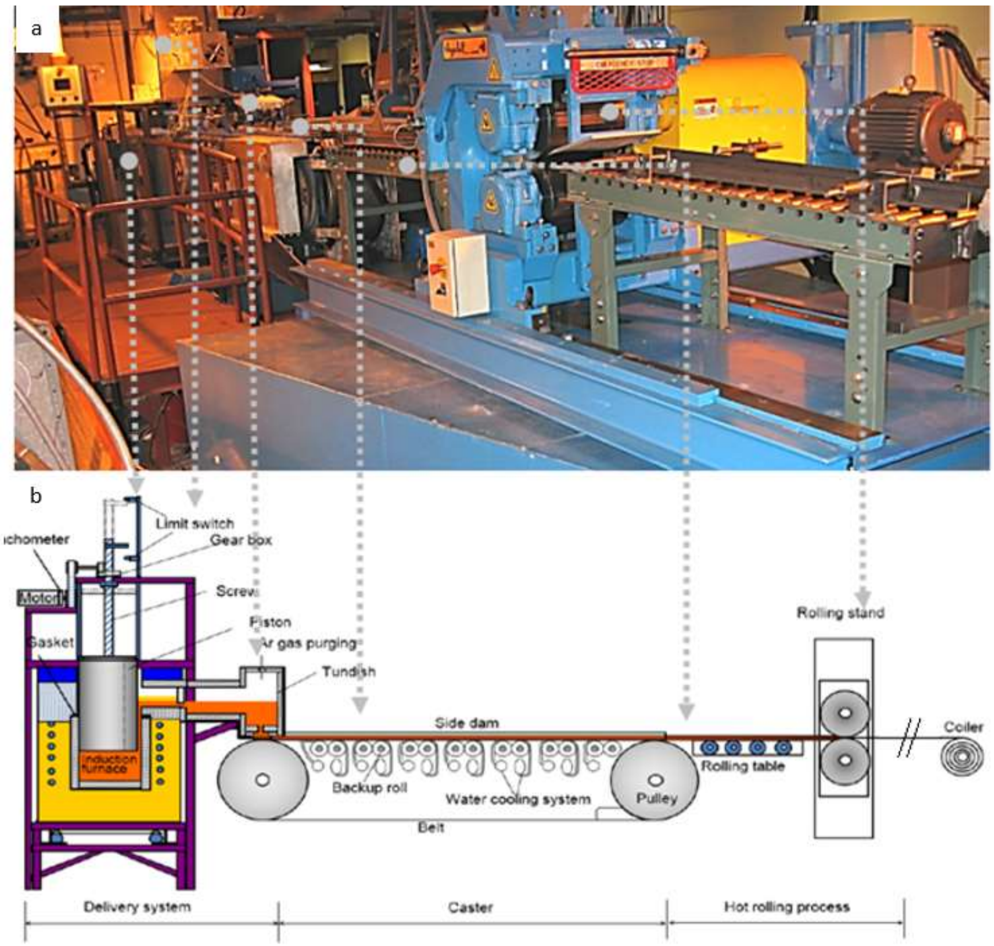

Figures 1. (a) A photograph of the HSBC pilot-scale plant, and b) a schematic of the HSBC pilot scale plant, located at MetSim Inc's High Temperature Laboratory, Montreal, Canada [1].

Table 1. Chemical composition of the plain carbon steel, and of ferro-alloys used to produce Fe-17%Mn-4%Al-3%Si-0.45%C (wt.%) TWIP steel.

Materials Used	Chemical Composition (as supplied by manufacturers)
Plain Carbon Steel	0.4Mn-0.20C-0.001Si-0.001P-Balance Fe
Fe-Mn Alloy	78.40Mn-1.47C-0.60Si-0.17P-Balance Fe
Fe-Si Alloy	76.50Si-0.10C-1.50Al-0.25Ti-0.04P-Balance Fe
Mn-Al Alloy	75Al-25Mn

The HSBC process features a compact design, which can provide better economic production capabilities for both ferrous, and non-ferrous, metallic sheet products [2]. The production of Advanced High Strength Steel (AHSS) strips of 10 mm thickness via the HSBC process at the

Salzgitter Group's Steelworks at Peine, Germany, is a commercial example which takes advantage of what the HSBC can offer, versus conventional strip manufacturing processes [6]. The excessive hot deformation steps associated with CCC (Conventional Continuous Casting) and TSC (Thin Slab Casting) processes can be significantly reduced by HSBC in making steel sheet material.

AHSS (Advanced High Strength Steel) grades are difficult to be processed conventionally owing to excessive work hardening of the material during hot rolling [6-8]. Excessive hot rolling of these slabs are necessary, in order to produce the final properties and desired thicknesses of AHSS sheet [8-11]. These restrictions are resolved with HSBC operations, since the cast strip thickness is only 10mm. This means that hot deformation steps required to produce 1mm thick sheet can be significantly reduced. The AHSS's developed on CCC machines to date, include Dual Phase (DP) Steels, Transformation Induced Plasticity (TRIP) steels, Complex Phase (CP) steels, Twinning Induced Plasticity (TWIP) steels, and Martensitic (MS) Steels [8].

The practical usefulness of AHSS is significant. AHSS grades are lighter than regular steels, and have unique combinations of mechanical strength and formability that render them a prime candidate material for automotive applications [8]. As a result, AHSS grades are being developed as a competitive steel material that provides a good balance between strength, performance and ease of production, compared with other materials, such as plastics and composites [8]. The main strengthening mechanisms behind AHSS's increased tensile strength and total elongation are; a) dislocation slip and b) the nucleation of symmetric twins for TWinning Induced Plasticity (TWIP) steels, and c) the transformation of austenite (γ) to martensite (α/ε) during plastic deformation for Transformation Induced Plasticity (TRIP) type steels [8-11]. These competing strengthening mechanisms are strongly dependent on the Stacking Fault Energy (SFE). According to the literature, a critical value of SFE, between 20-40 $\frac{\mathrm{mJ}}{\mathrm{mole}}$, is suggested for the twinning mechanism, whilst SFE values < 20$\frac{\mathrm{mJ}}{\mathrm{mole}}$ are determined for the TRIP mechanism. When the SFE exceeds 45 $\frac{\mathrm{mJ}}{\mathrm{mole}}$, AHSS gain strength through dislocation gliding mechanisms [8-11]. Accordingly, the SFE value of Fe-17%Mn-4%Al-3%Si-0.45%C wt.% steel, calculated using the Olson-Cohen modeling approach, was found to be 21 $\frac{\mathrm{mJ}}{\mathrm{mole}}$. In principal, this steel should demonstrate TWIP behavior upon plastic deformation, since the SFE is more than 20 $\frac{\mathrm{mJ}}{\mathrm{mole}}$, as described above.

Keeping in mind the suitability of the HSBC process to cast both ferrous and non-ferrous alloys and knowing the particular usefulness of AHSS in the production of the lightweighted steel automotive structures [9-11], the alloy Fe-17%Mn-4%Al-3%Si-0.45%C wt.%, was selected for the present HSBC strip production. In this research study, a double impingement feeding system was used in which the molten metal first interacts with the inclined refractory plane, followed by its second interaction with the moving belt [2]. These two-impingement points are shown in Figure 5. The prime objective of this research study was to determine optimum operating conditions for the casting of AHSS strip, employing a double impingement feeding system.

7.3. Objectives of the Present Research

Our previous research work [2] suggests that in a double impingement feeding system, the interaction of molten metal with the inclined refractory plane and moving belt results in the generation of molten metal/air interface fluctuations. These can significantly affect the surface quality of the cast strip [2]. Additionally, they explained the mechanism through which disturbances/fluctuations may intensify, thereby leading to air entrapment in the forming strip. In these simulation studies, the inclination angle of refractory plane, as well as belt speed, were held constant at 45° and 0.5 m/s respectively, whereas the molten metal velocity at the nozzle slot outlet was fixed at 0.8 m/s [2]. For these studies, AA6111 aluminum alloy was chosen and numerical simulations were carried out using Ansys Fluent 14.5 software.

This research study is a further extension of our previous group’s work in which, instead of analyzing the molten metal flow over an inclined plane, the focus was shifted to analyzing the instabilities/turbulence arising when molten metal encounters the moving belt. For this purpose, numerical simulations were carried out in which the belt speeds were varied from 0.4 m/s to 1.2 m/s, whilst the velocity at the nozzle slot outlet was fixed to 0.8 m/s. The refractory plane angle of inclination used for the numerical simulations, as well as for casting experiments, was 45°.

Heat transfer was also considered in the present work. Given a heat flux of 32 MW/m2 in the first instants of molten metal touching moving belt, it is believed that a very thin solidified metal layer will form (~ 20 microns) close to the point of contact. However, this will not significantly affect the flow of molten metal in the immediate vicinities of the two impingements. The result are presented in the following paragraphs. The simulation domain selected to carry out this study is presented in Figure 2.

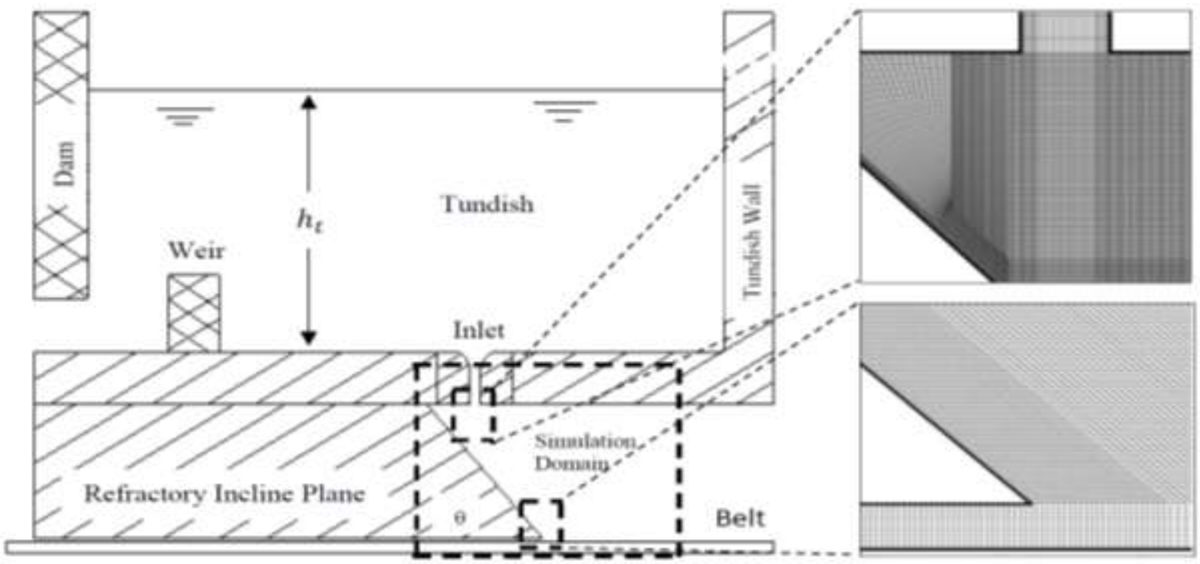

Figure 2. Simulation domain and structured meshes at the nozzle outlet and at the triple point.

7.4. The HSBC Simulator, Precursor for the Full-Scale Caster

The preliminary experimental work used the HSBC simulator, as shown in Figure 3. It comprises a stationary, refractory-lined vessel (tundish), to contain molten metal alloys [3]. The tundish is provided with a slot in its base, which remains closed, and is only opened once casting commences. The simulator is equipped with a compression spring system, which when activated, provides a sharp blow to propel the chilling copper substrate, located beneath the tundish, at a constant defined speed. Metal then instantaneously pours through the slot nozzle, and onto the moving cooling substrate. The substrate is a slab of high purity copper (99.99 %), 800 mm long,110 mm wide, and 12.7 mm thick [4].

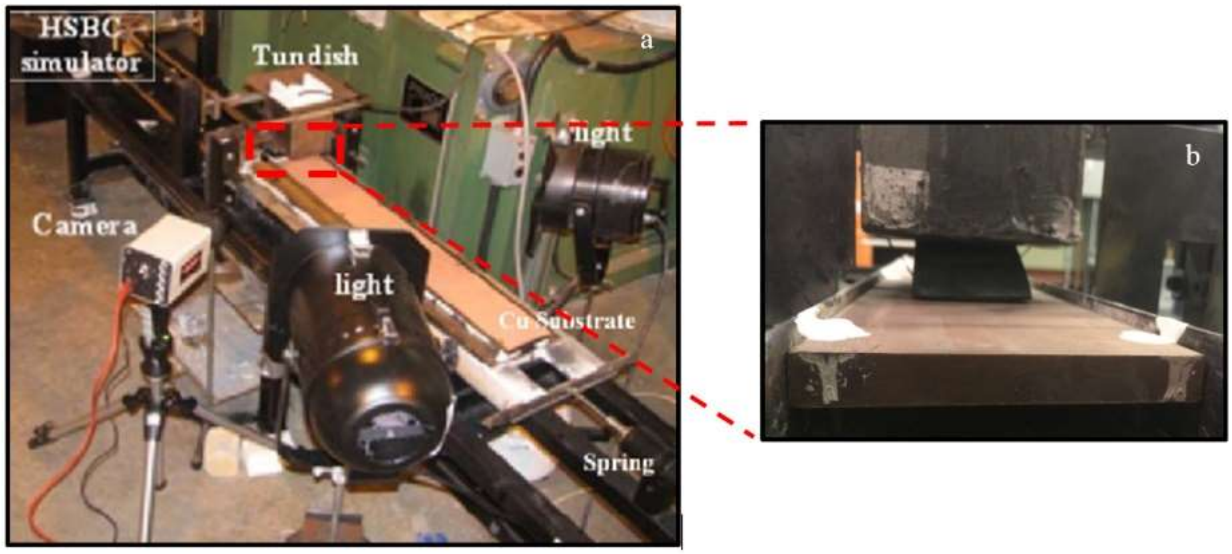

Figures 3. (a) A photograph of the HSBC simulator (b) Double impingement feeding system for HSBC Simulator.

The entire experimental procedure starts with pouring molten metal into the tundish. The molten metal stays there for a few seconds to dissipate the kinetic energy of turbulence. The compressed spring is then released to propel the chilled substrate laterally, at a constant speed. The melt flows through the nozzle slot, pours onto the moving substrate, where it solidifies under an argon (or other) gaseous environment [3]. At a substrate velocity of 0.8m/s, the experiment is completed within a second! However, before the start of an experiment, the tundish and the inclined refractory plane are heated to approximately 1000°C using an air/methane gas mixture, so as to preheat the refractory and avoid any premature freezing of the molten metal inside the tundish, or over the inclined refractory plane. To measure the heat flux through the molten metal during the solidification, two K-type thermocouples are used. These thermocouples are embedded inside the copper substrate, one very close to the surface, the other vertically underneath, so as to record the local temperature-time data during the casting process [12].

7.5. Details of Experimental Procedure

A TWIP steel, Fe-17%Mn-4%Al-3%Si-0.45%C (wt.%) was produced by first melting plain carbon steel in a pre-heated induction furnace under a protective argon atmosphere, followed by the addition of Fe-Mn, Fe-Si, and Mn-Al alloys. The chemical composition of the ferroalloys and plain carbon steel (in wt.%) is presented in Table 1. Good agitation was ensured, so as to completely dissolve/mix the alloy additives into the liquid plain carbon steel. The TWIP steel was then poured into the HSBC simulator tundish and was subsequently cast into a thin strip. Afterwards, specimens were sectioned from the strip and were prepared for metallographic analysis, using grinding and polishing operations. Polishing was performed using 1μm diamond paste, contained in an alcohol-based lubricating fluid. This was followed by etching with Nital (5wt% Nitric acid in alcohol) solution. The microstructure resulting is shown in Figure 15 and 16.

Table 2. Physical Properties of the Phases in the Model.

Operating Parameters/Assumptions	**Value**
Slot Nozzle Thickness.	3 mm
Inlet Velocity.	0.8 m/s
Surface Tension of the Melt in Air.	1.50 N/m [13]
Copper Substrate Longitudinal speed.	0.8 m/s
Turbulence Model.	SST k-ω
Contact Angle Between Melt and Alumina Refractory.	135° [3]
Contact Angle Between Melt and Sand Blasted Copper Substrate.	105° [3]
Distance Between Stationary Inclined Refractory Plane and Moving Belt.	0.4 mm

Table 3. Operating Parameters and Assumptions Made in the Model [3].

Property	**TWIP Steel**	**Air**	**Substrate (Pure Cu)**
Density, ρ, $(\frac{kg}{m^3})$	6950	1.225	8978
Specific Heat Capacity, C_p, $\left(\frac{KJ}{kg\ K}\right)$	0.720	1.006	381
Thermal Conductivity, K, $\left(\frac{W}{m\ K}\right)$	30.5	0.0242	387.6
Viscosity, μ, $\left(\frac{kg}{m\ s}\right)$	0.0063	1.75×10^{-5}	--
Molecular Weight, $\left(\frac{kg}{kmol}\right)$	55.8	28.97	63.55

7.6. Numerical Modeling, Experimental Results and Discussion

7.6.1. Mathematical Modeling

A two-dimensional, transient state, turbulent flow was modeled using ANSYS FLUENT 14.5 software. This code is based on the Finite Volume Method (FVM). The volume of the Fluid (VOF) multiphase model was applied to a fixed Eulerian mesh (mentioned above), to solve a single set of the momentum equations. In this way, the volume fraction of each fluid ($\alpha_{metal}, \alpha_{air}$) in all computational cells could be determined, and the melt-air interface tracked [14]. The VOF method solves a continuity equation of the following form:

$$\frac{1}{\rho_q}\left[\frac{\partial}{\partial t}\left(\alpha_q\rho_q\right) + \nabla\left(\alpha_q\rho_q\dot{u}_q\right) = S_{\alpha q} + \left(\dot{m}_{pq} - \dot{m}_{qp}\right)\right] \quad (1)$$

where $\alpha_{metal} + \alpha_{air} = 1$. Here ρ represents density, t is the time, α is the volume fraction, ū is the mean velocity, whilst subscript q represents the phase (melt or air), $\dot{m}_{pq}$ is the mass transfer from phase q to phase p and vice versa for $\dot{m}_{qp}$. Both terms are zero here, since molten metal and air are immiscible, insoluble and non-interpenetrating. Also, the source term, here designated as $S_{\alpha q}$ is zero, since there is no creation or destruction of any phase.

The relevant momentum equation is;

$$\frac{\partial(\rho\bar{u})}{\partial t} + \nabla.(\rho\bar{u}\bar{u}) = -\nabla p + \nabla.[\mu(\nabla\bar{u} + \nabla\bar{u}^T)] + \rho\bar{g} + \bar{F}_\sigma \tag{2}$$

where p represents the static pressure, μ is the dynamic viscosity, $\bar{g}$ is acceleration due to gravity and $\bar{F}_\sigma$ is the surface tension force. This momentum equation depends on the volume fractions of the phases in each control volume, through the properties ρ and μ evaluated by the following two equations;

$$\rho = \alpha_{melt}\,\rho_{melt} + \alpha_{air}\rho_{air},\;\; \mu = \alpha_{melt}\rho_{melt}\eta_{melt} + \alpha_{air}\rho_{air}\eta_{air} \tag{3}$$

where the primary and secondary phases for this study are air, and metal, respectively. An explicit time marching scheme was used to discretize and solve the transient VOF equations. The geometric reconstruction scheme (GRS) was selected to reconstruct the interface between the melt and air, using the Piecewise Linear Interphase Method. GRS assumes a linear slope of the fluids interface within each computational cell and uses this linear slope to evaluate the advection of the fluid through the cell phases [14].

For turbulence modeling, an additional single set of transport equations also needs to be solved. Turbulence variables are shared by the phases throughout the computational domain. In this study, the 2D turbulent molten metal flow is modeled using the SST k-w turbulence model. Details regarding turbulence modeling are not given here but can be found in the literature [14].

Also, surface tension effects, along the melt-air interface, was studied by incorporating the continuum surface force (CSF) model. The CSF model adds a source term in the momentum equations which can be calculated as per the following equation [14].

$$\vec{F}_\alpha = \sigma k\vec{n} \tag{4}$$

where σ is the surface tension coefficient, k is the free surface curvature and $\vec{n}$ is the interface normal vector. The semi-implicit method for pressure linked equation (SIMPLE) was used for coupling pressure and velocity in the governing equations. More details can be found in the literature [14]. To improve accuracy, the momentum equation was discretized using a second-order upwind scheme over the entire simulation domain, whereas the diffusion term was approximated by the central differencing scheme. To stabilize the interactive process, an under-relaxation factor of 0.7 for velocity, and of 0.3 for pressure, were used. The solution process was iterated until the residuals for all of the variables of the governing equation were reduced to $1x10^{-7}$. Different grids were tested until mesh-independent results were achieved. Finally, 688,656 computational grids were identified as being accurate, and least computationally demanding, number of grids needed for obtaining converged solutions. The molten metal was treated as a Newtonian incompressible fluid, and all the physical properties were assumed to be constant. The operating parameters and some of the assumptions of the models are presented in Tables 2 & 3.

7.6.2. Discussion of Modelling Results

Investigating the influence on the surface quality of the cast strip falling impingement of the molten metal on the refractory inclined plane/moving belt, plus the analysis of the meniscus behavior at the triple point, is difficult, experimentally. This is due to the inherent transient and turbulent nature of the flowing molten metal in the HSBC process. These impingements can significantly affect the surface, as well as the bulk quality, of the cast strip [2, 3, 12]. This research study is primarily focusing on investigating instabilities/turbulence that arise when molten metal encounters the moving belt. For this purpose, three belt speeds were tested i.e., 0.4, 0.8, and 1.2 (m/s), against a constant molten metal velocity of 0.8 m/s at nozzle slot outlet. The inclination angle of the refractory plane was kept at 45° in all cases. Only 0.8 m/s belt speed was tested experimentally, and the results are discussed in following paragraphs. It was difficult to perform experimental validations for other speeds 0.4 m/s and 1.2 m/s, owing to inherent limitations with the existing experimental setup. These limitations are now discussed.

Figure 4. An experiment casting AHSS steel on the pilot-scale HSBC machine.

7.6.2.1. Case-1 (Belt Velocity: 0.4 m/s, Molten Metal Initial Velocity at Nozzle Slot Outlet: 0.8 m/s)

In this case, the initial velocity of the molten metal is 0.8 m/s. However, due to gravitational acceleration, its velocity reaches approximately 1 m/s before it strikes the moving belt. Since the belt is running considerably slower than the incoming molten metal, it acts as an obstacle, forcing molten metal to transition into a subcritical flow. The transition from high to low velocity leads to a corresponding increase in the flow depth as shown in Figure 5a. The velocity profile is evaluated over a vertical line represented in Figure 5a and 6. This line is drawn where the peak of the first wave is observed. The transition in velocity can be clearly seen. These free surface instabilities travel further downstream. They were observed to be damped with distance as shown in Figure 5a.

7.6.2.2. Case 2 (Belt Velocity: 0.8 m/s, Molten Metal Initial Velocity at Nozzle Slot Outlet: 0.8 m/s)

The molten metal velocity right before it touches the moving belt is approximately 1 m/s as such the relative difference in the velocity of molten metal with respect to moving belt is only 0.2 m/s. This hindrance/resistance offered by the moving belt against the flow of the molten metal is not enough to trigger a strong jump as observed for the previous case (See Figure 5b and 6). These free surface instabilities travel further downstream, as shown in Figure 5b.

7.6.2.3. Case 3 (Belt Velocity: 1.2 m/s, Molten Metal Initial Velocity at Nozzle Slot Outlet: 0.8 m/s)

By looking into the velocity profile, over a line stretched where the first wave is observed (Figure 5c, 6), it can be clearly seen that molten metal is not able to fully acquire the belt velocity. The molten metal seemed to accelerate with the moving belt. In doing so, that part of the molten metal, adjacent to the free surface, flows with a velocity of 1 m/s, whereas further towards the belt, the molten metal velocity lies in the range of 0.9-1.2 m/s as shown in Figure 6. The non-uniform velocity profile of the molten metal over the moving belt could be a reason for these instabilities to form.

Furthermore, at higher belt speeds, the residence time of the molten metal over the moving belt decreases considerably, considering our belt length of 2.6 meters i.e. the belt length of pilot-caster operational at Met Sim Inc. [High Temperature Laboratory, Montreal, Canada]. This leads to molten metal leaving the moving belt in a mushy state. As such, it was not possible to experimentally verify the numerical predictions for 1.2 m/s.

In light of the above discussion, it can be clearly seen that the iso-kinetic feeding or near iso-kinetic feeding to be exact i.e. Case 2, appreciably suppresses the formation of molten metal/air interface fluctuations, as opposed to Case 1 and 3. This is the first time that the significance of iso-kinetic feeding is explained in the light of numerical simulations using Ansys Fluent 14.5 software. Numerical predictions for a 0.8 m/s belt speed was validated by physical experiment, and the two were found to be in good agreement.

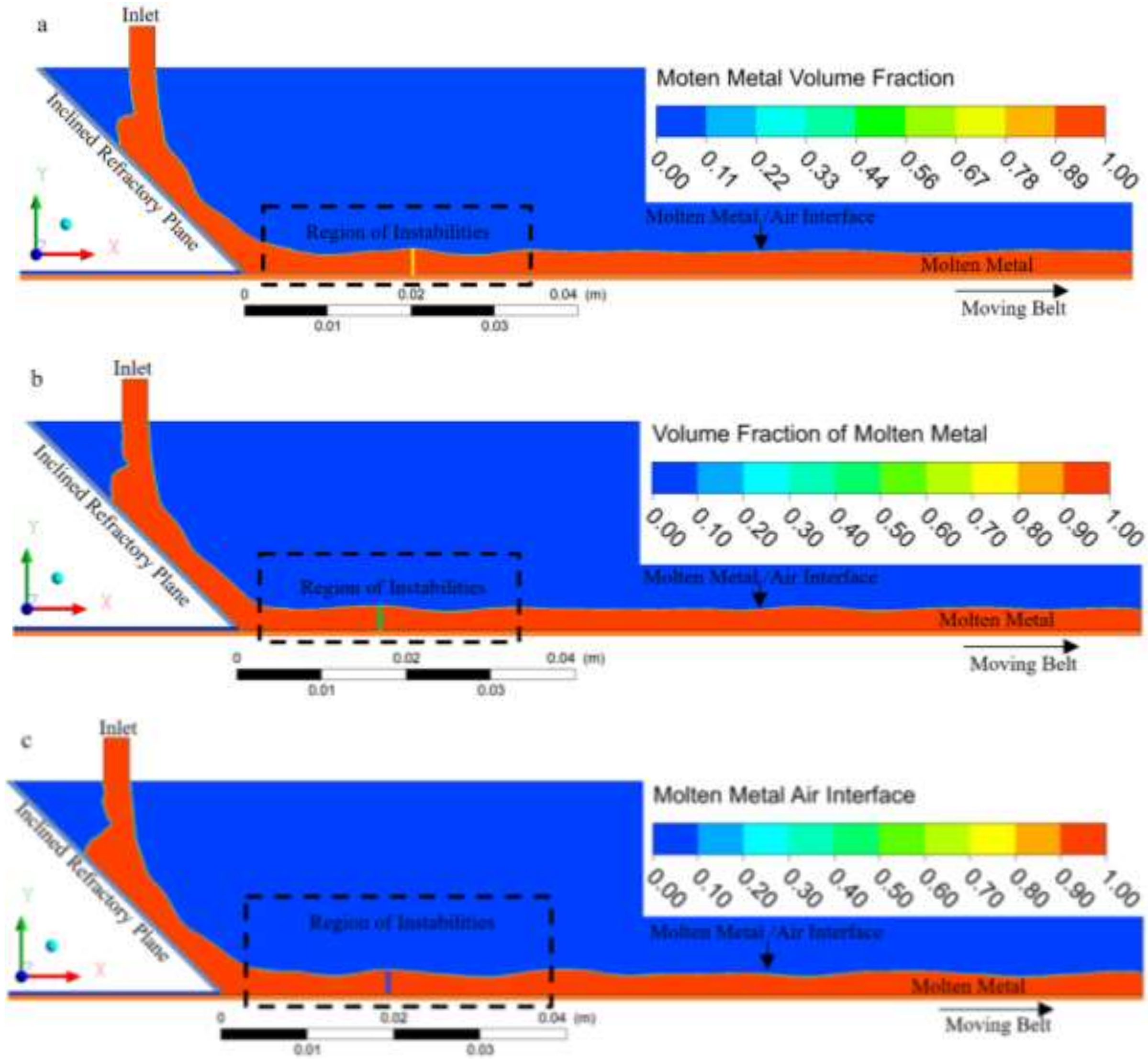

Figures 5. Molten metal flow in HSBC process with an inlet velocity of 0.8 m/s and belt moving at (a) 0.4 m/s, (b) 0.8 m/s, (c) 1.2 m/s.

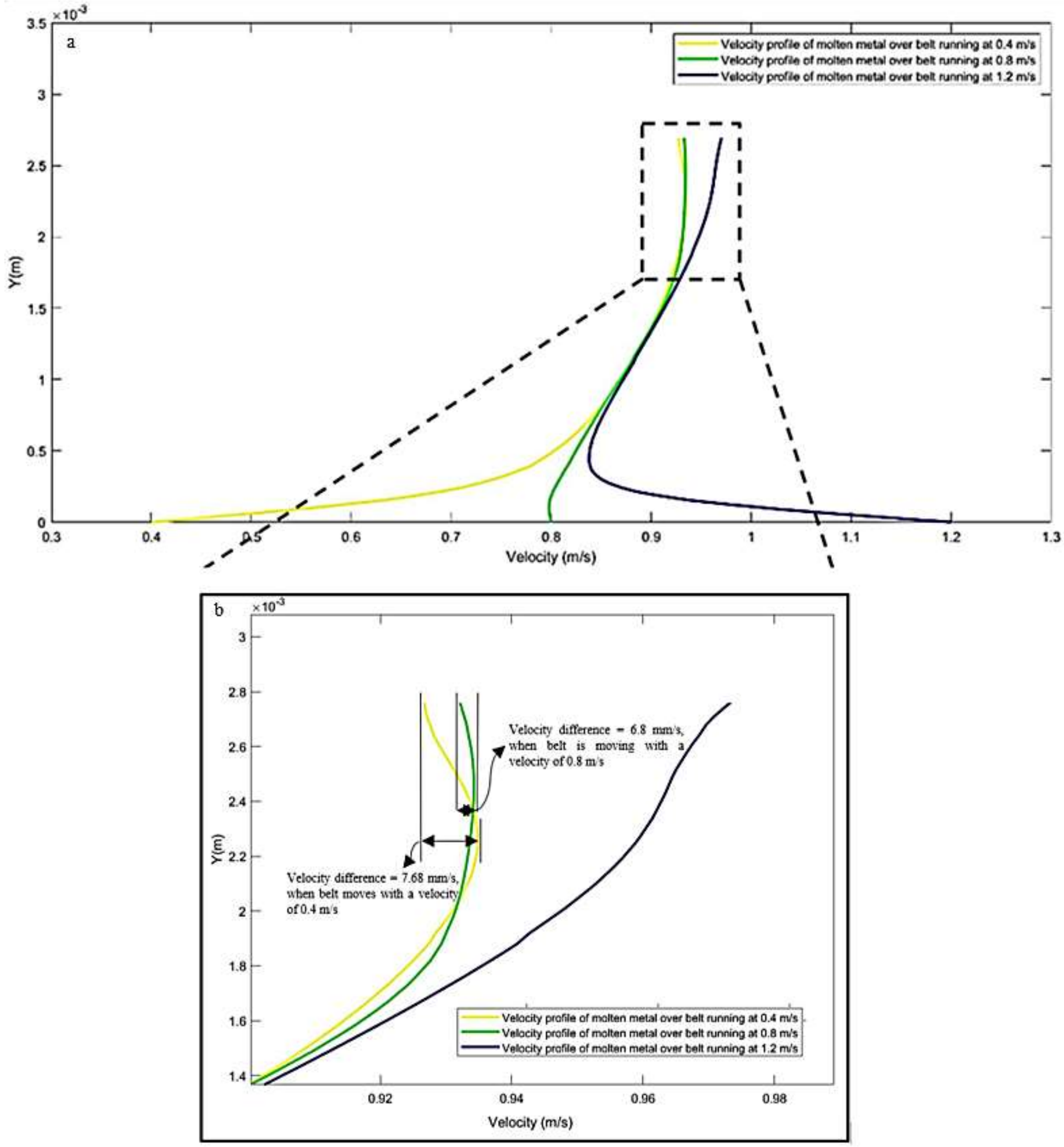

Figures 6. Transition in the velocity of molten metal over the moving belt running at three different velocities, 0.4, 0.8, and 1.2 m/s. The inlet velocity of molten metal at the nozzle slot outlet is 0.8 m/s.

7.6.3. Evaluation of Turbulent Kinetic Energies Near the Quadruple Point for Different Belt Speeds

The turbulence kinetic energies were evaluated near quadruple region i.e., the four-phase region where melt-refractory-belt-air coexist, as shown in Figure 7a, 7b, and 7c. Turbulent Kinetic Energy (TKE) is defined as mean kinetic energy per unit mass associated with eddies in turbulent flow. The TKE is used in this research study to describe the turbulence near the quadruple region [2, 12]. This turbulence can significantly affect the surface as well as bulk quality of the cast product, and the stability of meniscus near the quadruple region [2, 12].

The turbulent kinetic energy near the quadruple region generally increases with belt speed as determined by numerical simulations conducted to explain this concept [12]. In this section, different belt speeds were tested against the fixed molten metal entry velocity of 0.8 m/s, through the outlet of the slot nozzle. It has been determined (See Figure 7a, 7b, and 7c) that the TKE at the quadruple region, when the belt is moving at 0.4 m/s, is equal to 0.015 m^2/s^2. With an increase in the belt speed to 0.8 m/s, the turbulent kinetic energy value was raised to 0.02 m^2/s^2. When belt is moving at 1.2 m/s, the predicted peak turbulent kinetic energy value, at quadruple point, jumped up to 0.03 m^2/s^2.

Based on the above findings, it can be observed that the turbulent kinetic energy near the quadruple region can be reduced to 0.015 m^2/s^2 by decreasing the belt speed to 0.4 m/s. However, in order to ensure iso-kinetic feeding, the molten metal velocity at nozzle slot outlet has to be brought down to 0.4 m/s. This value corresponds to the metal head of 16mm inside the tundish from equation 5. Experimentally it has been observed that, for low metal heads (<20 mm), the molten metal experiences difficulty flowing through the thin refractory nozzle slot (250mm wide and 3mm thick). This could be caused by surface tension constraints.

$$V = \mathrm{Cd}\sqrt{2\mathrm{gh}} \qquad (5)$$

v is the velocity, h is the molten metal head inside the tundish

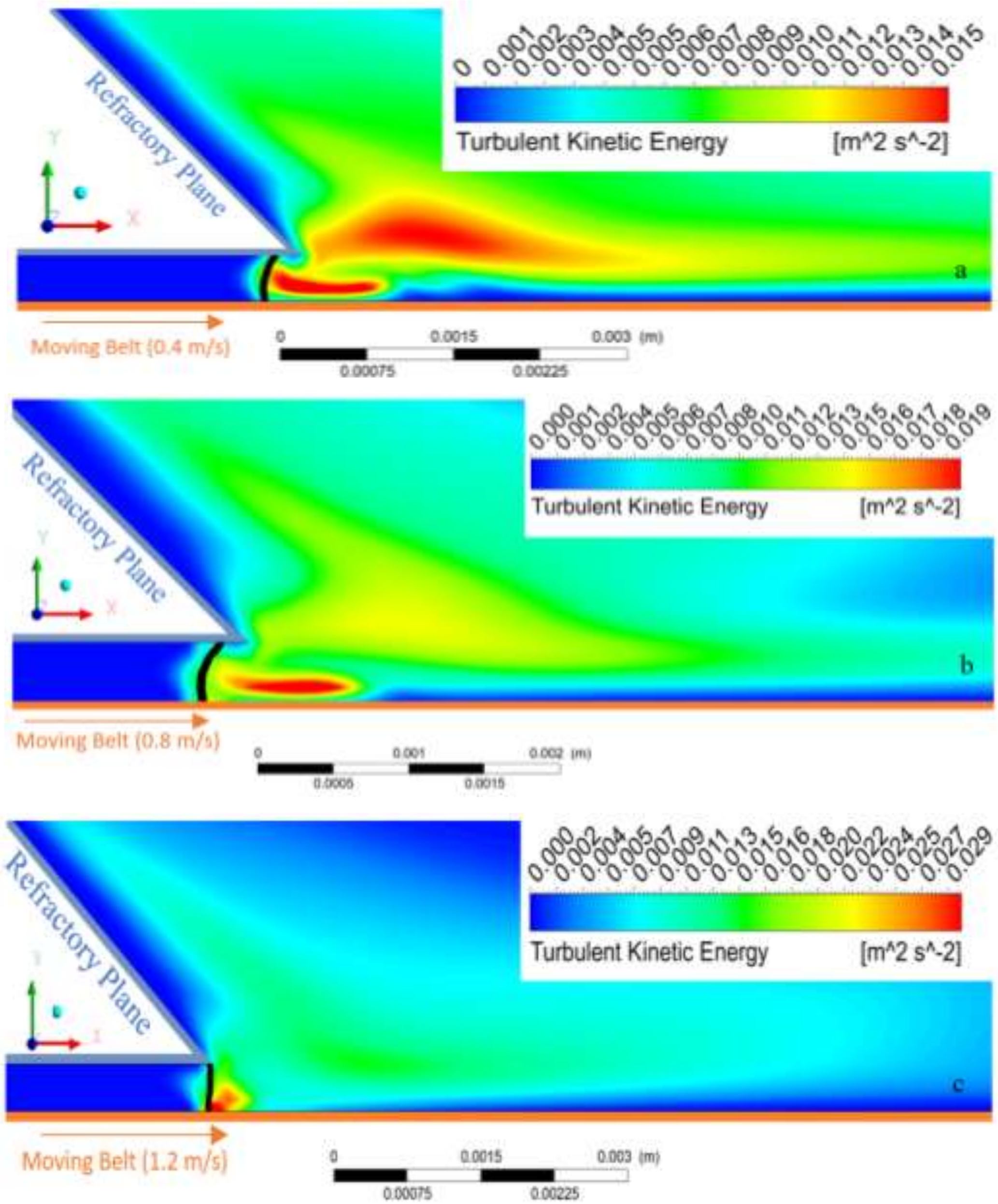

Figures 7. Turbulent kinetic energy at triple point with belt velocity (a) 0.4 m/s, (b) 0.8 m/s, (c) 1.2 m/s, molten metal velocity at nozzle slot outlet = 0.8 m/s.

7.6.4. Comparison of Turbulent Kinetic Energy Fields obtained for Single Impingement Feeding vs a Double Impingement Feeding System

Dr Ge Sa reported a peak turbulent kinetic energy value of 0.04 m^2/s^2, at the triple point, for a single impingement feeding system, as shown in Figure 8 [3]. This is significantly higher than the value obtained for the double impingement feeding system (0.015 m^2/s^2), under almost similar operating conditions (i.e., the speed of the belt and velocity of the metal at nozzle slot outlet of 0.5 m/s and 0.8 m/s, respectively).

This simply means that a double impingement feeding system has the inherent ability to lessen or moderate, the final impact of the molten metal with the moving belt in comparison with a single vertical impingement feeding system, in which the vertical motion of the molten metal is suddenly stopped by the horizontal moving belt. For a double impingement feeding system, a considerable portion of the molten metal's kinetic energy is converted into static pressure, at the point of contact with a stationary inclined refractory plane and at the moving belt, as shown in Figure 9. Also, the friction offered by the inclined refractory plane further reduces the velocity of molten metal before it impinges onto the moving belt. As a result, the final average speed of the molten metal is lower than what one would expect under constant gravitational acceleration.

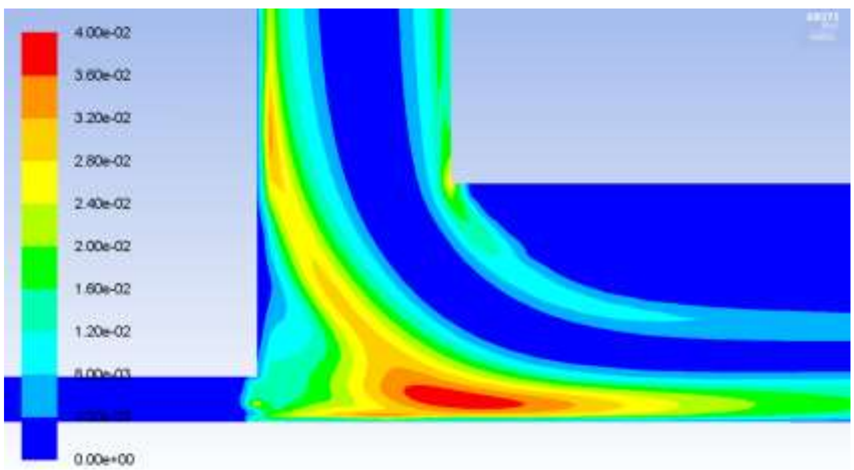

Figure 8. Turbulent kinetic energy at triple point, belt velocity = 0.5 m/s, molten metal velocity at nozzle slot outlet = 0.8 m/s adapted from [3].

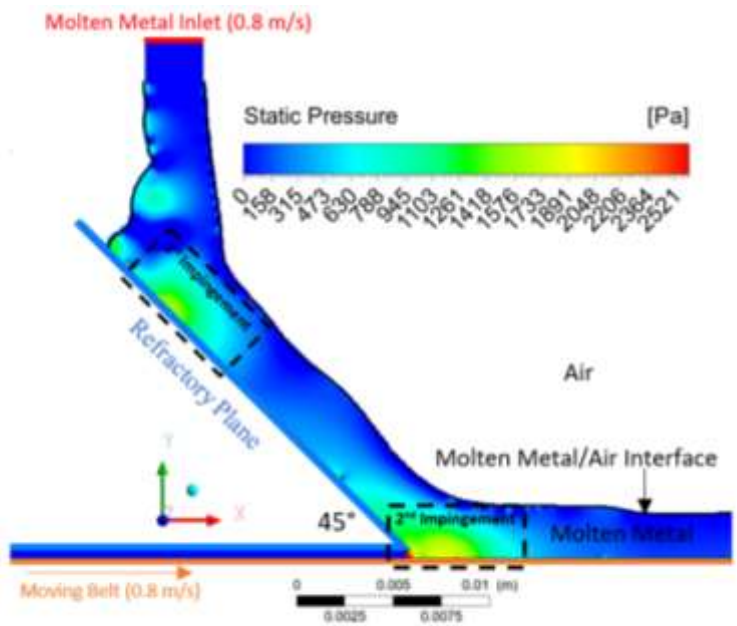

Figure 9. Static pressure at two impingement sites, the inclined refractory plane and moving belt.

7.6.5. Perturbations in the Quadruple Region and its Stability

Under the iso-kinetic feeding conditions, the molten metal/air interface at the back meniscus was observed to be stable and non-fluctuating. However, at some point in time, either due to turbulence near quadruple region, or the sharp molten metal velocity gradients that exists there, or other unknown reasons, the interface was found to be fluctuating, as shown in Figure 10. If this meniscus is highly unstable, it may lead to air entrapment phenomena in the forming strip [2]. This may degrade the bulk quality of the cast strip. One of the most obvious ways to counteract this problem is to reduce the distance between the stationary inclined refractory plane and the moving belt, so as to decease the molten metal/air interface length at quadruple region. For the numerical simulation studies and experiments, this distance was kept at 0.4mm. However, this can be further reduced, to 0.2mm, as per our experimental observations. Furthermore, the numerical simulation has predicted no backflow of the molten metal under the specified operating conditions. The experimental findings are in accord with the model predictions, where no backflow of molten metal at the quadruple region was observed.

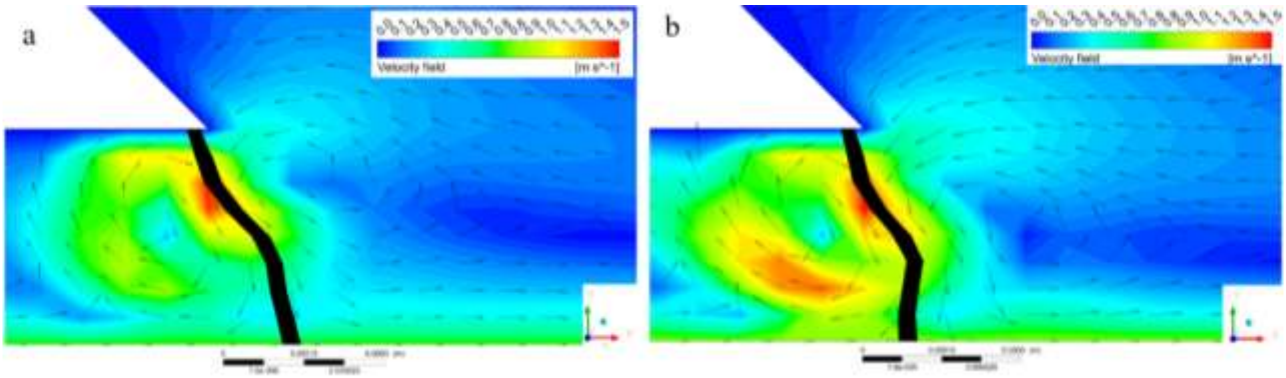

Figures 10. Velocity field, near the meniscus region and deformation of the melt/air interface at (a) 2.3 sec, (b) 2.5 seconds. The belt, as well as molten metal velocity, is equal to 0.8 m/s.

7.6.6. Solidification of the Molten Metal and Predicted Interfacial Heat Flux

The solidified shell profile, as well as the transient interfacial heat flux values, were numerically determined. The results are shown in Figure 12 and 13. There, it shows a maximum heat flux of 32 MW/m^2, which is in accord with the result reported by Sa for the strip casting of plain carbon steel via the HSBC process [3]. Also, the shape of the predicted heat flux graph approximates the results published for light metal alloys [4].

Figure 11. Cross-sectional appearance of the cast strip (mm).

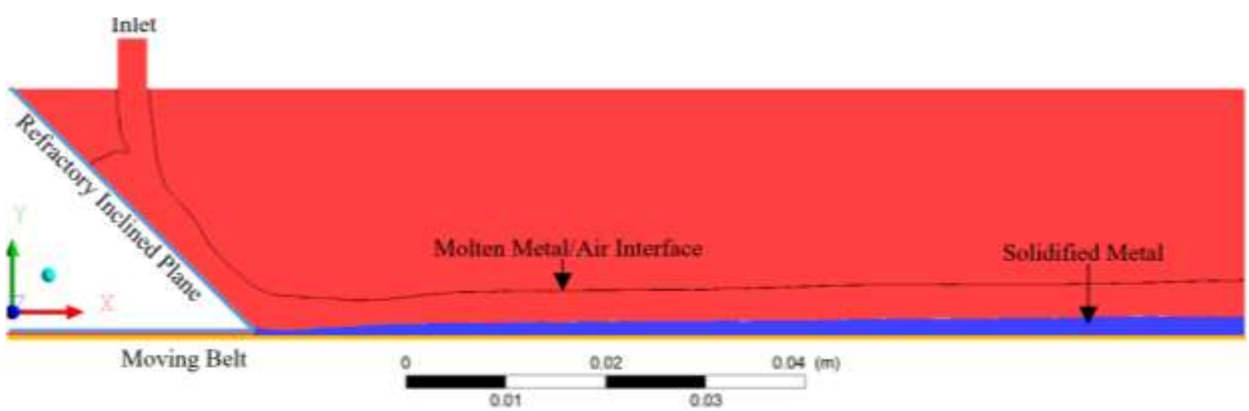

Figure 12. Predicted melt/solidified shell profile generated by the mathematical model. Liquid phase is colored red, fully solidified shell is in blue. The substrate velocity during casting is 0.8 m/s.

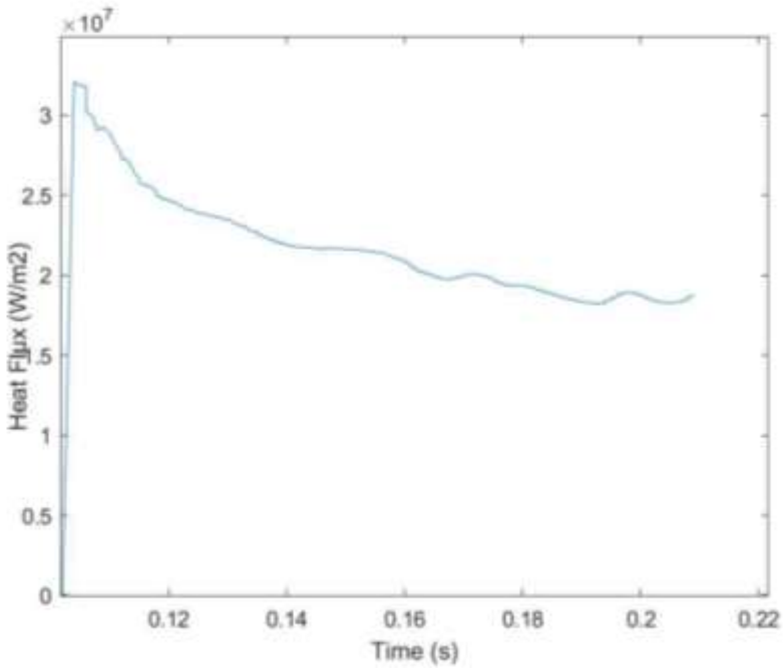

Figure 13. The predicted transient interfacial heat fluxes between liquid steel and the copper substrate.

7.6.7. Thermodynamic Calculations Using FactSage on the Selected Alloy

FactSage is a very useful tool that is commonly used to study Equilibrium and Non-Equilibrium phase transformation reactions [15]. Additionally, liquidus, solidus, and nucleation temperatures of primary and secondary phases, under equilibrium and non-equilibrium cooling conditions, can all be determined [15]. The Liquidus and Solidus temperatures of Fe-17%Mn-4%Al-3%Si-0.45%C wt.%, determined using FactSage software, were 1420℃ and 1320℃, respectively. These predictions are in accord with data in the available literature [16]. The nucleation temperatures of the different phases are shown in Figure 14a. Under Scheil cooling (non-equilibrium cooling), the microstructure, predicted by FactSage for Fe-17%Mn-4%Al-3%Si-0.45%C wt.% TWIP, is 100 % austenite. Furthermore, under equilibrium cooling, Fact Sage software has predicted ferrite, along with smaller quantities of carbides and the kappa phase. However, the former prediction is more relevant to us, since HSBC is a rapid solidification process under non-equilibrium cooling. Furthermore, the strip was water quenched after post processing, in order to avoid ferrite nucleation [17].

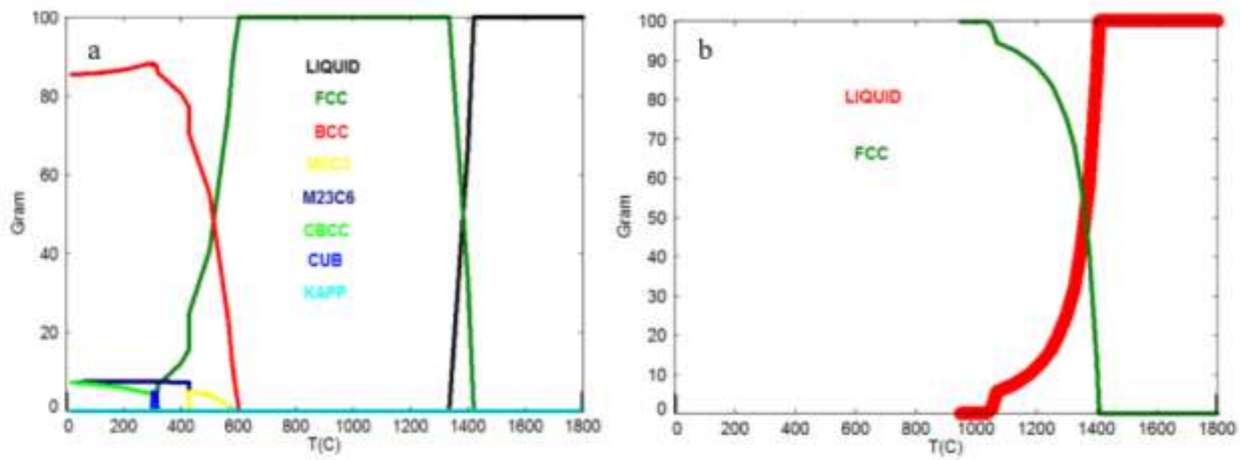

Figures 14. FactSage results: (a) The phases formed under Equilibrium Cooling, (b) under rapid, Non-Equilibrium Cooling.

7.6.8. Downstream Processing Procedures to achieve Desired Mechanical Properties in Fe-17%Mn-4%Al-3%Si-0.45%C wt.% TWIP Steel

The cast strip was hot deformed at 1150°C (above the ferrite nucleation temperature), determined using Fact Sage software (Figure 14a). The general purpose of the hot deformation is to increase the mechanical strength of the alloy via the transformation of a coarse dendritic structure into fine equiaxed grains, as shown in Figure 15. The micro/macro segregation as well as the other casting related defects were appreciably reduced by welding after the hot deformation. The material should be free of internal defects. If not the mechanical properties of the material will be lower than expected value.

After hot deformation, the samples were heated again to 1150 °C for ~ 10 minutes. This is an added procedure and was done because during hot forging, the temperature of the sample dropped to 750°C, which is the nucleation temperature for ferrite, as determined through Fact Sage software. If ferrite had nucleated, it will affect the SFE value of austenite [18-22]. After holding the samples for 10 minutes at 1150° C, the sample was quenched in water in order to obtain a fully austenitic microstructure. This was verified via optical/SEM microscopy analysis.

7.7. Characterization of the As-Cast and Heat-Treated Strip

The microstructural analysis of the as-cast and heat-treated strip was carried out using optical and scanning electron microscopy, as shown in Figure 15-16. The microstructure revealed a dendritic structure, which transformed into an equiaxed grain (48 μm) after heat treatment (Figure 15a). Annealing twins are also observed as shown in Figure 15b. The microstructure of the cold deformed sample reveals the presence of deformation twins, as shown in Figure 15c. Spark Optical Emission Spectroscopy (OES) and Energy Dispersive Spectroscopy (EDS) analyses were performed to determine the chemical composition of the strip (Table 5). Both OES/EDX confirmed the presence of Al, Si, Mn and Fe. Furthermore, no appreciable micro/macro segregation of the alloying element in the heat-treated steel sample was observed, as shown in Figure 16.

The yield (σ_{ys}) and ultimate tensile (σ_{us}) stress of hot deformed-heat-treated sample was determined using MTS model Alliance RF/200) shear testing machine [23]. For each sample, the Shear Punch (SPT) were performed at five different locations and an average value was used to document the tensile strength of the strip. These average values were found to be approximately 654 MPa and 880 MPa (Figure 17), respectively [9, 10].

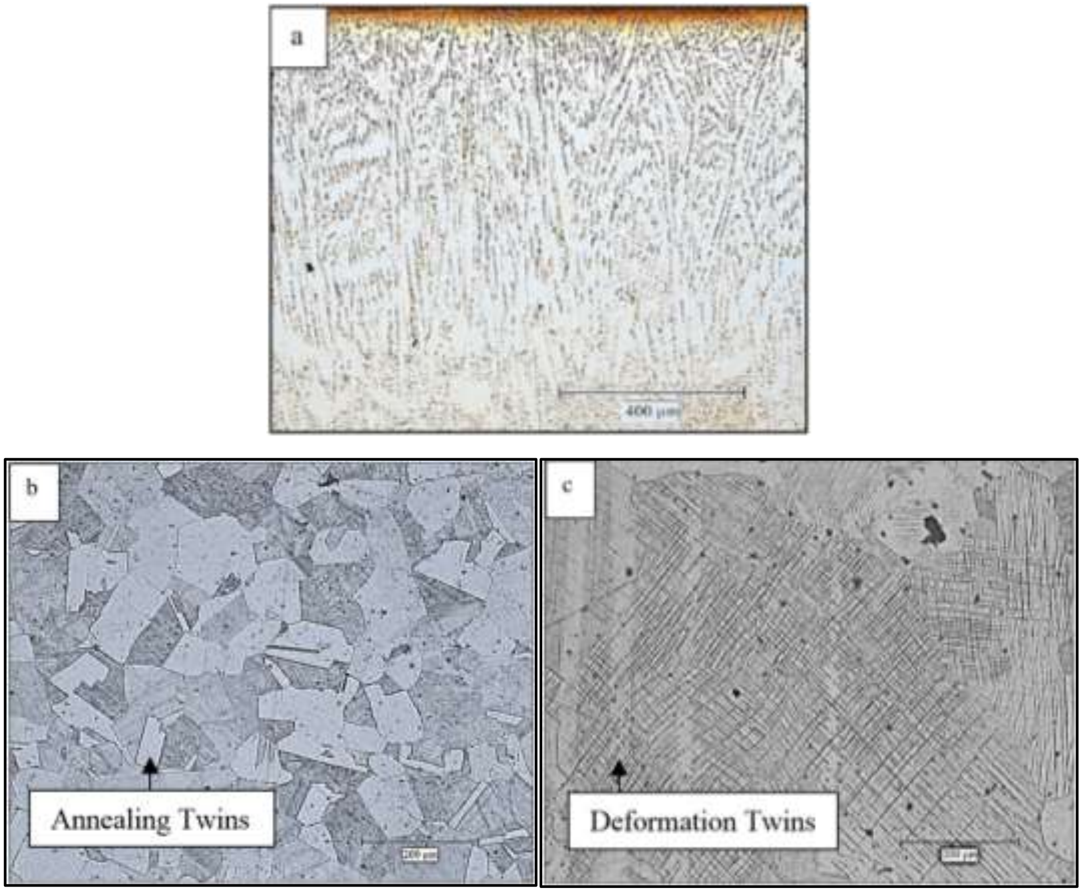

Figures 15. (a) Dendritic structure of the cast strip, (b) (100 X): HSBC cast Fe-17%Mn-4%Al-3%Si-0.45%C wt.%, soaked for 2 hours 45 min at 1150° C, followed by plastic deformation (60 %). After plastic deformation, the sample was water quenched. Annealing twins can easily be seen. (c) (200 X): Cold deformed (60 %) microstructure of Fe-17%Mn-4%Al-3%Si-0.45%C wt.% showing deformation twins after sample grinding and polishing, followed by etching using Nital (5wt% Nitric acid in alcohol).

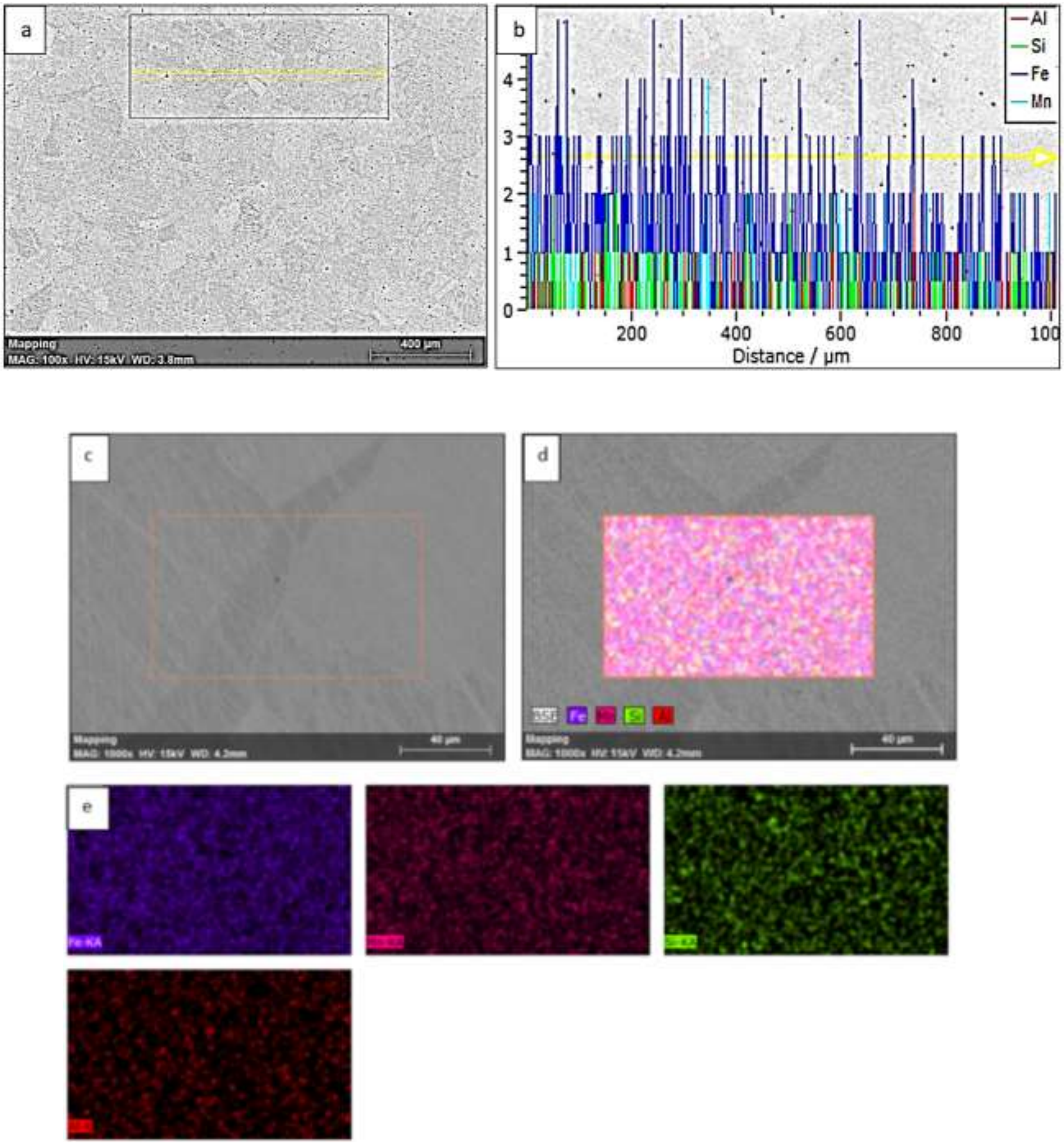

Figures 16. Secondary Electron (SE) image showing austenite microstructure after quenching heat treatment (a) 100X (b) Composition analysis along a line showing the homogenity in the distribution of alloying elements, (c) Secondary Electron (SE) image showing austenite microstructure at 1000X, (d) Composition analysis showing the homogenity in the distribution of alloying elements, (e) Elemental maps of individual alloying elements (Iron, manganese, silicon, & aluminum).

Table 4: Tensile Strength determined through Shear Punch Test (SPT).

Sample	Tensile Strength (MPa)
Sample 1	922
Sample 2	874
Sample 3	840
Sample 4	865
Sample 5	914
Average	**883**

As per the literature, steels that have tensile strength beyond 780 MPa are regarded as Advanced High Strength Steels (AHSS) [9, 10]. Based on this definition, of Fe-17%Mn-4%Al-2.5%Si-0.45%C wt.%, steel can be regarded as AHSS since it fulfills the mechanical properties criterion specified for AHSS [9, 10].

Table 5: Chemical composition (wt.%.) determination through Spark OES.

Mn	Al	Si	C	Fe
17	4	3	0.45	Remaining

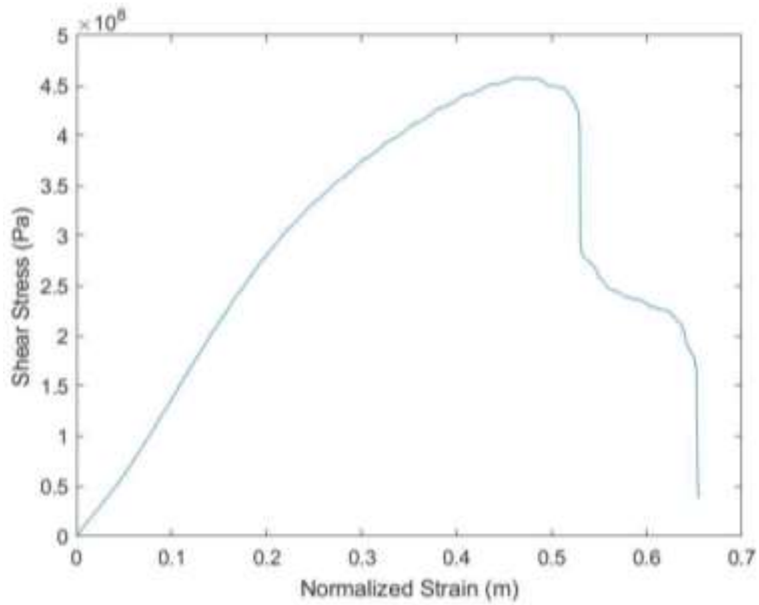

Figure 17. Shear stress vs normalized strain curve.

The surface waviness of the top/bottom sides of the strip were determined using a Nanovea 3D Profilometer. This technique works on the principle of measuring the physical wavelength of light, and directly relating it to a specific height. This ensures accurate measurement of surface roughness/finish [24]. The scan length for all the measurements was 3mm whereas the scan speed was 0.1mm/s. Ten random locations were selected for surface roughness measurements. These locations were largely selected from all over the strip. The surface profiles are almost identical to each other.

The upper surface roughness lies within the 100 μm (±50 μm) range, as shown in Figure 18a and 18c. Additionally, pin holes/blow holes were not detected on the surface of the cast strip, unlike continuously cast products, which can possess defects on their surfaces, and require surface grinding prior to hot rolling.

The strip bottom surface roughness was also measured, and lay in the 30μm range (±15 μm). As evidenced by the results of the line scans, the bottom surface quality is much superior to the top surface. This observation is credited to the fact that the molten metal is in direct contact with the moving belt, and conforms to its shape during the solidification process. On the other hand, the top surface of the cast strip is exposed to the atmosphere and is affected by disturbances in the flows of the molten metal.

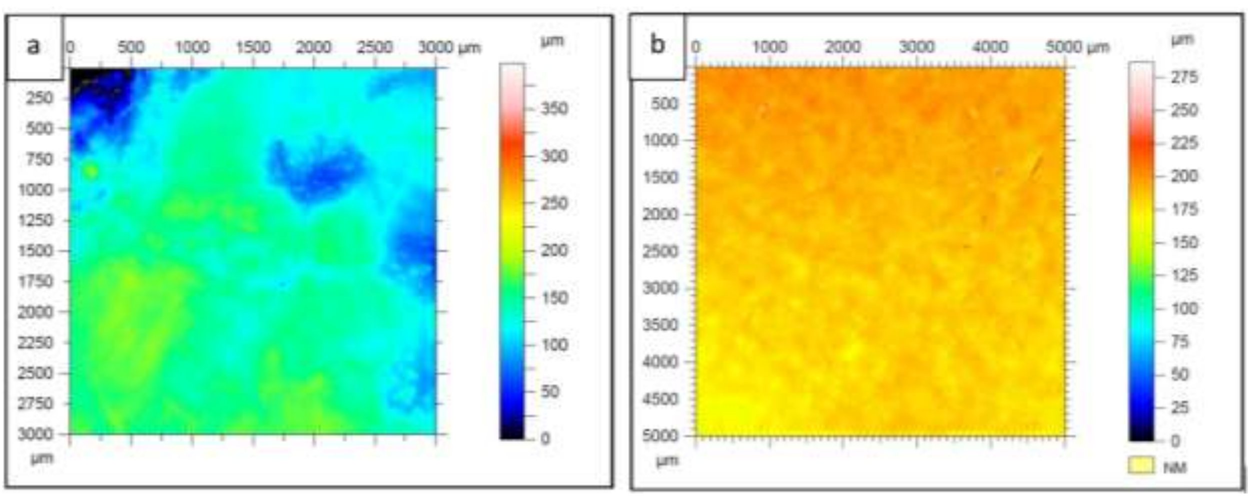

Figures 18. 3D profilometry results, a) strip top surface topography and b) strip bottom surface topography

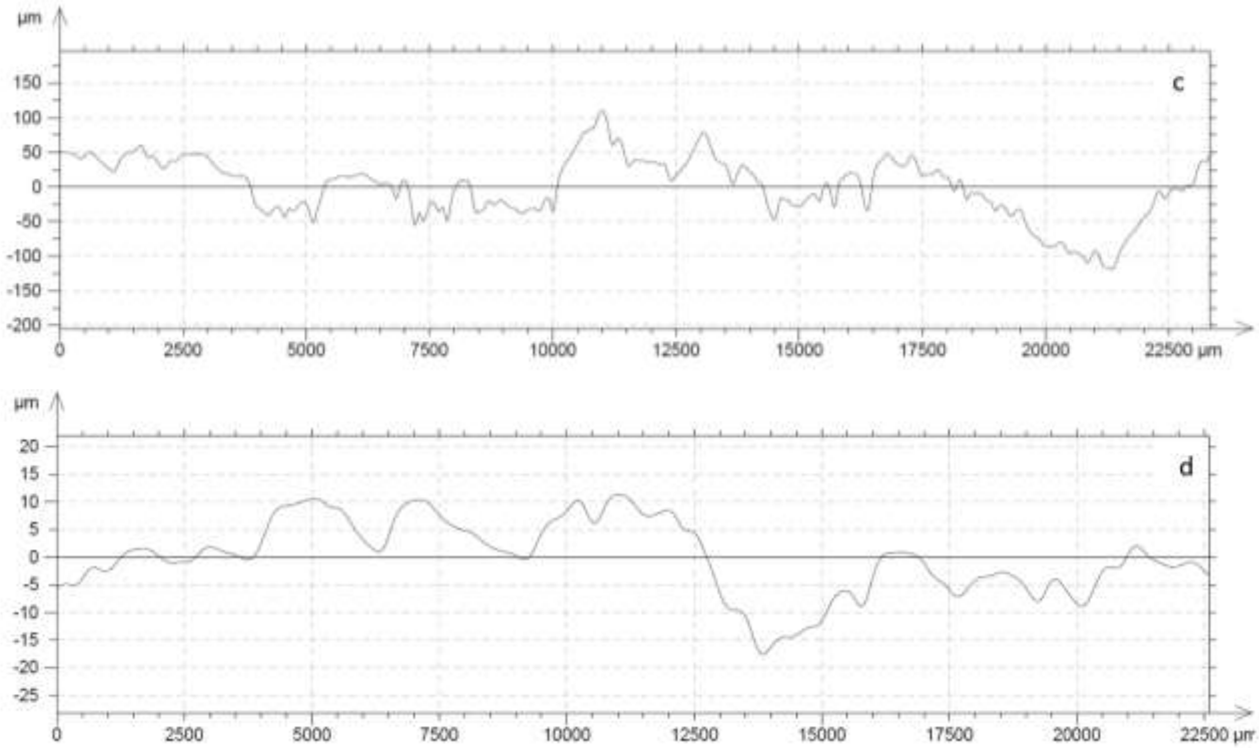

Figures 18. 3D profilometry results, c) measured top surface roughness (d) measured bottom surface roughness.

7.8. Conclusions

The following conclusions are drawn from this research.

1. For a fixed velocity of the molten metal at the slot nozzle outlet, the turbulent kinetic energy of molten metal near the quadruple region was observed to be increasing with belt speed.
2. In order to achieve high surface quality strip, the flow of the molten metal over the moving belt should be iso-kinetic, a condition in which belt velocity approaches the incoming molten metal velocity from delivery system.
3. The peak turbulent kinetic energy value, at the quadruple region, for a single impingement feeding system is 0.04 m^2/s^2.This is significantly higher than the value obtained for the double impingement feeding system (0.015 m^2/s^2), under similar operating condition i.e., the speed of the belt and velocity of the metal at nozzle slot outlet of 0.5 m/s and 0.8 m/s, respectively. This simply means that the double impingement feeding system has the inherent ability to lessen or moderate the final impact of the molten metal with the moving

belt, as opposed to a single impingement feeding system where the molten metal is suddenly stopped by the horizontally moving belt.

7.9. Acknowledgments

The authors would like to acknowledge the financial support received from the Natural Sciences and Engineering Research Council of Canada (NSERC), and the International Advisory Board of supporting companies of the McGill Metals Processing Centre (MMPC), in carrying out this research. The authors would also like to acknowledge the support received from ANSYS Inc. for software licensing to facilitate this research.

7.10 References

1. M. Celikin, D.H. Li, M. Isac and R.I.L. Guthrie, Horizontal Single Belt Casting (HSBC) of Al-Mg-Sc-Zr Alloys, Light Metals, 2013, p. 1037-1040.
2. M. Xu, M. Isac and R.I.L. Guthrie, A Numerical Simulation of Transport Phenomenon During the Horizontal Single Belt Casting Process Using an Inclined Feeding System, Metallurgical and Materials Transactions B, 2018, p. 1003-1013.
3. G. Sa, S. Chang, T. Wang, L.E. Calzado, M. Isac, J. Kozinski and R.I.L. Guthrie, Mathematical Modeling and Microstructure Analysis of Low Carbon Steel Strips Produced by Horizontal Single Belt Casting (HSBC), Metallurgical and Materials Transactions B, 2016, p. 1893-1904.
4. R.I.L. Guthrie and M. Isac, Horizontal Single Belt Casting of Aluminum and Steel, Steel Research International, 2014, p.1291-1302.
5. S. Ge, M. Isac and R. I. L. Guthrie., Progress of Strip Casting Technology for Steel; Technical Developments, ISIJ Int., 2013, p. 729-742.
6. J. Wans, C. Geerkens, H. Cremers, U. Grethe, P. Juchmann and R.S. Jurgensen, Belt Casting Technology-Experiences Based on the World Wide First BCT Caster, International part of the ABM week, 2015, p.111-117.
7. K.H. Spitzer, F. Ruppel, R. Viscorova, Direct Strip Casting (DSC) - An Option for the Production of New Steel Grades, Steel Research International, 2016, p. 724-731.

8. E. Evin, M. Tomas, B. Karalinic, E. Wessely, J. Kmec, Design of dual phase high strength steel sheets for auto body, DAAAM International Scientific Book DAAAM International Scientific Book, 2013, p.767-786.
9. S.T. Pisarik, D.C. Van Aken, K.R. Limmer, Thermodynamics, and crystallography of the $\gamma\rightarrow\epsilon\rightarrow\alpha'$ transformation in Fe-Mn-Al-Si-C steels, AISTech Iron and Steel Technology Conference Proceedings, 3, 2014, p. 3013- 3024
10. K. T. Park, K H. Jin, H. S. Sang, K.L. Choi, C.S. See, Stacking fault energy and plastic deformation of fully austenitic high manganese steels: effect of Al addition, Materials Science and Engineering A, 2010, p.3651-3661.
11. G. Olson, M. Cohen, A mechanism for the strain induced nucleation of martensitic Transformations, Journal of the Less Common Metals, 1972, p. 107-118.
12. M. Xu, M. Isac, R.I.L. Guthrie, Transport Phenomena during Horizontal Single Belt Casting Process using an Optimized Inclined Feeding System, Ironmaking & Steelmaking, 2018, p.878-885.
13. W. Bleck, D. Raabe, H. Dong, The 1st International Conference of High Manganese Steel, 2011.
14. FLUENT 14.5 Manual, ANSYS Inc., 10 Cavendish Court, Lebanon, NH, USA.
15. A.D. Pelton, Phase Diagrams and Thermodynamic Modeling of Solutions, 5th Edition, 2019.
16. X. Li, C. Wang, L. Lu, Microstructure and Impact Wear Resistence of TiN Reinforced High Manganese Steel Matrix, Journal of Iron and Steel Research, International, 2012, p.60-65.
17. N. Medvedeva, First Principles Study of Mn, Al and C Distribution and their Effect on Stacking Fault Energies in FCC Fe, Journal of Alloys and Compounds, Journal of Alloys and Compounds, 2014, p. 475-482.
18. A.O. Zambrano, Stacking Fault Energy Maps of Fe-Mn-Al-C-Si Steels: Effect of Temperature, Grain Size, and Variations in Compositions, Journal of Engineering Materials Technology, 2016, p.905-1010.
19. W. Bleck, O. K. Phiu, Effects of Microalloying in Multi Phase Steels for Car Body Manufacture, Microstructure and Texture in Steels, Microstructure and Texture in Steels, 2009, p.145-163.

20. D. Pierce, J. Jimenez, J. Bentley, The influence of manganese content on the stacking fault and austenite/ε-martensite interfacial energies in Fe–Mn–(Al–Si) steels investigated by experiment and theory, Acta Material, 2014, p.238-253.
21. S.J. Lee, Y.K. Lee, A. Soon, The Austenitic/ϵ Martensite Interface: A First Principles Investigation of the fcc Fe (111)/hcp Fe (0001) System, Applied Surface Science, 258, 2012, p.9977-9981.
22. K. L. Meyer, U. Brux, G. Frommeyer, O. Grassel, Stress Deformation of High Manganese (Al, Si) TRIP and TWIP Steels, Journal De Physique iv (J PHYS IV), 2003, p.189-199.
23. A.M. Fall, H. Monajati, A.R. Khodabandeh, M.H. Fesharaki, Local Mechanical Properties, Microstructure, and Microtexture in Friction Stir Welded Ti-6Al-4V Alloy, Materials Science and Engineering A, 2015, p.166-176.
24. Surface roughness determination using 3D Nanovea profilometer, Available https://nanovea.com/profilometry-roughness-finish.

Chapter 8

8.0. Conclusions

This doctoral thesis has discussed the production of aluminum Alloy (AA6111), and Advanced High Strength Steels (AHSS) strips via the HSBC process. For this purpose, various transport phenomena occurring during the operation of the HSBC process were studied, since the quality of the cast product is heavily dependent on these complex phenomena. The most important among them are the fluctuations of the molten metal/air interface on: the refractory inclined plane, the moving belt, and in the quadruple region. Apart from these, it is equally essential to carry out an in-depth study to critically examine the transfer of heat through the molten metal, as well as the solidification behavior of the molten metal over the moving belt.

In the present research thesis, the turbulent fluid flow in the HSBC process was modeled using Ansys Fluent 14.5 software. In order to obtain the desired results, the correct amount and type of the meshes were used, followed by defining initial and boundary conditions. In the end, numerical models and methods were selected to solve the system of governing equations i.e., the continuity, momentum, and energy equations. In this research thesis, the k-ω Shear Stress Transport model for turbulence was used, as it has the inherent ability to precisely model/predict near-wall flows.

Additionally, thermodynamic modeling was also conducted, so as to determine the deformation behavior of AHSS. Stacking Fault Energy (SFE) was calculated using the Olson-Cohen modeling approach, whilst FactSage software was used to study the nucleation temperatures of different phases present in the AHSS steels. Though both modeling and experimental results have already been discussed in previous chapters of this research thesis, some of the salient aspects are summarized hereunder:

The HSBC process is a gravity-driven flow system. This is to say that it does not use a closed mold or twin rolls, or twin belts, to define the shape of the forming as-cast plate. It was determined that many operating parameters, such as the feeding rate of the molten metal, the inclination of the refractory plane, the speed of the moving belt, and the transient heat flux through the plate, and separation distance between the back wall's bottom surface and the moving horizontal belt in the quadruple phase region, all play important roles in assuring high surface quality strip.

As explained in earlier chapters, the molten metal, while impinging/streaming over the inclined refractory plane, transitions from supercritical to subcritical velocities, creating Hydraulic Jumps. This sudden jump of the molten metal head due to this transition, leads to the generation of free surface waves, which travel further downstream, potentially harming the upper surface quality of the cast product. This phenomenon was carefully studied by implementing the VOF multiphase model. The refractory plane angle was varied from 30° - 60°, at a constant feeding rate, and velocity i.e., 0.8m/s. The depth, as well as the velocity of the molten metal at the hydraulic jump, was also determined. Based on the simulation results, the 45° inclined refractory plane was identified as the most suitable for achieving high surface quality strip. This is owing to the most rapid reduction in the fluctuations of the molten metal/air interface, near to the top of the inclined refractory plane and at the horizontally moving belt. It leads to the casting of defect-free material i.e., less porosity.

Furthermore, it was also determined that the inclined refractory plane of the double impingement feeding system has the tendency to lessen, or moderate, the final impact of molten metal on the moving belt, as opposed to the single impingement feeding system, where the vertical flow of molten metal encounters a sudden stoppage by the moving horizontal belt. This concept can be explained on the basis of the peak kinetic energy values of turbulence, documented for the single impingement feeding system at the triple point (0.05 m^2/s^2), which was significantly higher than the values obtained for the double impingement feeding system, in this research study (0.02 m^2/s^2) for steel casting.

Additionally, it has been concluded that in order to achieve high-quality plate, the belt velocity should preferably be, more or less, nearer to that of the molten metal velocity falling from the slot nozzle (iso-kinetic feeding). However, owing to the difficulty in achieving complete iso-kinetic feeding, a minor difference between them does exist, but that is unlikely to affect the strips' surface quality. This concept has been explicitly explained by evaluating the velocity profile at three different locations, one at the inclined refractory plane, the other two at 11mm and 75mm from the triple point. Closer to the triple point, the molten metal was observed to be transitioning from a high to a low-velocity flow, characteristic of a hydraulic jump. However, no such transition was noticed at the location which was farther away from the triple point. This occurred due to annihilation of free molten metal surface waves, as discussed in previous chapters.

Additionally, it was identified that in order to produce a thick plate, the velocity of the molten AA6111 alloy at the nozzle slot outlet must be raised, together with a corresponding decrease in the belt speed, in order to increase the net heat to be extracted through the 2.6 m belt. Under these operating conditions, free surface waves resulted due to the sudden impact of molten metal with the slow-moving belt, are not affecting the surface quality. This happens due to the temperature of the molten metal/air interface which remained above that of the liquidus temperature for a considerable distance/time, providing enough time to these surface waves to level off and to disappear with distance, as per the results of the numerical simulations. Additionally, heat transfer analysis was also carried out in order to predict the interfacial heat flux through the moving belt.

Last, but not least, a microstructural study was also carried out for AA6111 aluminum alloy strips. This revealed a fine equiaxed grain structure, with an average size of 85 µm. Also, the grain size at the bottom and the top of the AA6111 strip was observed to be 60 and 100 µm, respectively, due to different rates of cooling at the top and bottom surfaces of the strip. X-Ray micro-analyses revealed that inter-metallics uniformly dispersed inside the grain structure have the following stoichiometry: $Al_{17}Cu_2Mg_3Si_3$, $Al_{20}Cu_2Mg_{2.5}Si_5$, whereas the elongated inter-metallics distributed at the grain boundaries are in the category of $Al_{17}(CuMg)_2(FeMn)Si_2$, or $Al_{25}(CuMg)_{4.5}(FeMn)Si_5$.

For AHSS, both TRIP, as well as TRIP-TWIP steel strips, were produced. The AHSS strip, as cast, comprised a dendritic microstructure. The final microstructure resulting after the AHSS steels heat treatment followed by cold deformation, revealed annealing as well as deformation twins (TWIP steel), whereas the TRIP steel consisted of a mix of microstructures after cold deformation i.e., epsilon martensite, ferrite, and austenite.

Based on the above-mentioned findings, it can be concluded that HSBC process is capable of producing high-quality AA6111 aluminum alloy and AHSS strips, which could result in considerable economic benefits towards the production of sheet materials, in an environmentally conscious way, vs CCC or TSC steels, or DC cast aluminum.

8.1. Contribution to Original Knowledge

This research has been aimed at developing AA6111 alloy, and AHSS strip material using the HSBC process. The ferrous and non-ferrous grades were selected for the current research, based on their application in the automotive industries. In the HSBC process, the molten metal interacts with the inclined refractory plane and the moving belt. It is due to these impingements that the fluid flow in the HSBC process is highly unstable and turbulent, whilst examining its behavior experimentally, is extremely difficult and time-consuming. Similarly, these instabilities give rise to molten metal/air interface fluctuations, and render the meniscus at the quadruple region highly unsteady. Numerical simulation, therefore, is an approach used in this thesis to analyze these complex transport phenomena, as these fluctuations can significantly affect the surface, as well as the bulk quality of the cast strip. Solidification phenomenon was also considered in the present study, so as to numerically determine the heat flux. The following outcomes of this research study are claimed to be original, having been performed for the first time.

1. The development of 2D/3D models, incorporating the effects of turbulence, partial solidification, multiphase phase flow, and interface tracking, in order to process thin strips of AA6111 alloy, and AHSS alloy, via Horizontal Single Belt simulator, and HSBC pilot-scale, manufacturing technique, employing a double impingement feeding system. The models were found to accurately predict strip thickness, interfacial heat flux, the phenomenon of surface wave generation and its subsequent annihilation, and finally, to explain the inward flow of the molten metal in order to counteract shrinkage.

2. The important parameters that could cause free molten metal surface waves to be generated in the HSBC process are (a) the inclination of the refractory plane, (b) the molten metal velocity at the nozzle outlet, (c) the speed of the moving belt, (d) the physical properties of the molten metal i.e., density, viscosity, surface tension and (e) the rate at which the metal is solidifying on the chilled moving belt. The latter directly depends on the heat flux

through the moving belt. These operating parameters need to be precisely optimized in order to achieve high surface quality products.

3. Since the balance of the forces in the HSBC process is confined to gravity, surface tension, and friction, it was determined that, reducing the inclination angle of the refractory plane lower than 45°, severely increases the backflow of the molten AHSS upstream of the inclined refractory plane, thereby leading to the entrapment of air inside the strip, which is undesirable. Furthermore, the molten metal stream also becomes unstable when the inclination angle of the refractory plane reduces to 30° , or less.

4. It has been observed that these instabilities in the flow of the molten metal caused the generation of free surface waves, which travel downstream. This can be avoided if the inclination angle of the refractory plane increases to 45° or more, and the velocity of the moving belt approximates the incoming metal velocity from the delivery system i.e., iso-kinetic feeding.

5. The free surface waves on AA6111 alloy strip respectively, produced under non-isokinetic feeding conditions, are observed to be annihilated with distance downstream, thereby not affecting the surface quality. These non-isokinetic feedings (the increase in molten metal velocity at the nozzle slot outlet with respect to the belt speed) are desirable for producing thicker strips, which can afterward, be hot deformed to achieve appropriate mechanical properties and desired finish gauge thicknesses sheet materials.

6. The center shrinkage depressions observed in the center of the cast AA6111 products can be reduced by increasing the metal head in the tundish beyond 50 mm. Its occurrence can be ascribed to a lack of molten metal feeding towards the center, due to a reduction in the inward flow of the molten metal towards the center, at low metal heads.

7. The modification done on the HSBC simulator included (a) increasing the melting capability of the induction furnace, (b) designing a double impingement feeding system and, (c) installation of the moving side dams. The modifications done on the pilot-scale

HSBC were as follows. (a) the design of a new alumina refractory nozzle slot, as part of the metal feeding system, (b) enlarging the strip guidance system, improving the cooling capability of the HSBC machine to be able to cast strips of 250 mm width, (c) significantly extending the length of the run-out table.

8. The casting of AA6111 aluminum alloy, 250 mm wide and 6 mm thick strip was conducted for the first time. Additionally, for AHSS, appropriate heat treatment procedures were devised, and these were verified by the resultant microstructures, and their final mechanical properties.

References

1. Burger, G.B., Gupta, A.K., Jeffrey, P.W., Lioyd, D.J., Microstructure Control of Aluminum Sheet Used in Automobile Applications, International Metallographic Society Symposium on Microstructural Characterization of Light Weight Materials for Transportation, Materials Characterization, pp. 23-39, 1995.
2. Tamarelli, C.M., The Evolving Use of Advanced High Strength Steels for Automotive Applications, Southfield (MI): Steel Market Development Institute (SMDI), 2011.
3. Davies G, Environmental and Safety Considerations, Materials for Automobile Bodies, pp. 309-356, 2012.
4. Hilditch, T.B., De Souza, T, Hodgson, Properties and Automotive Applications of Advanced High-Strength Steels (AHSS), Welding and Joining of Advanced High Strength Steels (AHSS), pp. 9-28, 2015.
5. Benedyk, J.C., Aluminum Alloys for Light Weight Automotive Structures, Woodhead Publishing Limited, Illinois Institute of Technology, USA, 2010.
6. Guthrie, R.I.L., Isac, M., Horizontal Single Belt Casting of Aluminum and Steel, Steel Research International, pp. 1291-302, 2014.
7. Louhenkilpi, S., Industrial Processes, Treatise on Process Metallurgy, Elsevier, 2014.
8. Sa, G., Numerical and Physical Modeling of the Horizontal Single Belt Casting (HSBC) Process, Ph.D. Thesis, Department of Mining and Materials Engineering McGill University, 2015.
9. Strauss, K., Applied Science in the Casting of Metals, 1st Edition, 1970.
10. Baokuan, Li., Tsukihashi, F., Effects of Electromagnetic Brake on Vortex Flows in Thin Slab Continuous Casting Mold, ISIJ International, pp. 1833-1838, 2006.
11. Ge, S., Isac, M and R. I. L. Guthrie., Progress of Strip Casting Technology for Steel; Technical Developments, ISIJ Int., 2013.
12. Ge, S., Isac, M and R. I. L. Guthrie., Progress of Strip Casting Technology for Steel; Historical Developments, ISIJ Int., 2012.
13. Davies G, The Role of Demonstration, Concept and Competition Cars, Materials for Automobile Bodies, pp. 145-191.
14. The Evolving Use of Advanced High-Strength Steel for Automotive Applications, Steel Market Development Institute, www.autosteel.org.

15. Dieter, G., Mechanical Metallurgy, SI Metric Edition, McGraw–Hill, London, UK, 1988.
16. Callister, W. D., Fundamentals of Materials Science and Engineering, John Wiley & Sons, Hoboken, NJ, USA, 2001.
17. Hirsch, J., Skrotzki, B., Gottstein, G., Aluminum Alloys, Their Physical and Mechanical Properties, Wiley-VCH, Weinheim, Germany, 2008.
18. Gottstein, G., Physical Foundations of Materials Science, Springer, Berlin, Germany, 2004.
19. Humphreys, F. J., Hatherly, M., Recrystallization and Related Annealing Phenomena, Elsevier, Oxford, UK, 2004.
20. Paul, E., Black, J. T., Kohser, R. A., Materials and Processes in Manufacturing, John Wiley & Sons, Hoboken, NJ, USA, 2003.
21. Sanders, R. E., Technology Innovation in Aluminum Products, The Journal of Minerals, pp. 21–25, 2001.
22. Ramachandran, T. R., Advances in Aluminum Processing and Its Automotive Application, Workshop Lecture Notes, Indian Institute of Metals, Pune Chapter, pp. 41– 44, 2006.
23. Dons, A. L., The Alstruc Homogenization Model for Industrial Aluminum Alloys, Journal of Light Metals, pp.133–148, 2001.
24. Engler, O., Hirsch, J., Texture Control by Thermomechanical Processing of AA6xxx Al–Mg–Si Sheet Alloys for Automotive Applications - A Review, Materials Science and Engineering A, pp. 250–262, 2002.
25. Kuijpers, N. C. W., Kool, W. H., Koenis, P. T. G., Nilsen, K. E., Todd, I., Assessment of Different Techniques for Quantification of α-Al(FeMn)Si and β-AlFeSi Intermetallics in AA 6xxx alloys," Materials Characterization, pp. 409–420, 2002.
26. Zhang, S., Xiong, B., Zhang, Y., Li, X., The Microstructure Evolution of AA6111 Aluminum Alloy during Homogenization Treatment, Materials Science Forum, Trans Tech publications, pp. 223-228, 2013.
27. Zhong, H., Rometsch, P.A., Estrin, Y., Effect of Alloy Composition and Heat Treatment on Mechanical Performance of 6xxx Aluminum Alloy, Transactions of Non-Ferrous Metals Society of China, pp. 2174-2178, 2014.
28. Prillhofer, R., Rank, G., Berneder, J., Antrekowitsch, H., Property Criteria for Automotive Al-Mg-Si Alloys, Materials, pp. 5047-5068, 2014.

29. Wilsdorf, D., Theory of Plastic Deformation, Materials Science and Engineering A, pp. 1–42, 1989.
30. Schikorra, M., Donati, L., Tomesani, L., Tekkaya, A. E., Microstructure Analysis of Aluminum Extrusion: Prediction of Microstructure on AA6060 alloy, Journal of Materials Processing Technology, pp. 156–162, 2008.
31. Lapovok, R., Timokhina, I., McKenzie, P. W. J., Donnell, R. O., Processing and Properties of Ultrafine Grain Aluminum Alloy 6111 Sheet, Journal of Materials Processing Technology, pp. 441–450, 2008.
32. Lee, W. S., Shyu, J. C., Chiou, S. T., Effect of Strain Rate on Impact Response and Dislocation Substructure of 6061-T6 Aluminum Alloy, Scripta Materialia, pp. 51–56, 2000.
33. Mukhopadhyay, P., Samajdar, I., Sources of Recrystallized Grains and Their Contributions in Recrystallization of an AA3104 Aluminum alloy, Transactions of the Indian Institute of Metals, pp. 329–339, 2008.
34. Avner, H., Introduction to Physical Metallurgy, TATA Mc-Graw Hill, New Delhi, India, 2001.
35. Esmaeili, S., Lloyd, D. J., Modeling of Precipitation Hardening in Pre Aged AlMgSi(Cu) alloys, Acta Materialia, pp. 5257–5271, 2005.
36. Chakrabarti, D. J., Laughlin, and D. E., Phase Relations and Precipitation in Al–Mg–Si Alloys with Cu Additions, Progress in Materials Science, pp. 389–410, 2004.
37. Andersen, S. J., Zandbergen, H. W., Jansen, J., Træholt, C., Tundal, U., Reiso, O., The Crystal Structure of the β-Phase in Al–Mg–Si Alloys," Acta Materialia, pp. 3283–3298, 1998.
38. Shana, Y.Z., Zhengb, L.U., Huab, X.Y., Longb, D.S., Shenga, L.C., Effects of RRA Treatments on Microstructures and Properties of a New High-strength Aluminum-Lithium Alloy, School of Materials & Metallurgy, Northeastern University, Chinese Journal of Aeronautics, pp.187-192, 2006.
39. Easton, M., St John, D., Grain Refinement of Aluminum Alloys: Part I. The Nucleant and Solute Paradigms - A Review of the Literature, Metallurgical and Materials Transactions A, pp. 1613–1623, 1999.

40. Easton, M., St John, D., Grain Refinement of Aluminum Alloys: Part II. Confirmation of, and a Mechanism for, the Solute Paradigm, Metallurgical and Materials Transactions A, pp. 1625–1633, 1999.
41. Pattnaik, A.B., Das, S., Jha, B.B., Prasanth, N., Effect of Al–5Ti–1B Grain Refiner on the Microstructure, Mechanical Properties and Acoustic Emission Characteristics of Al5052 Aluminum Alloy, Journal of Materials Research and Technology, pp 171-179, 2015.
42. Ramachandran, T. R., Trace Elements in Aluminum and Aluminum Alloys, Workshop Lecture Notes, Indian Institute of Metals, Pune Chapter, 2006.
43. Martin, J. W., Precipitation Hardening, Pergamon Press, New York, NY, USA, 1968.
44. Orowan, E., Symposium on Internal Stresses, Institute of Metals, London, UK, 1947.
45. Kelly, A., Precipitation hardening, Progress in Materials Science, pp. 151–391, 1963.
46. Gleiter, H., Hornbogen, E., Precipitation Hardening by Coherent Particles, Materials Science and Engineering, pp. 285–302, 1967.
47. Mott, N. F., Nabarro, F. R. N., An Attempt to Estimate the Degree of Precipitation Hardening with a Simple Model, Proceedings of the Physics Society London, 1940.
48. Gerold, V., Haberkorn, H., On the Critical Resolved Shear Stress of Solid Solutions Containing Coherent Precipitates, Physica Status Solidi, pp. 675–684, 1966.
49. Hirsch, P. B., Kelly, A., Stacking Fault Strengthening, Philosophical Magazine, pp. 881–900, 1965.
50. Brown, L. M., Hamm, R. K., Strengthening Methods in Crystals, A. Kelly and R. B. Nicholson, Eds., Elsevier, London, UK, 1971.
51. McLean, D., Mechanical Properties of Metals, John Wiley & Sons, New York, NY, USA, 1962.
52. Meyers, M. A., Chawla, K. K., Mechanical Metallurgy, Prentice Hall, Englewood Cliffs, NJ, USA, 1984.
53. Roters, F., Raabe, D., Gottstein, G., Work Hardening in Heterogeneous Alloys, Acta Materialia, pp. 4181–4188, 2000.
54. Zhong, H., Rometsch, P.A., Cao, L., The Influence of Mg/Si Ratio and Cu Content on the Stretch Formability of 6xxx Aluminum Alloys, Material Science and Engineering A, pp. 688–697, 2015.

55. Sarkara, J., Kuttya, T.R.G., Wilkinsona, D.S., Embury, J.D., Tensile Properties and Bendability of T4 Treated AA6111 Aluminum alloys, Materials Science and Engineering, pp. 258–266, 2004.
56. Mukhopadhyay, P., Alloy Designation, Processing, and Use of AA6XXX Series Aluminum Alloys, ISRN Metallurgy, 2012.
57. Remoe, S.M., Marthinsen, K., The Effect of Alloying Elements on the Ductility of Al-Mg-Si Alloy, Materials Science & Engineering A, pp. 60-72, 2017.
58. Murayama, M., Hono, K., Miao, W.F., Laughlin, D.E., The Effect of Cu Additions on the Precipitation Kinetics in an Al-Mg-Si Alloy With Excess Si, Metallurgical and Materials Transactions A, pp. 239–246, 2001.
59. Miao, W.F., Laughlin, D.E., Effects of Cu Content and Preaging on Precipitation Characteristics in Aluminum Alloy 6022, Metallurgical and Materials Transactions A, pp. 361-371.
60. Svenningsen, G., Larsen, M. H., Nordlien, J. H., Nisancioglu, K., Effect of high temperature on intergranular corrosion of AlMgSi (Cu) model alloy, Corrosion Science, pp. 258-272, 2006.
61. Lievers, W.B., Pilkey, K., Lloyd, D.J., The Influence of Iron Content on the Bendability of AA6111 Sheet, Material Science and Engineering A, pp. 312-320, 2003.
62. Kearns, M. A., Cooper, P. S., Effects of Solutes on Grain Refinement of Selected Wrought Aluminum Alloys, Materials Science and Technology, pp. 650-654, 2013.
63. Shahrzad E, Precipitation Hardening Behaviour of AA6111, Ph. D Thesis, University of British Columbia, 2002.
64. Billur, E., Taylan, A., Three Generations of Advanced High-Strength Steels for Automotive Applications, Part I the First Generation, 2013.
65. Hall, J.N., Evolution of Advanced High Strength Steels in Automotive Applications. Presentation at Loint Policy Council, Auto/Steel Partnership, 2011.
66. Galan, J., Samek, L., Verleysen, P., Verbeken, K., Houbaert, Y., Advanced High Strength Steels for Automotive Industry, Revista de Metalurgia, pp.118-131, 2012.
67. Baluch, N.H., Mohamed, Z., Abdullah, C.S., Advanced High Strength Steel in Auto Industry: An Overview, Technology & Applied Science Research, pp. 686-689, 2014.

68. Matlock, D.K., et al., Recent Developments in Advanced High Strength Sheet Steels for Automotive Applications: An Overview, Jestech, pp. 1-12, 2012.
69. Srivastava, K.A., Bhattacharjee, D., Jha, G., Microstructural and Mechanical Characterization of C–Mn–Al–Si Cold-Rolled TRIP-Aided Steel, Material Science and Engineering A, pp. 549-557, 2007.
70. Chatterjee, S., Transformations in TRIP Assisted Steels: Microstructure and Properties, University of Cambridge, 2006.
71. Zaefferer, S., Ohlert, J., Bleck, W., A Study of Microstructure, Transformation Mechanisms and Correlation between Microstructure and Mechanical Properties of a Low Alloyed TRIP Steel, Acta Materialia, pp. 2765-2778, 2004.
72. Soulami, A., Choi, K.S., Shen, Y.F., Liu, W.N., Sun, X., Khaleel, M.A., On Deformation Twinning in a 17.5%Mn-TWIP steel: A Physically Based Phenomenological Model, Material Science and Engineering A, pp. 1402-1408, 2011.
73. Lindahl, B.B., Selleby, M., The Al-Fe-Mn System Revisited-An Updated Thermodynamic Description Using the Most Recent Binaries, Computer Coupling of Phase Diagrams and Thermochemistry (CALPHAD), pp. 86-93, 2013.
74. Bouaziz, O., et al., High Manganese Austenitic Twinning Induced Plasticity Steels: A Review of the Microstructure Properties Relationships. Current Opinion in Solid State and Materials Science, 2011, pp. 141-168.
75. Pisarik, S., Aken, D. V., Crystallographic Orientation of the $\varepsilon \rightarrow \alpha'$ Martensitic (Athermal) Transformation in a FeMnAlSi Steel. Metallurgical and Materials Transactions A, pp. 3173-3178, 2014.
76. Matlock, D.K., Speer J.G., Third Generation of AHSS: Microstructure Design Concepts, Microstructure and Texture in Steels, Proceeding of the International Conference on Microstructure and Texture in Steels and Other Materials, pp. 185-205.
77. Matsumura, O., et al., Effect of Retained Austenite on Formability of High Strength Sheet Steels. ISIJ International, pp. 1110-1116, 1992.
78. Krizan, D., Antonissen, J., Cooman, B. D., Retained Austenite Stability in the Cold-Rolled CMnAlSiP Micro-Alloyed TRIP Steels, Ghent University Academic Bibliography, 2004.
79. Caballero, F., et al., Design of Novel High Strength Bainitic Steels: Part 1. Materials Science and Technology, pp. 512-516, 2001.

80. Matlock, D.K., Bräutigam, V.E., Speer, J.G., Application of the Quenching and Partitioning (Q&P) Process to a Medium Carbon, High-Si Micro-Alloyed Bar steel, Materials Science Forum, 2003.
81. He., et al., Precipitation Stages and Reaction Kinetics of AlMgSi Alloys During the Artificial Aging Process Monitored by In-Situ Electrical Resistivity, Metals, 2018.
82. McGrath, M.C., et al., Mechanical Properties Dependence on Microstructures of Hot Rolled 3rd Generation Advanced High Strength Steels. Proceedings of the Materials Science & Technology Conference and Exhibition, ASM International, 2010.
83. Pisarik, S.T., Thermodynamics, and Crystallography of the $\gamma \rightarrow \epsilon \rightarrow \alpha'$ Transformation in Fe-Mn-Al-Si-C steels, Missouri University of Science and Technology, 2014.
84. Park, K.T., et al., Stacking Fault Energy and Plastic Deformation of Fully Austenitic High Manganese Steels: Effect of Al addition, Materials Science and Engineering: A, pp. 3651-3661, 2010.
85. Curtze, S., Kuokkala, V.T., Dependence of Tensile Deformation Behavior of TWIP Steels on Stacking Fault Energy, Temperature and Strain Rate, Acta Materialia, pp. 5129-5141, 2010.
86. Olson, G., & Cohen, M., A Mechanism for the Strain-Induced Nucleation of Martensitic Transformations. Journal of the Less-Common Metals, 1972 pp. 107-118.
87. Pisarik, S.T., et al., Developing a Third-Generation Advanced High-Strength Steel with Two-Stage Trip Behavior, Missouri University of Science and Technology, 2014.
88. Danaf, E.E., Kalidindi, S.R., Doherty, R.D., Influence of Grain Size and Stacking-Fault Energy on Deformation Twinning in FCC Metals, Metallurgical and Materials Transactions A, pp. 1223-1233, 1999.
89. Kim, H., Suh, D.W., Kim, N.J., Fe–Al–Mn–C Lightweight Structural Alloys: A Review on the Microstructures and Mechanical Properties, Science and Technology of Advanced Materials, 2013.
90. Zambrano, A.O., Stacking Fault Energy Maps of Fe-Mn-Al-C-Si Steels: Effect of Temperature, Grain Size, and Variations in Compositions, Journal of Engineering Materials Technology, 2016.
91. Frommeyer, G., Brux, U., Microstructures and Mechanical Properties of High Strength Fe-Mn-Al-C Light Weight TRIPLEX Steels, Steel Research International, pp. 627-633, 2007.

92. Frommeyer, G., Brüx, U., Neumann, P., Supra Ductile and High Strength Manganese TRIP/TWIP Steels for High Energy Absorption Purposes, ISIJ International, pp. 438-446, 2003.
93. Bleck, W., Phiu, O. K., Effects of Microalloying in Multiphase Steels for Car Body Manufacture, Microstructure, and Texture in Steels, pp. 145-163, 2009.
94. Grajcar, A., Kuziak, R., Zalecki, W., Third Generation of AHSS with Increased Fraction of Retained Austenite for the Automotive Industry, Archives of Civil and Mechanical Engineering, pp. 334-341, 2012.
95. Nemecek, S., Novy, Z., Stankova, H., Optimization of Heat Treatment of TRIP steels, 2nd International Conference, Heat Treatment and Surface Engineering in Automotive Applications, pp. 47-51, 2005.
96. Katsamas, A.I., Haidemenopoulos, G.N., Modelling of Transformations in TRIP Steels, Steel Research International, pp. 739-745, 2004.
97. Matlock, D.K., Speer, J.G., Processing Opportunities for New Advanced High Strength Sheet Steels, Materials and Manufacturing Processes, pp. 7-13, 2010.
98. Kuziak, R., Advanced High Strength Steels for Automotive Industry, Archives of Civil and Mechanical Engineering, pp. 104-116, 2008.
99. Hua, D., You, Z.T., Wei, L., Mei, L., Microstructures and Mechanical Properties of Fe-Mn-(A1 Si) TRIP/TWIP Steels, Journal of Iron and Steel Research International, pp. 66-70, 2006.
100. Grassel, O., Kruger, L., Frommeyer, G., Meyer, L.W., High strength Fe-Mn - (Al, Si) TRIP/TWIP Steels Development-Properties-Application, International Journal of Plasticity, pp. 1391-1409, 2000.
101. Ueji, R., Tsuchida, N., Terada, D., Tsuji, N., Tanaka, Y., Takemura, A., Kunishige, K., Tensile Properties and Twinning Behaviour of High Manganese Austenitic Steel with Fine-Grained Structure, Scripta Materialia, pp. 963-966, 2008.
102. Mahajan, S., Chin, G. Y., Formation of Deformation Twins in F.C.C. Crystals, Acta Metallurgica, 1973a, pp.1353-1362.
103. Venables, J.A., Deformation Twinning in Face-centred Cubic Metals, Cavendish Laboratory, University of Cambridge, 1961, pp. 379-396.

104. Barrett, C.D., Haitham, E.I., Kadiri, M.A., Breakdown of the Schmid Lam in Homogenous and Heterogenous Nucleation Events of Slip and Twining in Magnesium, Journal of the mechanics and physical of solids, 2012, pp. 2084-2099.

105. Cottrell, A.H., Bilby, B.A., A Mechanism for the Growth of Deformation Twins in Crystals, Taylor & Francis, 1951, pp.573-581.

106. Sleeswyk, A.W., ½<111> Screw Dislocations and the Nucleation of {112} <111> Twins in the BCC lattice, A Journal of Theoretical Experimental and Applied Physics, 1963, pp. 1467-1486.

107. Mahajan, S., Interrelationship Between Slip and Twining in BCC crystal, Acta Metallurgica, 1975, pp. 671-684.

108. Mahajan, S., Jin, S., Brasen, D., Microtwining in a Spinodally Decomposed Fe-Cr-Co Alloy, Acta Metallurgica, 1980, pp. 971-977

109. Venables, J. A., Deformation Twining in Face-Centered Cubic Metals, Philosophical Magazine, 1961, pp. 379-396.

110. J. W. Christian and S. Mahajan, “Deformation Twinning,” Progress in Materials Science, 1995, pp. 1-157.

111. Li, Y. L., Chang, Y., Yu, L., Liu, C., Chong, Li., Yuan, H., Jun, L.H., Zong, M., Effect of Deformation Twinning on High-Temperature Performance of Cold-Rolled S31042 Steel, Journal of Iron and Steel Research International, 2019.

112. Remy, L., The Interaction between Slip and Twinning Systems and the Influence of Twinning on the Mechanical Behaviour of FCC Metals and Alloys, Metallurgical Transaction A, 1981, pp. 387-408.

113. Fullman, R.L., Fisher,J.C., Formation of Annealing Twins during Grain Growth, Journal of Applied Physics, 1951, pp. 1350-1365.

114. Jin, Y., Annealing Twin Formation Mechanism, Ph.D. Dissertation, Ecole National Superieure des Mines De Paris, 2014.

115. Lin, B., Jin, Y., Hefferance, C.M., Li, S.F., Lind, J., Suter, R.M., Bernacki, M., Bozzolo, N., Rollett, A.D., Rohrer, G.S., Observation of Annealing Twin Nucleation at Triple Lines in Nickle during Grain Growth, Acta Metallurgica, 2015, pp.63-68.

116. Field, D.P., Bradford, L.T., Nowell, M.M., Lillo, T.M., The Role of Annealing Twins during Recrystallization of Cu. Acta Metallurgica, 2007, pp. 4233–4241.

117. Gleiter, H. The Formation of Annealing Twins. Acta Metallurgica. 1969, pp. 1421–1428.
118. Meyers, M.A., Murr, L.E., A Model for the Formation of Annealing Twins in F.C.C. Metals and Alloys. Acta Metallurgica, 1978, 26, pp. 951–962.
119. Li, C., Ma, B., Song, Y., Li, K., Dong, J., The Annealing Twins of Fe-20Mn-4Al-0.3C Austenite Steels during Symmetric and Asymmetric Hot Rolling, Metals, 2018, pp.882-894.
120. Mahajan, S., Pande, C.S., Imam, M.A., Rath, B.B., Formation of Annealing Twins in FCC Crystal, Acta Metallurgica, 1997, pp.2633-2638.
121. Mahajan, S., Chin, G.Y., Twin-Slip, Twin-Twin and Slip-Twin Interactions in Co-8wt.%Fe Alloy Single Crystals, Acta Mettalurgica, 1973b, pp. 173-179.
122. Bystrzycki, J., Przetakiewicz, W., Kurzydlowski, K.J., Study of Annealing Twins and Island Grains in FCC alloy, Acta Metallurgica, 1993, pp. 2639-2649.
123. Celikin, M., Li, D.H., Isac, M., Guthrie, R.I.L.**,** Horizontal Single Belt Strip Casting (HSBC) of Al-Mg-Sc-Zr Alloys. Light Metals, p.1037-1040, 2013.
124. Ge, S., Celikin, M., Isac, M., R.I.L. Guthrie., Mathematical Modeling and Microstructure Analysis of Al-Mg-Sc-Zr Alloy Strips Produced by Horizontal Single Belt Casting (HSBC), ISIJ International, pp. 294-303, 2014.
125. Luiten, E.E.M., Beyond Energy Efficiency-Actors, Networks and Government InterventIon in the Development of Industrial Process Technologies, Department of Science, Technology and Society. Utrecht University, 2001.
126. Bessemer, H., Improvement in the Manufacture of Iron and Steel, 1865, US.
127. Zapuskalov, N., Comparison of Continuous Strip Casting with Conventional Technology. ISIJ International, pp. 1115-1127, 2003.
128. Bessemer, H., Über die Herstellung von endlosem Blech aus schmiedbarem Eisen und Stahl Direkt aus Dem Flüssigen Metall (On the Production of Endless Sheet of Malleable Iron and Steel Directly from the Liquid Metal). Stahl und Eisen, 1891.
129. Cramb, A.W., New Steel Casting Processes for Thin Slabs and Strip. A Historical Perspective. Transactions of the Iron and Steel Society, pp. 61-76, 1989.
130. Norton, E., Notes on Experiments in Rolling Fluid Steel, The Iron Age, pp. 50-51, 1940.

131. Ferry, M., Institute of Materials Minerals and Mining, Direct Strip Casting of Metals and Alloys: Processing, Microstructure and Properties, Woodhead Publishing in Materials, Cambridge, 2006.
132. Hazelett, R.W., The Present Status of Continuous Casting between two Moving Belts. Iron and Steel Engineer, pp. 105-110, 1966.
133. Statistics, C.o., Steel Statistical Yearbook, International Iron and Steel Institute, Brussels, Belgium, 1980.
134. Haga, T., Twin Roll Casters for Aluminum Alloys. Journal of Japan Institute of Light Metals, pp. 509-520, 2009.
135. Birat, J., Innovation in Steel Continuous Casting: Past, Present and Future. Revue de Metallurgie, Cahiers d'Informations Techniques (France), pp. 1389-1399, 1999.
136. Birat, J.P., Steffen, R., Wilmotte, S., Steelmaking: State of the Art and Developments in Near-Net-Shape Casting of Flat Steel Products, European Commission: Düsseldorf, Germany, 1995.
137. Regan P.C., Szczypiorski W., Hazelett Twin-Belt Aluminum Strip-Casting Process: Caster Design and Current Product Programme of Aluminum Alloy Sheet, EMC '91: Non-Ferrous Metallurgy Present and Future. Springer, Dordrecht, p. 467-472, 1991.
138. Bagsarian, T., Unveiling project M. Iron Age New Steel, pp. 56-58, 1998.
139. McAloon, T., Coilcast Offers Second Chance to Allegheny Ludlum, Iron and Steelmaker (USA), 1991.
140. Warrian, P., Mulhern, C., Knowledge and Innovation in the Interface Between the Steel and Automotive Industries: The Case of Dofasco, Regional Studies, pp. 161- 170, 2005.
141. Office of Industrial Technologies, Project Fact Sheet - Strip Casting, Anticipating New Routes to Steel Sheet, Energy, Editor, U.S. Department of Energy, Washington, D.C, 1999.
142. Birat, J.P., Steffen, R., Current R&D Work on Near Net Shape Continuous Casting Technologies in Europe, Metallurgical Plant and Technology International, 1991.
143. Grosjean, J., et al., Thin Strip Casting Experiments at Irsid and Thyssen Stahl AG. Iron & Steelmaker, pp. 27-32, 1993.
144. Simon, R.W., et al., Direct Strip Casting on the Myosotis Industrial Pilot Plant. Metallurgical Plant and Technology, pp. 78-83, 1997.

145. Birat, J.P., The Future of Continuous Casting. Casting, Volume of AIST Steel Foundation, pp. 1-4, 2003.
146. Legrand, H., et al., Myosotis Direct Thin Strip Casting, Steel Times International (UK), 1997.
147. Anonymous, Direct strip casting by Nippon Metal Industry, Continuous Castings Supplement, 1987.
148. Gerber, H., Blazek, K., Wang, Y.H., Twin Roll Casting with an Electromagnetic Edge Dam, Industry Applications Conference, 2000. Conference Record of the 2000 IEEE. 2000.
149. Cramb, A., Strip Casting of Steels, Current Developments, Encyclopedia of Materials Science and Technology, New York, Elsevier Ltd, 2004.
150. Hohenbichler, G., et al., Eurostrip Direct Strip Casting of Carbon and Stainless Steels: Latest Results from Terni and Krefeld. Steel World (UK), pp. 40-44, 2002.
151. Walter, M., et al. Initial Operation Results of the Plant at Krefeld Works, Germany, Continuous Casting Conference, 2000.
152. Mascanzoni, A., Damasse, J., Hohenbichler, G., EUROSTRIP® Development of Carbon Steel Strip Casting, 8th Continuous Casting Conference, 2000.
153. Buchanan, S., Steel Recast in Future Mould, Metal Bulletin Monthly, pp. 16-17, 2003.
154. Guthrie, R.I.L., Herbertson, J.G., Continuous Casting of Thin Metal Strip, 1990.
155. De Reichelt, W.P.D.I.M., et al. 1990, Germany.
156. Guthrie, R.I.L., Steel Strips the Long and Winding Road, Iron and Steel Technology, 2006.
157. Guthrie, R.I.L., M. Isac, D. Li, Ab-Initio Predictions of Interfacial Heat Fluxes in Horizontal Single Belt Casting (HSBC), Incorporating Surface Texture and Air Gap Evolution, ISIJ International, pp. 1805-1813, 2010.
158. Guthrie, R.I.L., Isac. M., Design of Continuous Casting Processes for Steel, Handbook of Metallurgical Process Design, G.E. Totten, Funatani, K., Xie, L., Editors. 2006.
159. Moon, K.H., Physical and Mathematical Modeling of a Metal Delivery System for a Single Belt Caster, Department of Mining, Metals and Materials Engineering, Faculty of Engineering, McGill University: Montreal, QC, Canada, 2003.
160. Nystrom, R., Reichelt, W., Dubke, M., Strip Casting Experiences at MEFOS, Scandinavian Journal of Metallurgy, pp. 93-100, 2000.

161. Carlsson, G., et al., Single Belt Casting, A Promising Technique for the Production of Steel Strip, Scandinavian Journal of Metallurgy, pp. 242-248, 1997.
162. Recent Developments and Future Potentials of Near Net Shape Casting Belt Casting Te pp. 756-764, 2000.
163. Fischer, H., Schaperkotter, M., Recent Developments and Future Potentials of Near Net Shape Casting Belt Casting Technology, Materials Science Forum, pp. 3622-3627, 2010.
164. Spitzer, K.H., et al., Direct Strip Casting (DSC) An Option for the Production of New Steel Grades, Steel Research International, pp. 724-731, 2003.
165. Group, S., Salzgitter, Strip Casting Plant with Belt Casting Technology will be Built, in SMS Group Newsletter, SMS Group, 2010.
166. Yanagi, K., et al., Development of Twin Drum Strip Caster, Mitsubishi Heavy Industries Technical Review, 1996.
167. Yamada, M., et al., World's First Commercial Twin Drum Strip Casting Process at Hikari Works of Nippon Steel Corporation, Steel World (UK), pp. 49-54, 2002
168. Takeuchi, H., et al., Production of Stainless-Steel Strip by Twin Drum Strip Casting Process, Nippon Steel Technology, pp. 46-51, 1994.
169. Ibarrondo, I., Review of the Continuous Casting of Steel by Strip Casting Technology, Twin Roll Method System, Revista De Metalurgia, pp. 521-539, 2008.
170. Matsushita, T., et al., Development and Commercialization of Twin Roll Strip Caster IHI Engineering Review, 2009.
171. Waugh, J., Varcoe, D., Commercialisation of Strip Casting in South East Asia Iron & Steel Institute, 2000.
172. Campbell, P., et al., Recent Progress on Commercialization of CASTRIP Direct Strip Casting Technology at Nucor Crawfordsville. Metallurgist, pp. 507-514, 2004.
173. Sosinsky, D.J., et al., The CASTRIP Process Recent Developments at Nucor Steel's Commercial Strip Casting Plant, Metallurgist, pp. 691-699, 2008.
174. Corporation, N, Castrip Micro Mill Benefits both Customers and the Environment.
175. Castrip LLC, C. LLC, Editor., Charlotte, NC, US.
176. Kohl, C., SMS Demag in Castrip Deal, American Metal Market, 2000.
177. Smirnov, A.N., Safonov, V.M., Metallurgical Miniworks, Past, Present, and Future, Steel in Translation, pp. 47-52, 2007.

178. Switzerland, M., News. 2015, Available http://www.mainswitzerland.com/main/news.
179. Godat, M., et al., MAINSTRIP Twin Roll Casting Production Plant in 5^{th} European Continuous Casting Conference, L.R.d. Metallurgie, Editor 2005, La Revue de Metallurgie NICE, France.
180. Shin, Y., et al., Development of Twin Roll Strip Caster for Sheet Steels, Ironmaking & Steelmaking, pp. 35-44, 1995.
181. Moon, K.H., et al., Development of Strip Casting Process at POSCO/RIST, in Merton C, Flemings Symposium on Solidification and Materials Processing, H.D.B. Reza Abbaschian, Andreas Mortensen, Editor, 2000.
182. Choo, D.K., et al., Analysis and Prevention of Cracking During Strip Casting of AISI 304 Stainless Steel, Metallurgical and Materials Transactions A Physical Metallurgy and Materials Science, pp. 2249-2258, 2001.
183. Watanabe, T., Overview of Near Net Shape Continuous Casting for Steel Sheet, Tetsu-toHagane (Journal of the Iron and Steel Institute of Japan), pp. 107-116, 2002.
184. Chung, J.Y., Improvements & Innovations in the Continuous Casting Process at POSCO, Materials Science Forum, 2007.
185. Steel N.com, POSCO Constructs New Mass Production System of STS HRC with PoStrip Technology, 2010.
186. Lee, D.S., Lee, J.S., Kang, T., Robust Molten Steel Level Control in a Strip Casting Process, ISIJ International, pp. 1165-1172, 2005.
187. Mysteel.com, Current State and Outlook of the Continuous Strip Casting Technology in Korea and Baosteel, 2011, Available from: http://tech.mysteel.com.
188. Baosteel, Strip Casting Technology and Baosteel’s Pilot Plant, 2010.
189. Spitzer, K.H., et al., Method for Producing Hot Strips from Lightweight Steel, SMS Siemag AG: US, 2011.
190. Spitzer, K.H., DSC Strip Casting: Process Development and Perspectives for New Materials, Roderick Guthrie Honorary Symposium on Process Metallurgy, Montreal, Canada: McGill Metals Processing Centre, 2011.
191. Group, S., Successful Functional Tests BCT Belt Casting Plant Pre-Assembled, SMS Group Newsletter, 2012.
192. Spitzer, K.H., Pilot Plant at Peine, 2012.

193. Guthrie, R.I.L., Tavares, and R.P., Mathematical and Physical Modelling of Steel Flow and Solidification in Twin Roll/Horizontal Belt Thin Strip Casting Machines, Applied Mathematical Modelling, pp. 851-872, 1998.
194. Netto, P.G.Q., Tavares, R.P., R.I.L. Guthrie, Mathematical Models for Near Net Shape Casting Processes, ISIJ International, pp. S175-S179, 1996.
195. Tavares, R.P., Vertical Twin Roll Caster: Metal Mould Heat Transfer, Solidification and Product Characterization, Department of Mining and Metallurgical Engineering, McGill University, Montreal, Canada, 1997.
196. Tavares, R.P., Isac, M., R.I.L. Guthrie, Roll Strip Interfacial Heat Fluxes in Twin Roll Casting of Low Carbon Steels and their Effects on Strip Microstructure, ISIJ International, pp. 1353-1361, 1998.
197. Guthrie, R.I.L., et al., Measurements, Simulations, and Analyses of Instantaneous Heat Fluxes from Solidifying Steels to the Surfaces of Twin Roll Casters and of Aluminum to Plasma Coated Metal Substrates, Metallurgical and Materials Transactions B, Process Metallurgy and Materials Processing Science, pp. 1031-1047, 2000.
198. Xu, M., Isac, M., Guthrie, R.I.L., A Numerical Simulation of Transport Phenomenon During the Horizontal Single Belt Casting Process Using an Inclined Feeding System, Metallurgical and Materials Transactions B, pp. 1003-1013, 2018.
199. Guthrie, R.I.L., Isac, M., Li, D., Ab Initio Predictions of Interfacial Heat Flows During the High Speed Casting of Liquid Metals in Near Net Shape Casting Operations, Steel Research International, pp. 891-898, 2010.
200. Li, D., et al., Improving the Surface of AA6111 Sheet Material, Cast at High Speeds, Through the Use of Macroscopically Textured Substrates, TMS, The Minerals, Metals & Materials Society, 2009.
201. Li, D., et al, Numerical Prediction and Experiments on Casting Fe-Based Bulk Amorphous Strips on a Twin Roll Caster and on a Horizontal Single Belt Strip Caster, TMS, The Minerals, Metals & Materials Society, 2006.
202. Zhuang, L. Z., Langer, E. W., Effects of Alloy Additions on the Microstructures and Tensile Properties of Cast Co-Cr-Mo Alloy Used for Surgical Implants, Journal of Materials Science, pp 4324–4330, 1989.

203. Wang, P.F., Thomson, P.D.H., A Study of Pore Closure and Welding in Hot Rolling Process, Journal of Materials Processing Technology, pp. 95-102, 1996.

204. Fall. A. H, Monajatia. A, Khodabandehb. M.H, Fesharakib. H, Champliauda. M, Local Mechanical Properties, Microstructure, and Micro-Texture in Friction Stir Welded Ti-6Al-4V Alloy, Materials Science and Engineering A, p 234- 245.

205. Surface Roughness Determination Using 3D Nanovea Profilometer, Available https://nanovea.com/profilometry-roughness-finish.

206. Zhang, J., Zhao, Z., Wang, W., & Wang, Y., Comparison of the Microstructure of M2 Steel Fabricated by Continuous Casting and with a Sand Mould. *Metals*, pp. 560-571, 2019.

207. Homayonifar, P., Babaei, R., Attar, E., Shahinfar, S., Davami, P., Numerical Modeling of Splashing and Air entrapment in High-Pressure Die Casting, The International Journal of Advanced Manufacturing Technology, pp 219–228, 2008.

208. Merder, T., Pieprzyca, J., Optimization of Two Strand Industrial Tundish Work with Use of Turbulence Inhibitors, Physical and Numerical Modeling, Steel Research International, pp 1029-1039, 2012.

209. Vijayaram, T.R., Sulaiman, S., Hamouda, A.M.S., Ahmad, M.H.M., Numerical Simulation of Casting Solidification in Permanent Metallic Molds, Journal of Materials Processing Technology, pp. 29-33, 2006.

210. Páscoa, J. C., Silva, F. J., Pinheiro, J. S., Martins, D. J., Accuracy Details in Realistic CFD Modeling of an Industrial Centrifugal Pump in Direct and Reverse Modes, Journal of Thermal Science, pp 491–499, 2010.

211. Anderson, J., Dick, E., Degrez, G., Grundmann, R., Degroote, J., Vierendeels, J., Computational Fluid Dynamics, An Introduction, JohnF.Wendt Editor, 2009.

212. Howard, H.H., Computational Fluid Dynamics, Chapter 10, Fluid Mechanics (Fifth Edition), pp. 421-472, 2012.

213. Versteeg, H.K., Malalasekera, W., An Introduction to Computational Fluid Dynamics, United Kingdom, Longman, 1995.

214. Anderson, J.D. and Wendt, J., Computational Fluid Dynamics (Vol. 206). New York: McGraw-Hill, 1995.

215. Kurien, S., Taylor, M.A., Direct Numerical Simulations of Turbulence; Data Generation and Statistical Analysis, Los Alamos Science 29, pp. 142-151, 2005.

216. ANSYS Inc, ANSYS FLUENT 14.5- Theory Guide, ANSYS Inc., 2013.
217. Patankar, S.V., Numerical Heat Transfer and Fluid Flow, Hemisphere Publishing Crop, Washington, D.C., 1980.
218. Launder, B.E., Spalding, D.B., Mathematical Models of Turbulence, Academic Press, New York, 1972.
219. Yakhot, V., Orszag, S.A., Renormalization Group Analysis of Turbulence, Basic Theory, Journal of Scientific Computing, pp. 3-51, 1986.
220. T.H. Shih, W.W. Liou, A. Shabbir, Z. Yang, and J. Zhu, "A New k-ϵ Eddy Viscosity Model for High Reynolds Number Turbulent Flows", Computers & Fluids, 1995, Vol. 24 (No. 3): pp. 227-238.
221. Wilcox, D. C., Turbulence Modelling for CFD, DCW Industries Inc., Canada, 1993.
222. Doormaal, J. P. V., Raithby, G. D., Enhancement of the SIMPLE Method for Predicting Incompressible Fluid Flows, Numerical Heat Transfer, pp. 147-163, 1984.
223. Issa, R. I., Solution of the Implicity Discretized Fluid Flow Equations by Operator-Splitting, Journal of Computational Physics, pp. 40-65, 1985.
224. Charles, J., Berghezan, A., Lutts, A., High Manganese-Aluminum Austenite Steels for Cryogenic Applications, Some Mechanical and Physical Properties, J. Physics Colloques, pp. 619-623, 1984.